

# University of St Andrews



Full metadata for this thesis is available in  
St Andrews Research Repository  
at:

<http://research-repository.st-andrews.ac.uk/>

This thesis is protected by original copyright

**The Characterisation and NMR Study of the  
High-Temperature Superconductor  
(Y<sub>1-x</sub>Ca<sub>x</sub>)Ba<sub>2</sub>Cu<sub>3</sub>O<sub>6+δ</sub>.**



A Thesis Presented by

**Heather F. Booth**

to

The University of St. Andrews  
in Application for the Degree of  
**Doctor of Philosophy.**

May 1995



Th 13792

## Abstract

In this work, samples of  $(Y_{1-x}Ca_x)Ba_2Cu_3O_{6+\delta}$  for the range  $0.00 \leq x \leq 0.25$  were synthesised, characterised and studied by NMR. Reduced oxygen contents were obtained by quenching, with  $\delta = 0.16 \pm 0.02$  as determined by thermogravimetric analysis and iodometric titration. The measurement of  $\delta$  by electron microprobe analysis was also attempted. Structure and phase purity was confirmed by x-ray powder diffraction and electron microscopy. Lattice parameters did not vary over the doping range, indicating that any change in the properties are due to variations in the hole concentration.

Superconductivity was observed for  $x > 0.16$ , with maximum  $T_c \approx 40K$  at  $x = 0.25$ , as determined by resistivity and susceptibility measurement. The conductivity of the normal state of these samples was comparable to a poor metal. The samples became more insulating as the doping concentration decreased and antiferromagnetism was observed for  $x = 0.00$ . Semiconducting behaviour or variable range hopping mechanisms with a Coulomb gap were possible for the intermediate samples.

$^{89}Y$  NMR using a spin-echo technique on uniaxially aligned samples studied the doping concentration, orientation and temperature dependence of this system. A double-peaked structure was a common feature for samples aligned parallel to the magnetic field. Two models were found to explain the spectra, fractions of aligned and random samples, and possible local variations in the spin-susceptibility of the lattice caused by the introduction of calcium. Spin-lattice relaxation measurement indicated a possible Korringa-type temperature dependence.

Finally,  $^{63}Cu$  NMR for  $x = 0.25$  exhibited an unusual orientation dependence. In the perpendicular orientation a narrow line was observed, but was rapidly destroyed for all other orientations.

## **Declaration**

I, Heather F.Booth, hereby certify that this thesis, which is approximately 41500 words in length, has been written by me, that it is the record of work carried out by me and that it has not been submitted in any previous application for a higher degree.

I was admitted as a research student in October 1991 and as a candidate for the degree of Doctor of Philosophy in October 1991; the higher study for which this is a record was carried out in the University of St.Andrews between 1991 and 1995.

In submitting this thesis to the University of St.Andrews I understand that I am giving permission for it to be made available for use in accordance with the regulations of the University Library for the time being in force, subject to any copyright vested in the work not being affected thereby. I also understand that the title and abstract will be published, and that a copy of the work may be made and supplied to any bona fide library or research worker.

date 2/5/95.....signature of candidate..

I hereby certify that the candidate has fulfilled the conditions of the Resolution and Regulations appropriate for the degree of Doctor of Philosophy in the University of St.Andrews and that the candidate is qualified to submit this thesis in application for that degree.

date 2/5/95.....signature of supervisor..

## **Acknowledgements**

I would like to thank my supervisor Dr David Tunstall, for his endless help, support and patience throughout this project, especially during his 6 month absence from the department due to illness.

I would also like to thank Dr John Irvine, Susan Fray and Markus Koppers (formerly from the Department of Chemistry, University of Aberdeen) for the time and effort put into determining the concentration of oxygen in my samples.

The x-ray diffraction and electron microscopy experiments would not have been possible without the help of Angus Calder and Donald Herd (Geology Department), and Dr Phil Lightfoot (Chemistry Department). In addition, I extend my appreciation to all the technical support staff of both the Departments of Physics and Chemistry who have aided my research, particularly the cryogenics staff, the engineering workshop, and the electronics staff - for their repeated assistance when trying to run the MSL 500 Spectrometer.

Most of all, I am indebted to all of my family and friends. I would like to thank Geoff, Wendy, Bernd and Guangping Dai for their help and support throughout my PhD; all my friends for their encouragement when times were hard; and especially my parents and sister who have helped more than they could possibly imagine!

Finally I would like to thank the EPSRC for financing this project, and to both the EPSRC and the University of St. Andrews for providing the funds required for the conferences and meetings attended during the last 3<sup>1</sup>/<sub>2</sub> years.

# CONTENTS

## Chapter 1: INTRODUCTION

1.1. Overview .....	1
1.2. The Discovery of Superconductivity .....	1
1.3. High Temperature Superconductivity .....	5
<b>References</b> .....	<b>9</b>

## Chapter 2: REVIEW OF $\text{YBa}_2\text{Cu}_3\text{O}_{6+\delta}$ AND ITS PROPERTIES

2.1. Introduction .....	12
2.2. The $\text{YBa}_2\text{Cu}_3\text{O}_{6+\delta}$ Parent Compound .....	12
2.2.1. Structure .....	12
2.2.2. Superconductivity .....	14
2.2.3. Antiferromagnetism .....	15
2.2.4. Copper Valency Considerations .....	16
2.3. Doping of $\text{YBa}_2\text{Cu}_3\text{O}_{6+\delta}$ .....	18
2.3.1. Effect of Doping With Oxygen .....	18
2.3.2. Effect of Substituting Copper .....	20
2.3.3. Substitutions Away From The $\text{CuO}_2$ Planes .....	21
2.3.3.1. Substitution of Yttrium .....	21
2.3.3.2. Substitution of Barium .....	22
2.4. Substitution of Calcium into $\text{YBa}_2\text{Cu}_3\text{O}_{6+\delta}$ .....	23
2.4.1. Calcium Doping of Tetragonal $\text{YBa}_2\text{Cu}_3\text{O}_6$ .....	24
2.4.2. Calcium Doping of Orthorhombic $\text{YBa}_2\text{Cu}_3\text{O}_7$ .....	25
<b>References</b> .....	<b>27</b>

## **Chapter 3: BACKGROUND THEORY AND INFORMATION**

3.1. Overview .....	33
3.2. X-Ray Diffraction .....	33
3.3. Electron Microscopy .....	35
3.4. Resistivity - The Van der Pauw Method .....	40
3.5. Susceptibility .....	41
3.6. Nuclear Magnetic Resonance .....	43
3.6.1. Introduction .....	43
3.6.2. Simple Resonance Theory .....	43
3.6.3. Thermal Equilibrium and Spin Relaxation .....	45
3.6.4. Magnetic Shifts .....	46
3.6.4.1. The Chemical Shift .....	47
3.6.4.2. The Knight Shift .....	47
3.6.4.3. Temperature Dependency .....	48
3.6.4.4. Orientation Dependence of the Knight Shift .....	49
3.6.4.5. Quadrupole Effects .....	50
<b>References</b> .....	<b>54</b>

## **Chapter 4: EXPERIMENTAL TECHNIQUES**

4.1. Introduction .....	56
4.2. Synthesis .....	56
4.3. Sample Alignment .....	60
4.4. X-Ray Powder Diffraction .....	63
4.5. Electron Microscopy .....	64
4.6. Determination Of The Oxygen Content .....	66
4.6.1. Iodometric Titration .....	66
4.6.1.1. Experimental Precautions .....	67
4.6.1.2. Preparation Of A Starch Solution .....	67

4.6.1.3. Standardisation Of Sodium Thiosulphate .....	68
4.6.1.4. Standard Iodometry .....	68
4.6.2. Reductive Thermogravimetric Analysis .....	69
4.7. Critical Temperature Measurement .....	70
4.7.1. Resistivity Measurement .....	70
4.7.2. Susceptibility Measurement .....	73
4.8. Nuclear Magnetic Resonance (NMR) Study .....	76
4.8.1. Introduction .....	76
4.8.2. The General Pulsed NMR Spectrometer .....	76
4.8.3. The Bruker MSL 500 Spectrometer .....	78
4.8.4. Pulse Sequences .....	79
4.8.4.1. The Spin-Echo .....	79
4.8.4.2. Saturation Recovery .....	81
4.8.5. Fourier Transforms .....	83
4.8.6. $^{89}\text{Y}$ NMR Experiments .....	84
4.8.7. $^{63}\text{Cu}$ NMR Experiments .....	88
<b>References</b> .....	<b>90</b>

## **Chapter 5: EXPERIMENTAL RESULTS**

5.1. Introduction .....	93
5.2. Sample Synthesis And X-Ray Analysis .....	93
5.2.1. Sintered Samples .....	93
5.2.2. Reduced Oxygen Samples .....	96
5.3. Aligned Samples And X-Ray Analysis .....	98
5.4. Electron Microscopy .....	104
5.5. Results of Oxygen Content Determination .....	107
5.5.1. Iodometric Titration .....	107
5.5.2. Thermogravimetric Analysis .....	108
5.6. Critical Temperature Measurement .....	110

5.6.1. Resistivity Results .....	110
5.6.2. AC Susceptibility Results .....	116
5.7. Results of the $^{89}\text{Y}$ NMR Experiments .....	118
5.8. Results of the $^{63}\text{Cu}$ NMR Experiments .....	131
<b>References</b> .....	<b>134</b>

## **Chapter 6: DISCUSSION**

6.1. Introduction .....	135
6.2. Crystal Structure and Phase Purity .....	135
6.3. Oxygen Concentration .....	138
6.4. Superconducting Critical Temperature .....	140
6.5. Further Analysis of the Resistivity Results .....	142
6.6. Yttrium NMR .....	145
6.6.1. Double-Peaked Spectra .....	145
6.6.1.1. Aligned and Unaligned Fractions of Sample .....	146
6.6.1.2. Inequivalent Yttrium Sites Due to the Presence of Calcium .....	148
6.6.1.3. Comparison of the Two Models .....	153
6.6.2. Temperature Dependence of the Samples .....	155
6.6.3. Spin-Lattice Relaxation of the Samples .....	156
6.7. Copper NMR .....	157
<b>References</b> .....	<b>165</b>

## **Chapter 7: CONCLUSIONS AND FURTHER WORK** 167

<b>References</b> .....	<b>174</b>
-------------------------	------------

<b>Appendix 1: X-Ray Spectra For Samples Before Quenching</b>	<b>A1.1</b>
<b>Appendix 2: X-Ray Spectra For Quenched Powder Samples</b>	<b>A2.1</b>
<b>Appendix 3: X-Ray Spectra For Aligned Samples</b>	<b>A3.1</b>
<b>Appendix 4: Calculation of the Mobility</b>	<b>A4.1</b>
<b>Appendix 5: Contributions to Scientific Journals and Meetings</b>	<b>A5.1</b>

# Chapter 1

## INTRODUCTION

### 1.1. Overview

Great excitement followed the American Physical Society Meeting of 1987, as hundreds of scientists and engineers hurried back to their laboratories to confirm the report of an amazing breakthrough in superconductivity. This historical announcement was the discovery of a new type of superconducting material with a transition temperature of 92K, four times higher than that of any previously known superconductor. Suddenly, the revolutionary applications of superconductivity became possible: resistanceless flow of electric currents in power lines, strong magnetic fields in electromagnets, and even frictionless levitated transport systems!

This chapter aims to give the reader a flavour of the excitement of superconductivity from its discovery at the beginning of the century to the recent breakthrough into the realms of high temperature superconductivity. This is by no means a complete or technical account, but suggestions for further reading will appear throughout the text.

### 1.2. The Discovery Of Superconductivity

There is little doubt that the discovery of superconductivity by Kamerlingh Onnes at the University of Leiden in 1911<sup>1</sup> was a consequence of the liquefaction of helium three years earlier. Temperatures as low as 1K became possible, though research in this regime was considerably difficult and expensive.

At the time, Lorentz and Kelvin produced contradicting theories for the resistive behaviour of metals at low temperature. Lorentz's prediction was that the electrical resistivity of the metal would decrease as the temperature was lowered, to become negligible at absolute zero. He perceived the conduction electrons of the metal as being

like a gas of electrons and as the temperature decreased, the mean free path (undeflected by collisions) would get longer. To the contrary, Lord Kelvin supported the hypothesis that at lower temperature, the electrons would “condense” onto their atoms. He predicted that there would be a minimum in the resistivity at lower temperature, which would increase sharply as the condensation occurred.

Onnes now had the facilities to carry out the low temperature resistivity experiments and started by using gold and platinum. He observed a drop in the resistivity as he cooled the metals down, but towards a finite value dependent upon the purity of the metals being tested. Perhaps for pure metals, Lorentz’s theory would be correct. Mercury was an obvious choice to repeat the experiment, since in its liquid form it was much easier to purify than other metals. To his amazement, the electrical resistivity of mercury dropped abruptly to zero below a certain temperature, now referred to as the critical or transition temperature ( $T_c$ ). Furthermore, this behaviour was independent of impurity quantities and hence the property was not one just due to very pure metals: it was in fact a new phenomenon.

The resistivity in the superconducting state is not simply very small, it is indeed zero. The supercurrent decay in a solenoid has been studied by File and Mills<sup>2</sup>, by measuring the magnetic field associated with the supercurrent using precision nuclear magnetic resonance techniques. The conclusion was that the decay time was no less than 100,000 years. The importance of this discovery was soon realised: the possibility of transporting electrical currents over great distances without the heat losses normally encountered in resistive materials, and the production of magnetic fields much higher than those possible with conventional metals.

Research into the new phenomenon continued. The magnetic properties were found to be as dramatic as the electrical ones, and could not be explained by assuming it was a normal conductor with zero electrical resistance. Meissner and Ochsenfeld were the first to investigate the magnetic properties in 1933<sup>3</sup>. They found that as the material was cooled below its transition temperature, the magnetic flux originally present was suddenly expelled from its interior and re-routed to its periphery. Thus the

superconductor was a perfect diamagnet. This was deemed possible by setting up surface currents in the superconductor, establishing an opposing magnetisation and cancelling the interior field. The absence of magnetic flux in a superconductor is now known as the Meissner effect. The industrial possibilities for this were astounding, since frictionless motion could become possible by magnetic levitation.

As a consequence of the Meissner effect, the electrical currents set up must be superficial. This was confirmed by Stark and Steiner in 1937<sup>4</sup>. However, it was obvious that the current could not be entirely superficial and that there must be a finite depth of current penetration, which would also be the depth of penetration of the magnetic field into the superconductor. The field decays exponentially into the superconductor, vanishing deeper into the interior. This is known as the penetration depth and is denoted by  $\lambda$ .

It was disappointing to discover that for these materials, now known as Type I or “soft” superconductors, a magnetic field as small as a few hundred oersteds penetrated abruptly into the sample above a critical magnetic field<sup>5</sup>. Similarly, there was an upper limit on the current density, above which it reverted back to the normal state<sup>6</sup>. The reason for this may be explained simply. It costs the superconductor a certain amount of energy to set up the supercurrents required to expel the magnetic field from its interior. For low magnetic fields, this cost is counterbalanced by the gain in energy the sample obtains by remaining in the superconducting state. For high fields however, the cost of setting up the currents becomes too large and hence superconductivity is destroyed.

As research continued, superconductivity was found in metal alloys with higher critical temperatures up to 23K<sup>7</sup>. These were interesting in that they were capable of carrying large current densities. They are known as Type II superconductors and exhibit features quite distinct from Type I materials (see Figure 1.1). For these superconductors, the energy required to expel large magnetic fields from the interior is reduced by allowing some field to penetrate. This penetration is not uniform throughout

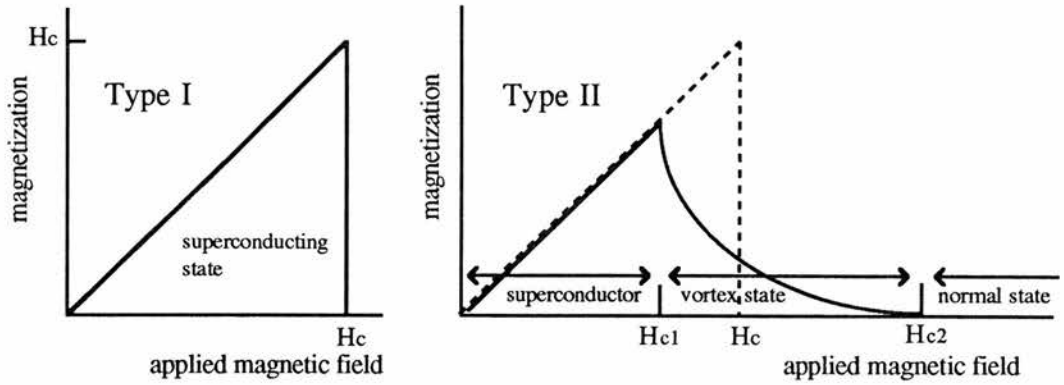


Figure 1.1. The magnetisation of Type I and Type II superconducting materials in an applied magnetic field.

the sample but occurs in fluxoids, ie. bundles of magnetic field lines, each with circulating shielding currents called vortices. Where this occurs the material is in the normal state, but the surrounding parts remain superconducting. For most conventional superconducting materials, these vortices are pinned to the lattice by defects or impurities, thus not affecting the current flow in the superconductor.

The vital clue which brought about a theory for superconductivity came about in 1950. The critical temperature was found to vary with isotopic mass<sup>8,9,10</sup>, indicating the importance of an electron-phonon interaction for superconductivity. An all-encompassing theory of superconductivity came in 1957 by Bardeen, Cooper and Schrieffer, known as BCS theory<sup>11,12</sup>. This demonstrated that the local electrical polarization of the lattice associated with the deformation, could interact with another electron to indirectly produce an attractive force between the two electrons. Cooper showed that any attractive force between two electrons, no matter how weak, would produce an instability in the Fermi sea and if some bound pairs were formed, these would lead to further pairing<sup>13</sup>. This co-operative effect resulted in a ground state separated from the allowed excited states by an energy gap. Cooper pairs, as they are now known, are achieved by binding an electron with wave vector  $+\mathbf{k}$  and an electron with  $-\mathbf{k}$ , with their spins anti-parallel so that the net spin is zero. The net linear momentum of a Cooper pair is zero, the mass  $2m$  and charge  $2e$ . Each has a total wavevector  $+\mathbf{k} - \mathbf{k} = 0$ , which corresponds to a condensation in  $\mathbf{k}$ -space. The range of the binding interaction of the pair is called the Pippard coherence length<sup>14</sup>,  $\xi_0$ . The

coherence length is of the order  $1\mu\text{m}$ , indicating that of the order  $10^6$  Cooper pairs exist in a volume  $\xi_0^3$ .

Unfortunately, by the very nature of the BCS theory of superconductivity, it was unlikely that superconductivity would ever be found above 30K in any material.

### **1.3. High Temperature Superconductivity**

It will come as no surprise then, that the discovery of the new ceramic high temperature superconductors in 1986 caused an explosive increase in superconductivity research. It was Bednorz and Müller who were the first to confirm superconductivity in the La-Ba-Cu-O system in 1986<sup>15</sup>, earning them the Nobel prize in Physics the following year. There was great excitement at the possibility of non-BCS-like superconductivity, and that room-temperature superconductivity may not be impossible after all. Hundreds of research workers began the search for new high  $T_c$  materials. Within months, researchers Chu and Wu raised the transition temperature of  $\text{La}_{2-x}\text{Sr}_x\text{CuO}_4$  from 35K to above 50K with the application of pressure<sup>16</sup>. Whilst attempting to produce a similar pressure effect by chemical substitution, they discovered a new compound,  $\text{YBa}_2\text{Cu}_3\text{O}_7$ , with a  $T_c$  of 92K<sup>17</sup>, the first to be above the temperature of liquid nitrogen (77K). Since then, many cuprate materials have been found to exhibit these superconducting properties, and the critical temperature increased further. A diagram of superconductivity progress is shown in Figure 1.2. To date, the system with the highest critical temperature reported (and confirmed) is for  $\text{HgBa}_2\text{Ca}_2\text{Cu}_3\text{O}_{8+\delta}$  with  $T_c=135\text{K}$  at ambient pressure, increasing to 153K at 150kbar<sup>18</sup>, half-way between absolute zero and room temperature.

The search for high temperature superconductors has gone even further afield to novel compounds such as organic materials<sup>19,20</sup> and “bucky-balls”. The new elemental form of carbon,  $\text{C}_{60}$ , was discovered in 1985<sup>21</sup>, and led to the discovery that fullerene compounds were superconductors when doped, for example  $\text{K}_3\text{C}_{60}$  with  $T_c=18\text{K}$ <sup>22</sup> and  $\text{Rb}_3\text{C}_{60}$  with  $T_c=28\text{K}$ <sup>23</sup>.

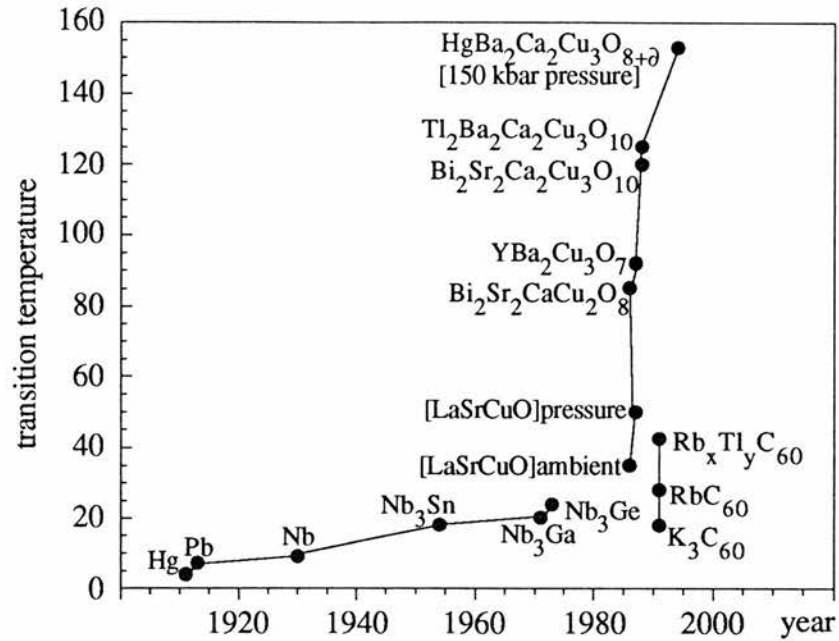


Figure 1.2. Progress in superconductivity with known transition temperatures.

The high  $T_c$  ceramic materials exhibit different properties to their conventional counterparts. Their critical field is surprisingly high, indicating that they may be useful for producing very powerful magnets. Unfortunately the maximum critical current density possible for the superconducting state is smaller than that of conventional materials, which is thought to be due to the lack of pinning of the fluxoids. An indication of a different superconducting mechanism is demonstrated by the fact that the critical temperature is insensitive to isotopic mass, a property important to BCS theory. The charge carriers do still appear to be bound in pairs, but the coherence length  $\xi_0$ , is much shorter by a factor of approximately 100. An energy gap is also evident, suggesting that the excitations of the superconductor may still be considered as quasi-particles, though their nature is still unknown.

All the cuprate superconductors have perovskite structure and have parallel layers of  $\text{CuO}_2$  planes which act as the conduction path. These planes account for the highly anisotropic behaviour of the compounds and play an important role for superconductivity. As a general rule for the cuprates, the superconducting transition temperature increases with the number of  $\text{CuO}_2$  planes in the unit cell. The novel

properties, both in the normal and superconducting states, are believed to arise from the strongly correlated motion of charge carriers in the copper oxide planes. The other ions in the crystal provide structural stability and control the number of charge carriers.

As yet, there is no firmly established theory to explain even the normal state transport properties of the cuprate superconductors. The BCS theory of phonon-assisted electron pairing could not produce the high  $T_c$  values observed. At present there are several approaches to the theory of the cuprate superconductors. The first is essentially similar to BCS theory, ie. pairing of fermionic quasi-particles below the transition temperature due to an indirect attractive interaction via lattice phonons, spin fluctuations or excitonic electron states<sup>24,25</sup>. The two-dimensional nature of the conduction path, and the strong correlation of the quasi-particles could account for the significant differences in the electronic properties of these materials.

Another approach, suggested by Philip Anderson, is a resonating valence bond or RVB model<sup>26,27,28,29</sup>. This postulates an entirely new state of matter, where the charge and the spin of the conduction electrons/holes dissociate into two distinct quasi-particles. These have been named holons and spinons. A holon has unit charge and no associated spin, and a spinon has  $1/2$  integral spin but no charge. This approach does not violate the familiar rules of single-particle statistics. Further, it has been shown<sup>30</sup> that two-dimensionality could lead to what are known as anyon charge carriers, with statistics intermediate between those of fermions and bosons.

The third approach is one which assumes that paired electron boson states exist above  $T_c$ <sup>31,32,33,34</sup>. This is the formation of bipolarons, which are associated with local lattice distortions. Superconductivity would result from the Bose-Einstein condensation of the paired states at  $T_c$ , analogous to the superfluid transition in liquid helium.

So, there is still a long way to go before high-temperature superconductivity is completely understood. Hundreds of research scientists all over the world continue to synthesise and characterise new superconducting materials, towards the ultimate achievement : room-temperature superconductivity.

Further information concerning the history of superconductivity<sup>35,36,37</sup> and progress in high-temperature superconductivity<sup>38,39,40</sup> may be found in these additional texts and review articles. Superconducting properties and characteristics<sup>41,42,43,44,45,46</sup> and current theories<sup>47,48</sup> may also be found in greater detail elsewhere.

## References

- 1 H.K.Onnes. *Akad. van Wetenschappen (Amsterdam)* **14**, 113 (1911) 818.
- 2 J.File and R.G.Mills. *Phys. Rev. Lett.* **10** (1963) 93.
- 3 W.Meissner and R.Ochsenfeld. *Naturwissenschaften*, **21** (1933) 787.
- 4 J.Stark and K.Steiner. *Phys. Z.*, **38** (1937) 277.
- 5 H.K.Onnes. *Commun. Phys. Lab. Univ. Leiden*, **139f** (1914).
- 6 H.K.Onnes. *Commun. Phys. Lab. Univ. Leiden*, **Suppl. no.34** (1913).
- 7 J.R.Gavaler. *Appl. Phys. Lett.*, **23** (1973) 480.
- 8 E.Maxwell. *Phys. Rev.*, **78** (1950) 477.
- 9 E.Maxwell. *Phys. Rev.*, **79** (1950) 173.
- 10 C.A.Reynolds, B.Serin, W.H.Wright and L.B.Nesbit. *Phys. Rev.* **78** (1950) 487.
- 11 J.Bardeen, L.N.Cooper and J.R.Schrieffer. *Phys. Rev.*, **106** (1957) 162.
- 12 J.Bardeen, L.N.Cooper and J.R.Schrieffer. *Phys. Rev.*, **108** (1957) 1175.
- 13 L.N.Cooper. *Phys. Rev.*, **104** (1956) 1189.
- 14 A.B.Pippard. *Proc. R. Soc. A*, **216** (1953) 547.
- 15 J.G.Bednorz and K.A.Müller. *Z. Phys. B*, **64** (1986) 189.
- 16 C.W.Chu, P.H.Hor, R.L.Meng, L.Gao and Z.J.Huang. *Science*, **235** (1987) 567.
- 17 M.K.Wu, J.R.Ashburn, C.J.Torng, P.H.Hor, R.L.Meng, L.Gao, Z.J.Huang, Y.Q.Wang and C.W.Chu. *Phys. Rev. Lett.*, **58** (1987) 908.
- 18 C.W.Chu, L.Gao, F.Chen, Z.J.Huang, R.L.Meng and Y.Y.Xue. *Nature*, **365** (1993) 323.
- 19 D.Jérome. *Science*, **252** (1991) 1509.
- 20 A.E.Underhill. *J. Mater. Chem.*, **22** (1992) 1
- 21 H.W.Kroto, J.R.Heath, S.C.O'Brien, R.F.Cure and R.E.Smalley. *Nature*, **318** (1985) 162.

- 22 A.F.Hebard, M.J.Rosseinsky, R.C.Haddon, D.W.Murphy, S.H.Glarum, T.T.M.Palstra, A.P.Ramirez and A.R.Kortan. *Nature*, **350** (1991) 600.
- 23 M.J.Rosseinsky, A.P.Ramirez, S.H.Glarum, D.W.Murphy, R.C.Haddon, A.F.Hebard, T.T.M.Palstra, A.R.Kortan, S.M.Zahurak and A.V.Makhija. *Phys. Rev. Lett.*, **66** (1991) 2830
- 24 J.Friedel. *J.Phys.[Condensed Matter]*, **1** (1989) 7757
- 25 A.A.Mikhailovsky, S.V.Shulga, A.E.Karakozov, O.V.Dolgov and E.G.Maksimov. *Solid State Commun.*, **80** (1991) 511.
- 26 P.W.Anderson. *Science*, **235** (1987) 1196.
- 27 P.W.Anderson. *AIP Conf. Proc.(USA)*, **169** (1988) 141.
- 28 P.W.Anderson, G.Baskaran, Z.Zou, J.Wheatley, T.Hsu, B.S.Shastry, B.Doucot and S.Liang. *Physica C*, **153-155** (1988) 527. (International Conference on High Temperature Superconductors and Materials and Mechanisms of Superconductivity, Interlaken, Switzerland. 28 Feb - 4 March 1988.)
- 29 P.W.Anderson and R.Schrieffer. *Phys. Today*, **44** (1991) 54
- 30 R.B.Laughlin. *Science*, **242** (1988) 525.
- 31 J.W.Lynn (ed.). “*High Temperature Superconductivity*”, Springer-Verlag, Berlin (1990).
- 32 R.Micnas, J.Ranninger and Robaszkiewicz. *Rev. Mod. Phys.*, **62** (1990) 113.
- 33 N.F.Mott. *Physica A*, **168** (1990) 221.
- 34 N.F.Mott. *Advances in Physics*, **39** (1990) 55.
- 35 C.J.Gorter. *Rev. Mod. Phys.*, **36** (1964) 1.
- 36 D.Shoenberg. “*Superconductivity*”, Cambridge University Press (1952).
- 37 G.Vidali. “*Superconductivity. The Next Revolution?*”, Cambridge University Press (1993).
- 38 C.Gough. *Physics World*, (December 1991) 26.
- 39 N.Bontemps, R Combescot and P.Monod. *La Recherche* (in French), **23** (1992) 180.

- 40 J.-M.Triscone and Ø.Fischer. *La Recherche* (in French), **24** (1993) 279.
- 41 D.P.Tunstall and W.Barford (eds.). "*High Temperature Superconductivity*", Proceedings of the Thirty-Ninth Scottish Universities Summer School in Physics, St.Andrews, June 1991.
- 42 V.Z.Kresin and S.A.Wolf. "*Fundamentals of Superconductivity*", Plenum Press, New York (1990).
- 43 C.Kittel. "*Introduction to Solid State Physics*" (Sixth Edition), John Wiley and Sons, Inc. (1986).
- 44 D.R.Tilley and J.Tilley. "*Superfluidity and Superconductivity*", (Third Edition), Adam Hilger (1990).
- 45 D.M.Ginsberg. "*Physical Properties of High Temperature Superconductors*", Volumes I, II, III and IV. World Scientific Publishing Co. Pte, Ltd.
- 46 J.C.Phillips. "*Physics of High- $T_c$  Superconductors*", Academic Press Inc.(1989)
- 47 J.P.Carbotte. *Rev. Mod. Phys.*, **62** (1990) 1027.
- 48 V.J.Emery. *Physica B*, **169** (1991) 17.

## Chapter 2

# REVIEW OF $\text{YBa}_2\text{Cu}_3\text{O}_{6+\delta}$ AND ITS PROPERTIES

### 2.1. Introduction

To understand more fully the characteristics and behaviour of the ceramic high-temperature superconductors, this chapter gives the reader a foundation of knowledge, especially regarding the  $\text{YBa}_2\text{Cu}_3\text{O}_{6+\delta}$  series of compounds.

Initially, the parent compound will be described, with its crystal structure, conduction behaviour, range of phases, and other information considered relevant to the work undertaken here. A brief account of the effect of doping onto various sites of the lattice will also be given.

Detail will be given for the calcium doped compound, and will include a summary of the work carried out by other researchers in this field.

### 2.2. The $\text{YBa}_2\text{Cu}_3\text{O}_{6+\delta}$ Parent Compound

#### 2.2.1. Structure

$\text{YBa}_2\text{Cu}_3\text{O}_{6+\delta}$  has an open, layered structure and is generally considered to be a perovskite, tripled along the **c**-axis of the unit cell<sup>1,2</sup>. The material is orthorhombic (and superconducting) with space group Pmmm for values of  $\delta \geq 0.4$ . The oxygen which resides in the Cu(1) layers, takes the O(4) sites along the **b**-axis forming Cu-O chains. Typical lattice parameters are **a**=3.822Å, **b**=3.891Å and **c**=11.677Å ( $\approx 3\mathbf{a}$ ). At lower oxygen,  $\delta \leq 0.4$ , the crystal structure is tetragonal with space group P4/mmm. The small quantity of oxygen present above  $\delta=0$ , distributes randomly in the **ab** plane of the Cu(1) layers, and so the **a** and **b** axes become equivalent. The unit cells of both

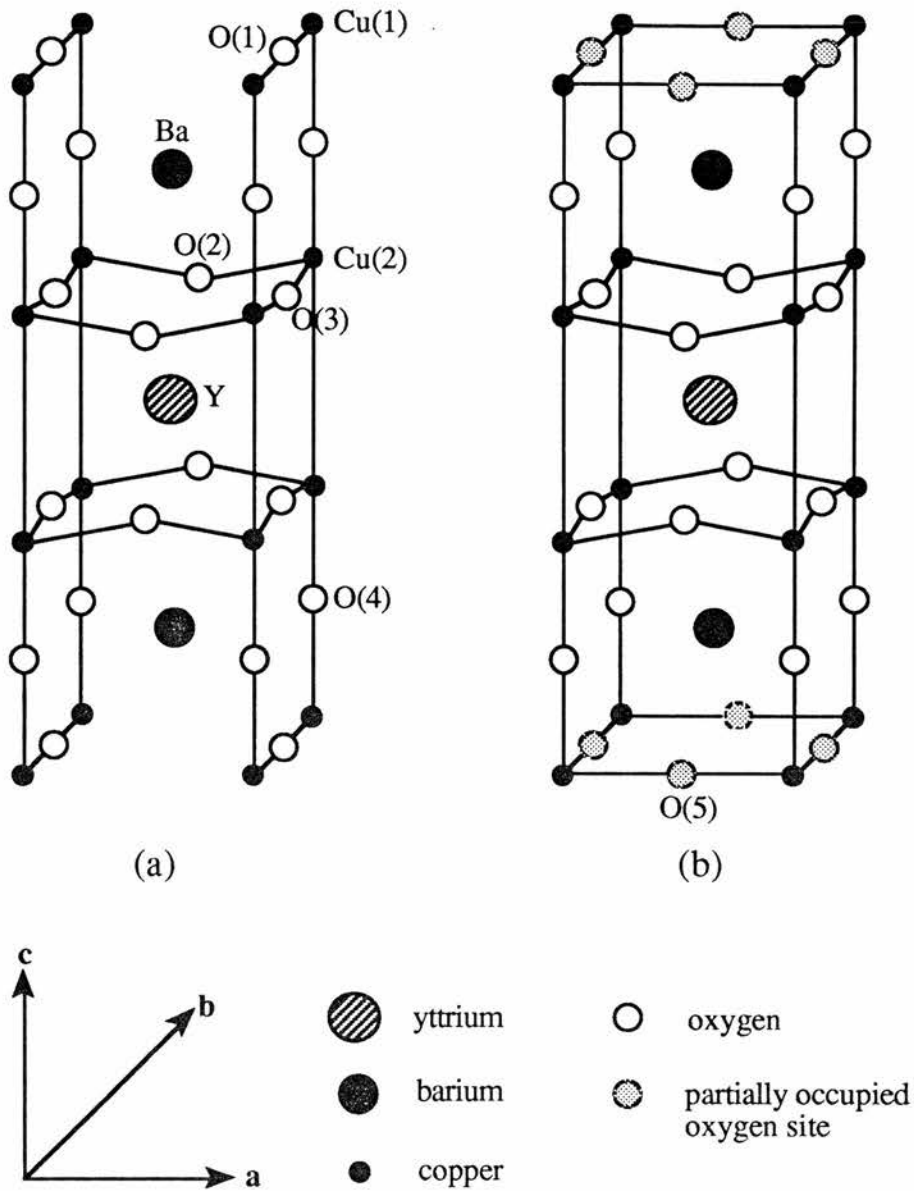


Figure 2.1. The unit cells of  $YBa_2Cu_3O_{6+\delta}$  for (a)  $\delta \geq 0.4$  with orthorhombic structure, and (B)  $\delta < 0.4$  with tetragonal structure.

the orthorhombic and tetragonal structures are represented in Figure 2.1, as determined by neutron scattering experiments from a powder sample<sup>3</sup>. In a true perovskite the copper would be octahedrally coordinated, as shown in Figure 2.2, which would make the formally filled structure  $YBa_2Cu_3O_9$ . In actual fact, for the deficient material the tripled perovskite contains two inequivalent copper planes sandwiched between barium planes for Cu(1), and yttrium and barium planes for Cu(2). Also comparing to the original perovskite structure, no oxygen exists in the yttrium plane (leaving Cu(2) five-

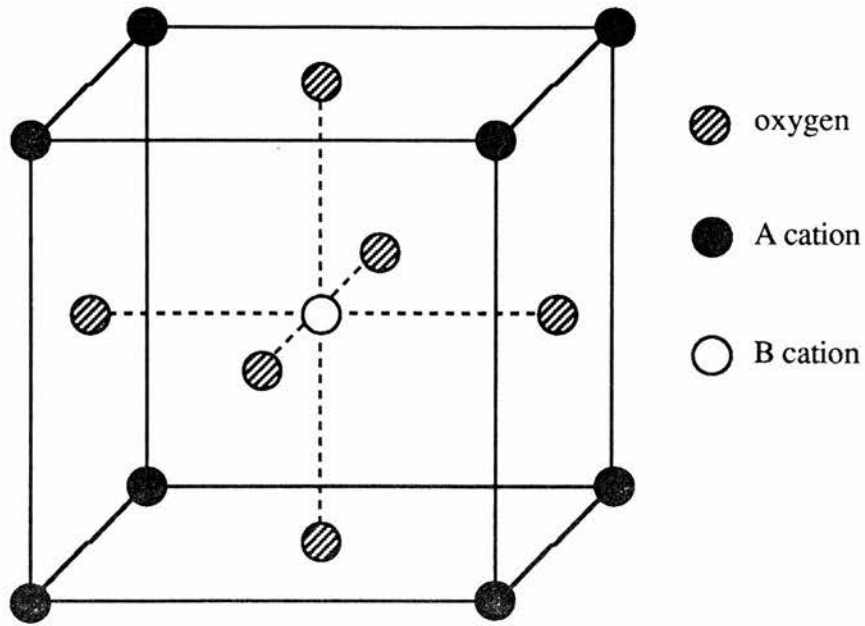


Figure 2.2. The true perovskite structure.

fold co-ordinated), and some oxygen is lost from the Cu(1) plane (making Cu(1) four-fold co-ordinated).

The above structures have been determined by Bragg diffraction techniques. In principle these techniques provide information on both the order and disorder of the lattice. However, they are generally dominated by the ordered contribution. Both diffraction and other techniques<sup>4,5</sup> suggest that substantial disorder may occur in these compounds.

### 2.2.2. Superconductivity

$YBa_2Cu_3O_{6+\delta}$  is superconducting for values of  $\delta$  between 0.4 and 1.0, with transition temperatures reaching as high as  $T_c=94K$ . The superconducting phase coincides with the structural orthorhombic phase. The change of properties which occur when doping with oxygen are discussed further in Section 2.3.1. Through doping studies (see Section 2.3), the Cu(1) and Cu(2) sites have been found to contribute in different ways to superconductivity. The Cu(2) sites form two conducting

near-neighbour parallel planes, which support superconductivity. The Cu(1) sites however, form Cu-O chains along the **b**-axis, which have been found to act as a reservoir of conduction holes for superconductivity in the planes. The decrease in  $T_c$  observed when disordering occurs in the oxygen chains, implies that the chains play a major role in the mechanism of high temperature superconductivity.

The variation of superconducting transition temperatures with hole concentration ( $T_c$  increases with the number of holes) has been the subject of intensive study. The  $YBa_2Cu_3O_{6+\delta}$  system moves from an underdoped regime with a maximum  $T_c$  of 94K for  $x=0.94$ , to an overdoped regime for  $0.94 < x < 1$  where  $T_c$  decreases to 92K<sup>6,7,8</sup>.

### **2.2.3. Antiferromagnetism**

Antiferromagnetism is observed for the tetragonal phase of  $YBa_2Cu_3O_{6+\delta}$  ( $0 \leq \delta \leq 0.4$ ). The possible importance of the observed antiferromagnetic interactions to superconductivity in the perovskites was initially stressed by Anderson<sup>9</sup>. A number of models have been proposed for electron (or hole) pairing which require strong antiferromagnetic superexchange interactions and spin fluctuations between the copper atoms<sup>10,11</sup>.

The antiferromagnetic arrangement in the cuprate lattice has been determined by muon spin rotation experiments<sup>12</sup>, superlattice reflections observed by neutron diffraction experiments<sup>13</sup> and confirmed by other groups<sup>14,15,16</sup>. This is shown schematically in Figure 2.3.(a) for low oxygen content. To simplify the diagram, only the copper atoms have been shown. The non-magnetic  $Cu^{1+}$  ions present at the Cu(1) sites do not order and are represented by the patterned sites in the lattice. The black and white sites represent the magnetic  $Cu^{2+}$  ions, black being of opposite spin to white. The spin direction is perpendicular to the **c**-axis, and as can be seen from the diagram, the copper atoms within the  $CuO_2$  layers (intraplanar) couple to form a simple antiferromagnetic Néel lattice, as do the planes to each other (interplanar)<sup>17</sup>. Due to the

position of the copper atoms in the lattice, the two-dimensional antiferromagnetic correlations are stronger than the three-dimensional ones.

As the oxygen concentration is increased, but the system remains tetragonal, some of the  $Cu^{1+}$  ions are converted to  $Cu^{2+}$ -ions, leading to a frustration of the interplanar coupling and eventually to a second type of ordering<sup>18,19</sup>. This ordering can be seen schematically in Figure 2.3.(b). Again the black and white sites represent opposite spins perpendicular to the  $c$ -axis. The 3d hole of the  $Cu^{2+}$  ion in the Cu(1) site (B layer in diagram) is orthogonal to the 3d holes of the  $Cu^{2+}$  neighbours in the Cu(2) planes (A and C in the diagram), and it follows that the A-B-C coupling is antiferromagnetic<sup>20</sup>. The decrease in the Néel temperature and ordered moment<sup>21</sup> with increasing oxygen can be explained by these fluctuations in the local order.

There is no evidence of antiferromagnetic ordering in the superconducting, orthorhombic phase. However, magnetic susceptibility measurements suggest two-dimensional magnetic behaviour just above the orthorhombic-tetragonal transition which undergoes a smooth and gradual changeover to Pauli-like behaviour at higher oxygen concentrations.

#### **2.2.4. Copper Valency Considerations**

All the high temperature superconductors discovered so far contain an element whose oxidation state can vary over a range of values. This element is copper for all the cuprate superconductors, and its oxidation state depends on the oxygen stoichiometry and metal content. For  $YBa_2Cu_3O_{6+\delta}$  ( $0 \leq \delta \leq 1$ ), yttrium and barium can only be in the  $3+$  and  $2+$  oxidation states respectively (any other oxidation state is extremely unlikely), and so the variable oxidation state occurs for copper. Copper is commonly found in the  $1+$  or  $2+$  states and although the  $3+$  state is rare, it is not unknown. By changing the quantity of oxygen in this system, the relative amounts of  $Cu^{1+}$ ,  $Cu^{2+}$  and  $Cu^{3+}$  change, thus affecting the quantity of available charge carriers (holes). When  $\delta=1$ , one-third of the copper is in the  $3+$  state and two-thirds is in the  $2+$  state. At  $\delta=0.5$  all the copper is  $2+$ , and as the oxygen content is reduced towards  $\delta=0$ ,

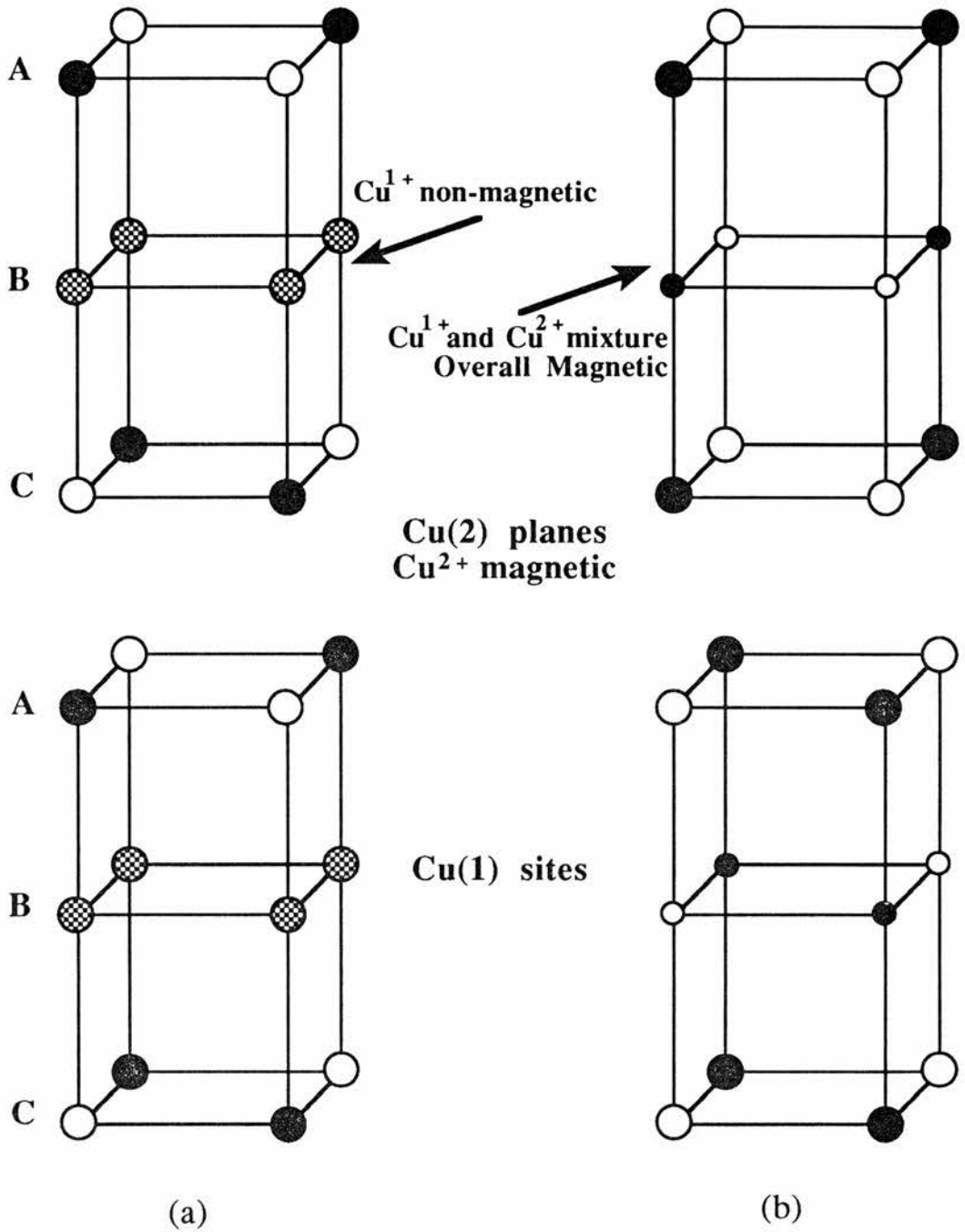


Figure 2.3. Antiferromagnetic ordering in the oxygen deficient  $YBa_2Cu_3O_{6+\delta}$  system for (a)  $\delta \approx 0$ , and (b)  $\delta > 0$  but still in the tetragonal phase.

one third of the coppers become  $\text{Cu}^{1+}$ . The superconducting state occurs for this system when the average oxidation state exceeds  $2^+$ .

Further studies on the oxidation states of the copper in these superconducting materials has cast doubt on the existence of integer copper valencies<sup>22,23,24</sup>. It would seem that any description of localised holes in  $\text{YBa}_2\text{Cu}_3\text{O}_{6+\delta}$  is simplistic, and would be better described by holes in electronic bands.

### **2.3. Doping of $\text{YBa}_2\text{Cu}_3\text{O}_{6+\delta}$**

The properties of the parent compound  $\text{YBa}_2\text{Cu}_3\text{O}_{6+\delta}$  may be changed dramatically by substituting atoms at the various possible sites in the lattice. The effect of each substitution depends on the importance of the role of the particular site onto which the substitution is made. It is easily possible to vary the quantity of oxygen in  $\text{YBa}_2\text{Cu}_3\text{O}_{6+\delta}$  between  $\delta=0$  and  $\delta=1$  and the effects of oxygen doping are outlined in Section 2.3.1. A common position for substitution is onto the copper site, which rapidly destroys any superconducting properties and appears to directly affect the carrier concentration and disrupt order in the conduction path. The other substitution positions are away from the conduction path, for example onto the yttrium or barium sites. For these, changes are usually in the crystal lattice and there are indirect effects on the conduction layers.

The work carried out on doped  $\text{YBa}_2\text{Cu}_3\text{O}_{6+\delta}$  is vast, and the aim of the account given here is only to give the reader an idea of the changes which occur when doping onto various sites in the lattice. Consequently only the most common dopants have been briefly mentioned. This information has been extracted from a selection of reviews on the subject of doping cuprate superconductors<sup>25,26,27,28,29</sup>.

#### **2.3.1. Effect of Doping With Oxygen**

The quantity of oxygen in the high-temperature superconducting system  $\text{YBa}_2\text{Cu}_3\text{O}_{6+\delta}$  for  $0 \leq \delta \leq 1$  is easily varied, and the properties of the material change dramatically between these two extremes. As in most p-type superconductors, if the

correct cation concentration is chosen and the correct crystal structure is obtained, the optimum oxygen content to produce a fully superconducting compound follows naturally. The crystal structure does not allow the absorption of more than  $\delta=1$  oxygens using conventional processing techniques (this has been shown by thermogravimetric analysis<sup>30</sup> and plasma oxidation experiments), which happens to be the optimum level for superconductivity. This material therefore has advantages over many other high-temperature superconductors in that it may be processed to "over-oxygenate" and not degrade the superconductivity. Not only does the diffusion of oxygen within the crystal occur easily, but the quantity of oxygen also comes to equilibrium with the quantity of  $O_2$  gas in the external surroundings, in a process known as reversible absorption. Since the perovskites are efficient intercalators of oxygen<sup>31</sup>, it is natural to study the properties at different stoichiometries.

Reduction of the material causes oxygen loss from the O(1) chain sites of the unit cell, as shown by neutron diffraction studies<sup>1,32,33</sup>. The O(1) oxygen is not strongly bound to the lattice, and with reduction  $T_c$  decreases from 90K to a semiconducting state. This process is reversible and is a general feature of cuprate superconductors, having first been observed in  $La_{2-x}Sr_xCuO_{4-y}$  in 1987<sup>34</sup>. The phase diagram of  $YBa_2Cu_3O_{6+\delta}$  as  $\delta$  varies is shown in Figure 2.4. The method of reduction of oxygen in the material is important, and two samples with identical oxygen concentrations obtained by different techniques (for example, annealing followed by a slow cool or a rapid quench), will exhibit different properties<sup>35,36</sup>.

It has been suggested<sup>37</sup> that for each oxygen removed, one electron converts a  $Cu^{2+}$  to a  $Cu^{1+}$  ion, and the other electron eliminates a conduction hole which results in the eventual destruction of conductivity. This is supported by XANES measurements<sup>37</sup> which give  $Cu^{1+}$  formation, and bond valence calculations<sup>38,39</sup> which indicate the transfer of 1 electron of charge for every oxygen lost.

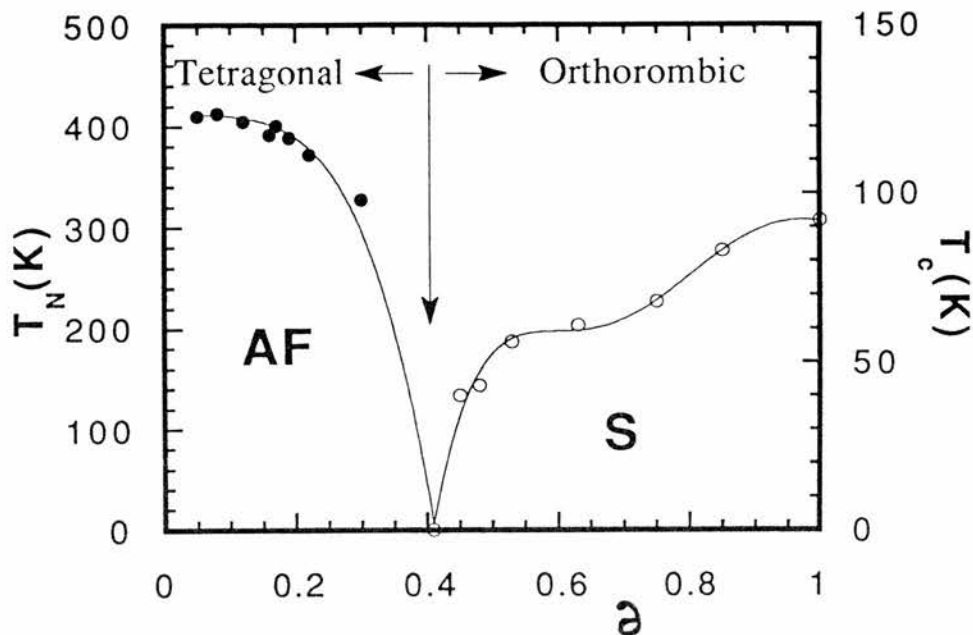


Figure 2.4. The phase diagram of the  $\text{YBa}_2\text{Cu}_3\text{O}_{6+\delta}$  system for  $0 \leq \delta \leq 1$ . (Taken from ref.<sup>40</sup>)

### 2.3.2. Effect Of Substituting Copper

Another vast area of research in superconductivity, is the doping of copper sites and studying the effects on the properties. The dopants which are commonly studied and produce single phase materials in the  $\text{YBa}_2(\text{Cu}_{3-x}\text{M}_x)\text{O}_{6+\delta}$  system are  $M = \text{Fe}, \text{Co}, \text{Ni}, \text{Zn}, \text{Ga}$  and  $\text{Al}$ . The discrepancies reported for these materials in the extensive literature can be accounted for by differing processing temperatures and techniques. These can affect the solubility range of the compound.

Zinc and nickel are interesting dopants to study, since they have similar ionic radii to copper ( $\text{Zn} = 0.88\text{\AA}$ ,  $\text{Ni} = 0.81\text{\AA}$  and  $\text{Cu} = 0.87\text{\AA}$ ), nickel removes and zinc adds a conduction electron, and furthermore nickel is magnetic and zinc diamagnetic, allowing magnetic studies to be made.

There are two distinct copper sites present in the layered structure of  $\text{YBa}_2\text{Cu}_3\text{O}_{6+\delta}$ .  $\text{Cu}(1)$  chain sites with a four-fold square planar coordination of oxygen, and  $\text{Cu}(2)$  plane sites with a five-fold pyramidal coordination of oxygen. It is important to discover which of the copper sites a dopant has replaced, in order to study

the physical properties and to understand which aspects of the crystal structure are important to superconductivity. The position a particular dopant takes in the lattice is generally governed by strain energies caused by physical size and electronegativity differences. The elements zinc and nickel have been found to preferentially substitute onto the Cu(2) plane sites, but others such as iron and cobalt, substitute initially onto the Cu(1) sites and then as the concentration increases, begin to substitute Cu(2).

A dopant study with gallium<sup>41</sup> revealed conclusively that superconductivity occurred mainly in the planes, and that the chain sites acted as a charge reservoir. It follows that substitutions made directly onto the Cu(2) plane sites destroy superconductivity much more effectively than if substitutions are made onto the Cu(1) sites, independent of the dopant or whether the substitution is magnetic or non-magnetic.

A similarity has been observed between the effects of doping trivalent atoms (such as Fe, Co, Al and Ga) onto the copper sites, and reducing the oxygen in the material. Both result in an increase of the unit cell volume and induce an orthorhombic to tetragonal transition<sup>28</sup>.

### **2.3.3. Substitutions Away From The $CuO_2$ Planes**

Generally, as yttrium or barium are replaced in the lattice, the most significant affect on the lattice is a change in the lattice parameters and the unit cell volume. A correlation has been observed between the change in these parameters and the change of the superconducting transition temperature.

#### **2.3.3.1. Substitution of Yttrium**

Yttrium can be replaced in the lattice by most trivalent Rare Earth elements to produce ~90K superconductors with orthorhombic structure, for example La, Nd, Sm, Eu, Gd, Dy, Ho, Er, Tm, Yb and Lu. Of these, Gd, Dy, Er and Ho materials have been found to exhibit long-range magnetic ordering in the lattice. The rare earths Ce,

Pr and Tb, do not produce superconductors down to 4K and is thought to be because they do not exist as purely trivalent ions in the  $RBa_2Cu_3O_7$  system (R = rare earth).

Rare earth substitutions onto the Y site (other than Ce, Pr and Tb) of the 90K superconductor do not have such a dramatic effect on the superconductivity or electronic transport, structural or magnetic properties of the material<sup>42</sup> as do substitutions for copper and variations in oxygen. This suggests that there is only a small exchange interaction between the spin of the superconducting electrons and the angular momentum of the  $R^{3+}$  ions, since  $R^{3+}$  ions with partially filled 4f electron shells ordinarily depress  $T_c$  through pair breaking effects. In support of this, Mössbauer measurements on  $^{155}Gd$  have shown that there is an absence of conduction electrons at the Gd site, and hence no exchange coupling exists between the Gd ion and the conduction electrons<sup>43</sup>.

Yttrium can also be replaced by mono-valent alkali and divalent ions. The predominant divalent substitution is  $Ca^{2+}$ , which will be discussed in more detail in Section 2.4. In general, replacement with lighter mono-valent alkali ions ( $Li^+$ ,  $Na^+$ ) depresses the superconducting transition temperature below that of  $YBa_2Cu_3O_7$ , but for the heavier alkali ions ( $Rb^+$ ,  $K^+$ ), the change is insignificant.

So in general,  $T_c$  can only be maintained if the yttrium is wholly or partially replaced by trivalent rare-earth elements. The transition temperature is depressed if the yttrium is replaced by smaller trivalent ions, ions whose valency has not been determined, monovalent ions whose ionic radii are similar to  $Y^{3+}$ , or divalent  $Ca^{2+}$ . In all cases of substitution at this site, the crystal structure remains orthorhombic. There is no evidence of trivalent ions such as  $Fe^{3+}$ ,  $Ga^{3+}$ ,  $In^{3+}$  or tetravalent  $Hf^{4+}$  or  $Zr^{4+}$ , or large monovalent  $K^+$  or  $Rb^+$  substituting onto the yttrium site.

### **2.3.3.2. Substitution of Barium**

Yttrium and barium both represent the same position in the original perovskite structure, and so research has been carried out to discover whether substitutions onto both sites have similar effects. It may be noted that  $Y^{3+}$  cannot occupy the  $Ba^{2+}$  site

under normal conditions simply due to its size, and so disorder between the two in the lattice is not a problem.

A common choice of substitution for barium is by another alkaline earth ion. All alkaline earths have similar chemistry, but their ionic radii differ through the series, decreasing with an increase in atomic number.  $Sr^{2+}$  is similar in size to the  $Ba^{2+}$  ion and on replacement,  $T_c$  is depressed monotonically with increasing Sr content. There is also a possibility of the barium and strontium atoms becoming ordered in the lattice<sup>44</sup>. Calcium does not easily replace barium, and does not occur under standard synthesis conditions. When it does substitute, it is limited to 12.5% doping concentration. Since calcium is much smaller than the barium ion, the unit-cell volume, orthorhombic distortion and  $T_c$  all decrease linearly with calcium concentration<sup>45</sup>. This contraction of the unit cell indicates the replacement of the barium ion, and is in contrast to the unit cell expansion which occurs as calcium replaces the yttrium. It is likely that the reason  $T_c$  is reduced when  $Sr^{2+}$  and  $Ca^{2+}$  are substituted onto the barium site is due to vacancies which appear in the Cu-O chains. This is supported by lattice parameter studies, which show that with increasing substitution, the **b** parameter decreases whilst the **a** parameter remains the same. The alkaline-earth ion  $Mg^{2+}$  does not appear to replace barium at all, but preferentially occupies oxygen vacancies in the basal plane<sup>46</sup>.

When barium is replaced by  $La^{3+}$ , the structure undergoes an orthorhombic-tetragonal transition<sup>47,48,49</sup>. The oxygen content is found to be affected by the substitution, increasing with higher lanthanum doping concentrations. This extra oxygen occupies the O(5) vacancies in the basal plane.

## **2.4. Substitution of Calcium into $YBa_2Cu_3O_{6+\delta}$**

The oxygens in the chain sites of the  $YBa_2Cu_3O_{6+\delta}$  system are thought to dope holes to the conducting planes, increasing the average oxidation state of the  $Cu^{2+}$  ions yielding a superconductor with an increased transition temperature. If this idea is correct, then a similar doping effect could be achieved by heterovalent substitutions onto the  $Y^{3+}$  or  $Ba^{2+}$  sites. Calcium is an obvious choice for such a substitution, and

replacement of yttrium should dope holes to the conduction planes. Similar substitutions of this kind have not replaced solely the yttrium atom, and have produced multi-phase materials. The advantage of doping with the calcium ion, is that it has a similar ionic radius to the yttrium, and so minimal structural changes should occur in the lattice.

Calcium doping has also been studied by other groups. They have worked on doping the oxygen deficient compound<sup>36,50,51,52,53,54,55,56</sup>, the superconducting parent compound<sup>52,57,58,59,60,61,62,63,64,65,66,67,68,69,70,71</sup>, the 124 and 247 phases<sup>72</sup>, and also co-doping onto the yttrium site<sup>73,74</sup>. For comparison, papers have also been published on calcium substitution at the barium site<sup>75,76,77,78</sup>.

#### 2.4.1. Calcium Doping of Tetragonal $YBa_2Cu_3O_6$

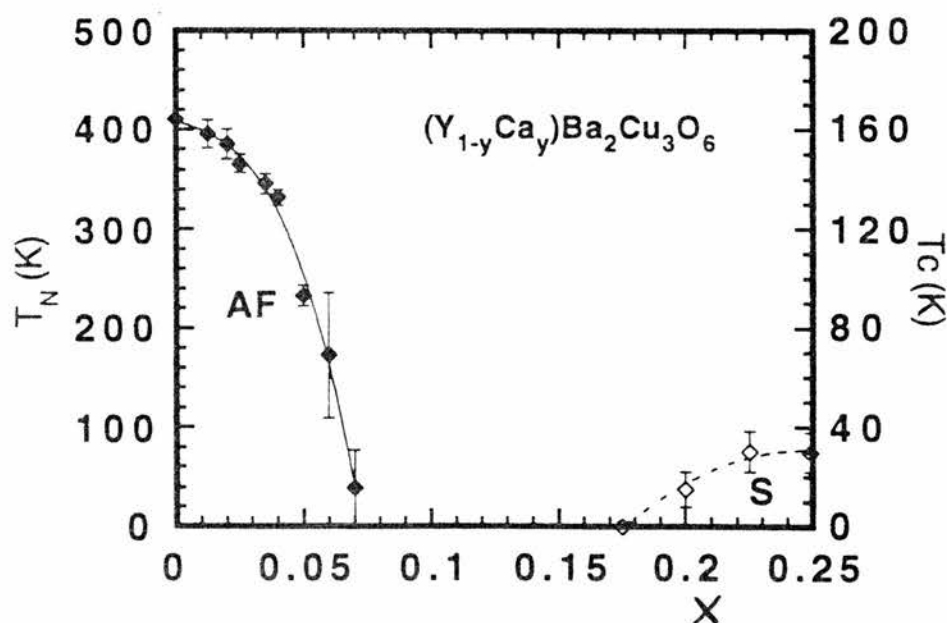


Figure 2.5. Phase diagram for the  $Y_{1-x}Ca_xBa_2Cu_3O_{6+\delta}$  system. (Taken from ref.<sup>55</sup>) AF represents the antiferromagnetic phase and was determined by  $^{89}Y$  NMR, and S represents the superconducting phase measured by AC susceptibility. ( $T_C$  was taken as the mid-point of the transition.)

As calcium is doped onto the yttrium sites of  $YBa_2Cu_3O_6$ , the tetragonal antiferromagnetic insulator becomes a superconductor with a transition temperature of  $\sim 50$ K. X-ray and neutron diffraction studies<sup>50</sup> have confirmed that the structure

remains tetragonal with space group P4/mmm, and so a superconducting system has been produced with the absence of Cu-O chains, which were originally thought to play an essential role for superconductivity. The structural similarities between this superconductor and its antiferromagnetic parent compound, make it an ideal material to study the nature of the superconductivity in the planes. It is agreed that the material possesses a very limited stoichiometry range since the solid solubility limit is reached at  $x \approx 0.3$ <sup>57</sup>, and there is evidence<sup>51</sup> that this is the point at which calcium becomes homogeneously distributed.

The calcium has been confirmed to take the yttrium site in the lattice. The results imply therefore that Cu-O planes can alone support superconductivity up to 50K (at  $\delta=0.5$  in the parent compound), but the chains are necessary in order to increase  $T_c$  up to  $\sim 90$ K.

The predominant effects on the lattice, as studied by neutron diffraction, are that the Cu(2)-O(2) distance decreases whilst the Cu(2)-O(1) distance increases. This is consistent with  $Cu^{3+}$  being produced in the planes due to  $Ca^{2+}$  substitution<sup>79</sup>. The planes are also more flattened in the doped material. This, and the maximum oxidation state for the Cu(2) site due to Cu-O bonding<sup>80</sup>, is thought to limit the solubility of the calcium. The lack of variation in the Cu(1)-O(1) distance indicates that the quantity of  $Cu^{1+}$  remains identical to that in the parent compound.

#### **2.4.2. Calcium Doping of Orthorhombic $YBa_2Cu_3O_7$**

As calcium is doped into  $YBa_2Cu_3O_7$ , the transition temperature is found to decrease as calcium is added<sup>57</sup>. Single-phase compounds can only be synthesized for  $0 \leq x \leq 0.3$  in  $Y_{1-x}Ca_xBa_2Cu_3O_{7-\alpha}$ , indicating that the solid solubility limit is independent of oxygen content. At high oxygen, these structures are all orthorhombic, with space group Pmmm. The basal-plane area and the unit-cell volume have both been found to increase with increasing calcium concentration, consistent with the larger  $Ca^{2+}$  ion substituting for  $Y^{3+}$ . However, the **b**-axis decreases with increasing calcium, indicating the loss of oxygen from this site consistent with lower values of oxygen,  $\alpha$ .

## *Chapter 2: Review Of $YBa_2Cu_3O_{6+\delta}$ And Its Properties*

The oxidation state of the copper in the system could not be increased with calcium doping, and remained at a maximum for all doping concentrations. This was due to the loss of oxygen from the chain sites.

## References

- 1 J.D.Jorgensen, M.A.Beno, D.G.Hinks, L.Soderholm, K.J.Volin, R.L.Hitterman, J.D.Grace, I.K.Schuller. *Phys. Rev. B*, **36** (1987) 3608.
- 2 R.J.Cava, B.Batlogg, R.B.van Dover, D.W.Murphy, S.Sunshine, T.Siegrist, J.P.Remeika, E.A.Rietman, S.Zahurak and G.P.Espinosa. *Phys. Rev. Lett.*, **58** (1987) 1676.
- 3 M.K.Wu, J.R.Ashburn, C.J.Torng, P.H.Hor, R.L.Meng, L.Gao, Z.J.Huang, Y.Q.Wang and C.W.Chu. *Phys. Rev. Lett.*, **58** (1987) 908.
- 4 F.W.Lytle, R.B.Gregor and A.J.Panson. *Phys. Rev. B*, **37** (1988) 1550.
- 5 D.S.Ginley, E.L.Venturini, J.F.Kwak, R.J.Baughman, B.Morosin and J.E.Schirber. *Phys. Rev. B*, **36** (1987) 829.
- 6 T.Graf, G.Triscione and J. Muller. *J.Less Comm. Metals*, **159** (1990) 349.
- 7 J.W.Loram, J.R.Cooper and K.A.Mirza. *Supercond. Sci. Technol.*, **4** (1991) S391.
- 8 J.L.Tallon and N.E.Flower. *Physica C*, **204** (1993) 237.
- 9 P.W.Anderson. *Science*, **235** (1987) 1196.
- 10 V.J.Emery. *Phys. Rev. Lett.*, **58** (1987) 2794.
- 11 S.A.Kivelson, D.S.Rokhsar and J.P.Sethna. *Phys. Rev. B*, **35** (1987) 8865.
- 12 N.Nishida, H.Miyatake, D.Simada, S.Hikami, E.Torikai, K.Nishiyama and K.Nagamine. *Jpn. J. Appl. Phys., Part 2*, **26** (1987) L799.
- 13 J.M.Tranquada, D.E.Cox, W.Kunnmann, H.Moudden, G.Shirane, M.Suenaga, P.Zolliker, D.Vaknin, S.K.Sinha, M.S.Alvarez, A.J.Jacobson and D.C.Johnston. *Phys. Rev. Lett.*, **60** (1988) 156.
- 14 W.-H.Li, J.W.Lynn, H.A.Mook, B.C.Sales and Z.Fisk. *Phys. Rev. B*, **37** (1988) 9844.
- 15 J.Rossat-Mignod, P.Burlet, M.J.G.M.Jurgens, J.Y.Henry and C.Vettier. *Physica C*, **152** (1988) 19.

- 16 D.Petitgrand and G.Collin. *Physica C*, **153-155** (1988) 192.
- 17 J.M.Tranquada. *J. Appl. Phys.*, **64** (1988) 6071.
- 18 H.Kadowaki, M.Nishi, Y.Yamada, H.Takeya, H.Takei, S.M.Shapiro and G.Shirane. *Phys. Rev. B*, **37** (1988) 7932.
- 19 A.H.Moudden, G.Shirane, J.M.Tranquada, R.J.Birgeneau, Y.Endoh, K.Yamada, Y.Hidaka and T.Murakami. *Phys. Rev. B*, **38** (1988) 8720.
- 20 Y.Guo, J.-M.Langlois and W.A.Goddard III. *Science*, **239** (1988) 896.
- 21 J.M.Tranquada, A.H.Moudden, A.I.Goldman, P.Zolliker, D.E.Cox, G.Shirane, S.K.Sinha, D.Vaknin, D.C.Johnston, M.S.Alvarez, A.J.Jacobson, J.T.Lewandowski and J.M.Newsam. *Phys. Rev. B*, **38** (1988) 2477.
- 22 M.W.Shafer, R.A.de Groot, M.M.Plechaty and G.J.Scilla. *Physica C*, **153-155** (1988) 836
- 23 M.W.Shafer, R.A.de Groot, M.M.Plechaty, G.J.Scilla, B.L.Olson and E.I.Cooper. *Mat. Res. Bull.*, **24** (1989) 687.
- 24 P.Salvador, E.Fernandez-Sanchez, J.A.Garcia Dominguez, J.Amador, C.Cascales and I.Rasines. *Solid State Commun.*, **70** (1989) 71.
- 25 I.Felner. *Thermochimica Acta*, **174** (1991) 41.
- 26 T.A.Vanderah (ed.). "*Chemistry of Superconductor Materials: Preparation, Chemistry, Characterization and Theory*", Noyes (1992).
- 27 D.M.Ginsberg (ed.). "*Physical Properties of High Temperature Superconductors I*", World Scientific, Singapore (1989).
- 28 D.M.Ginsberg (ed.). "*Physical Properties of High Temperature Superconductors II*", World Scientific, Singapore (1990).
- 29 J.C.Phillips. "*Physics of High- $T_c$  Superconductors*", Academic Press Inc. (1989).
- 30 J.-M.Tarascon, W.R.McKinnon, L.H.Greene, G.W.Hull and E.M.Vogel. *Phys. Rev. B*, **36** (1987) 226.
- 31 N.Nguyen, F.Studer and B.Raveau. *J. Phys. Chem. Solids*, **44** (1989) 1373.

- 32 J.E.Greedan, A.O'Reilly and C.V.Stager. *Phys. Rev. B*, **35** (1987) 8770.
- 33 J.D.Jorgensen. *Jpn. Appl. Phys.*, **26 Suppl. 26-3** (1987) 2017.
- 34 J.-M.Tarascon, L.H.Greene, W.R.McKinnon, G.W.Hull and T.H.Geballe. *Science* **235** (1987) 1373.
- 35 C.Namgung, J.T.S.Irvine, J.H.Binks and A.R.West. *Supercond. Sci. Technol.*, **1** (1988) 169.
- 36 R.S.Liu, J.R.Cooper, J.W.Loram, W.Zhou, W.Lo, P.P.Edwards, W.Y.Liang and L.S.Chen. *Solid State Commun.*, **76** (1990) 679.
- 37 J.M.Tranquada, S.M.Head, A.R.Moodenbaugh and Y.Xu. *Phys. Rev. B*, **38** (1988) 8893.
- 38 P.F.Miceli, J.-M. Tarascon, L.H.Greene, P.Barboux, J.D.Jorgensen, J.J.Rhyne and D.A.Neumann. Proceedings of the 1989 Spring MRS Meeting, "*High Temperature Superconductors: Relationships Between Properties, Structure and Solid State Chemistry*". Mat. Res. Soc., Pittsburgh (1989).
- 39 P.F.Miceli, J.-M.Tarascon, L.H.Greene, P.Barboux, F.J.Rotella and J.D.Jorgensen. *Phys. Rev. B*, **37** (1988) 5932.
- 40 D.P.Tunstall and W.Barford (eds.). "*High Temperature Superconductivity*", Proceedings of the 39<sup>th</sup> Scottish Universities Summer School in Physics, St.Andrews, IOP Publishing Ltd. (1991). Section by H.Alloul.
- 41 G.Xiao, M.Z.Cieplak, D.Musser, A.Garvin, F.H.Streitz, C.L.Chien, J.J.Rhyne and J.A.Gotaas. *Nature*, **332** (1988) 238.
- 42 See 27. Section by J.T.Markert, Y.Dalichaouch and M.B.Mapte.
- 43 A.P.Ramirez, L.F.Schneemeyer and J.V.Waszcak. *Phys. Rev. B*, **36** (1987) 7145.
- 44 B.W.Veal, W.K.Kwok, A.Umezawa, G.W.Crabtree, J.D.Jorgensen, J.W.Downey, L.J.Nowicki, A.W.Mitchell, A.P.Poulikas and C.H.Sowes. *Appl. Phys. Lett.*, **51** (1987) 279.

- 45 Y.Zhao, H.Zhang, S.Sun, M.Zhang, Z.Chen and Q.Zhang. *Physica C*, **153-155** (1988) 1665.
- 46 K.Mori, M.Sasakawa, Y.Isikawa, T.Okabe, K.Kobayashi, K.Sato and K.Rokudo. *Physica C*, **153-155** (1988) 884.
- 47 R.Liang, M.Itoh, T.Nakamura and R.Aoki. *Physica C*, **157** (1989) 83.
- 48 M.R.Chandrachood, I.S.Mulla and A.P.B.Sinha. *Solid State Comm.*, **68** (1988) 1005.
- 49 S.Mazumder, H.Rajagopal, A.Sequeira, R.Venkatramani, S.P.Garg, A.K.Rajaraman, L.C.Gupta and R.Vijayaraghavan. *J. Phys. C*, **21** (1988) 5967.
- 50 E.M.McCarron, M.K.Crawford, and J.B.Parise. *J. Solid State Chem.*, **78** (1989) 192.
- 51 J.B.Parise, P.L.Gai, M.K.Crawford and E.M.McCarron. *Mat. Res. Soc. Proc. High  $T_c$  Supercond.*, San Diego, **Proc. 156** (1989) 105. (Edited by J.Jorgensen et al.)
- 52 C.Legros-Glédél, J.-F.Marucco, E.Vincent, D.Favrot, B.Poumellec, B.Touzelin, M.Gupta and H.Alloul. *Physica C*, **175** (1991) 279.
- 53 A.J.Vega, M.K.Crawford, E.M.McCarron and W.E.Farneth. *Phys. Rev. B*, **40** (1989) 8878.
- 54 A.J.Vega, M.K.Crawford, E.M.McCarron and W.E.Farneth. *Physica C*, **162-164** (1989) 8878.
- 55 H.Casalta, H.Alloul and J.-F.Marucco. *Physica C*, **204** (1993) 331.
- 56 H.F.Booth, D.P.Tunstall and J.T.S.Irvine. *Physica C*, 235-240 (1994) 1585.
- 57 A.Manthiram, S.-J. Lee and J.B.Goodenough. *J. Solid State Chem.*, **73** (1988) 278.
- 58 Y.Tokura, J.B.Torrance, T.C.Huang and A.I.Nazzal. *Phys. Rev. B*, **38** (1988) 7156.
- 59 C.Greaves and P.R.Slater. *Supercond. Sci. Technol.*, **2** (1989) 5.

- 60 Y.Sun, G.Strasser, E.Gornik, W.Seidenbusch and W.Rauch. *Physica C*, **206** (1993) 291.
- 61 B.Fisher, J.Genossar, C.G.Kuper, L.Patlagan, G.M.Reisner and A.Knizhnik. *Phys. Rev. B*, **47** (1993) 6054.
- 62 J.J.Neumeier, T.Bjørnholm, M.B.Maple and I.K.Schuller. *Phys. Rev. Lett.*, **63** (1989) 2516.
- 63 V.P.S.Awana and A.V.Narlikar. *Phys. Rev. B*, **49** (1994) 6353.
- 64 Z.Jirák, J.Hejtmánek, E.Pollert, A.Tríska and P.Vasek. *Physica C*, **156** (1988) 750.
- 65 A.Tokiwa, Y.Syono, M.Kikuchi, R.Suzuki, T.Kajitani, N.Kobayashi, T.Sasaki, O.Nakatsu and Y.Muto. *Japanese Journal of Applied Physics*, **27** (1988) L1009.
- 66 D.E.Morris, P.K.Narwankar and A.P.B.Sinha. *Physica C*, **169** (1990) 7.
- 67 J.W.Radcliffe, N.Athanassopoulou, J.M.Wade, J.R.Cooper, J.L.Tallon and J.W.Loram. To be published in *Physica C* for the *Proceedings of the M<sup>2</sup>SHTSC Conference, Grenoble, July 1994*.
- 68 B.Touzelin. *Journal of the Less-Common Metals*, **169** (1991) 115 (in French).
- 69 C.Legros-Glédél, J.-F.Marucco and B.Touzelin. *Physica C*, **165** (1990) 437.
- 70 M.R.Chandrachood, I.S.Mulla, S.M.Gorwadkar and A.P.B.Sinha. *Appl. Phys. Lett.*, **56** (1990) 183.
- 71 T.Honma and K.Yamaya. *Physica C*, **185-189** (1991) 1245.
- 72 D.E.Morris, P.Narwankar, A.P.B.Sinha, K.Takano, B.Fayn and V.T.Shum. *Phys. Rev. B*, **41** (1990) 4118.
- 73 R.G.Kulkarni, I.A.Shaikh, J.A.Bhalodia, G.J.Baldha and D.G.Kuberkar. *Phys. Rev. B*, **49** (1994) 6299.
- 74 K.Matsuura, T.Wada, Y.Yaegashi, S.Tajima and H.Yamauchi. *Phys. Rev. B*, **46** (1992) 11923.
- 75 I Mangelschots, M.Mali, J.Roos, H.Zimmermann, D.Brinkmann, S.Rusiecki, J.Karpinski, E.Kaldis and E.Jilek. *Physica C*, **172** (1990) 57.

- 76 G.J.Baldha, R.B.Jotania, H.H.Joshi, H.N.Pandya and R.G.Kulkarni. *Solid State Commun.*, **71** (1989) 839.
- 77 D.Palles, N.Poulakis, Th.Leventouri and E.Liarokapis. To be published in *Physica C* for the *Proceedings of the M<sup>2</sup>SHTSC Conference, Grenoble, July 1994*.
- 78 Th.Leventouri, G.A.Soifer, M.Calamiotou, O.Papageorgiou and V.Perdikatsis. To be published in *Physica C* for the *Proceedings of the M<sup>2</sup>SHTSC Conference, Grenoble, July 1994*.
- 79 C.C.Torardi, E.M.McCarron, P.E.Bierstadt and A.W.Sleight. *Solid State Commun.*, **64** (1987) 497.
- 80 R.J.Cava, B.Batlogg, C.H.Cheu, E.A.Rietman, S.M.Zahurak and D.Werder. *Nature*, **329** (1987) 423.

## Chapter 3

# BACKGROUND THEORY AND INFORMATION

### 3.1. Overview

This chapter gives the necessary background information required to understand the experimental techniques used for the work here. Of these techniques, x-ray diffraction, electron microprobe analysis (and general electron microscopy) and nuclear magnetic resonance require a certain level of understanding in order to carry out the experiments and interpret the results. Only a general physics background is required to understand resistivity and susceptibility, and so the information related here has been limited to specific knowledge of the van der Pauw method for measuring resistivity, and useful hints for the interpretation of susceptibility results.

### 3.2. X-Ray Diffraction

A basic overview of the x-ray diffraction method is given below. Further detail may be obtained from texts and papers<sup>1,2,3,4</sup>.

#### Overview of the Basic Theory

In 1912, it occurred to the German physicist Max von Laue that the regular array of atoms in a crystal could act as a natural three-dimensional diffraction grating for electromagnetic waves with short wavelengths, such as x-rays ( $\lambda \approx 10^{-10}\text{m}$ ).

A crystal basically comprises of a regularly repeated unit of atoms. This unit is known as the unit cell and is characteristic to the particular crystal type. Due to this regular nature, the atoms in the crystal lattice may be visualised as being arranged in planes, with an interplanar spacing,  $d$ . When an x-ray beam enters a crystal, the x-rays are scattered in all directions. Interference occurs between the reflected rays, either

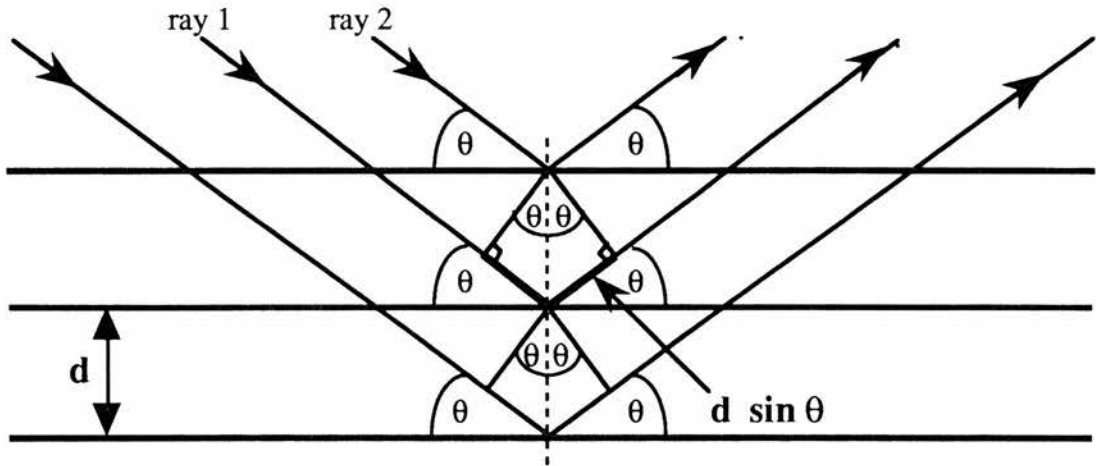


Figure 3.1. The reflection of incident x-rays at the crystal planes to produce constructive interference.

constructively to produce intensity maxima, or destructively producing intensity minima.

The process of diffraction of x-rays from a crystal is in reality quite complicated since the atoms do not reflect the x-rays as such, but scatter or diffract them in all directions. However, this is simplified because the maxima occur in directions as if the x-rays had been reflected by these crystal planes. The planes do not act as if they were perfectly reflecting, otherwise only the first plane of a parallel set would see the radiation, and any wavelength could be reflected. Each plane reflects  $10^{-3}$  to  $10^{-5}$  of the incident beam so that reflection may occur at  $10^3$  to  $10^5$  planes of a perfect crystal, each contributing to the Bragg-reflected beam. The reflection from each plane is specular, and hence the angles of incidence and reflection are represented by  $\theta$ . Contrary to the usual convention in optics, this angle is measured relative to the surface of the reflecting plane, rather than normal to it. Initially, two incident rays arrive at the crystal in phase (see Figure 3.1). Since x-rays do not refract upon entering a crystal, the relative phase between the reflected rays is determined solely by their path length difference. For the rays to be in phase, the difference in path length must be an integer multiple of the wavelength,  $\lambda$ , of the x-rays. As demonstrated by the diagram, the difference in path length is found to be  $2d\sin\theta$ . This is true for any pair of adjacent planes in the system

and is known as Bragg's Law. This can be written:

$$2d \sin\theta = m\lambda \quad \text{for } m=1,2,3,\dots$$

where  $m$  is the order number of the intensity maxima of the supposed reflections of the x-rays. The angle of incidence and reflection,  $\theta$ , is known as the Bragg angle. Bragg reflection can only occur for wavelengths  $\lambda \leq 2d$ .

There are many sets of crystal planes in a lattice from which the x-rays can be said to reflect, and so the x-rays may enter at any angle. Each new Bragg angle requires a new set of planes and interplanar spacing,  $d$ , hence Bragg's law will always apply, regardless of the orientation of the crystal. An example is shown in Figure 3.2.

Each set of lattice planes are labelled by assigning three numbers ( $hkl$ ) known as Miller indices. To assign the appropriate numbers, a plane must pass through the origin of the unit cell, and the positions at which the adjacent plane in the same set intersects the three axes must be noted as fractions of the cell edges, eg. ( $a/2, b, c/3$ ). The corresponding Miller indices are then the reciprocals of these fractions, eg.(213).

The d-spacing between adjacent planes of a set may be represented in terms of the lattice parameters  $a$ ,  $b$  and  $c$ . For orthogonal crystals, eg.  $\text{YBa}_2\text{Cu}_3\text{O}_{6+\delta}$ , the d-spacing for any set of planes is given by the formula

$$\frac{1}{d_{hkl}^2} = \frac{h^2}{a^2} + \frac{k^2}{b^2} + \frac{l^2}{c^2}$$

This simplifies for tetragonal crystals where  $a = b$

$$\frac{1}{d_{hkl}^2} = \frac{h^2 + k^2}{a^2} + \frac{l^2}{c^2}$$

### 3.3. Electron Microscopy

Electron microscopy is a powerful technique, giving both structural and elemental information over a wide range of magnification. It is useful for observing

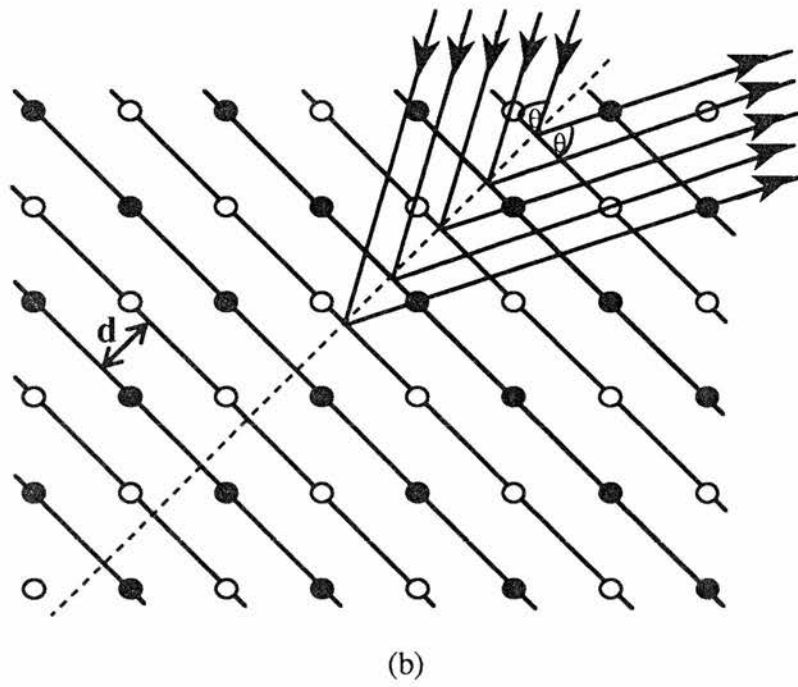
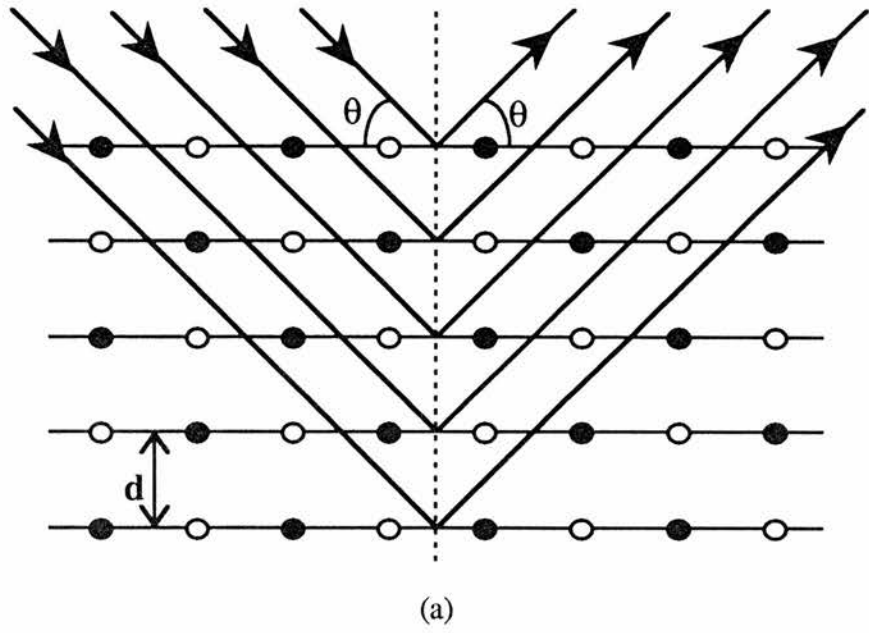


Figure 3.2. X-ray diffraction occurs for all orientations of a crystal, but each different Bragg angle requires different sets of planes and  $d$ -spacings. Examples are shown in (a) and (b).

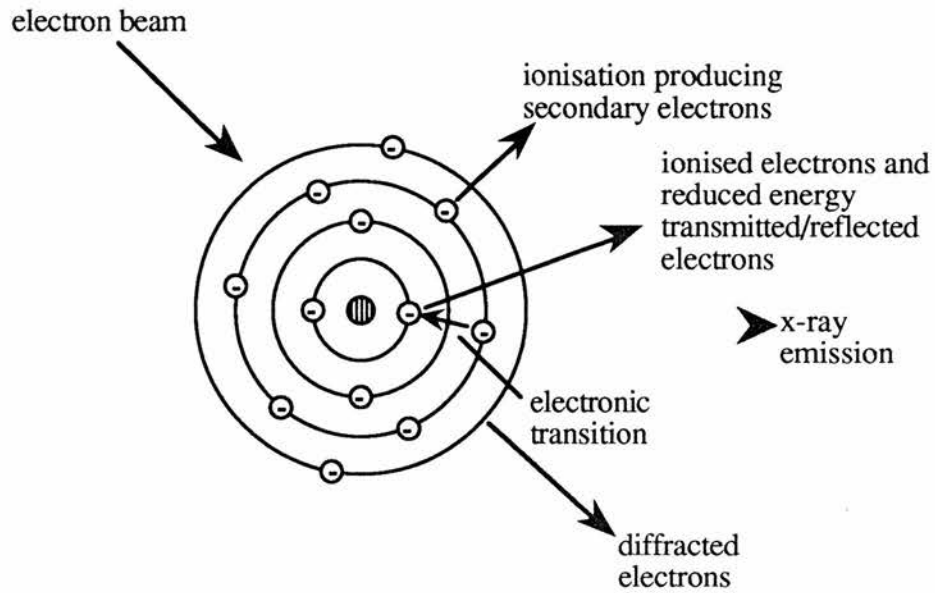


Figure 3.3. Possible interactions which occur when an atom is bombarded by a beam of high-energy electrons.

polycrystalline texture, surface structure, crystal structure and defects, as well as for elemental analysis and phase identification. Further details may be found in recommended texts on this subject<sup>5,6,7</sup>.

The bombardment of a material by high-energy electrons causes many processes to occur (see Figure 3.3), including the emission of x-rays. These x-rays are emitted at specific frequencies, and the spectra obtained are characteristic to the elements present in the sample, which consequently may be identified. This method can be quantitative if using a suitable calibration procedure. Quantitative determinations are more accurate for heavier elements, since lighter ones (up to sodium) do not give suitable spectra. The elemental analysis of sample composition using this technique is known as Electron-Probe Microanalysis (EPMA).

2-50keV electron beams are used for electron microprobes. Inelastic collisions occur between the bombarding electrons and the core electrons of the sample atom, causing the core electrons to be ejected. The remaining electrons in the atom then decay back to the ground state and in the process, emit x-rays of wavelengths dependent on the particular atom. Figure 3.4. demonstrates this process and indicates that the

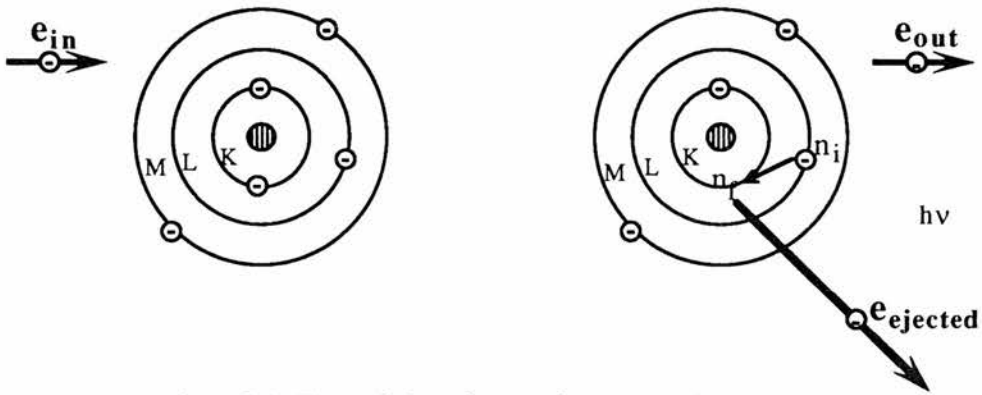
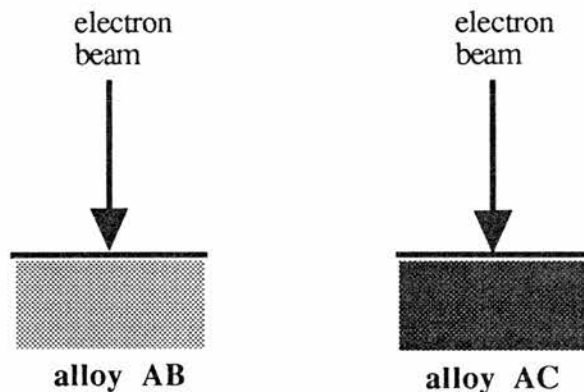


Figure 3.4. The emission of x-rays from a sample as electrons decay back to the electronic ground state.

wavelength emitted is also dependent on which of the levels the electrons decay between. These x-rays are detected and for quantitative analysis, the intensities of the wavelengths obtained for the unknown sample are compared to those of a known standard. This intensity ratio between the unknown sample and the standard gives (to a first approximation) the ratio of weight concentrations:

$$\frac{(\text{x-ray intensity of unknown sample})}{(\text{x-ray intensity of standard sample})} = \frac{(\text{weight concentration of element in sample})}{(\text{weight concentration of same element in standard sample})}$$

The reason this is so, rather than the intensities being directly proportional to the ratio of atomic concentrations, is that the majority of inelastic collisions do not result in ionisations. The stopping power is approximately proportional to the density of the material which defines the ionisation volume. This is illustrated below.



Alloy AB is lighter than AC, therefore  $\frac{A}{AB} > \frac{A}{AC}$

The signal intensity is greater for the less dense material, since the ionisation volume is greater in the AB alloy even though the atomic fraction of A is the same in both.

Further EPMA analysis involves making corrections to this first approximation.

These are outlined below:

- The stopping power is not exactly proportional to density, because elastic scattering has not been considered. This is known as the "Z" correction.
- Not all of the emitted x-rays leave the sample, since they can be reabsorbed. This is known as the absorption "A" correction.
- The characteristic x-rays which are reabsorbed by the sample, interact with further sample atoms and subsequently emit characteristic x-rays themselves. This is known as the fluorescence "F" correction.

The linewidth of the x-rays emitted from light elements such as oxygen is affected by the bonding environment of the atoms. This is because the same electrons are involved in chemical bonding and core transitions, and causes the  $O_{k\alpha}$  wavelength to vary slightly among materials. In this case, the area of the peak is more accurate than the intensity. Rather than measure the area each time, the area to peak factor (APF) can be measured once and then used to convert the intensities, since this remains the same for any one material.

If quantitative analysis is to be carried out, good standard samples are required for calibration. These should be electrically conducting, of well known composition and should contain a reasonably high concentration of the required element. It is difficult to find suitable standards for the cuprate superconductors, since many of the elements are rare, and their compounds are insulating.

Electron microscopes use either transmission or reflection techniques. Samples less than  $2000\text{\AA}$  thick are required for transmission, and so this method cannot be used for polycrystalline solids. For reflection however, sample thickness is not a problem, but the surface must be coated with an electrical conductor to prevent charge build-up.

If charge does build up in the specimen, a back electric field results which alters the effective beam energy and consequently the x-ray field.

In the scanning electron microscope, the high-energy beam of electrons is focussed onto a small spot on the surface of the sample (50-100Å diameter), and is then systematically scanned over the whole area. The sample emits x-rays and secondary electrons, and although the x-rays may be used for chemical analysis, it is the secondary electrons that are used to build up an image of the sample surface, which is displayed on a screen or may be photographed.

### 3.4. Resistivity - The Van der Pauw Method

The van der Pauw technique<sup>8,9</sup> is a four-point method of measuring resistivity. The sample may be of arbitrary shape, but must be thin, plane-parallel, and must not contain any isolated holes. Four small electrical contacts must be placed on the circumference of the sample, in arbitrary positions, but labelled A,B,C and D in successive order (see Figure 3.5).

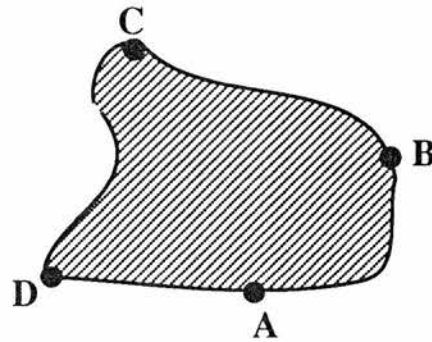


Figure 3.5. Arbitrary shaped sample with four electrical contacts placed at the circumference.

The resistance  $R_{AB,CD}$  is defined as being the potential difference ( $V_D - V_C$ ) between contacts D and C, per unit current passing through the contacts (from A to B).  $R_{BC,DA}$  is defined in a similar way. The van der Pauw method only requires the measurement of  $R_{AB,CD}$ ,  $R_{BC,DA}$  and the thickness of the sample,  $t$ .

It is shown in the original paper<sup>8</sup>, that the resistivity,  $\rho$ , is uniquely determined by these parameters according to the equation

$$\exp\left(\frac{-\pi R_{AB,CD}t}{\rho}\right) + \exp\left(\frac{-\pi R_{BC,DA}t}{\rho}\right) = 1$$

If the sheet resistance  $R_s$  is defined as being

$$R_s = \frac{\rho}{t}$$

then

$$\exp\left(\frac{-\pi R_{AB,CD}}{R_s}\right) + \exp\left(\frac{-\pi R_{BC,DA}}{R_s}\right) = 1$$

$R_s$  may be calculated from  $R_{AB,CD}$  and  $R_{BC,DA}$  in the above equation, and consequently the value of the resistivity,  $\rho$ , may be determined.

### 3.5. Susceptibility

AC susceptibility is a method used to study the magnetic properties of materials and is commonly used to determine the transition temperature,  $T_c$ , of a superconducting sample. The differential magnetic susceptibility,  $\chi$ , is defined as:

$$\chi = \frac{dM}{dH}$$

where  $M$  is the magnetic moment per unit volume of a magnet, and  $H$  is the magnetic intensity due to a current element. The magnetic susceptibility has a real (in-phase) part  $\chi'$  and an imaginary (or out-of-phase) part  $\chi''$ . The real part is a measure of the diamagnetism of the sample, whereas the imaginary part is a measure of the losses in the system.

A diamagnetic material may be described as a material that resists the application of a magnetic field. Eddy currents are induced in the material, resulting in the production of a magnetic field opposite in direction to the applied field. For a perfect diamagnet, this induced magnetic field is the same magnitude as the applied field, exactly cancelling the field within the sample.

For a material in the normal state, the AC magnetic field produced by the coil extends throughout the sample. As the temperature is decreased below the transition temperature, the material becomes superconducting. Initially the individual grains become superconducting, each supporting a supercurrent within a penetration depth of the surface, shielding the interior from the applied magnetic field. The penetration depth is often large when compared to the grain size. In this case, only a small change is usually observed in the magnetic susceptibility since the magnetic field still exists within the penetration depth of each grain and in the regions between the grains.

As the temperature is decreased further, the weak links between the individual superconducting grains become strong enough to support supercurrents around the bulk of the specimen. Shielding supercurrents are supported within a penetration depth of the bulk of the sample, which is small when compared to the size of the sample. The applied magnetic field is excluded from the interior of the bulk of the sample, giving rise to a greater change in the susceptibility measurement.

When measuring the superconducting transition temperature in a material it is often advantageous to measure both the real and imaginary components of the susceptibility. At the transition there is a sudden change in  $\chi'$  indicating the onset of diamagnetic behaviour. This is accompanied by an increase in  $\chi''$  due to the losses incurred in setting up the shielding currents in the superconductor.

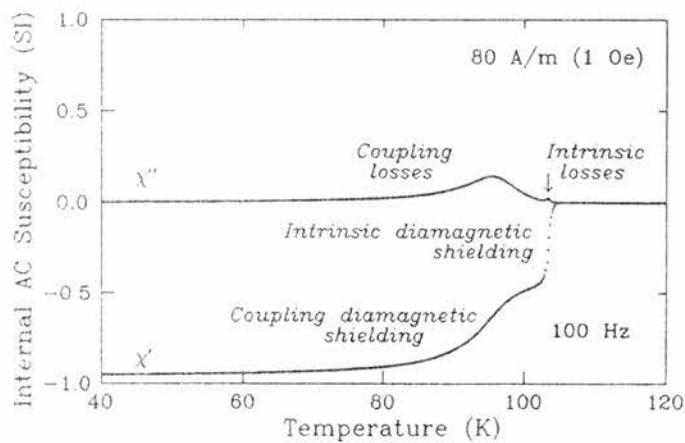


Figure 3.6. The superconducting phase transition as measured by AC susceptibility.  $\chi'$  is the in-phase component and  $\chi''$  the out-of-phase component.

Broad features in susceptibility graphs may be explained by the Bean model<sup>10</sup>, but account must also be taken of the behaviour of the grains and weak links. Initially the grains go superconducting, then the junctions between the grains become sufficiently strong to support supercurrents around the bulk of the specimen.

There are problems with this method of measuring the superconducting transition temperature, in that the inductive signal amplitude may not necessarily be connected with the volume of superconducting material contained in the sample. If the superconducting material forms a shell around the bulk of the sample, then the signal would be the same as if the sample were completely superconducting. In order to test for this, smaller and smaller subsamples should be tested and the signal amplitude should scale with the sample volume. Also, it is wrong to associate an extremely small signal with a tiny fraction of superconducting material, because if part of the sample undergoes an insulator-metal transition, this may mimic a superconducting transition. However, in this case the intensity should be frequency dependent, vanishing as the frequency approaches zero.

## **3.6. Nuclear Magnetic Resonance**

### **3.6.1. Introduction**

Nuclear magnetic resonance (NMR) is a technique used to study molecular structure, by the interaction of radio-frequency radiation with the nuclei in the material whilst in a strong magnetic field. Several references are recommended for this subject, both as introductory texts<sup>11,12,13,14</sup>, and for more detailed study<sup>15,16,17,18</sup>.

### **3.6.2. Simple Resonance Theory**

The nucleus consists of many particles coupled together. Each nucleon (proton or neutron in the nucleus) possesses spin  $I=1/2$ , therefore a nucleus with an odd mass number will always possess a half-integer spin, ie.  $I = n/2$  where  $n$  is an odd integer. The spin angular momentum vector is  $I\hbar$ , where  $\hbar = h/2\pi$  ( $h$  is the Planck constant). A

nucleus with both spin and charge has a magnetic moment  $\mu$ , proportional to the magnitude of the spin.

$$\mu = \gamma\hbar\mathbf{I}$$

where  $\gamma$  is the gyromagnetic ratio, which is unique to a specific nucleus. Nuclear spin states are quantised, and the nuclear spin quantum number  $m_I$ , can have one of a discrete set of values  $+I, (I-1), \dots, -I$ .

A magnetic field  $\mathbf{B}_0$ , is applied to the nucleus, and produces an interaction energy which can be represented by the Zeeman Hamiltonian

$$H = -\mu \cdot \mathbf{B}_0$$

If the magnetic field defines the direction of the  $z$ -axis, then this can be written

$$H = -\gamma\hbar B_0 I_z$$

where  $I_z$  is the allowed component of the nuclear spin in the  $z$ -direction. Eigenvalues of the Hamiltonian are multiples of the eigenvalues of  $I_z$ . Allowed energies are

$$E = -\gamma\hbar m_I B_0 \quad \text{for } m_I = I, I-1, \dots, -I.$$

An example is shown in Figure 3.7.

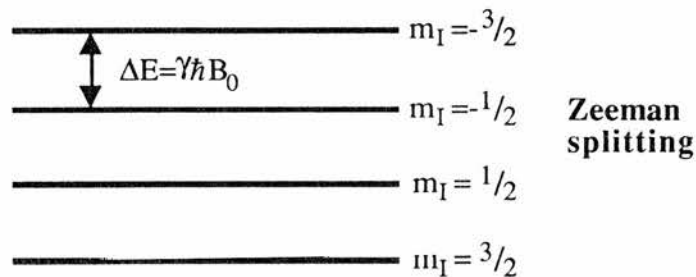


Figure 3.7. Allowed energies for a nucleus with  $I=3/2$ , with corresponding  $m_I=3/2, 1/2, -1/2, -3/2$ . The energies are equally separated by  $\Delta E = \gamma\hbar B_0$ .

These energy levels may be detected by spectral absorption. An interaction is required to induce transitions between levels. Since energy must be conserved, the interaction must be time dependent, with an angular frequency  $\omega$ , such that

$$\hbar\omega = \Delta E$$

where  $\Delta E$  is the difference in energy between the initial and final Zeeman energies. An alternating magnetic field  $\mathbf{B}_1$  is used for this purpose, applied perpendicular to the static field  $\mathbf{B}_0$ . Allowed transitions are between adjacent energy levels

$$\hbar\omega = \Delta E = \gamma\hbar B_0$$

giving

$$\omega_0 = \gamma B_0$$

$\omega_0$  is known as the Larmor Frequency. This equation specifies the frequency at which the oscillating field satisfies the resonance condition. In order to change the frequency of the resonance the magnetic field must also be changed, but it is advantageous to use large fields since the absorbed quanta are then larger and the resonance is correspondingly stronger. The range of required frequencies fall into the radio-frequency band of the spectrum.

### 3.6.3. Thermal Equilibrium and Spin Relaxation

Resonance absorption can only be detected when there is a population difference of the spin states in a material. This section gives insight into how the populations vary, and under what conditions.

A macroscopic sample of  $N$  spins will be considered, for simplicity nuclei with  $I=1/2$  allowing two states  $m_I = +1/2$  and  $-1/2$ . The numbers of nuclei in each state are given by  $N_+$  and  $N_-$  respectively (note that  $N=N_++N_-$ ). In the absence of a magnetic field the population of both states will be equal. When placed in a static magnetic field ( $\mathbf{B}_0$ ), there are more spins in the  $+1/2$  state than the  $-1/2$  state (at thermal equilibrium). Their ratio is given by the Boltzmann distribution

$$\frac{N_+}{N_-} = e^{\Delta E/kT} = e^{\gamma\hbar B_0/kT}$$

where  $k$  is the Boltzmann constant and  $T$  is the temperature. At ordinary temperatures  $\gamma\hbar B_0 \ll kT$  and the population of the spin states are almost equal.

Thermal equilibrium is maintained by weak spin-spin interactions at a temperature  $T_S$  (spin temperature) equivalent to the surroundings which have a lattice temperature  $T_L$ . When an oscillating magnetic field ( $B_1$ ) is applied to the spin system, the population levels change as a result of the induced transitions. This perturbation causes  $T_S$  to increase and consequently become greater than  $T_L$ . In order to regain thermal equilibrium, interactions occur between the nuclei and the surroundings (transfer of energy), allowing the spin orientations to revert back to their equilibrium state. This process is known as **spin-lattice relaxation**. The decay of the population difference back to its equilibrium state is exponential. The time taken for it to decay is the spin-lattice relaxation time,  $T_1$ . This energy difference between the perturbed state and equilibrium is that which is detected by the receiver coil in the NMR experiment.

So far, the description has given the impression that resonance occurs at one specific frequency, which implies that the resonance lineshape is a  $\delta$  function. This is far from the truth, and there are many reasons why line-broadening exists. Firstly, for spin-relaxation the spin states have a finite lifetime, and the line-broadening associated with this can be estimated from the uncertainty relationship  $\Delta\nu\Delta t \approx 1$ . Other processes have the effect of varying the relative energies of the spin levels, rather than the lifetime. The **spin-spin relaxation time** or transverse relaxation time  $T_2$  is characterised by these. Even though  $T_1$  and  $T_2$  do not appear connected in any way, they may be closely related since the interactions which lead to finite lifetimes of the spin states, may also affect the energy levels. For many solids  $T_1 \gg T_2$ , where  $T_2$  is of the order of submilliseconds and  $T_1$  varies anywhere between milliseconds and days.

#### **3.6.4. Magnetic Shifts**

The positions at which the resonance lines of nuclei occur can be calculated for the bare nucleus. Experimentally, the resonance line is displaced from this expected position, and this displacement is known as the magnetic shift ( $\Delta K$ ). This is due to magnetic fields that the nucleus experiences in addition to the applied field  $B_0$ . The

shift is proportional to the applied field, and hence the frequency of the resonance (omitting quadrupole effects) can be written as

$$\begin{aligned}\omega &= \gamma(B_0 + \Delta B) && \text{and hence} \\ \omega &= \gamma B_0 + \Delta K\end{aligned}$$

where  $\Delta B$  is the additional field experienced by the nucleus.

The total magnetic shift ( $\Delta K$ ) can be separated into two contributions, the chemical shift ( $\sigma$ ) and the Knight shift ( $K$ ).

$$\Delta K = K + \sigma$$

In practice the total magnetic shift of a sample has to be compared to that of a known material, since it is very difficult to isolate the nucleus.

#### **3.6.4.1. The Chemical Shift**

The chemical shift,  $\sigma$ , is due to the screening effect of the electrons surrounding the nucleus. Electronic currents are induced in the atom by the external magnetic field  $B_0$ , which produces an additional field  $\Delta B$  to oppose  $B_0$  at the nucleus. The strength of the induced field is proportional to the applied field, such that

$$\Delta B = -\sigma B_0$$

$\sigma$  is also known as the screening constant. This contribution to the total magnetic shift is usually relatively small in metals.

#### **3.6.4.2. The Knight Shift**

The unpaired electrons in a metal produce shifts which are many times larger than the ordinary shifts seen in diamagnetic molecules and are known as Knight shifts<sup>19,20,21</sup>. These are due to the very strong local magnetic fields which result from hyperfine interactions. This shift depends on temperature in a characteristic way.

The Knight shift can be separated into several contributions, and may be written

$$K_{\text{total}} = K_s + K_{\text{dia}} + K_{\text{orb}} + \text{higher order terms}$$

The  $K_s$  term represents the Fermi contact interaction between the resonating nucleus and the s-electrons. It can be written

$$K_s = \langle a \rangle \chi_p$$

where  $\chi_p$  is the Pauli paramagnetic spin susceptibility per atom, and  $\langle a \rangle$  represents the hyperfine field.

The conduction electron diamagnetic contributions to the Knight shift are generally very small, but may be significant in some metals. The diamagnetic Knight shift term  $K_{dia}$  is written as

$$K_{dia} = (\frac{8\pi}{3}) \chi_{dia}$$

The orbital term  $K_{orb}$  comes from the orbital magnetic moment of the conduction electrons induced by the applied magnetic field, and is especially important for transition metals. It can be written

$$K_{orb} = \langle b \rangle \chi_{orb}$$

where  $\langle b \rangle$  is an appropriate orbital hyperfine coupling constant. There is little or no temperature dependence in this term, in analogy to Van Vleck temperature independent paramagnetism in ionic salts.

There is an anisotropic component to the Knight shift, which has not been shown in the above equation. This exists when the resonating nuclei are in non-cubic surroundings. This component does not contribute to the shift of the centroid of the NMR resonance.

To deconvolute the individual contributions to the Knight shift, the behaviour of  $K$  and  $\chi$  has to be observed as a function of temperature, and the Korringa relation has to be used (see below).

### **3.6.4.3. Temperature Dependency**

Each component of the Knight shift may have its own temperature dependency, to the extent where the Knight shift changes sign with temperature, although this is rare.

For simple metals, the contact interaction term dominates both the Knight shift and nuclear spin-lattice relaxation. Korringa<sup>22</sup> derived the relationship between the spin-lattice relaxation time ( $T_1$ ), the Knight shift ( $K$ ) and temperature ( $T$ ) to be

$$K^2 T_1 T = S$$

where 
$$S \equiv \left( \frac{\gamma_e}{\gamma_n} \right)^2 \left( \frac{h}{8\pi^2 k_B} \right)$$

$$\text{Korringa ratio} = \frac{K^2 T_1 T}{S}$$

For an ideal simple metal the Korringa ratio is 1. Many deviations from the ideal case may occur. These are usually due to the contact term in the Knight shift not being the dominant effect, eg. for some transition metals exchange enhancement is strong enough to cause negative Knight shifts and d-interactions are assumed to dominate. Another cause of deviations are electron-electron interactions, which affect the Knight shift and spin-lattice relaxation differently.

#### **3.6.4.4. Orientation Dependence of the Knight Shift**

The orbital, spin and Knight shifts may all have anisotropic components. For the Knight shift, anisotropic effects are observed for nuclei in surroundings of less than cubic symmetry. This is caused by the electron-nuclear dipole interaction. In this work only the case of axial symmetry is relevant, and lower order symmetries may be found elsewhere<sup>15</sup>.

For the case where the nucleus is in an axially symmetric position, the Knight shift depends on the angle  $\theta$  between the crystal symmetry axis and the applied magnetic field, but not the azimuthal angle  $\phi$ .

$$K_{ax} \propto (3\cos^2\theta - 1)$$

The axial shift gives a measure of the amplitude of the frequency shift variations with sample rotation  $\theta$ , and results in an orientation dependence similar to those observed for axial quadrupole effects.

For a randomly distributed powder, the above term averages out to zero, and so there is no net effect on the total Knight shift. The shift of the centroid ( $\nu_0$ ) remains unchanged, but the lineshape is no longer symmetrical. The lineshape was calculated by Bloembergen and Rowland<sup>23</sup> and is demonstrated in Figure 3.8.

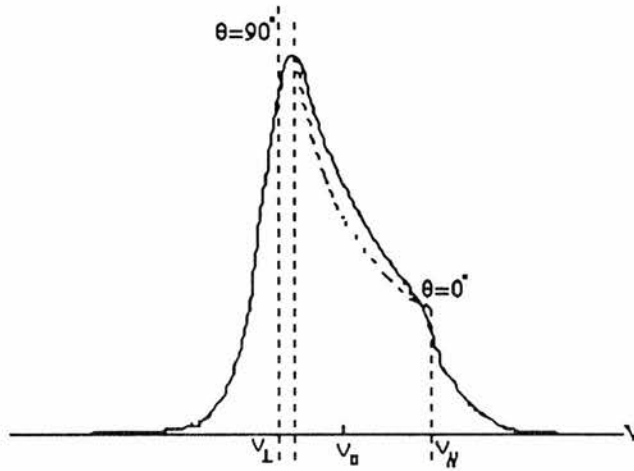


Figure 3.8. The Knight shift lineshape obtained for an axially symmetric material. The intensity  $I(\nu)$  is shown as a function of frequency,  $\nu$ . The theoretical lineshape is shown by the dotted line, and the broadened lineshape is in bold. Taken from reference<sup>15</sup>.

### 3.6.4.5. Quadrupole Effects

Only the case of axial symmetry will be considered in this work.

The Hamiltonian of a nuclear spin with a quadrupole moment can be written as

$$\mathcal{H} = \gamma\hbar B_0 I_z + \frac{e^2 q Q}{4I(2I-1)} \left\{ \begin{array}{l} \frac{1}{2}(3\cos^2\theta - 1)(3I_z^2 - I(I+1)) \\ + \frac{3}{2}\sin\theta\cos\theta [I_z(I_+ + I_-) + (I_+ + I_-)I_z] \\ + \frac{3}{4}\sin^2\theta(I_+^2 + I_-^2) \end{array} \right\}$$

where the  $z$ -axis is taken to be parallel to the applied magnetic field  $\mathbf{B}_0$ , and  $I_{\pm} = I_x \pm I_y$ .

From this equation, the various energy levels can be written as

$$E_m = E_m^{(0)} + E_m^{(1)} + E_m^{(2)} + \text{higher order terms}$$

where  $E_m^{(p)}$  is the energy contribution due to a perturbation of order  $p$ . To simplify the following equations let

$$v_Q = \frac{3e^2qQ}{h2I(2I-1)} \quad a = I(I+1) \quad \mu = \cos\theta \quad v_L = \frac{\gamma B_0}{2\pi}$$

then each of the energy contributions can be written as

$$E_m^{(0)} = -\gamma\hbar B_0 m = -hv_L m$$

$$E_m^{(1)} = \frac{1}{4} hv_Q (3\mu^2 - 1)(m^2 - \frac{1}{3}a)$$

$$E_m^{(2)} = -h \left( \frac{v_Q^2}{12v_L} \right) m \left\{ \frac{3}{2} \mu^2 (1 - \mu^2)(8m^2 - 4a + 1) + \frac{3}{8} (1 - \mu^2)^2 (-2m^2 + 2a - 1) \right\}$$

The zero-order term is the Zeeman splitting term corresponding to a nucleus in a magnetic field, as discussed in Section 3.6.2. The first and second-order terms correspond to quadrupole interactions and are discussed in more detail below. The quadrupole effects split the single resonance frequency into several frequencies, which are given by

$$v_m = \frac{E_{m-1} - E_m}{h} = v_L + v_m^{(1)} + v_m^{(2)} + \dots$$

#### First-Order Quadrupole Effects

$$E_m^{(1)} = \frac{1}{4} hv_Q (3\mu^2 - 1)(m^2 - \frac{1}{3}a)$$

For a nucleus of  $I=1/2$  this first-order term disappears, which is why only nuclei with spin  $I>1/2$  possess electric quadrupole moments. The Zeeman energy levels as described in Section 3.6.2 are shifted due to the perturbation of the system by the static electric field gradient. This lifts the  $m_I$  degeneracy, and the resultant splitting is no longer equal. This is demonstrated in Figure 3.9. For half-integer spins, the  $m_I=1/2 \rightarrow -1/2$  transition does not shift the central resonance, since the  $m_I=1/2$  and  $-1/2$  levels have been shifted by equal amounts. The remaining transitions cause satellite lines to appear on either side (ie. for  $m_I \leftrightarrow (m_I - 1)$ ,  $m_I \neq 1/2$ ). Figure 3.10. demonstrates

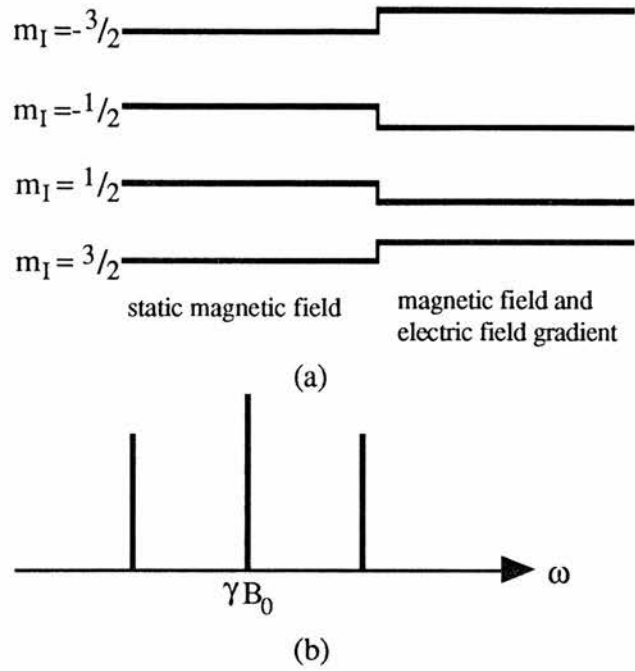


Figure 3.9. (a) Splitting of the  $m_I$  degeneracy by quadrupole effects. To first order, each level is shifted by the same energy, but the energy difference for the central transition remains unaffected. (b) shows the corresponding frequencies.

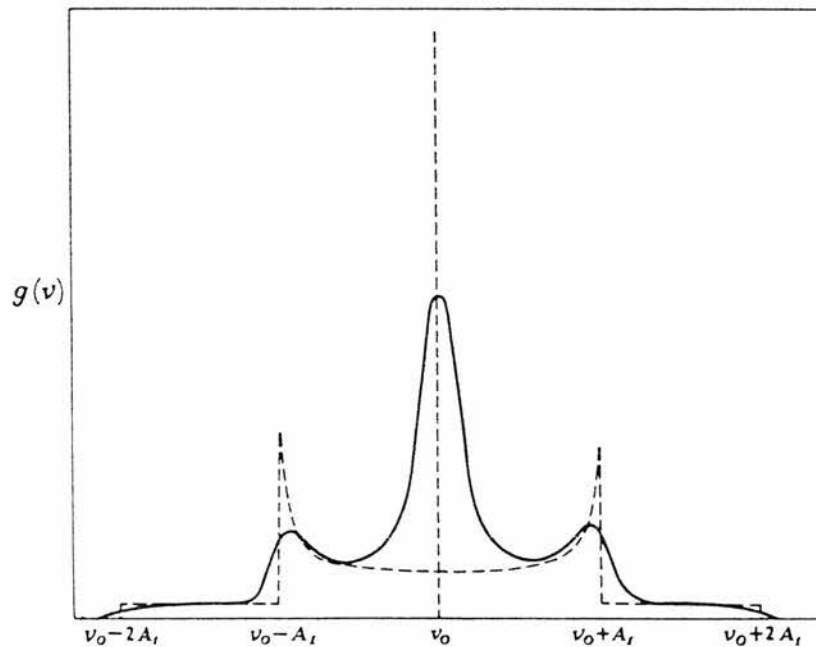


Figure 3.10. The dashed line represents the lineshape for  $I=3/2$  in a powder sample of axially symmetric crystals, when accounting for first order quadrupole perturbations. The solid line represents the lineshape with dipolar broadening. Taken from reference<sup>15</sup>.

the position of the central resonance and the satellite lines for an  $I=3/2$  nucleus, with the additional effects of broadening. The only other condition where the quadrupole resonance disappears is for an  $I>1/2$  nucleus at a site of cubic symmetry.

Second-Order Quadrupole Effects

$$E_m^{(2)} = -h \left( \frac{\nu_Q^2}{12\nu_L} \right) m \left\{ \frac{3}{2} \mu^2 (1 - \mu^2) (8m^2 - 4a + 1) + \frac{3}{8} (1 - \mu^2)^2 (-2m^2 + 2a - 1) \right\}$$

Second-order quadrupole effects lead to a shift to lower frequency of the central transition, and a second order quadrupole broad line. At high enough fields and frequencies, this second order term becomes negligibly small and so only the first-order effects remain. The lineshape for the  $m=1/2 \rightarrow -1/2$  transition for a randomly distributed powder of axially symmetric crystals is shown in Figure 3.11. The lineshape may vary greatly depending on the amount of line broadening. At one extreme no central structure or asymmetry is observable at all, and at the other extreme the step discontinuity may be visible. The effects of less-than axial symmetry will not be discussed here.

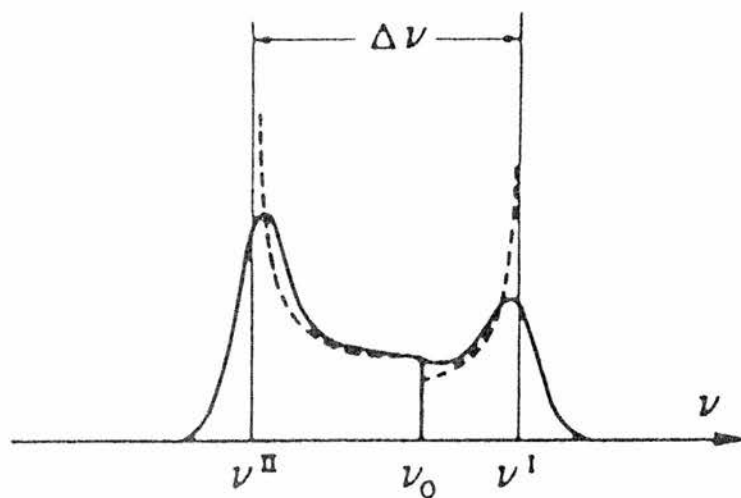


Figure 3.11. The central resonance ( $m=1/2 \leftrightarrow -1/2$ ) where second order quadrupole effects are present. The dashed line is the lineshape function, and the solid line is the case with dipolar broadening.  $\nu^I$  and  $\nu^{II}$  correspond to  $\theta$  values such that  $\mu = \cos\theta = 0$  and  $\sqrt{5/9}$  respectively. Note that  $\nu_0$  is no longer equal to  $\nu_{c.g.}$ . Taken from reference<sup>15</sup>.

**References**

- 1 A.R.West. *"Solid State Chemistry And Its Applications"*, John Wiley and Sons Ltd. (1984).
- 2 A.Guinier. *"X-Ray Diffraction"*, W.H.Freeman and Co. (1963).
- 3 M.M.Woolfson. *"An Introduction To X-Ray Crystallography"*, Cambridge University Press (1970).
- 4 H.S.Peiser, H.P.Rooksby and A.J.Wilson (eds.). *"X-Ray Diffraction By Polycrystalline Materials"*, Chapman and Hall (1960).
- 5 V.Scott and G.Love (eds.). *"Quantitative Electron Probe Microanalysis"*, Van Nostrand Reinhold (1983).
- 6 S.J.B.Reed. *"Electron Microprobe Analysis"*, Cambridge University Press (1975).
- 7 K.F.J.Heinrich. *"Electron Beam X-Ray Microanalysis"*, Van Nostrand Reinhold (1981).
- 8 L.J.van der Pauw. *Philips Res. Repts.*, **13** (1958) 1.
- 9 L.J.van der Pauw. *Philips Res. Repts.*, **16** (1961) 187.
- 10 C.P.Bean. *Rev. Mod. Phys.*, **36** (1964) 31.
- 11 A.Carrington and A.D.McLachlan. *"Introduction to Magnetic Resonance"*, Chapman and Hall Ltd. (1979).
- 12 R.K.Harris. *"Nuclear Magnetic Resonance Spectroscopy"*, Longman Group UK Ltd. (1986).
- 13 R.S.Macomber. *"NMR Spectroscopy. Essential Theory And Practice"*, HBJ College Outline Series, Florida (1988).
- 14 E.Fukushima and S.B.W.Roeder. *"Experimental Pulse NMR - A Nuts and Bolts Approach"*, Addison-Wesley Publishing Company Inc. (1981).

- 15<sup>\*</sup> G.C.Carter, L.H.Bennett and D.J.Kahan. "*Metallic Shifts in NMR - Part 1: Review Chapters NMR Tables*", Progress in Materials Science **Vol.20**, Pergamon Press (1977).
- 16 C.P.Slichter. "*Principles of Magnetic Resonance*", 3rd Edition, Springer-Verlag (1989).
- 17 A.Abragam. "*Principles of Nuclear Magnetism*", Oxford University Press (1961).
- 18 J.Winter. "*Magnetic Resonance in Metals*", Oxford University Press (1973).
- 19 C.H.Townes, C.Herring and W.D.Knight. *Phys. Rev.*, **77** (1950) 852.
- 20 W.D.Knight. *Solid State Physics (eds. F.Seitz and D.Turnbull)*, **2** (1956) 93-136.
- 21 W.D.Knight. *Phys. Rev.*, **76** (1949) 1259.
- 22 J.Korringa. *Physica*, **16** (1950) 601.
- 23 N.Bloembergen and T.J.Rowland. *Acta Met.*, **1** (1953) 731.

## Chapter 4

# EXPERIMENTAL TECHNIQUES

### 4.1. Introduction

This chapter aims to describe thoroughly all the experimental techniques carried out to characterise the  $Y_{1-x}Ca_xBa_2Cu_3O_{6+\delta}$  materials. Details of the initial sample synthesis are also given.

Basic techniques to confirm sample purity and structure were x-ray diffraction and electron-probe microanalysis. X-ray diffraction was carried out periodically to ensure that degradation of the samples had not occurred. The oxygen content was determined by three methods: an improved iodometric titration technique, thermogravimetric analysis, and electron-probe microanalysis. The lattice parameters obtained from x-ray diffraction studies were also an indication of oxygen content. Sample resistivity and susceptibility measurements demonstrated the electrical and magnetic properties of the samples and were used to determine the critical temperatures for the superconducting samples.

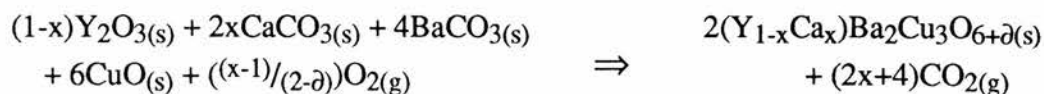
A major nuclear magnetic resonance (NMR) study was carried out on the samples. Experiments were performed for both the yttrium and copper nuclei, to study all three phases present: the antiferromagnetic insulating state, the superconducting state, and a region intermediate between the two.

### 4.2. Synthesis

The chemicals used were:

$Y_2O_3$	Aldrich Chemical Company	99.99%
$CaCO_3$	Johnson Matthey	99.95%
$BaCO_3$	Johnson Matthey	Puratronic
$CuO$	Aldrich Chemical Company	99.99+%

The starting materials were initially dried in a muffle furnace, CuO at 700°C and the other reagents at 350°C for at least 4 hours, and then stored in a desiccator until required. In total, 8 samples of  $(Y_{1-x}Ca_x)Ba_2Cu_3O_{6+\delta}$  were separately synthesised, with nominal compositions of  $x=0.00, 0.10, 0.12, 0.14, 0.16, 0.18, 0.20,$  and  $0.25$ . Appropriate molar amounts of  $Y_2O_3, CaCO_3, BaCO_3$  and CuO were weighed out accurately ( $\pm 0.1\text{mg}$ ) on a Stanton Instruments Unimatic CL41 four-figure balance to satisfy the equation



where  $x$  and  $\delta$  are from the stoichiometric formula  $(Y_{1-x}Ca_x)Ba_2Cu_3O_{6+\delta}$ . The quantity of calcium,  $x$  is controlled to produce the material required. The oxygen content  $\delta$  is not controlled and is the value obtained naturally for the reaction conditions used.

They were thoroughly mixed and ground together into a paste using acetone in an agate pestle and mortar (agate has a smooth, non-porous surface which minimises sample contamination), and were then dried to a homogeneous powder using the heat from a standard lamp. The powder was then placed in alumina crucibles and heated in a muffle furnace at 700-730°C for 24 hours. On removal, they were again mixed and ground, then cold-pressed into pellets 2-3mm thick and 12mm diameter using a stainless-steel dye under a pressure of 1500lb/in<sup>2</sup>. The pellets were placed in the alumina crucibles on a bed of powder of the same nominal composition in order to prevent reaction of the pellets with the crucible walls, and were then annealed at 940°C at ambient pressure for 2-3 days. At the end of this period, the samples were slowly cooled down to 350°C before removing from the furnace.

The long reaction times and high temperatures were needed due to the slow decomposition of  $BaCO_3$ . During sintering, reaction initially takes place at the grain boundary between the barium carbonate and copper oxide. Carbon dioxide is given off as  $BaCuO_2$  is formed at the boundary, a precursor to  $YBa_2Cu_3O_{6+\delta}$ . This slows the reaction, since the migration of the ions involved in forming the product across the grain boundary becomes increasingly difficult<sup>1</sup>. For this reason, the process of

grinding and repelletising was carried out several times during this period to ensure the complete reaction and homogeneity of the oxide.

After removal from the furnace, all but one pellet from each sample were crushed to a powder and stored in a vacuum desiccator. Small amounts of each were analysed by x-ray diffraction using  $\text{CuK}\alpha_1$  radiation to confirm the complete reaction of the constituents (see section 4.4 for more detail).

Once phase purity had been confirmed, each sample was quenched to reduce the amount of oxygen and produce the tetragonal phase of the compound. Each sample was placed in a platinum crucible and annealed overnight in the uniform zone of the vertical tube furnace (Carbolite Tube Furnace, Model MTF 12/38B) at  $730^\circ\text{C}$ . This was carried out in a controlled nitrogen atmosphere, nominally oxygen free, but in fact containing a small but significant amount (3ppm). The sample was then quenched to room temperature by dropping onto copper shot. A schematic diagram of the vertical quench furnace is shown in Figure 4.1. The furnace has an accurate temperature control, to within  $1^\circ$ , measured by a thermocouple present in the uniform zone (12cm long) at the centre of the furnace. The glass and quartz-ware were designed to produce a closed system so that flowing nitrogen (or any other desired gas) could be passed through it. The gas flow was controlled by the regulator on the gas cylinder and was monitored by bubbling the outgoing gas through water. The sample was contained in a platinum crucible (platinum is inert to YBCO for the temperatures used here) with a close fitting lid with a small hole in it to allow the gas to circulate. This was placed in a platinum wire holder and suspended from the top of the tube by a thin platinum thread wrapped around two hooked electrodes. In order to quench the sample, a large electric current was passed through the electrodes, sufficient to fuse the platinum thread and allow the crucible and holder to fall from the hot zone of the furnace to a bed of copper shot at room temperature. Copper was chosen in this form since it has a high thermal conductivity and could cool the sample to below  $400^\circ\text{C}$  in several seconds (below this temperature the oxygen content is stable<sup>2</sup>). Faster quenching techniques have been

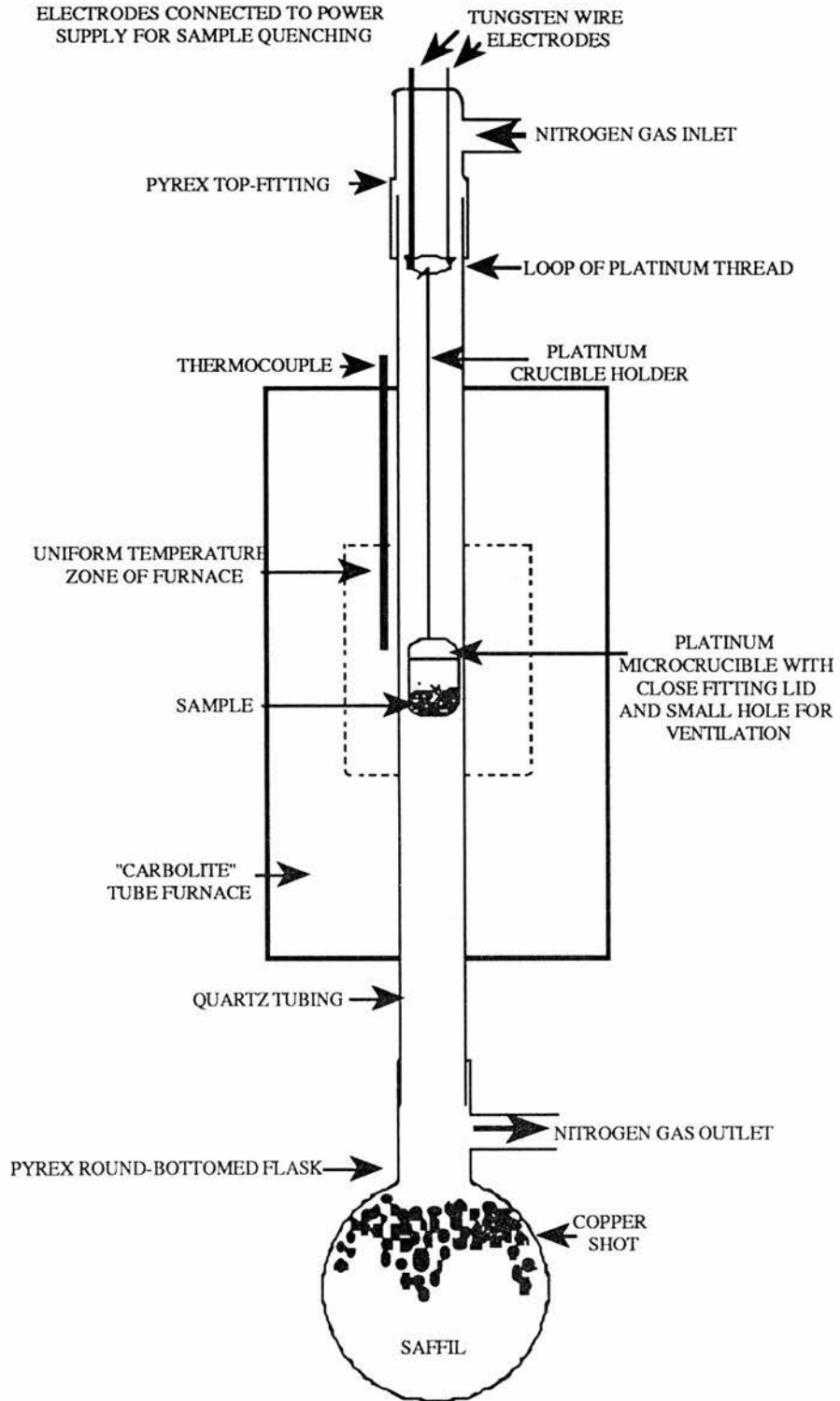


Figure 4.1. Schematic diagram of the equipment required for the vertical quenching technique.

developed<sup>3,4</sup> in which the sample drops to a bath of mercury or liquid nitrogen, but in both cases the sample initially has to fall through air.

The final products were carefully handled to reduce contact with moisture and were stored in a vacuum desiccator. In order to fulfil requirements of subsequent characterisation experiments, each sample was produced in the form of a pellet as well as ground powder.

### **4.3. Sample Alignment**

The signals obtained by NMR on powders, especially on YBCO related materials usually have poor resolution and are very broad. Improvements in the signal are obtained by increased order, preferably by using single crystals. However, the crystals required would have to be much larger than any synthesised by the solid state technique described above, and so a compromise has to be made. The granular solids produced can be finely ground until single crystallites are obtained and can then be aligned in a magnetic field and set in a non-magnetic matrix. This produces a pseudo-single crystal, with all the crystallites having a common axis, usually the *c*-axis for YBCO materials<sup>5</sup>. In this way, the signal linewidths are reduced and the resolution may be improved. A study has previously been made by Webster<sup>6</sup> on the optimum method for aligning the cuprates in this way. The method used for aligning the  $(Y_{1-x}Ca_x)Ba_2Cu_3O_{6+\delta}$  compounds here is based on that study.

A portion of each of the powder samples was finely ground to 1-10 $\mu$ m, the optimum particle size for obtaining single crystallites. This was done by initial grinding with an agate pestle and mortar, followed by milling in a stainless-steel ball-mill. Care was taken to prevent exposure of the fine powder to air, since faster degradation was expected to occur with smaller particle size, and also to prevent particle clustering which would impede the alignment process. Hence the powder was loaded and sealed into the stainless-steel milling container in a glove box, under an atmosphere of dry argon. Each sample was vigorously shaken in the ball-mill for 30 minutes, using

approximately ten, 5mm diameter stainless steel balls. It was assumed that all the samples would have approximately the same particle size since they had undergone the same process, but as a precaution, and in order to take into account varying hardnesses of the samples, three were examined by a particle size analyser.

The material chosen to set the crystallites was Stycast 1266, due to its non-magnetic and amorphous nature. It has also been found to protect the samples from moisture<sup>7,8</sup> allowing longer exposure to air. Stycast is initially in two parts, the resin A and the catalyst B, to be mixed in proportions 100:28 by weight respectively.

The experimental procedure is outlined below. Each step must be carried out efficiently, since the pot-life of the mixed epoxy is approximately 30 minutes, and when it becomes too viscous, it becomes difficult to handle and also introduces the risk of failure of the alignment process.

Clean, thin-walled glass tubes were arranged ready for use. The inner diameter was the same as that for the yttrium and copper NMR samples required. The length of the tubes were longer than required to allow for the insertion of the rubber bung. Also, 10ml small conical flasks were arranged and labelled, one for each sample composition. The samples and the epoxy were to be mixed in the ratio of 1:9 by volume. Initially, the correct volume of epoxy was decided upon, and the volume of the corresponding sample was calculated. This volume was then converted into a mass, using a value for the density calculated from the volume and the relative molecular mass of the unit cell. This mass was then weighed accurately using the four-figure balance and was placed in the correspondingly labelled conical flask.

After the weighing of the samples, part A of the epoxy was heated slightly to reduce the viscosity and to help drive off any water that may have been present. The correct proportion was then poured into a small beaker and was placed under a vacuum (achieved by placing the beaker in a continuously pumped vacuum dessicator) for a minimum of 30 minutes to remove any dissolved air. Part B could not be given the same treatment due to its volatility. Parts A and B in their correct proportions were then

thoroughly mixed, and the resulting epoxy was again pumped for several minutes to reduce the amount of dissolved air caused by the mixing procedure.

Batches of the mixed epoxy were then measured out to the desired volume in a 5ml measuring cylinder and were added to each of the conical flasks. The sample and epoxy were thoroughly stirred using looped wire. Ultrasonic dispersion was then carried out by inserting an ultrasonic drill bit in the mixture for approximately 1 minute. The aim of this was to evenly distribute the particles among the epoxy. The mixture was then poured out into the previously prepared glass tubes, and were sealed using rubber bungs and PTFE tape.

The filled glass tubes were placed on their sides in a brass former and were marked by drawing a vertical line on the end of each tube, to indicate the direction of the magnetic field. The former was then inserted into the bore of the superconducting magnet, with uniform field strength 11.74 Tesla, and the epoxy was allowed to cure for 8 hours.

After curing, the brass former was removed from the magnetic field. The epoxy-set samples were removed from the glass tubes by dropping them in liquid nitrogen and carefully peeling away the broken glass. The vertical line indicating the field direction was transferred to the sample by scratching a corresponding line in the epoxy. In many cases, this direction could be confirmed by comparing the line with the bubbles set in the sample, which naturally marked the highest point of the tube whilst the epoxy had set.

In order to deduce the success or failure of the alignment procedure, thin slices taken from the end of the epoxy-set samples were analysed by x-ray diffraction. This procedure also checked for impurities and possible degradation introduced by the mixing procedure. The powder distribution could also be examined by electron microscopy.

#### 4.4. X-Ray Powder Diffraction

X-ray diffraction is used to qualitatively identify the crystalline phases and compounds present in a sample. Although the analysis does not give information about the elements present in a sample, the positions and intensities of the observed peaks can be used as a fingerprint for crystal identification, giving information about the regularly repeating planes in the crystal, and consequently information about the unit cell. This x-ray diffraction technique has been carried out on the  $(Y_{1-x}Ca_x)Ba_2Cu_3O_{6+\delta}$  samples by two different diffractometers. The Philips PW1049 diffractometer was used to check the completeness of reaction of the initial constituents, determine the degree of crystal alignment for epoxy-set powders, and also to periodically check for possible degradation of the samples. An instrument with superior resolution, the STÖE STADI/P transmission powder diffractometer, was used to accurately determine the lattice parameters of the crystals.

The powder samples were finely ground, ideally to 1-10 $\mu$ m. For the Philips diffractometer, the powders were individually mounted on small plates using acetone, and for the STÖE, glass capillary tubes were filled with the powder. Mounted in this way, the crystals were ideally randomly arranged in every possible orientation, thus the various lattice planes were also present in every possible orientation. For each set of planes there will always be at least some of the crystals orientated at the Bragg angle  $\theta$  to the incident beam, and so diffraction will occur. If however, the crystals are not sufficiently small, there is a higher probability of the crystals lying on a face, reducing the random nature of the distribution and thus introducing errors into the observed intensities.

The x-ray diffraction technique was described in more detail in Section 3.2. The terms used below are described there. The x-rays diffracted from the powder samples formed cones of radiation at an angle  $2\theta$  to the undiffracted beam as shown in Figure 4.2. A movable counter was set to scan a range of  $2\theta$  values at a constant angular velocity and the intensities detected were then plotted as a function of  $2\theta$ . Each

peak was labelled with its Miller indices and the corresponding d-spacings were calculated using Bragg's Law. For this, the wavelength of the source must be known. The incident x-ray beam was produced either by using a copper  $\text{CuK}_{\alpha 1}$  source ( $\lambda=1.5405\text{\AA}$ ), or a cobalt  $\text{CoK}_{\alpha 1}$  source ( $\lambda=1.7890\text{\AA}$ ). The particular source used has been specified for each spectrum. It is also possible to improve the accuracy of the  $2\theta$  scale by mixing an internal standard, whose d-spacings are known accurately, with the sample. A convenient standard to use with YBCO is NaCl, since very few of the observed peaks overlap.

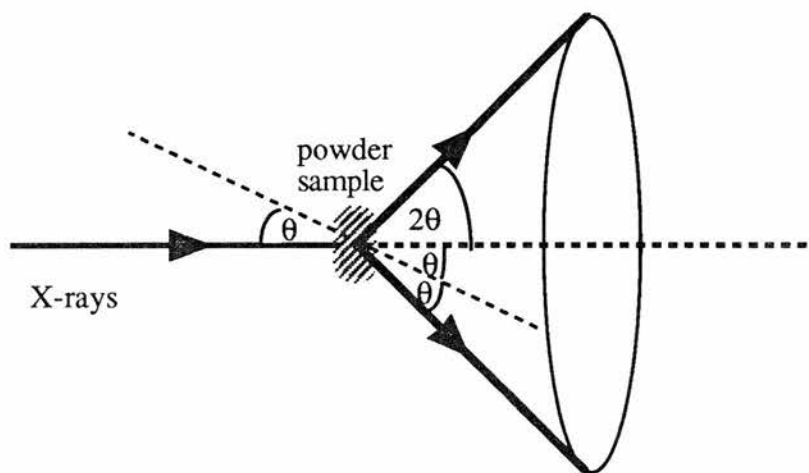


Figure 4.2. Cones of radiation formed by the x-rays diffracted from the powder samples.

#### 4.5. Electron Microscopy

Further studies of the  $(\text{Y}_{1-x}\text{Ca}_x)\text{Ba}_2\text{Cu}_3\text{O}_{6+\delta}$  samples were carried out with the aid of a JEOL JCSA-733 Superprobe with attached scanning electron microscope (SEM) and backscattered electron detector. This was used to search for sample inhomogeneities<sup>9</sup>, observe particle sizes and ultimately to determine the oxygen stoichiometries of the samples<sup>10</sup>. Further information on electron microprobe analysis may be obtained in the suggested texts<sup>1,11,12,13,14</sup>.

The samples were required in various forms depending upon the experiment being carried out. However, all of them had to be set into an epoxy mount of set

dimensions for loading into the machine. For the particle size and distribution study, a cylindrical slice was removed from the end of the  $x=0.10$  and  $x=0.16$  aligned epoxy-set samples. This was then mounted in an epoxy block as described above. For the oxygen determination experiment, large grain powders were mixed with epoxy and then set into the mount. The upper surface of these epoxy mounts were polished and then coated with a conductive layer of carbon by sputtering. To eliminate effects due to inconsistencies in the carbon layers between mounts, all samples to be compared were sputtered together. For a later experiment, a different technique was used to make the conductive path. The powder sample was mixed with conductive silver epoxy, which was then set in the mount. This eliminated the need for a carbon layer.

Two known standards (Manufactured by the Aldrich Chemical Company Ltd.) were used for this experiment, 99.9%  $\text{YBa}_2\text{Cu}_3\text{O}_{6.8(\pm 0.1)}$   $2\mu\text{m}$  powder and  $\text{YBa}_2\text{Cu}_3\text{O}_{6.5}$  unspecified powder size. The latter was annealed at  $650^\circ\text{C}$  and slowly cooled to  $400^\circ\text{C}$  in flowing oxygen at ambient pressure to maximise the oxygen content. A measured  $T_c=93\text{K}$  by AC susceptibility on this material indicated that the oxygen content was close to 7. Both powders were prepared in epoxy as described above.

For the aligned powders set in epoxy, it was possible to observe the particle distribution even at low magnifications. At higher magnifications, for all samples, it was possible to observe the details of the grains. In backscatter mode, the intensity was dependent upon atomic number and sample contours, hence any different phases could be detected. Effects due to sample contours were minimised by the polishing procedure and could be taken into account by cross-referencing with the corresponding secondary electron image. For the oxygen stoichiometry experiments, flat, uniform sections of a particle were chosen for analysis.

## 4.6. Determination Of The Oxygen Content

The importance of oxygen stoichiometry for an accurate study of the effects of calcium doping have been stressed previously. It is generally agreed among cuprate researchers, that an accurate measurement of the oxygen content is very difficult. The techniques that can be used are varied, from measuring the oxygen loss on heating, to measuring the average copper valence of the material. Several techniques were used to characterise our materials in order to improve the accuracy of the results. Iodometric titration and thermogravimetric analysis were the major techniques used. A less common method was also employed, ie. electron probe microanalysis (see section 4.5), but with less success.

Iodometric titration and thermogravimetric analysis was carried out with collaborators (J.T.S.Irvine, M.Koppers and S.Fray) at the Department of Chemistry, University of Aberdeen.

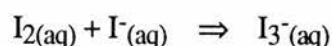
### 4.6.1. Iodometric Titration

The iodometric titration method<sup>15,16,17,18,19</sup> determines both the number and average oxidation state of the copper ions in  $(Y_{1-x}Ca_x)Ba_2Cu_3O_{6+\delta}$ . This information can then be used to determine the oxygen content.

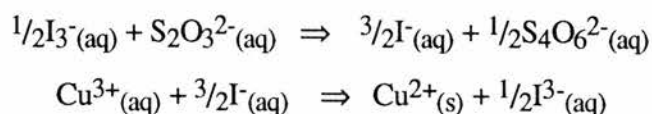
The standard iodometric technique involves the reaction of both  $Cu^{2+}$  and  $Cu^{3+}$  ions with iodide to produce iodine. The quantity of iodine produced is then directly proportional to the degree of oxidation greater than  $Cu^+$ . Knowing this and the total number of copper ions in the sample, allows the average oxidation state of copper in the material to be calculated. Assuming that the cation stoichiometry of the material is known, the oxygen content of the material may be calculated. It is important for iodometric determinations to avoid the loss of holes by the production of oxygen gas on dissolving the sample. For example, if  $YBa_2Cu_3O_7$  is dissolved in pure hydrochloric

hydrochloric acid  $O_2$  is evolved, but if excess iodide is present iodine is produced instead of  $O_2$  evolution.

For the following titration procedures, iodine has been written as  $I_2$ . This is technically incorrect, since there is initially an excess of iodide ions present during the titration procedure, leading to the formation of the reactive tri-iodide ion



Thus it is accurate to write  $I_3^{-}$  rather than  $I_2$ , for example



However,  $I_2$  has been written for simplicity.

#### **4.6.1.1. Experimental Precautions**

Due to the rapid reaction of iodide with atmospheric oxygen at low pH, precautions were necessary and all experiments involving acid were carried out under argon atmosphere. Hence a small glove box was used and was flushed with fresh argon each day. In order to remove any dissolved oxygen, the reagents were placed in the glove box and were saturated by bubbling with argon gas for at least 30 minutes. After bubbling, the reagents were allowed to equilibrate in stoppered flasks for approximately 10 minutes, with the occasional release of pressure.

#### **4.6.1.2. Preparation Of A Starch Solution**

0.1g of soluble starch was mixed to a paste with a little water and then, whilst constantly stirring, was poured into 100ml of boiling water and was boiled for 1 minute. After cooling, 2-3g of potassium iodide was added. In order to preserve the solution, 1mg of  $HgI_2$  was also added, and the final solution was kept in a stoppered bottle.

#### 4.6.1.3. Standardisation Of Sodium Thiosulphate

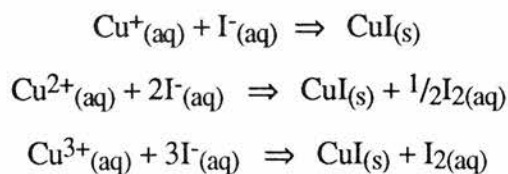
2.4g of pure potassium iodate,  $\text{KIO}_3$ , which had been dried at  $120^\circ\text{C}$  for a minimum of 4 hours, was accurately weighed out. It was then dissolved in distilled water and made up to 1 litre in a volumetric flask. 1g of potassium iodide, KI, and 5ml of 1M sulphuric acid were then added and the final solution diluted to 25ml with more distilled water. The following reaction took place to liberate iodine:



The iodine produced was then titrated with sodium thiosulphate solution ( $\sim 0.03\text{M}$ ) in a 10ml microburette whilst constantly stirring. When the liquid became a pale yellow colour, 3 drops of 1% starch solution were added as an indicator. The sodium thiosulphate solution was preserved by adding either 0.1g of sodium carbonate or 3 drops of  $\text{CHCl}_3$ .

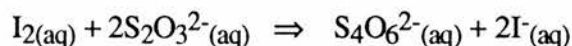
#### 4.6.1.4. Standard Iodometry

The finely ground sample was accurately weighed (approx.  $1.5 \times 10^{-5}$  moles), placed in a 100ml wide-necked conical flask and covered with finely ground potassium iodide. This was placed in the glove box, and 0.5g KI dissolved in 10ml 2M HCl was added, and the flask quickly stoppered with a rubber bung. The flask was then left to stand for 15 minutes, to allow the KI saturated solution to capture the evolved oxygen. The following reactions occur:



The solution was subsequently neutralised with 6ml 2M  $\text{Na}_2\text{CO}_3$  solution and was removed from the glove box. 1M acetic acid was then added dropwise, until a final pH of 4.0-4.3 was reached (at lower pH values the rate of oxidation by air rapidly

increases, and at higher pH values the  $\text{Cu}^{2+}$  is not fully reduced and so undertitration follows). The amount of liberated iodine was then determined by titrating with 0.03M  $\text{Na}_2\text{S}_2\text{O}_3$ . As the colour of the iodine began to disappear, 3 drops of 1%(w/v) starch solution were added as indicator.

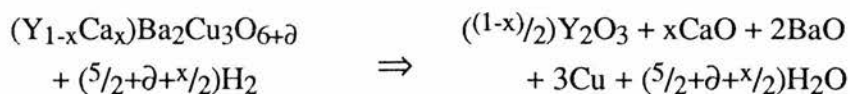


#### 4.6.2. Reductive Thermogravimetric Analysis

The oxygen contents of the  $(\text{Y}_{1-x}\text{Ca}_x)\text{Ba}_2\text{Cu}_3\text{O}_{6+\delta}$  samples were determined by the reduction of each sample in a thermogravimetric analyser. The instrument used was a simultaneous TG-DTA Stanton Redcroft Model STA 1000, allowing for close atmospheric control<sup>2</sup>. The reductions were carried out in a 5%  $\text{H}_2$  atmosphere, the remaining 95% being a precautionary measure of  $\text{N}_2$ , to avoid the hazard of an explosion.

The sample (typically 30mg) to be analysed was placed in an alumina microcrucible and accurately weighed ( $\pm 0.05\text{mg}$ ) on a digital balance. It was then transferred to the simultaneous thermal analyser. The sample was heated at  $10^\circ\text{Cmin}^{-1}$  in the flowing reducing atmosphere up to  $1000^\circ\text{C}$  and was held at that temperature for approximately 40 minutes, until no further weight loss was observed. The corresponding temperatures and recorded weights were plotted as a function of time by a chart recorder.

When heated in  $\text{H}_2/\text{N}_2$  to  $950\text{-}1000^\circ\text{C}$ ,  $(\text{Y}_{1-x}\text{Ca}_x)\text{Ba}_2\text{Cu}_3\text{O}_{6+\delta}$  undergoes reduction to  $\text{BaO}$ ,  $\text{CaO}$ ,  $\text{Y}_2\text{O}_3$  and  $\text{Cu}$  metal according to the equation:



If required, further analysis of the decomposition products by standard techniques could be made.

A calculation was then made to determine the oxygen stoichiometry of the sample. This was an iterative technique based on the theoretical percentage weight loss of a single oxygen from the starting material and the actual weight loss. Initially the oxygen content of the sample was assumed, then was corrected as the iterations proceeded until a consistent value for the stoichiometry was obtained to 3 significant figures.

## **4.7. Critical Temperature Measurement**

The electric and magnetic properties of all the samples were investigated by resistivity and susceptibility experiments<sup>20,21,22</sup>. As well as determining the superconducting transition temperatures, the susceptibility measurements also gave an indication of the superconducting volume fraction. The resistivity experiment differentiated between the different phases in the range of samples, from the insulating to the metallic and the superconducting regimes.

### **4.7.1 Resistivity Measurement**

Measurements were carried out by an AC resistance method owing to the wide range of the resistivities expected for the system. The optimum AC frequency was determined by varying the frequency at a specific temperature, and choosing a frequency value in the range where the measured resistance corresponded to the true bulk resistance of a sample, or when the out-of-phase component was a minimum. The value chosen by this method was 30Hz and was used for all the experiments.

The samples used to measure the Van der Pauw resistivity<sup>23,24</sup> were cylindrical pellets of annealed powder synthesised as described in Section 4.2. These could be considered as being isotropic, despite YBCO having highly anisotropic behaviour, since they are bulk granular samples comprised of many small crystals of random orientation. Due to the nature of the steel dye used to press them, the pellets were flat and of uniform thickness.

The resistivity probe (cryostat insert) was initially designed as a simple mechanism allowing for the easy change of samples. This design is shown in Figure 4.3(a). It is a shaped PTFE block with four sprung-pins diametrically inserted such that they would hold the sample firmly in place, whilst at the same time acting as the four electrical contacts to the sample to make the measurements.

After several test experiments, it was soon realised that the electrical contacts to the sample were not sufficient, and produced a large out-of-phase component of the reactance. Thus the system was adapted such that fine silk-clad copper wires ( $40\mu\text{m}$ ) were attached to the sample using silver-loaded electrically conductive paint. Again the contacts failed, possibly due to the nature of the paint, and it was replaced by silver dag. This proved to be the best method, despite the fact that the dag was very thick, making neat contacts very difficult.

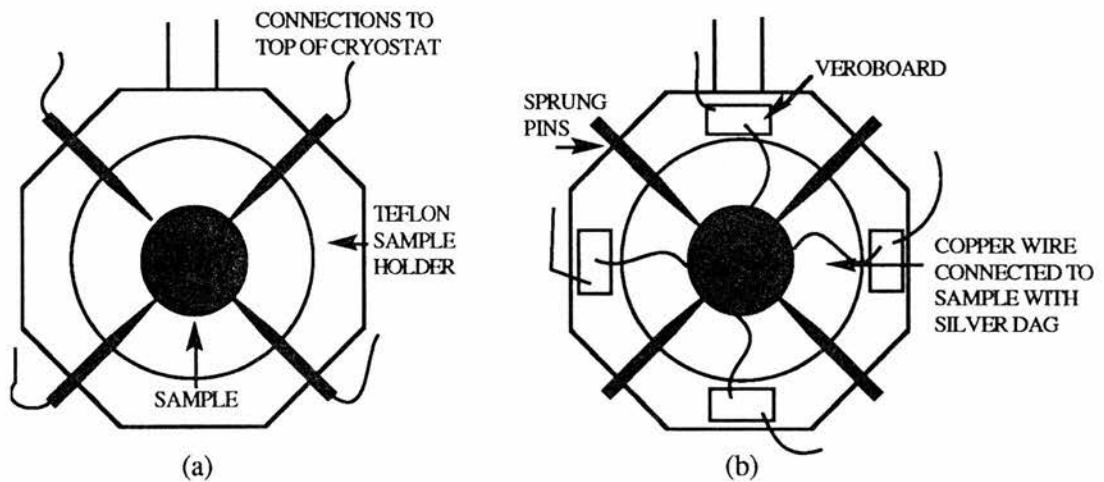


Figure 4.3. The resistivity probe-head (a) initial design, (b) final version.

This method was not always successful. Silver contacts frequently detached from the samples and the thin copper wires snapped easily. These occurrences were minimised by keeping the wires as short as possible, and soldering them to small pieces of veroboard attached to the PTFE block. The veroboard was permanently wired to the socket system at the top of the probe. The final design of the probe-head is shown in Figure 4.3(b).

Once a sample had been successfully mounted, the insert was placed into the continuous-flow cryostat (Oxford Instruments CF1200). The remaining equipment was connected as shown in Figure 4.4. The VDP relay box and LIA box were homemade and the circuit diagrams are given in Figure 4.5(a) and (b). Although the temperature had to be controlled manually, the rest of the equipment was controlled by computer (COMPAQ Deskpro 286e). It was programmed to switch between the two positions  $R_{AB,CD}$  and  $R_{BC,DA}$ , averaging for 30 seconds in each position, record both the in-phase and out-of-phase components measured by the lock-in amplifier (Model SR850 DSP Lock-In Amplifier, Stanford Research Systems), and the corresponding cryostat temperature. Good electrical contacts were assumed if, at room temperature, the in-phase component was much larger than the out-of-phase component, and that the value for resistivity seemed reasonable as compared to published data<sup>25,26</sup>.

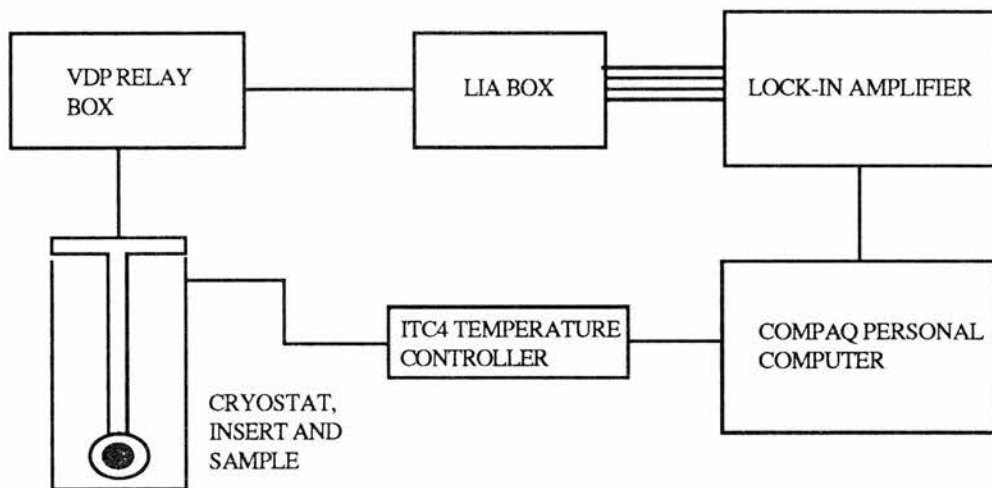


Figure 4.4. Equipment layout for the Van der Pauw resistivity experiment.

The experiment was repeated several times for each sample, using new contacts each time to check the feasibility of the results. The methods by which the temperature was controlled appeared to affect the results. Initially, the cryostat was rapidly cooled from room temperature to 3.5K, then was immediately warmed in  $3^\circ$  steps using the heater control connected to the ITC4 (Temperature Controller, Oxford Instruments). Problems occurred using this method, since the sample temperature took a very long

time to equilibrate especially after the fast cool-down. Also, fast oscillations in temperature were observed between 7K and 13K, causing the real temperature of the sample to average out (probably to about 10K), and consequently the resistivity measurements appeared as a plateau for this range. The process of changing the temperature in 3° steps, and waiting for the system to come to equilibrium each time was difficult and very slow. Errors are likely to have been introduced by this method by not waiting a sufficiently long time for the sample temperature to settle.

Several improvements were made on this initial attempt. The sample was very slowly cooled to 3.5K whilst recording data, and was then left at this low temperature for typically 1 hour in order for it to completely settle. After this time, all pressure was taken off the helium dewar and the cryostat was allowed to warm up without the aid of the heater. This prevented the temperature oscillations from occurring, and allowed the sample to warm up very slowly and at an almost constant rate. Moreover, this method could be repeated almost precisely for each sample. It was hoped that the slow rise in temperature would cause very little discrepancy between the temperature recorded in the cryostat and the actual sample temperature.

#### **4.7.2 Susceptibility Measurement**

The samples used for this experiment were in the form of ground powder, closely packed into glass tubes and tightly sealed with a bung and PTFE tape. In order to make a comparison of the results, an attempt was made to pack the same amount of sample into each tube. However, variations will have occurred since the powders were not all ground to the same size and hence the packing will have been different.

The glass tube containing the sample was placed within a wound coil, connected to the remaining equipment as shown by the schematic diagram in Figure 4.6. A second coil was placed in series with the original coil, wound in the opposite direction but not containing any sample. This was used to make the measurements differential, so that any background temperature dependencies in the coil itself were cancelled out.

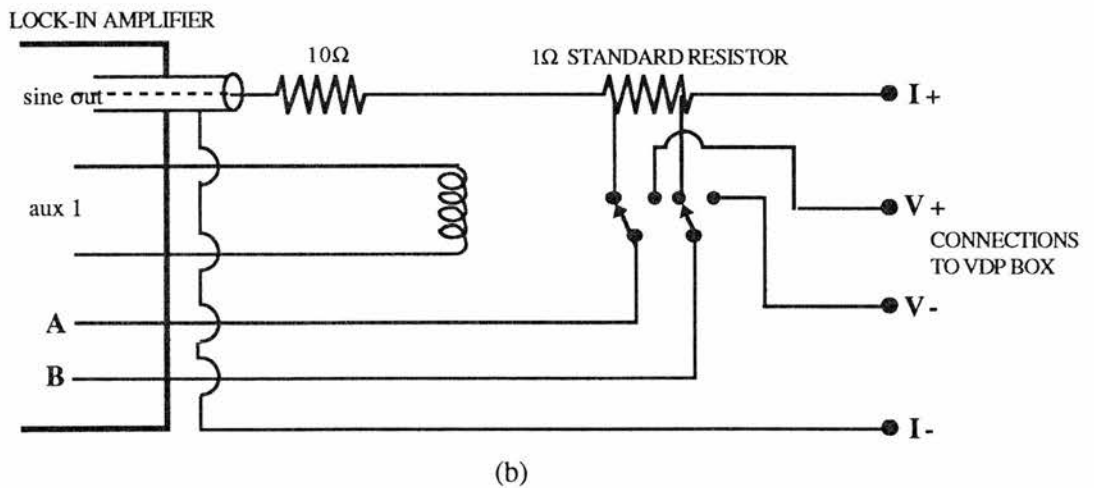
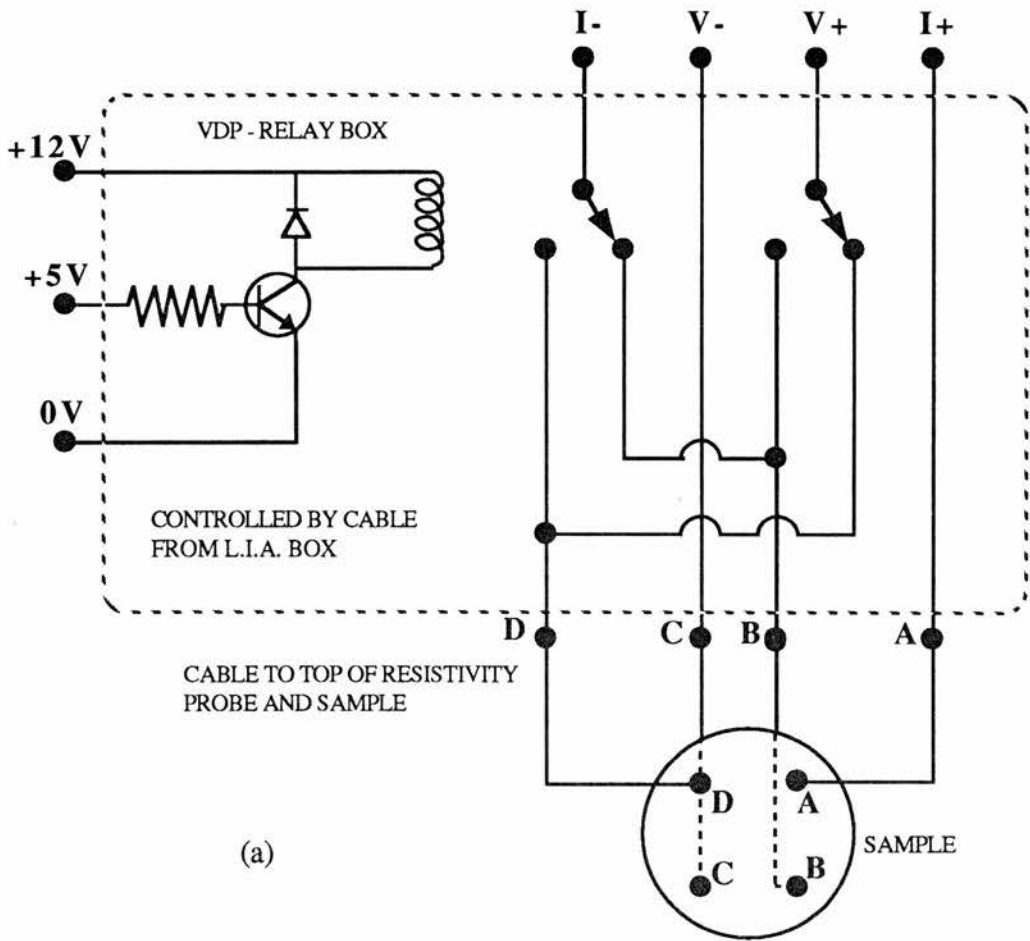


Figure 4.5. Circuit diagrams for (a) the VDP relay box, and (b) the L.I.A. box.

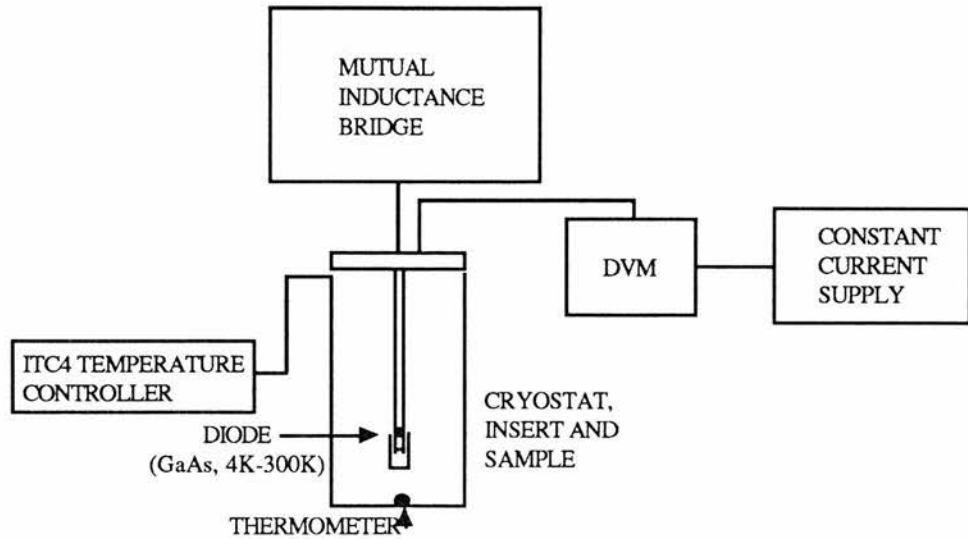


Figure 4.6. Schematic diagram of the experimental equipment for susceptibility measurement.

The temperature of the system was measured using two devices, the ITC4 (Temperature Controller, Oxford Instruments) and an independent GaAs diode placed at the bottom of the cryostat insert's central rod. The distance between these two was 12cm and thus, due to the gas flow system, both could be at different temperatures. The sample was suspended at a measured distance between the two. The temperature at this point was calculated using the temperature gradient between the two devices and the distance of the sample from the diode.

The cryostat was initially cooled to 5K. The settling time could be judged by the rate of change of the diode voltage read by the voltmeter (DVM). Using this technique, the sample was warmed in 3-5K increments to 100K using the ITC4 heater. At each settled temperature, the quadrature component was balanced by the mutual inductance bridge, followed by the balancing of the in-phase component. Both in-phase and quadrature readings were recorded and plotted as a function of sample temperature.

## 4.8. Nuclear Magnetic Resonance (NMR) Study

### 4.8.1. Introduction

Nuclear magnetic resonance (NMR) is a very lucrative and yet non-destructive technique. In the YBCO ceramics, the interesting sites to observe are those of the  $^{89}\text{Y}$  and the  $^{63}\text{Cu}$  atoms. Yttrium is ideal for monitoring effects and changes of the  $\text{CuO}_2$  planes, since it has a spin of  $I=1/2$  and only couples with electrons of the  $\text{CuO}_2$  planes via the weak magnetic hyperfine interactions. It is centrally positioned in the unit cell and sits between the two copper planes.

The major study here is of the  $^{89}\text{Y}$  site, although  $^{63}\text{Cu}$  was also studied. The general pulsed NMR spectrometer is described briefly at the beginning of this section, followed by more specific information about the Bruker MSL 500 spectrometer used for the work here. The pulse programs and data manipulation procedures are explained towards the end of the section, along with a summary of the experiments accomplished. The following texts are recommended for further information regarding nuclear magnetic resonance<sup>27,28,29,30,31</sup>.

### 4.8.2. The General Pulsed NMR Spectrometer

A simplified diagram of a pulsed NMR spectrometer is shown in Figure 4.7. The sample is placed within the RF coil, which in turn sits within the magnetic field  $B_0$  (which defines the  $z$ -axis). The NMR probe is basically an LC circuit tuned to the Larmor frequency. The sample acts as the circuit inductance. Matching is achieved by circuitry at position A. In the modern spectrometer, the same coil is used as both the transmitter and receiver. Also positioned at A is circuitry to separate the transmitter and receiver signals. The transmitter is essentially an RF frequency generator, which operates continuously. In order to produce RF pulses, the signal is passed through a gate, which is controlled by a pulse generator. The pulsed signal is then amplified

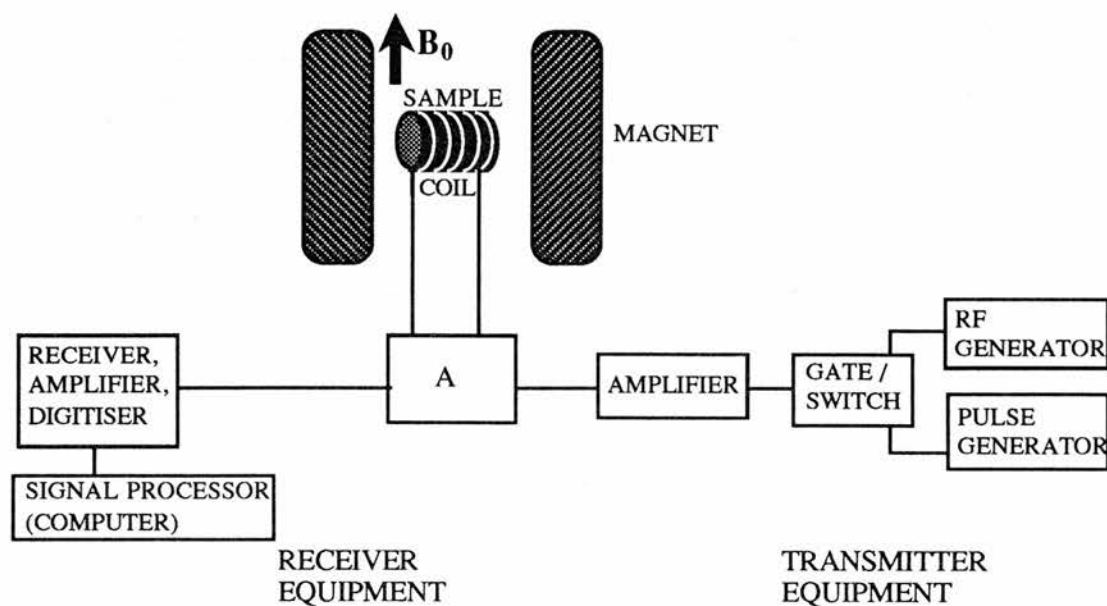


Figure 4.7. A general pulsed NMR spectrometer.

before being transmitted to the coil. The sinusoidal RF current in the coil generates a magnetic field  $B_1$ . The induced magnetisation of the sample is then sensed by the receiver coil and is amplified and processed by the computer.

The separation of the transmitter and receiver signals at A is not perfect and in practice there are always some transmitter pulse leaks through to the receiver. For this short period, the free-induction decay (FID) is corrupted. In addition, the start of the FID is affected by the decay of the RF pulse (known as ringdown) and by mechanical oscillations in the coil caused by the transmitted pulse. This corrupted section of the FID is known as the deadtime. To minimise these effects, signal is sent to the receiver only after a period equivalent to the deadtime has elapsed. Any remaining corrupted data points must be removed before data analysis. The spin-echo technique, to be discussed later in detail, eliminates the problem of corrupted signal at the beginning of the FID.

### 4.8.3. The Bruker MSL 500 Spectrometer

All NMR measurements were carried out using the Bruker MSL 500 Spectrometer. The RF coil and sample are contained in a probe which is inserted into the 89mm bore of an 11.74T magnet. This superconducting cryomagnet was manufactured by Oxford Instruments and further details may be obtained from the manual<sup>32</sup>. Shim coils exist in the bore of the magnet for high-resolution NMR, but the settings were not changed for the work here since the lines observed are so broad. The spectrometer is computer controlled using an Aspect 3000, which allows data acquisition and data manipulation to be carried out simultaneously on three independent channels. The software used is standard Bruker DISMSL software. Pulse programs may be written using the Bruker Specific Programming Language, to control the transmitter and receivers of the spectrometer via an onboard System Process Controller (SPC).

Further details and specifications for the Bruker MSL 500 Spectrometer and the Aspect 3000 Computer Controller may be found in the reference manuals<sup>33,34</sup>.

A continuous frequency range of 17 to 215MHz is available with the low-frequency transmitter for pulsed NMR. In addition, there is a proton frequency transmitter for work at 500MHz.

The probe used for all experiments here was a simple solenoid probe. This could be used over a wide continuous frequency range by changing the solenoid probeheads, each of which tune to smaller frequency ranges. For  $^{89}\text{Y}$  NMR, the frequency range of the required probehead is 19.5 - 27MHz, since  $\gamma=2.087$  and  $\nu_0=24.506\text{MHz}$ . For  $^{63}\text{Cu}$  NMR a probehead with frequency range 125 - 165MHz must be used since  $\gamma_{(\text{bare})}=11.285$  and  $\nu_{0(\text{bare})}=132.486\text{MHz}$ . The coils in the Bruker probe-heads are made from copper wire and subsequently contribute to the Cu NMR signal. This complication was avoided by building a replica probe-head for the same frequency range with a silver coil.

The size of the coils in the two probe-heads used here were different, and hence two sets of samples were required for NMR. The probe-head used for  $^{89}\text{Y}$  NMR had a coil which allowed the insertion of a cylindrical sample of 10.3mm diameter and 34mm maximum length. The  $^{63}\text{Cu}$  probehead required a sample of 5.0mm diameter and 34mm maximum length. The samples used for NMR were fine powders suspended and set in epoxy in a magnetic field, such that the individual crystals have aligned with the *c*-axis parallel to the applied magnetic field. This procedure has been outlined earlier in section 4.3. Aligned samples are preferred for solid state NMR, since the increased order reduces the signal linewidths and improves resolution.

Variable temperature measurements may be carried out for the Bruker MSL 500 spectrometer. A double-walled glass dewar must be fitted over the coil probe-head, sealed by rubber O-rings. Changes in temperature are produced by a heater and gas-flow system. Usually a dewar of liquid nitrogen would be connected to the probe by an insulated flexible transfer tube. A heater in the liquid nitrogen causes a constant boil-off, and the nitrogen gas then flushes the probe from the bottom, where it is heated to the correct temperature via a heater controlled by the variable temperature unit. The nitrogen passes through the coil and sample area, then is flushed out of the system through a long plastic tube to the laboratory. This system minimises the effects of the build-up of ice in the bore of the magnet.

#### **4.8.4. Pulse Sequences**

This section describes the pulse sequences used for this work to acquire the NMR data. Brief explanations of the purposes of the sequences is given along with the parameters used in each of the programs.

##### **4.8.4.1. The Spin-Echo**

The spin-echo technique was developed by Hahn in 1950<sup>35</sup> as a method of removing the effects of field inhomogeneities. The sample is placed within the RF coil in a magnetic field. If a  $90^\circ$  pulse is applied at time 0 along, for example, the  $x'$

direction (in the rotating reference frame), the entire magnetisation will be rotated through the appropriate angle in a very short time. Each component of the magnetisation will then precess with its own characteristic Larmor frequency. Due to the slight inhomogeneities of the magnetic field, not all parts of the sample will precess at the same rate. The magnetisation of the sample in a slightly larger magnetic field will precess faster than that in a smaller field. This results in the magnetisation fanning out and getting out of phase as demonstrated below in Figure 4.8. The net magnetisation consequently decays to zero along the  $y'$  axis.

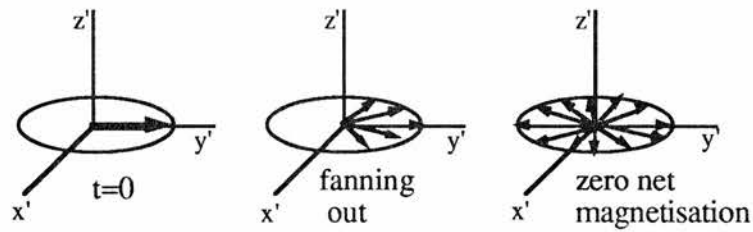


Figure 4.8. The dephasing of the sample magnetisation following a  $90^\circ$  pulse in the  $x'$  direction, shown in the rotating reference frame.

The spin-echo technique involves applying a further  $180^\circ$  pulse along  $x'$  at a time  $\tau$  later. This has the effect of rotating the spins  $180^\circ$  and so the spins which were previously ahead of the others by a certain amount, now lag behind by the same quantity and vice versa. Therefore following the  $180^\circ$  pulse, the spins begin to rephase to form a net magnetisation. The magnetisation becomes focussed along the  $-y'$  axis at a time  $2\tau$ , causing an inverted spin-echo, which is two FIDs (free-induction decays) back to back. If the  $180^\circ$  pulse is applied along the  $y'$  axis, the echo has the same sign as the FID. This sequence of events is shown in Figure 4.9.

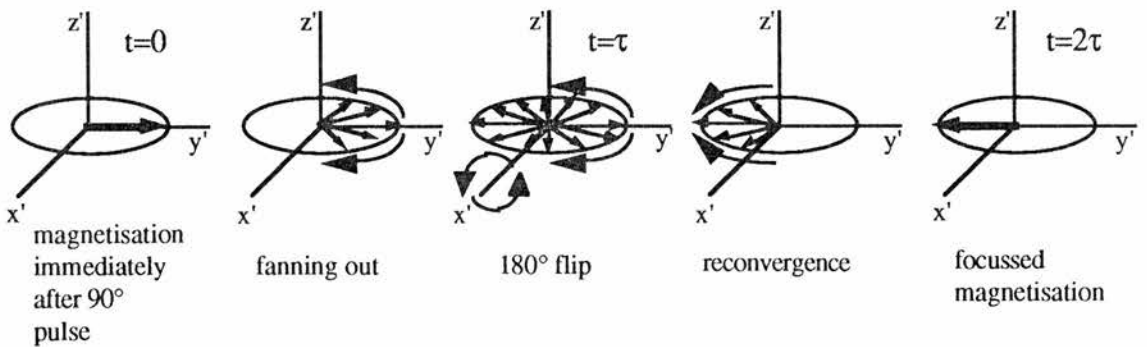


Figure 4.9. Effects of the  $90^\circ$  and  $180^\circ$  pulses on the sample magnetisation.

The pulse sequence, with the parameters used for the program SAM1ECHO.PC is shown below (Figure 4.10).

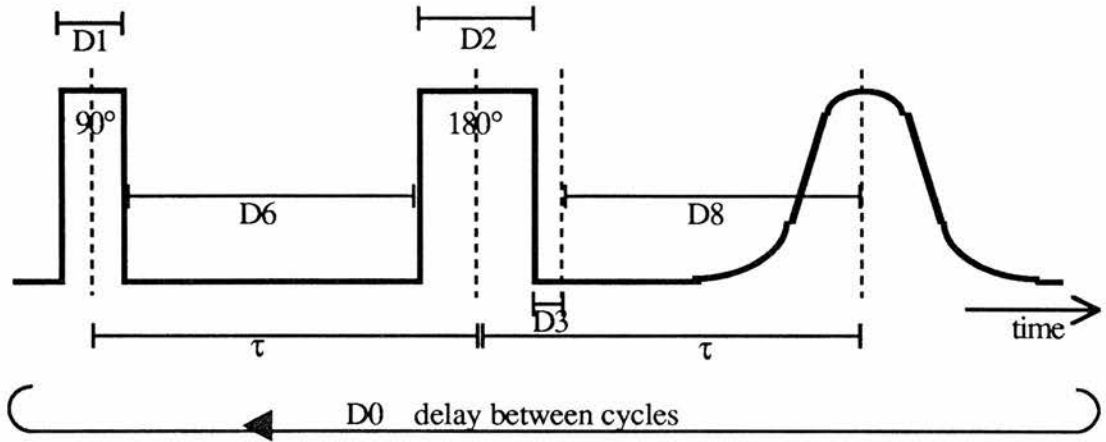


Figure 4.10. SAM1ECHO.PC pulse sequence as used for spin-echo sequences.

#### 4.8.4.2. Saturation Recovery

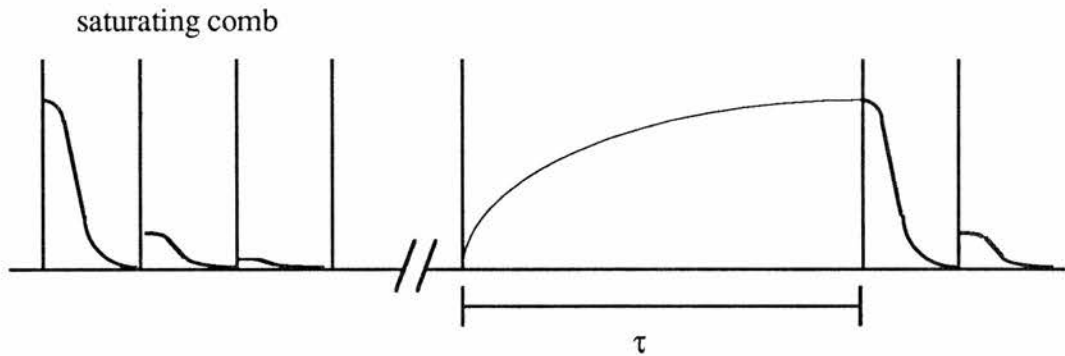


Figure 4.11. Destroying the net magnetisation using a comb of pulses.

The spin-echo sequence may be adapted in order to measure the spin-lattice relaxation time,  $T_1$ . The saturating comb of pulses starting the sequence has the effect of setting the magnetisation to zero, as demonstrated in Figure 4.11, and the recovery is sampled at later stages. The pulses should be almost  $90^\circ$ , and the pulse spacing within the comb should be set to a value between  $T_1$  and  $T_2$ . The number of pulses in the comb is dependent upon how close each pulse is to  $90^\circ$ . A comb of 20 pulses was found to be sufficient for the saturation recovery experiments here. The magnetisation

is detected at a time VD (variable delay) from the initialising comb of pulses, by a spin-echo sequence.

Measurements of the magnetisation are taken for various delays after the initial comb of pulses in order to be able to plot the magnetisation as a function of time, and hence calculate the spin-lattice relaxation time  $T_1$ . The magnetisation is given by

$$\frac{M(\tau)}{M_0} = 1 - \exp\left(\frac{-\tau}{T_1}\right)$$

where  $\tau$  is the time taken for the magnetisation to have recovered completely (to an intensity  $M_0$ ). An example of the lineshape acquired for the magnetisation is shown in Figure 4.12.

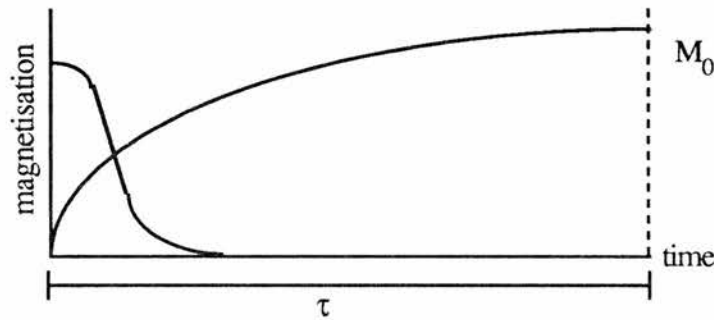


Figure 4.12. Typical recovery of the magnetisation following a saturating comb of pulses.

The pulse sequence with the parameters required for the XDNMRT1.PC program is shown below (Figure 4.13).

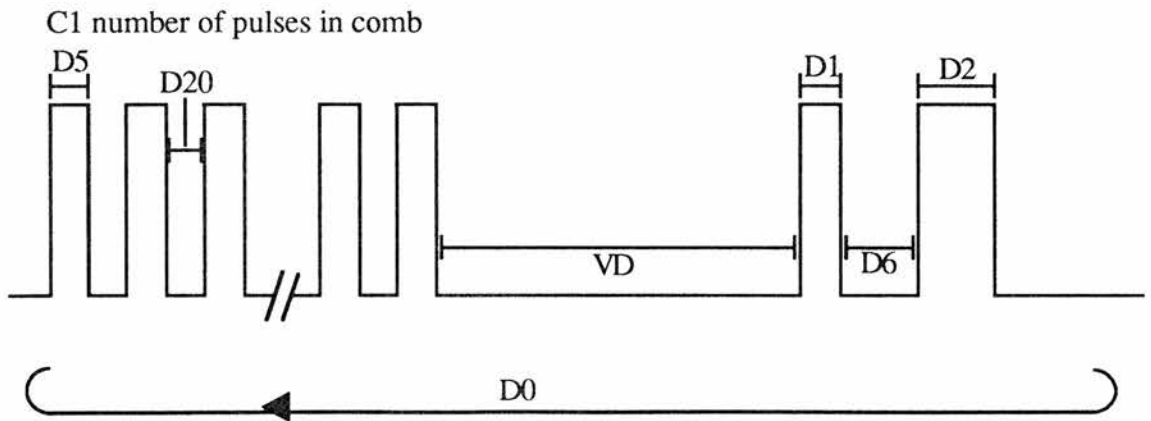


Figure 4.13. XDNMRT1.PC pulse sequence used to measure  $T_1$  by saturation recovery.

### 4.8.5. Fourier Transforms

Fourier transforms allow representations in the time domain to be transformed to equivalent representations in the frequency domain and vice versa. A simple example would be two superimposed sine waves of different amplitudes and frequencies. This is represented in the time domain as an interference pattern with beats, as shown in Figure 4.14 (a). This may also be represented in the frequency domain as two spikes which occur at the corresponding frequencies (Figure 4.14 (b)).

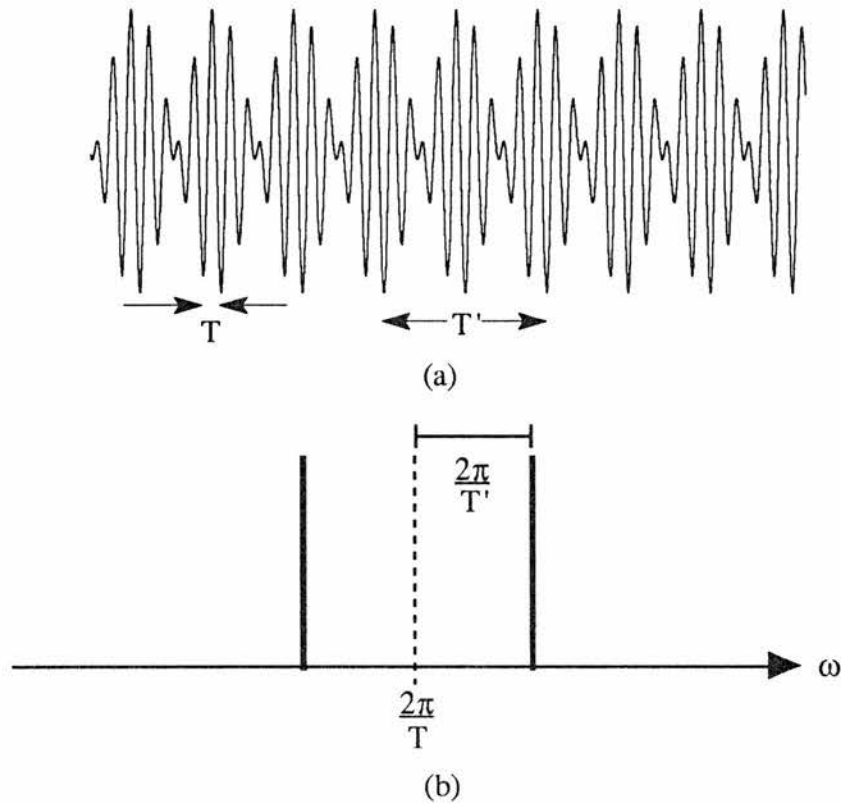


Figure 4.14. Two superimposed sinusoids of differing amplitudes and frequencies represented in both (a) the time domain, and (b) the frequency domain.

This representation works for increasingly more added sinusoidal waves, which result in the appearance of more spikes in the frequency spectrum. The two representations above hold the same information, and one can be transformed into the other using Fourier transformation.

The Fourier transform is represented by

$$A(t) = \frac{1}{2\pi} \int_{-\infty}^{+\infty} A(\omega) e^{i\omega t} d\omega$$

and

$$A(\omega) = \int_{-\infty}^{+\infty} A(t) e^{-i\omega t} dt$$

The pioneers of this technique for NMR purposes were Lowe and Norberg in 1957 (cw NMR)<sup>36</sup> and Ernst and Anderson in 1966 (pulsed NMR)<sup>37</sup>. Fourier transformation was used to convert the Free-Induction Decay (FID) in the time domain, into a peak in the frequency domain. Figure 4.15. transforms a typical NMR FID into the frequency domain.

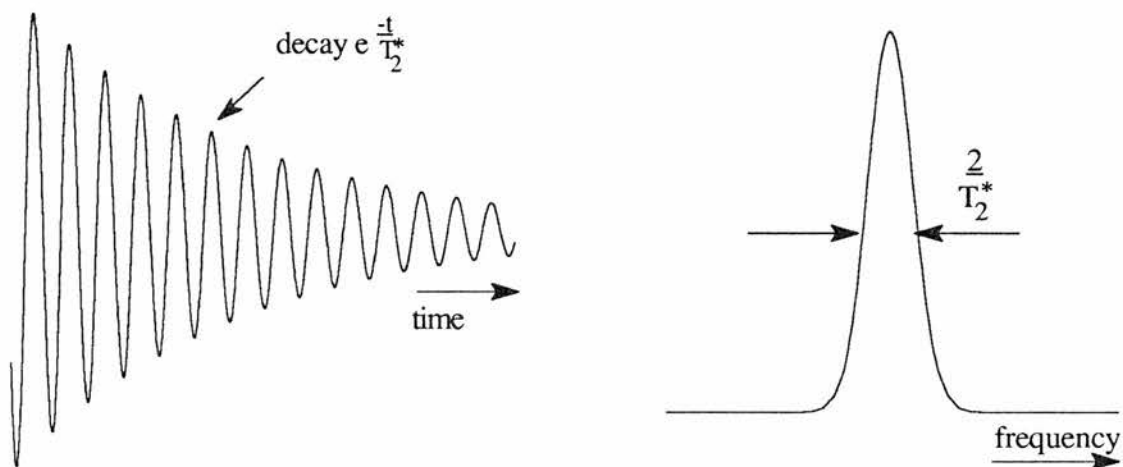


Figure 4.15. Fourier transformation of a typical NMR decay into the frequency domain.

#### 4.8.6. $^{89}\text{Y}$ NMR Experiments

Using the spin-echo technique,  $^{89}\text{Y}$  NMR was carried out in a 11.74T magnetic field at a corresponding frequency of 24.506MHz, on all eight samples of  $\text{Y}_{1-x}\text{Ca}_x\text{Ba}_2\text{Cu}_3\text{O}_{6+\delta}$ .

The parameters required to perform NMR are now described. The FID is sampled at regular intervals. These points are those which are processed and displayed on the screen, and then may be saved to disk. This interval between points is specified by DW. The number of points displayed on the screen is specified by TD. SI is the



features of EP are the baseline correction mode, which is used to straighten and flatten the baseline to aid more accurate spectrum analysis, and signal-to-noise ratio values, as well as integrating modes, all of which aid the analysis. Following manipulation, the frequency spectrum could be plotted, and accurate shift measurements could be made.

In order for measured shifts to be comparable, each spectrum was calibrated to an aqueous  $\text{YCl}_3$  reference source. This was measured at a frequency of 24.506MHz at room temperature.

A brief description of the experiments carried out using SAMIECHO.PC is given below.

- All eight samples were observed at room temperature, with the sample orientation such that the c-axis was parallel to the magnetic field. This was to study the effects of increasing calcium doping concentrations, with all other conditions the same.
- One particular sample, the  $x=0.14$ , was used to conduct an orientation experiment, again at room temperature. The sample was placed at different angles to the magnetic field ( $0^\circ$ ,  $30^\circ$ ,  $45^\circ$ ,  $60^\circ$ ,  $90^\circ$ ), with all other conditions the same.
- A brief study of the  $x=0.10$  sample at various temperatures was started, with the c-axis parallel to the field. More substantial temperature studies were made for the  $x=0.25$  and  $0.20$  samples as part of the saturation recovery experiments (see below).
- Repeatability of results was confirmed, by comparison of the same experiments carried out at different times and possibly with different numbers of acquisitions. This study was not made specifically, but was a consequence of the experiments carried out.

The saturation recovery experiments were carried out under similar conditions to those described for the spin-echo experiments. In order for the spin-lattice relaxation time  $T_1$  to be measured, a series of experiments under the same experimental conditions had to be carried out. The only difference between these individual experiments was the length of the delay,  $\text{VD}$ , following the saturating comb of pulses. This was achieved by automating the sequence of experiments using a program which uses the

next value for VD in its list when a new experiment starts. This program was called TONEAQ.AUM and required a complimentary list called VDLIST.001 containing the appropriate delay values, VD. The program automatically saved the data to the hard disk after the completion of a run, so that it could be analysed at a later time. In addition to the automation program, an NE flag needed to be set to indicate the number of experiments to be performed. If this number was less than the number of values of VD in the VDLIST.001, then it only carried out the first NE experiments from the list.

The values of VD accepted for the program were in a range of 1-100secs. For the YBCO material studied, 100secs was not sufficient time for the magnetisation to have fully recovered, and hence it was necessary to extend this upper limit. This was only possible by changing the pulse program XDNMRT1.PC slightly. This adjustment required the variable delay, VD, to be repeated immediately after the first, effectively doubling it in length. The values placed in the VDLIST.001 were therefore set to be half of that required for the experiments. The command required to start the experiments running was AU (execute automation program).

The data processing for these experiments was identical to that for the spin-echo sequence above. However, in order for the intensities of all the spectra in a series of experiments to be comparable, it was important to set an AI flag, which set the absolute intensity to a specified value.

The specific parameters used for these experiments are listed below (W=words, K=1000 words, s=second,  $\mu$ s=microsecond):

DW=10	SW=50000
TD=500W	SI=1K
D1=24 $\mu$ s	D2=48 $\mu$ s
D5=20 $\mu$ s	D6=1000 $\mu$ s
D20=1000 $\mu$ s	D0=6ms

C1=20 (number of pulses in the comb)

VD=usually any reasonable set of values to a maximum of 120s

NS=depended upon the experiment.

Experiments carried out using the saturation recovery technique are outlined below.

- Study of how  $T_1$  varies with temperature for the  $x=0.25$  and  $0.20$  samples.  $T_1$  was measured using the saturation recovery technique with various delays. The samples were always placed in the spectrometer with the aligned  $c$ -axis parallel to the magnetic field.
- Using the above results, it was also possible to determine the variation of  $T_1$  with doping concentration. The crystal  $c$ -axis was orientated parallel to the magnetic field.
- The individual spectra obtained using this technique were similar to those obtained by the simple spin-echo technique above. By comparing spectra in this manner, the variation with temperature for the  $0.25$  and  $0.20$  samples could be studied. The spectra chosen here had long and equivalent variable delays.

#### **4.8.7. $^{63}\text{Cu}$ NMR Experiments**

The  $^{63}\text{Cu}$  NMR experiments were carried out in an  $11.74\text{T}$  magnetic field, again using the spin-echo technique. At this magnetic field strength, the bare copper nucleus has a resonance frequency of  $132.569\text{MHz}$ .

The  $^{63}\text{Cu}$  spectra cover a broad frequency range from  $128\text{MHz}$  to  $136\text{MHz}$ . To observe the signal over such a range, many individual experiments have to be carried out at regular frequency intervals. A spectrum is then built up by plotting the intensities (taken as either the peak height or the integrated area) for each of the frequencies. The solenoid probe was re-tuned at each frequency interval.

The spectra recorded for each of the frequency intervals were acquired and processed in the same way as for the  $^{89}\text{Y}$  NMR described in Section 4.8.6, which basically involved saving the spin-echo to disk, taking the Fourier transform and then analysing the resulting frequency spectrum using the EP (expand and phase) routine to find the relative height of each peak and the area (by integration).

The copper reference position was always taken to be 132.569MHz. This is because the copper signal for these materials is over such a large range (8MHz) that the reference fluctuations between experiments are negligible.

The majority study by  $^{63}\text{Cu}$  NMR was carried out on the  $x=0.25$  sample and involved comparing spectra taken with the  $c$ -axis of the sample at various orientations to the applied magnetic field  $\mathbf{B}_0$ , ie.  $0^\circ$ ,  $22^\circ$ ,  $45^\circ$ ,  $67^\circ$  and  $90^\circ$ . The  $x=0.20$  sample for  $c$  parallel to  $\mathbf{B}_0$  was also briefly examined for comparison. To aid the analysis of these spectra, it was necessary to carry out an identical experiment with no sample, and again with a random powder sample.

The parameters used for these experiments are listed below and were defined in Section 4.8.6 (W=words, K=1000 words, s=second,  $\mu\text{s}$ =microsecond):

DW=0.2	SW= $2.5 \times 10^6$
TD=200W	SI=1K
D1= $5\mu\text{s}$	D2= $10\mu\text{s}$
D3= $2.5\mu\text{s}$	D6= $10\mu\text{s}$
D8= $10\mu\text{s}$	D0=5ms
NS=50,000	

## References

- 1 A.R.West. "Solid State Chemistry And Its Applications", John Wiley and Sons Ltd., (1984).
- 2 J.T.S.Irvine, J.H.Binks, A.R.West and S.B.Warrington. *Stanton Redcroft Technical Information*, paper no. STA/11.87/509.
- 3 R.S.Liu. *PhD Thesis*, University of Cambridge (1992).
- 4 C.Namgung, J.T.S.Irvine and A.R.West. *Physica C*, **168** (1990) 346.
- 5 D.E.Farrell, B.S.Chandrasekhar, M.R.DeGuire, M.M.Fang, V.G.Kogen, J.R.Clem and D.K.Finnemore. *Phys. Rev. B*, **36** (1987) 4025.
- 6 W.J.Webster. *PhD thesis*, University of St.Andrews (1993).
- 7 M.R.DeGuire, I.Manas-Zloczower, M.Tabib-Azar, D.E.Farrell, C.J.Kim, W.H.Lu, H.Ng and F.Royal. *Jnl. Mater. Sci.*, **25** (1990) 2881.
- 8 I.M.Low and F.W.Lim. *Jnl. Mater. Sci. Lett.*, **10** (1991) 1119.
- 9 H.Takahashi, Y.Kondo, T.Okumura and Y.Seo. *JEOL News*, **27E**, 2 (1989) 2.
- 10 A.P.Mackenzie. *Physica C*, **178** (1991) 365.
- 11 S.J.B.Reed. "Electron Microprobe Analysis", Cambridge University Press (1975).
- 12 K.F.J.Heinrich, "Electron Beam X-Ray Microanalysis", Van Nostrand Reinhold (1981).
- 13 V.Scott and G.Love (eds.). "Quantitative Electron Probe Microanalysis", Van Nostrand Reinhold (1983).
- 14 M.W.Davidson. *Microscopy and Analysis*, **32** (1992) 5.
- 15 T.A.Vanderah (ed.). "Chemistry Of Superconductor Materials: Preparation Chemistry, Characterization And Theory", Noyes (1992).
- 16 I.M.Kolthoff and E.B.Sandell. "Textbook of Quantitative Inorganic Analysis", Macmillan, New York (1953).

- 17 H.Vlaeminck, H.H.Goosens, R.Mouton, S.Hoste and G.Van der Kelen.  
*J.Mater. Chem.*, **1** (1991) 863.
- 18 A.I.Nazzal, V.Y.Lee, E.M.Engler, R.D.Jacowitz, Y.Tokura and J.B.Torrance.  
*Physica C*, **153-155** (1988) 1367.
- 19 M.Koppers and J.T.S.Irvine. To be published in the *Proceedings of the Fourth Conference of Materials and Mechanisms of Superconductivity, High Temperature Superconductivity*, Grenoble (July 1994).
- 20 Notes from the *Cambridge Winter School in Superconductivity* (January 1993).
- 21 Notes from the *Low Temperature Techniques Course*, University of Birmingham (November 1991).
- 22 V.Z.Kresin and S.A.Wolf. "*Fundamentals of Superconductivity*", Plenum Press, New York (1990).
- 23 L.J.Van der Pauw. *Philips Res. Repts.*, **13** (1958) 1.
- 24 L.J.Van der Pauw. *Philips Res. Repts.*, **16** (1961) 187.
- 25 J.C.Phillips. "*Physics Of High- $T_c$  Superconductors*", Academic Press Inc.(1989).
- 26 See section by B.Batlogg. K.S.Bedell, D.Coffey, D.E.Meltzer, D.Pines and J.R.Schrieffer (eds.). *High Temperature Superconductivity Proceedings - The Los Alamos Symposium* (1989).
- 27 C.P.Slichter. "*Principles of Magnetic Resonance*", 3rd Edition, Springer-Verlag (1989).
- 28 E.Fukushima and S.B.W.Roeder. "*Experimental Pulse NMR - A Nuts and Bolts Approach*", Addison-Wesley Publishing Company Inc. (1981).
- 29 A.Carrington and A.D.McLachlan. "*Introduction to Magnetic Resonance*", Chapman and Hall Ltd. (1979).
- 30 R.K.Harris. "*Nuclear Magnetic Resonance Spectroscopy*", Longman Group UK Ltd. (1986).

- 31 R.S.Macomber. *"NMR Spectroscopy. Essential Theory And Practice."*, HBJ College Outline Series, Florida (1988).
- 32 Reference Manual: *"500/89 Superconducting Magnet System"*, Oxford Instruments (1989).
- 33 Several specialist reference manuals are available for the individual sections of the MSL Spectrometer, Bruker (1989).
- 34 Reference Manuals: *"Aspect 3000 System Software Manual"* and *"Aspect 3000 MSL (CXP) Software Manual"*, Bruker (1989).
- 35 E.L.Hahn. *Phys. Rev.*, **80** (1950) 580.
- 36 I.J.Lowe and R.E.Norberg. *Phys. Rev.* **107** (1957) 46.
- 37 R.R.Ernst and W.A.Anderson. *Rev. Sci. Instrum.*, **37** (1966) 93.

## Chapter 5

# EXPERIMENTAL RESULTS

### 5.1. Introduction

This chapter contains the results obtained by the experimental techniques described in Chapter 4. These include studies of the purity of the samples, a determination of their oxygen content, measurement of any superconducting transition temperatures and a study of the series by nuclear magnetic resonance (NMR).

The x-ray diffraction results have been separated and placed with the relevant section, ie. as a method of analysis for synthesis (before and after quenching) and for powder alignment.

These results will be discussed further in Chapter 6.

### 5.2. Sample Synthesis And X-Ray Analysis

The synthesis process was completed in two stages, the initial sintering and annealing of the reactants, followed by the quenching procedure to reduce the oxygen contents of the samples. At both stages the products were examined and analysed by x-ray powder diffraction.

#### 5.2.1. Sintered Samples

The eight samples were synthesised in two batches. The first batch contained the  $x=0.00$ , 0.10, 0.12 and 0.14 samples, and the second contained the 0.16, 0.18, 0.20 and 0.25 samples. Towards the end of the sintering period, the pellets became very difficult to grind and it appeared as though the sample hardness increased with increasing calcium content. Difficulties were encountered with loss of sample in the

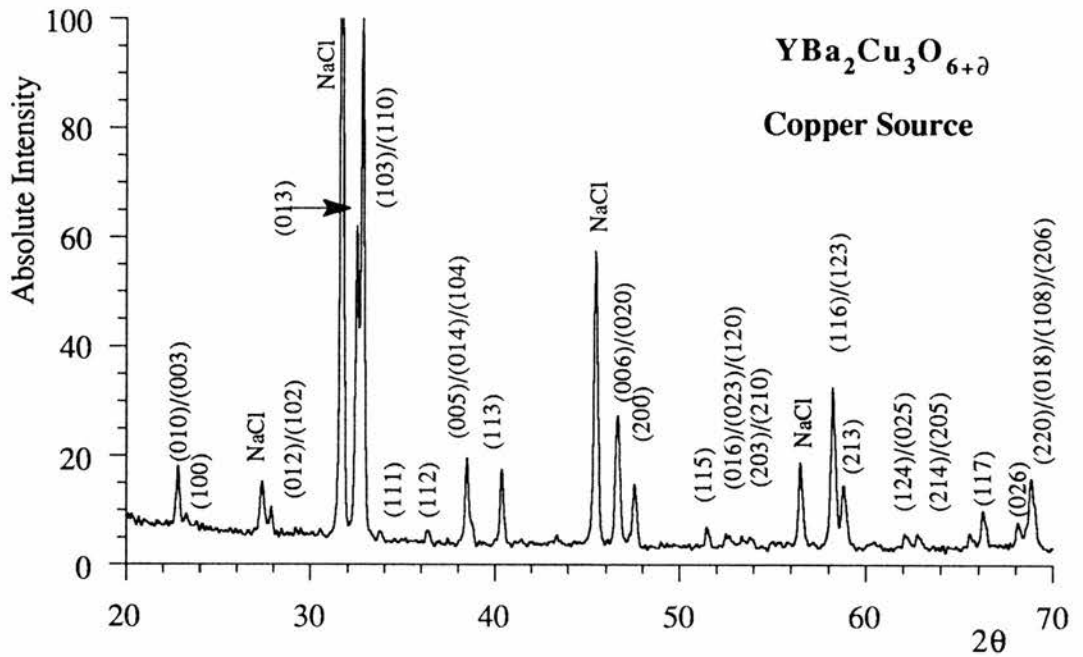
crushing process, and in obtaining a fine powder from which pellets could be reformed.

Throughout the synthesis procedure the stage of completion of reaction of the reactants could be seen visually. Initially the mixture was light grey and after one stage of heating had become notably darker, but with many lighter flecks of unreacted sample. By the end of the sintering period, the samples had become a homogeneous dark slate grey, which when powdered appeared black.

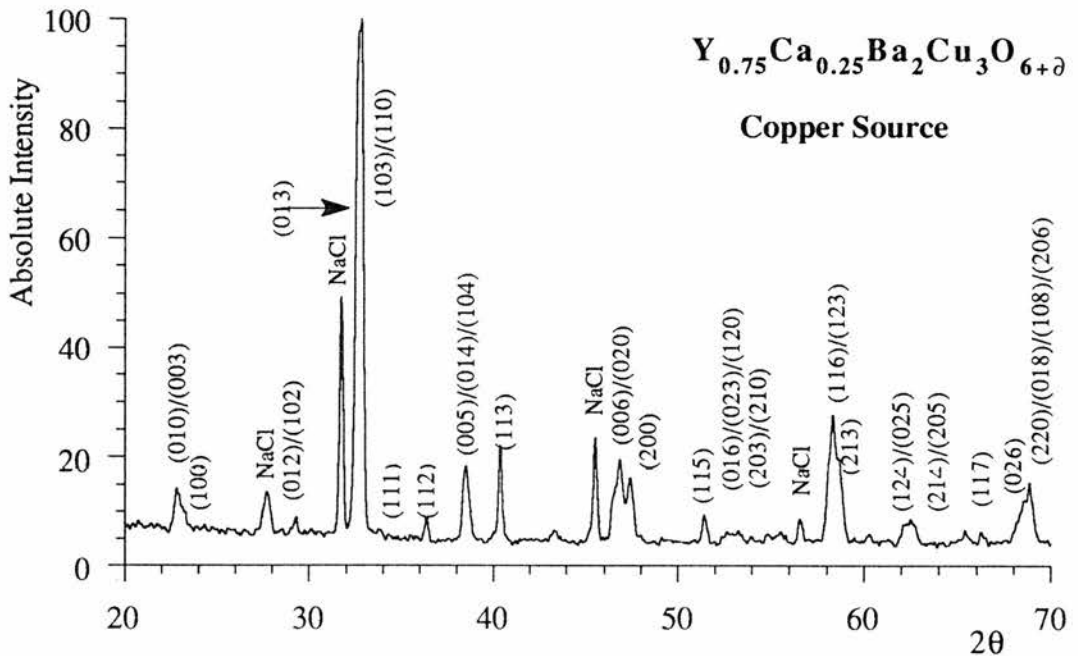
The accuracy of the nominated values of calcium content,  $x$ , has been calculated, since this is important when analysing results for further characterisation experiments. An initial assumption has been made, that any powder lost from the sample mixture during the synthesis process will have been of proportional quantities of constituents. This is a reasonable assumption, since the powders were thoroughly mixed and ground together before any process was carried out. The constituents were weighed on a four-figure balance as accurately as possible. The difference between the actual weight and the required weight differed only in the fourth figure and so the error in the assigned value of  $x$  has been calculated to be at worst case 1%. An example would be for 10% doping,  $x=0.100 \pm 0.001$ . It can therefore be assumed for the purposes here that the calcium contents are accurate.

Analysis by x-ray powder diffraction was carried out on the materials after removal from the furnace. The Philips PW1049 spectrometer was used in this case, with a  $\text{CuK}_{\alpha 1}$  source ( $\lambda=1.5405\text{\AA}$ ). NaCl was mixed with each sample as an internal standard to confirm the correct calibration of the  $2\theta$  scale.

Two x-ray spectra are shown in Figure 5.1. for comparison. These are for the parent compound  $x=0.00$ , and for the maximum doped sample  $x=0.25$ . The remaining spectra may be found in Appendix A1. All peaks have been identified and labelled. This demonstrates the purity of the samples since there are no other crystalline materials present. A useful reference for identification of other possible phases present in YBCO materials can be found<sup>1</sup>. The spectra have been indexed on an orthogonal



(a)



(b)

Figure 5.1. X-ray powder diffraction spectra for (a)  $x=0.00$  and (b)  $x=0.25$  samples after synthesis, but before oxygen removal.

crystal structure. Lattice parameters have been calculated for all samples and the results are shown in Table 5.1.

	a(Å)	b(Å)	c(Å)	cell volume(Å <sup>3</sup> )
0.00	3.8198	3.8921	11.6679	173.47
0.10	3.8234	3.8982	11.6637	173.84
0.14	3.8270	3.8862	11.6931	173.91
0.18	3.8306	3.8842	11.7132	174.28
0.25	3.8356	3.8813	11.7062	174.27

Table 5.1. Lattice parameters obtained by x-ray powder diffraction for the orthorhombic samples.

### 5.2.2. Reduced Oxygen Samples

The eight samples were individually quenched in a nitrogen atmosphere from 730°C to room temperature. The experimental set-up appeared to be very reliable and the experimental conditions were consistent. The only apparent variations between quenches were slight differences in the nitrogen flow rate. This was solely monitored by the bubbling of the outgoing gas in water, and hence could not easily be controlled. This was not considered too great a problem since the gas was nominally oxygen-free and should not have affected the oxygen-loss from the samples. The possibility of oxygen inhomogeneities has been considered, due to the nature of the lidded crucible with only a small hole for ventilation. This should have been overcome by overnight sintering, allowing plenty of time for circulation to occur and for the oxygen to equilibrate.

X-ray powder diffraction was carried out on all samples after the quenching procedure. The STÖE STADI/P transmission powder diffractometer was used in order to obtain increased resolution and hence accurate lattice parameters. All samples were found to be tetragonal with space group P4/mmm. Again, indexed spectra are given in Figure 5.2 for the x=0.00 and 0.25 samples, and the remaining spectra can be found in

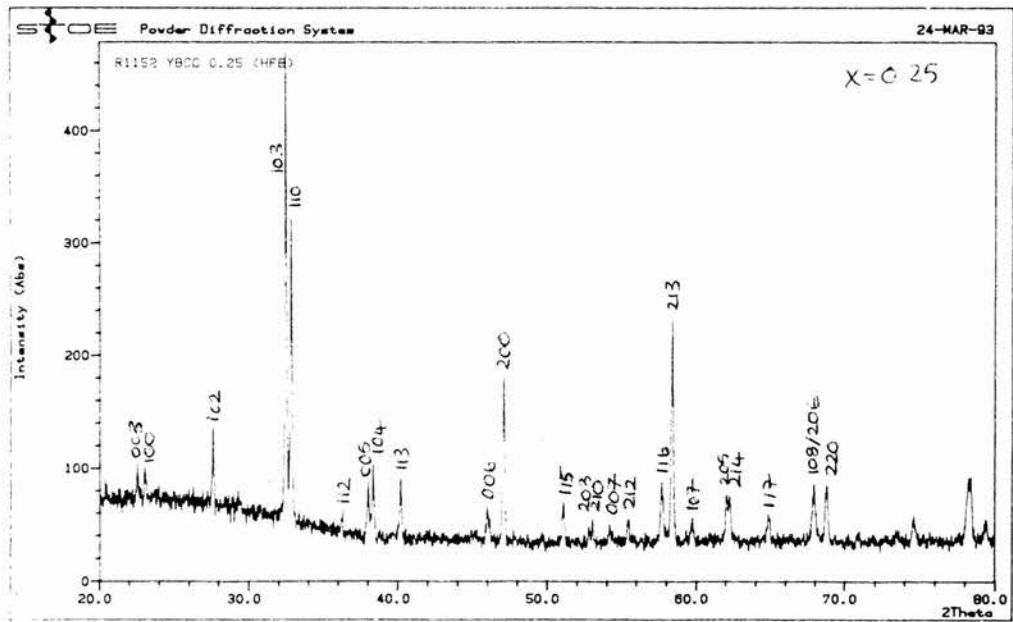
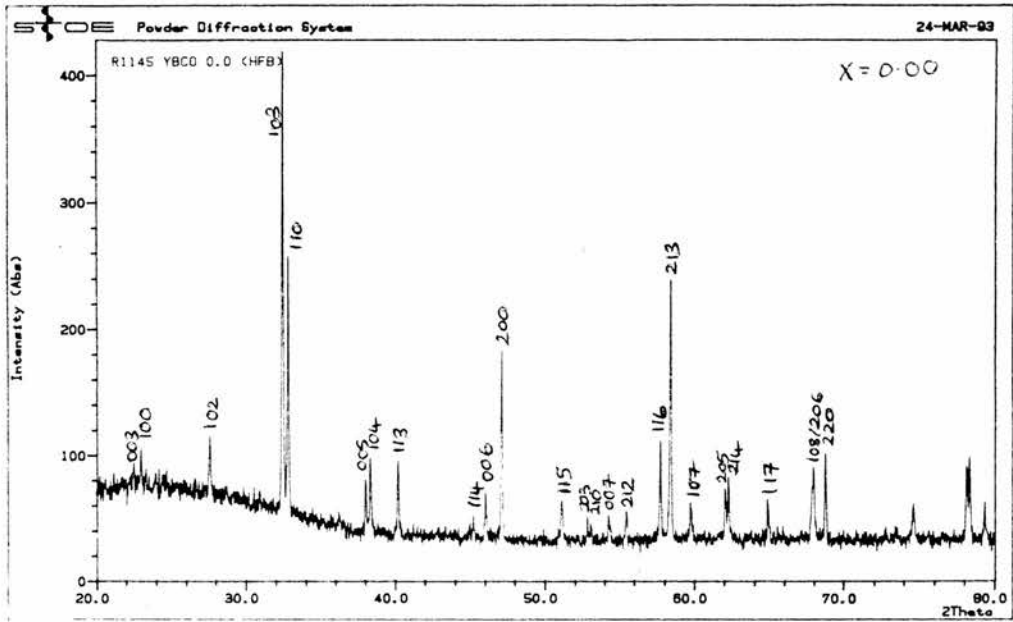


Figure 5.2. STÖE x-ray spectra obtained for the  $x=0.00$  and  $x=0.25$  samples after quenching.

Appendix A2. All peaks can be identified for this structure, indicating that no sample had degraded and no impurities had been picked up. Moreover, the spectra confirmed that all the samples had undergone the orthorhombic-tetragonal transition. The refined lattice parameters and unit cell volumes are shown in Figure 5.3. The lattice parameters obtained indicate a low oxygen content of 6.1 to 6.2, when compared to published parameters for the  $x=0.00$  parent compound. However, an accurate determination could not be made since the lattice parameters vary only slightly in this region<sup>2,3</sup>. For the very same reason, the oxygen homogeneity could not be determined. Ordinarily, the broadening of certain peaks would indicate a spread in lattice parameters caused by deviations in oxygen.

Since the lattice parameters do not appear to change with the increase in calcium doping, it would seem reasonable to assume that the oxygen contents vary only slightly between samples, and that the introduction of calcium does not structurally affect the lattice. Even though the  $\text{Ca}^{2+}$  ion is larger than the  $\text{Y}^{3+}$  ion, this can be justified since the lattice will contract due to the charge imbalance, leaving the lattice parameters unchanged.

### **5.3. Aligned Samples And X-Ray Analysis**

The alignment procedure was carried out twice, because the first attempt was unsuccessful. Initially a set of samples ground in an agate pestle and mortar were mixed proportionally with epoxy and cured overnight in a 11.74T magnetic field. When examined by x-ray diffraction, the alignment procedure had been unsuccessful, and small proportions of sample had degraded in the epoxy. An example of an x-ray spectrum obtained for a poorly aligned and degraded sample is shown in Figure 5.4.

After further study with an electron microscope, the particle size was discovered to be far too large, of the order  $150\mu\text{m}$ . Therefore each grain comprised of a cluster of crystallites of random orientation, which explains the lack of alignment in the samples. To improve the method, the powders would have to be finely ground and an attempt to remove any moisture from the epoxy should be made.

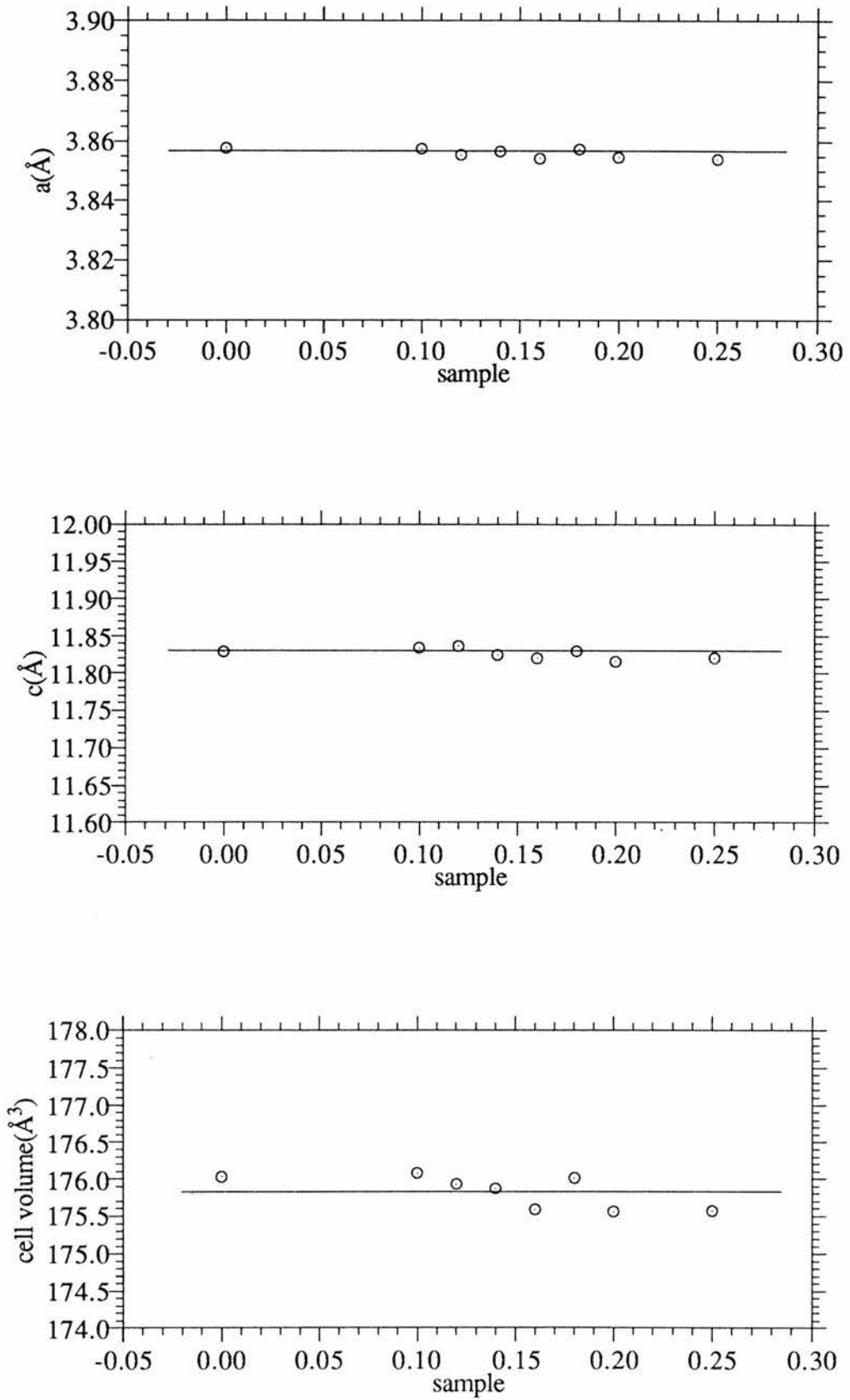


Figure 5.3. Refined lattice parameters and unit cell volume for the quenched samples.

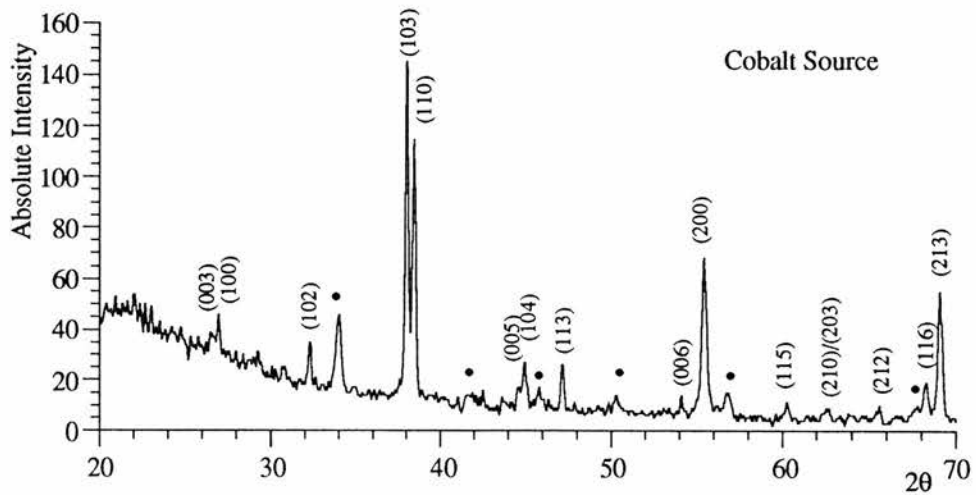


Figure 5.4. X-ray spectrum of a poorly aligned and degraded sample set in epoxy.

In order to obtain powder sizes of approximately  $10\mu\text{m}$  suitable for the second alignment attempt, each sample was vigorously shaken using a ball mill. In every case, the surface of the stainless steel balls was found to be damaged by the ceramic powder. This indicates the hardness/brittleness of the materials. Despite this, there was no evidence of any stainless-steel fragments in the resulting powders.

To determine the size of the grains obtained by this method, several were examined by a particle size analyser. Since all of the samples had undergone the same process, it was thought unnecessary to analyse all of them. Three samples were analysed,  $x=0.00$ ,  $0.16$  and  $0.25$ . The particle size distributions are shown in the histograms of Figure 5.5.

The powders obtained for the  $0.16$  and  $0.25$  samples were found to be of suitable size for alignment. The  $x=0.00$  distribution had a larger average particle size, which may be an indication of a less brittle sample. It was still thought to be suitable to use.

After curing, thin slices were removed from one end of each of the epoxy-set samples. These were analysed by x-ray powder diffraction using the Philips spectrometer, in order to determine the success of the alignment procedure. Figure 5.6 shows the spectrum for the  $x=0.25$  sample after the alignment attempt, which is typical

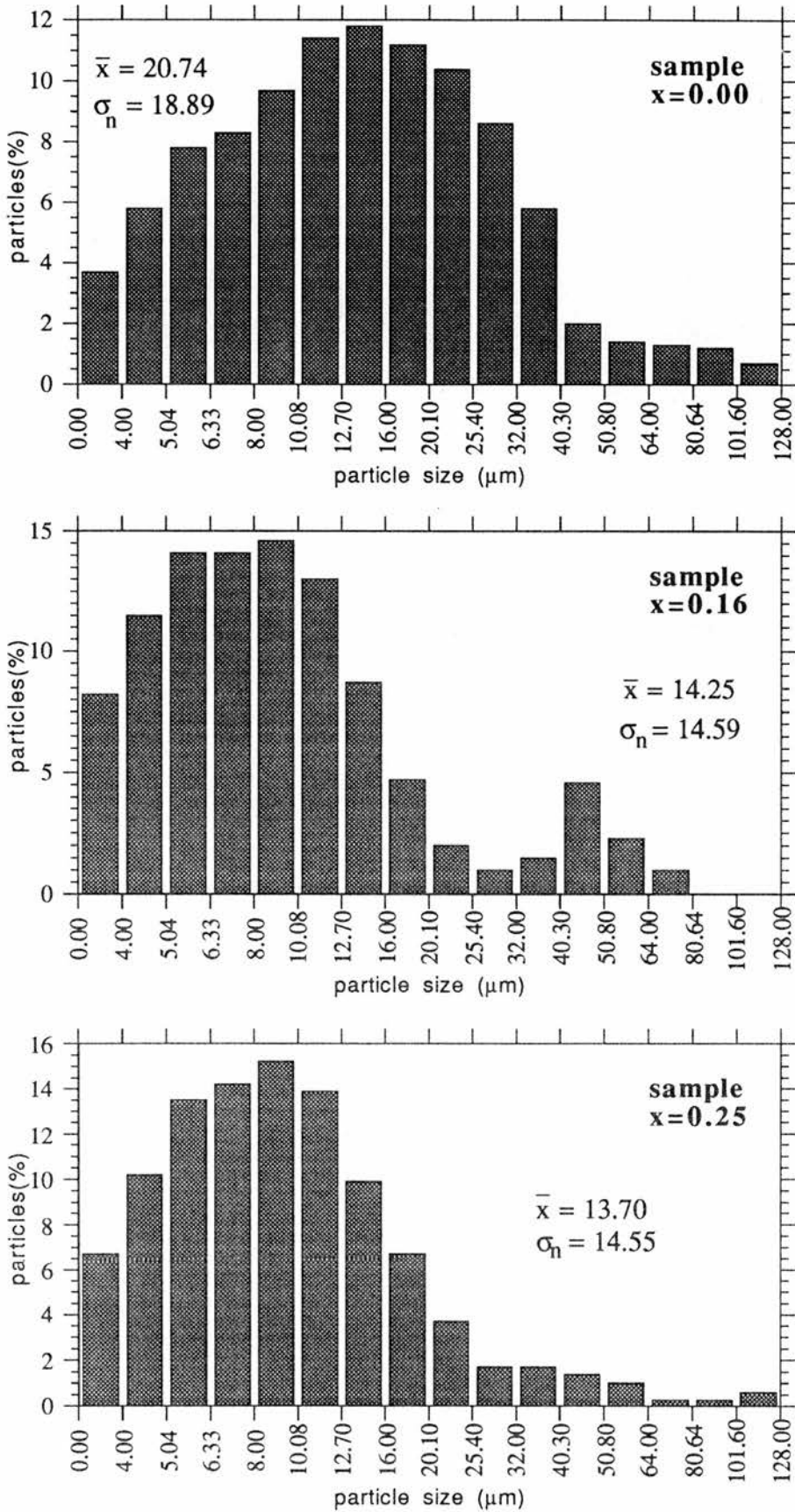


Figure 5.5. Size distributions for the 0.00, 0.16 and 0.25 samples obtained using a particle size analyser.

of all the spectra obtained. The remaining spectra for all samples, set in both small and large casts may be found in Appendix A3.

The percentage alignment of the epoxy-set samples was calculated by comparing the intensities of the peaks in the x-ray spectra obtained before and after the alignment attempt. If the sample was 100% aligned along the *c*-axis, all peaks indexed with (h,k,l) where  $l \neq 0$  should completely disappear, and all remaining (h,k,0) peaks would be enhanced. It is more likely however, that the samples would only be partially aligned along the *c*-axis and that most peaks, when compared to the random pattern, would still be present. It is by comparing the heights of the peaks for the aligned powder and the random powder that an estimated figure for the percentage alignment arises. Take for example, the 0.25 sample. The x-ray spectrum for the large aligned sample is shown in Figure 5.6, and the random powder pattern can be seen in Figure 5.2 for comparison. In both cases, the peaks are then scaled such that the (110) peak has an intensity of 100. Table 5.2. shows the relative intensities of the two spectra.

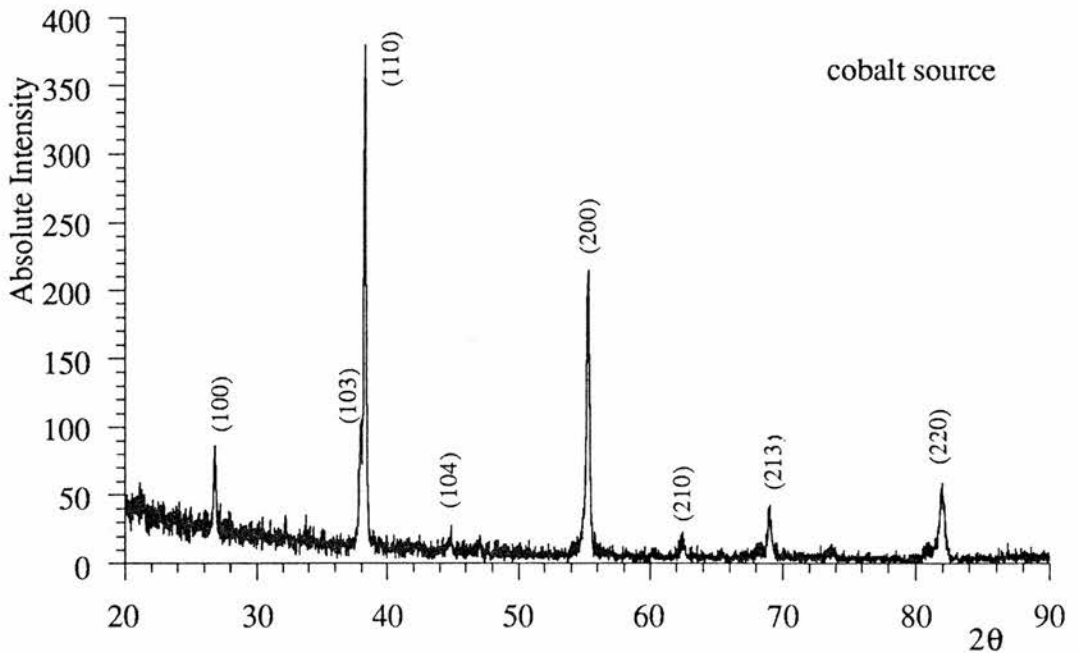


Figure 5.6. X-ray spectrum for the 0.25 sample aligned in epoxy.

(h,k,l)	random powder	aligned powder
(100)	8.64	16.16
(103)	150.62	24.24
(110)	100.00	100.00
(104)	24.69	5.05
(200)	53.09	56.57
(210)	7.41	5.05
(203)	71.60	10.10
(220)	18.52	15.15

Table 5.2. The relative intensities of the peaks in the aligned and unaligned spectra, having normalised the 110 peak in each to an intensity of 100.

The percentage alignment is then found using the following equation

$$\%alignment = \left[ \frac{I_{103}(random) - I_{103}(aligned)}{I_{103}(random)} \right] \times 100$$

This is calculated for the (103), (104) and (213) peaks, but the error for the latter two will be larger, due to the smaller intensity of the peaks. To compare the results, the percentage alignment obtained for each of the three peaks are shown below (Table 5.3).

(h,k,l)	% alignment
(103)	83.9
(104)	79.5
(213)	85.9

Table 5.3. Percentage alignment calculated using the three (h,k,l≠0) peaks.

Other methods of calculating the percentage alignment were considered<sup>4,5,6</sup>. The method chosen depended mostly upon the nature of the x-ray spectra obtained. The method used here, for example, would not work if the (103) and (110) peaks

overlapped, since this would greatly affect the relative intensities. The method outlined by Lusnikov et al.<sup>4</sup> gave low values for the percentage alignments, much less than expected for a sample with an x-ray spectrum which would be judged instinctively as being well aligned. In agreement with Webster<sup>5</sup>, I feel that the assumptions made in this paper are not justified. The results of the alignment procedure are summarised below in Table 5.4.

large sample	alignment(%)	small sample	alignment(%)
0.00	96%	0.00	92%
0.10	90%	0.10	94%
0.12	85%	0.12	86%
0.14	91%	0.14	92%
0.16	91%	0.16	92%
0.18	89%	0.18	92%
0.20	87%	0.20	83%
0.25	85%	0.25	85%

Table 5.4. Percentage alignment of the epoxy-set samples as calculated from x-ray spectra before and after alignment.

#### 5.4. Electron Microscopy

Two attempts were made to align the powder samples in epoxy resin, to be used for NMR experiments. Particle size and distribution was only studied by electron microscopy for the first attempt, although it was the second set that were used for NMR. The  $x=0.10$  and  $x=0.16$  aligned samples had an even distribution of particles over the whole cross-section, and so the method of mixing the powder and epoxy as described in Section 4.3 was successful. The particle sizes were varied in each, ranging from a few  $\mu\text{m}$  to approximately  $150\mu\text{m}$ . These larger particles were likely to consist of several randomly orientated crystals, and so when placed in the magnetic

field for alignment, the average *c*-direction aligned with the magnetic field, resulting in most of the crystals in the particle not being correctly aligned. This was confirmed by the poor alignment results obtained by x-ray diffraction for this set of samples.

This knowledge allowed a second set of epoxy-set samples to be made with better alignment. The powder particles were ground much more finely under an argon atmosphere to prevent clustering. The method of distributing the powder in the epoxy remained the same as for the first set of samples. It was not thought necessary to examine the second set of samples by the electron microscope, since the alignment was successful. More details on sample alignment are given in Section 4.3 and Section 5.3.

Backscatter and secondary electron images were compared at high magnification to search for impurities and inhomogeneities. The calcium was homogeneously distributed in the particles, and no other phases could be seen. The porosity of the samples was clearly demonstrated by pits and holes.

Quantitative electron-probe microscopy (EPMA) was attempted to determine the oxygen concentration in the samples. Initially, the correct stoichiometry had to be obtained for a known standard, to confirm calibration. The standard used was the Aldrich 99.9% pure  $\text{YBa}_2\text{Cu}_3\text{O}_{6.8(\pm 0.01)}$  which was prepared in epoxy, and sputtered with carbon to produce a conducting surface. The results did not correspond to the Aldrich specifications, and fluctuated on each measurement. Initially this was thought to be because the particle size was too small and so the second Aldrich sample, which had been oxygenated (see Section 4.5) was attempted. Again the results were inconsistent, even when several experiments were carried out at exactly the same position on the sample.

A method other than that of carbon sputtering was then attempted to provide the conduction path. Powder ( $x=0.25$  and  $x=0.20$ ) was mixed with electrically conducting silver-loaded epoxy and so no carbon layer was required. This appeared to enhance the images. For quantitative analysis, inconsistencies were still observed. Since standardisation could not be achieved, this method was abandoned. Some of the values obtained by each method are shown in Table 5.5, to demonstrate the variations.

sample	Y (atom%)	Ba (atom%)	Cu (atom%)	O (atom%)
Aldrich 99.9% YBa <sub>2</sub> Cu <sub>3</sub> O <sub>6.8</sub> carbon sputtered	7.379	15.605	25.970	51.046
	7.051	15.532	25.840	51.569
	7.177	15.948	26.173	50.691
	7.284	15.898	25.918	50.900
	7.261	15.195	22.740	54.805
	7.172	15.231	22.241	55.356
	7.716	15.249	21.928	55.101
	7.377	15.099	22.096	55.407
	7.762	14.889	22.422	54.906
	7.748	14.787	22.196	55.270
oxygenated Aldrich YBa <sub>2</sub> Cu <sub>3</sub> O <sub>7</sub> carbon sputtered	7.109	15.573	22.925	54.365
	7.273	15.019	22.513	55.18
	7.254	15.461	22.744	54.534
	7.244	15.616	22.733	54.377
	7.448	15.385	22.514	54.609
	8.029	15.076	22.516	54.375
Aldrich YBa <sub>2</sub> Cu <sub>3</sub> O <sub>7</sub> silver loaded epoxy	4.672	17.138	22.241	55.949
	7.477	16.526	18.751	57.244
	10.743	15.602	14.687	58.968
	6.386	17.526	21.023	55.065

Table 5.5. Table of atomic compositions obtained by quantitative EPMA, demonstrating fluctuations between results.

## 5.5. Results of Oxygen Content Determination

### 5.5.1. Iodometric Titration

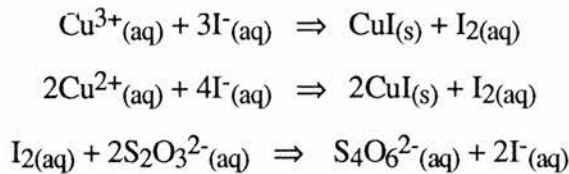
An attempt at determining the oxygen content by iodometric titration was made for the  $x=0.18$  sample only. The experiment was repeated 3 times in order to clarify the results and give an indication of the accuracy of the method. The calculation will only be followed through once as a demonstration.

In this method, all of the species in the sample oxidised beyond  $\text{Cu}^+$  react to yield a quantity of iodine directly proportional to the degree of oxidation greater than  $\text{Cu}^+$ . The quantity of iodine is then determined by titration, and the average charge calculated, assuming that the stoichiometry of the sample is known. Knowing the average charge of the copper then leads to a value for the oxygen content in the sample.

Initially it is assumed that the molecular formula for the material is  $(\text{Y}_{0.82}\text{Ca}_{0.18})\text{Ba}_2\text{Cu}_3\text{O}_{6+\delta}$  with  $\delta=0$ . Hence the formula weight is calculated to be 641.405.

The mass of sample used for the first experiment was 0.0242g (with an error of  $\sim 1\%$ ) which corresponds to  $3.773 \times 10^{-5}$  moles. Since there are 3 coppers per formula weight, the total number of coppers present is  $1.13 \times 10^{-4}$  moles.

The sample reacted to yield a quantity of iodine which titrated against 2.93ml (with an error of  $\sim 1\%$ ) of 0.03028 molar sodium thiosulphate solution, corresponding to  $8.87 \times 10^{-5}$  moles  $\text{S}_2\text{O}_3^{2-}$ . This value is directly proportional to the quantity of holes in the system as can be seen from the following equations:

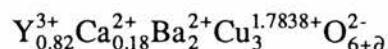


Therefore the ratio of holes to copper in the system is calculated to yield a value of

$$\left[ \frac{\text{S}_2\text{O}_3^{2-}}{\text{Total Cu}} \right] = \frac{8.87 \times 10^{-5}}{1.13 \times 10^{-4}} = 0.7838(\pm 2\%)$$

This is the average oxidation state of the copper above  $\text{Cu}^+$ , and so the average copper oxidation state is +1.7838.

In order to determine the quantity of oxygen originally present in the sample, the charges are balanced in the molecular formula



and so  $\partial$  is calculated to be 0.0857. The calculation is then reiterated using this more accurate value for  $\partial$ .

The formula weight of  $\text{Y}_{0.82}\text{Ca}_{0.18}\text{Ba}_2\text{Cu}_3\text{O}_{6.0857}$  is now 642.776. The quantity of sample used in the experiment now corresponds to  $3.7649 \times 10^{-5}$  moles, and hence the number of coppers present is  $1.1295 \times 10^{-4}$  moles. The ratio of holes to copper in the system (above  $\text{Cu}^+$ ) is 0.7855, and so the average copper oxidation state is +1.7855. This yields a value of  $\partial = 0.09 \pm 0.02$  for the oxygen content.

The remaining titrations were analysed in the same way, and the final results are shown in Table 5.6.

experiment	mass of sample (g)	vol. of $\text{S}_2\text{O}_3^{2-}$ (ml)	1 <sup>st</sup> iteration ( $\partial$ )	2 <sup>nd</sup> iteration ( $\partial$ )
1	0.0242	2.93	0.086	0.088
2	0.0334	4.00	0.073	0.075
3	0.0375	4.47	0.067	0.069

Table 5.6. Results of the iodometric titration experiments calculated using an iterative technique.

### 5.5.2. Thermogravimetric Analysis

Oxygen determination by thermogravimetric analysis was carried out on all samples of  $\text{Y}_{1-x}\text{Ca}_x\text{Ba}_2\text{Cu}_3\text{O}_{6+\partial}$  (YBCO). The accuracy of the results obtained was highly dependent on the experimental conditions, particularly the position of the thermal analyser, which was situated in a busy laboratory. Most samples were analysed several

times and the best runs used for oxygen determinations, otherwise an average of the results were taken.

A typical chart recording is shown in Figure 5.7. The oxygen content begins to decrease at around 350°C and continues to do so until, at 1000°C all excess oxygen has been lost.

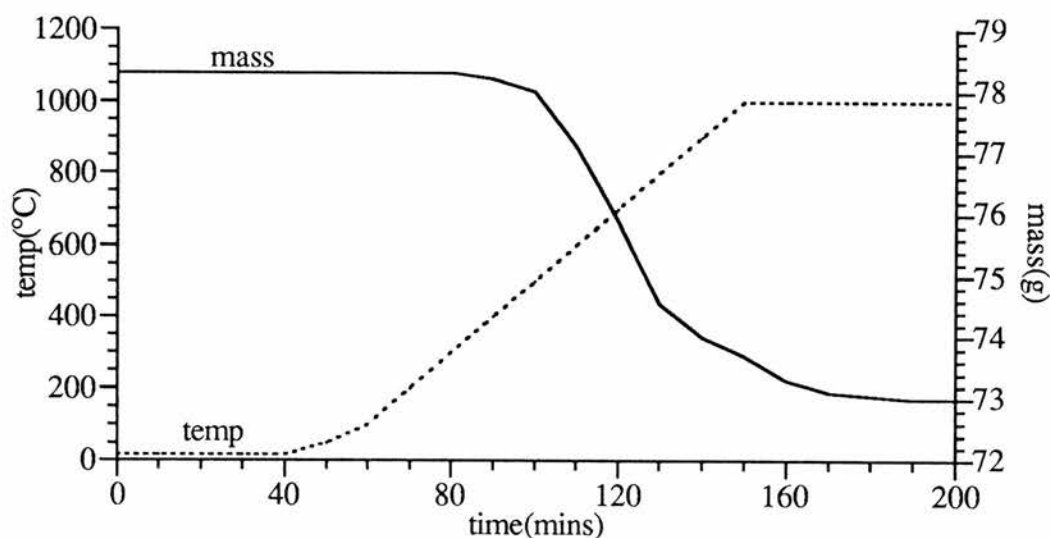
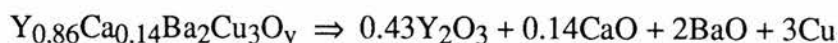


Figure 5.7. Typical chart recording obtained for thermogravimetry, when heating YBCO in a reducing atmosphere to 1000°C.

An example of the iterative calculation used to determine the oxygen content from the recording is as follows:

78.3mg of the 0.14 sample was analysed by thermogravimetry (TG). When heated to 1000°C, the following reduction occurs.



Thus at 1000°C there will be 3.43 oxygens incorporated in the residue. The remaining oxygen will have been removed from the system and recorded as the weight loss. The weight loss recorded by the TG analyser was 5.25mg, ie. 6.705% of the original weight.

For the first iteration, the theoretical weight loss to reduce the material from  $y=7$  to  $y=6$  is calculated to be

$$\frac{16}{659.304} \times 100 = 2.427\%$$

and so the weight loss experimentally corresponds to 2.763 oxygens. The total oxygen content of the starting material is therefore

$$3.430 + 2.763 = 6.193$$

The calculation is then reiterated several times until the values have converged sufficiently, each time using the improved values for the oxygen.

Some of the reductions were carried out to 950°C rather than 1000°C. At this temperature, some of the material may have been reduced to BaO, CaO, Y<sub>2</sub>O<sub>3</sub> and Cu metal, but the majority will have remained as oxygen deficient YBCO. A correction for the oxygen loss was made for these runs. A value of 0.11 (oxygens in YBCO) was obtained by recording the weight loss for several samples when heated from 950°C to 1000°C. The final results were reported as being reproducible, probably ±0.02 (oxygens in YBCO) and are shown in Table 5.7.

sample	0.00	0.10	0.12	0.14	0.16	0.18	0.20	0.25
oxygen content	6.13	6.16	6.16	6.18	6.15	6.13	6.00	6.18

Table 5.7. Results of the oxygen contents obtained for the Y<sub>1-x</sub>Ca<sub>x</sub>Ba<sub>2</sub>Cu<sub>3</sub>O<sub>6+δ</sub> samples by thermogravimetric analysis.

Omitting the x=0.20 sample, the oxygen contents are 6.155±0.02 over the entire range. The 0.20 sample consistently gave low oxygen values, and could be due to some sort of inert impurity.

A comparison of these results to those obtained by iodometric titration is given in Section 6.3.

## 5.6. Critical Temperature Measurement

### 5.6.1. Resistivity Results

After several attempts at measuring the resistivity of the samples by the four-point method, the technique improved and more reliable results were obtained. Particular problems were encountered with electrical contacts and temperature control.

Electrical contacts were made to the granular pellet by attaching fine copper wires to the circumference using silver dag. The fine wire easily snapped or detached with movement of the sample, particularly when loading it onto the probe-head. A more common problem was poor electrical contact, resulting in substantial capacitance at the sample surface. In these cases, the resistive (in-phase) component of the reactance was insignificantly small when compared to the capacitive (out-of-phase) component and measurements could not be made. Further problems were encountered with the temperature control. At low-temperatures between 5 and 15K, oscillations occurred in the continuous-flow cryostat, causing an averaged resistance to be measured at an unknown temperature. This was overcome by cooling the cryostat to 3.5K and allowing the system to equilibrate for at least an hour. The cryostat was then allowed to warm up without the aid of the heater, which avoided the temperature oscillations and was repeatable for all experiments. This may have introduced a systematic error in the recorded temperature, since the computer was programmed to record the temperature at the end of its period of data acquisition. Even so, this technique was considered more consistent than trying to control the temperature with the heater of the ITC4 temperature controller.

To summarise, the experiments which were considered successful had silver dag electrical contacts, rather than conductive paint. These contacts were checked and only used if the out-of-phase component of the reactance was considered to be at an acceptable level. Finally, the temperature for all runs was controlled simply by allowing the cryostat to warm-up naturally, rather than by heater control. This was at least consistent between runs.

A brief outline of the calculation of the resistivity by the Van der Pauw method is given below. More details may be found in Section 3.4 and also from the original papers<sup>7,8</sup>.

Experimentally measure resistances  $R_{AB,CD}$ ,  $R_{BC,DA}$  and  $t$ , the thickness of the sample. The equation

$$\exp\left(\frac{-\pi R_{AB,CD}t}{\rho}\right) + \exp\left(\frac{-\pi R_{BC,DA}t}{\rho}\right) = 1$$

determines uniquely the value of  $\rho$  as a function of  $R_{AB,CD}$ ,  $R_{BC,DA}$  and  $t$ . The solution of  $\rho$  from the above equation is facilitated by writing it in the form

$$\rho = \frac{\pi t}{\ln 2} \left( \frac{R_{AB,CD} + R_{BC,DA}}{2} \right) f \left( \frac{R_{AB,CD}}{R_{BC,DA}} \right)$$

where  $f$  is a function of the ratio  $R_{AB,CD}/R_{BC,DA}$  only and satisfies the relation

$$\left( \frac{R_{AB,CD} - R_{BC,DA}}{R_{AB,CD} + R_{BC,DA}} \right) = f \times \operatorname{arccosh} \left\{ \frac{\exp\left(\frac{\ln 2}{f}\right)}{2} \right\}$$

Figure 5.8. graphically shows the solutions of  $f$  for all values of  $R_{AB,CD}/R_{BC,DA}$ . The values for this graph were computer generated by an iterative technique.

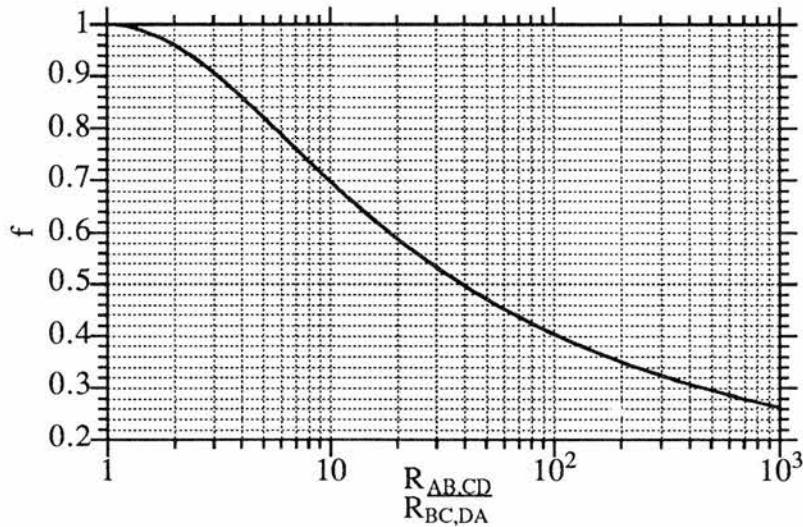


Figure 5.8. The function  $f$  for all values of  $R_{AB,CD}/R_{BC,DA}$ .

Seven of the eight samples of  $(Y_{1-x}Ca_x)Ba_2Cu_3O_{6+\delta}$  were tested using the resistivity technique outlined above. It was not possible to measure the resistivity for the  $x=0.00$  sample on the equipment used, since the resistance was so high. The parent

compound for low oxygen concentrations has been confirmed to be an antiferromagnetic insulator with a Néel temperature of 410K<sup>9</sup>. Antiferromagnetism is destroyed quickly with the addition of calcium. Three samples were identified as being superconductors by a sudden drop of the resistivity towards zero. In the normal state all three were found to be poor metals. For the  $x=0.20$  and  $x=0.25$  samples the resistivity dropped to zero within the temperature range available, and hence the transition temperature was easily identified. However for the 0.18 sample, the resistivity begins to fall at 30K, but since the transition is broad, the resistivity never fell to zero before the lowest temperature available was reached. The results for the superconducting samples  $x=0.18$ , 0.20 and 0.25 are given in Figure 5.9. and Table 5.8. For a more accurate determination of  $T_c$ , a comparison of the resistivity and AC susceptibility results should be made.

The resistivity measurements of all the samples (except  $x=0.00$ ) are shown in Figure 5.10. The resistivity has been plotted on a logarithmic scale to demonstrate the wide variation in behaviour over the series from the metallic to the insulating state. It can be seen from the figure that there are inconsistencies in the series. The 0.10 sample would be expected to be the most insulating for these samples due to the small amount of doping. However the 0.12 sample has the highest resistivity. In addition, peculiar behaviour is observed for the  $x=0.14$  sample at low temperature. The resistivity suddenly drops, indicating a possible transition to the superconducting state. No such transition was indicated by susceptibility measurement. Both of these anomalies can be explained by variations in the oxygen between samples, although this is not indicated by the results obtained for the oxygen determinations.

sample	$T_c(\text{onset})$	$T_c(\rho=0)$
$x=0.25$	65	40
$x=0.20$	45	27
$x=0.18$	32	below 3K

Table 5.8. Superconducting transition temperatures as determined by resistivity measurement.

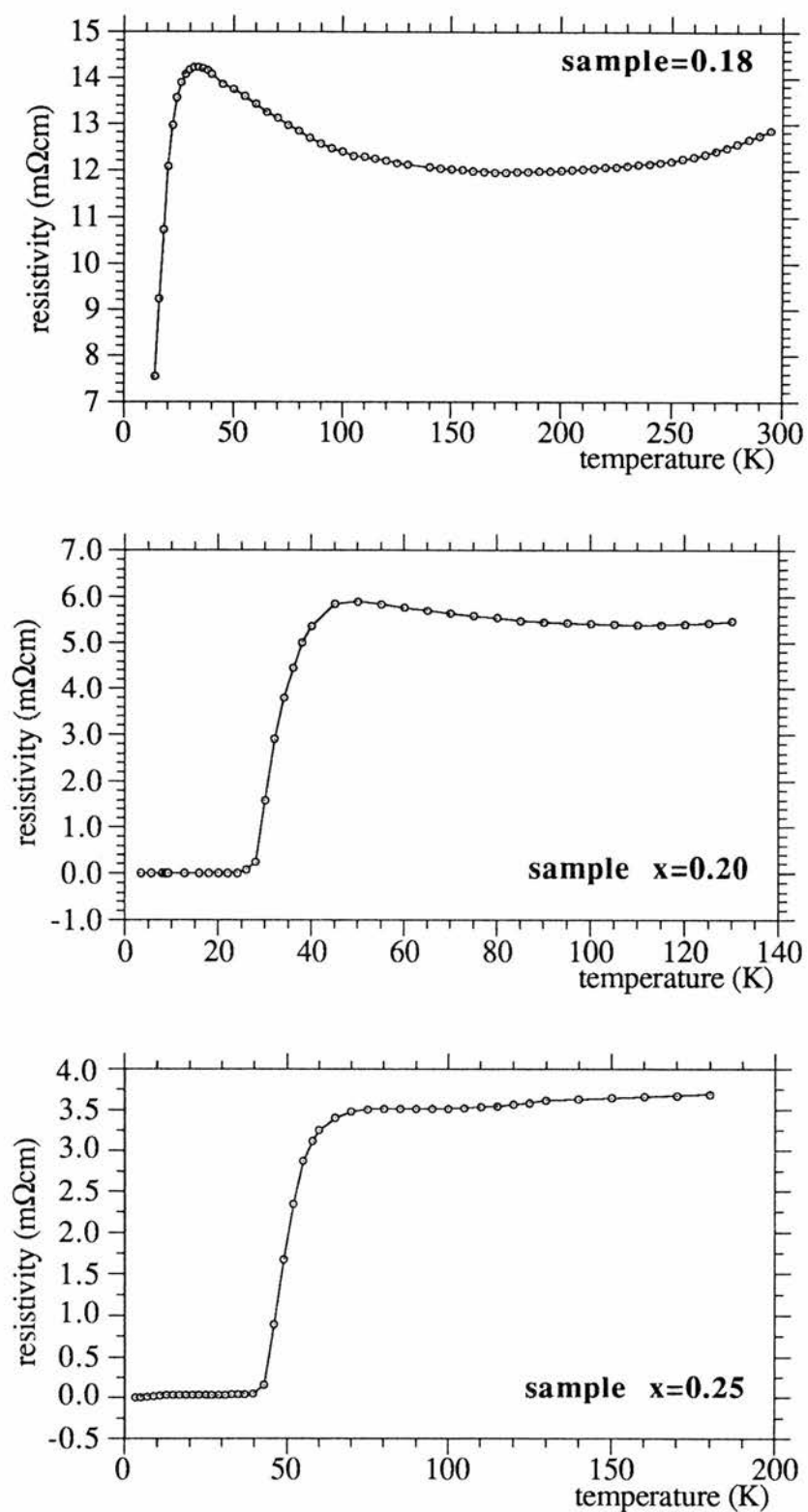


Figure 5.9. Superconducting transition temperatures measured by resistivity.

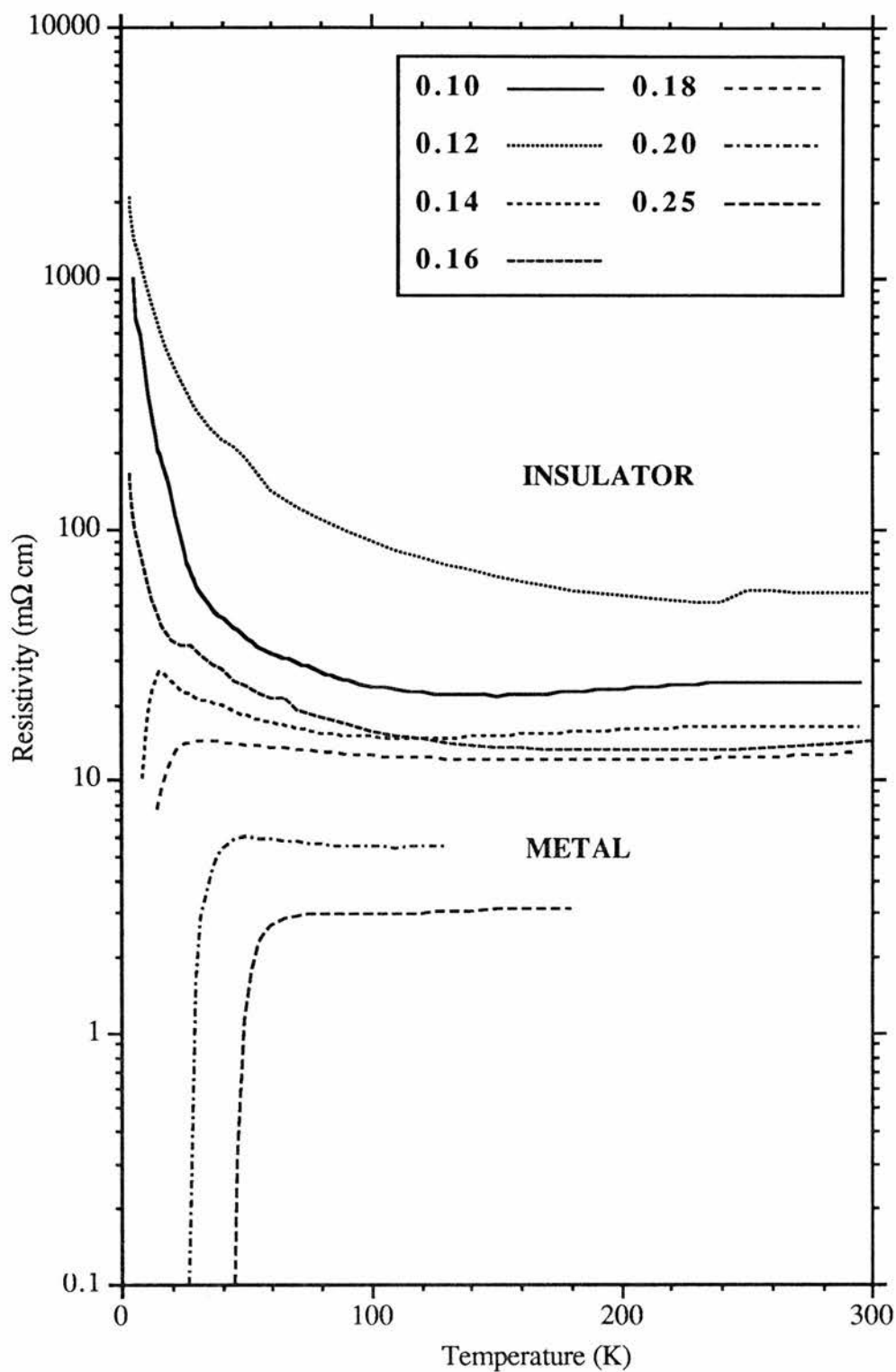


Figure 5.10. Resistivities for all samples, demonstrating the variation in behaviour between the superconducting samples and the insulators.

### 5.6.2. AC Susceptibility Results

AC susceptibility measurements were carried out on all eight samples of  $(Y_{1-x}Ca_x)Ba_2Cu_3O_{6+\delta}$ . Approximately the same volume of powder was used in each case, in order to compare the results.

At the onset of superconductivity, the magnetic field is excluded from the interior of the sample due to the superconducting shielding currents flowing in opposition to the applied field. The dramatic change in field profile appears as changes in both the real (in-phase) and the imaginary (out-of-phase) component of the voltage across the coil. Experimentally, both the in-phase and quadrature components were measured using the mutual inductance bridge, but the quadrature components were very weak and did not provide any useful information. Transitions to the superconducting state were therefore observed by monitoring the in-phase component.

Out of the eight samples tested, three were found to be superconductors at lower temperature and the rest remained in the normal state. The 0.16 and 0.18 samples were repeated a second time when the continuous-flow cryostat was able to cool to lower temperatures, in order to improve the results and ensure no transitions for the  $x=0.16$  sample occurred in this region. The superconducting transitions for the  $x=0.25$ , 0.20 and 0.18 samples are shown in Figure 5.11. and Table 5.9.

sample	$T_c$
0.25	38K
0.20	31K
0.18	9.5K

Table 5.9. Superconducting transition temperatures as determined by AC susceptibility.

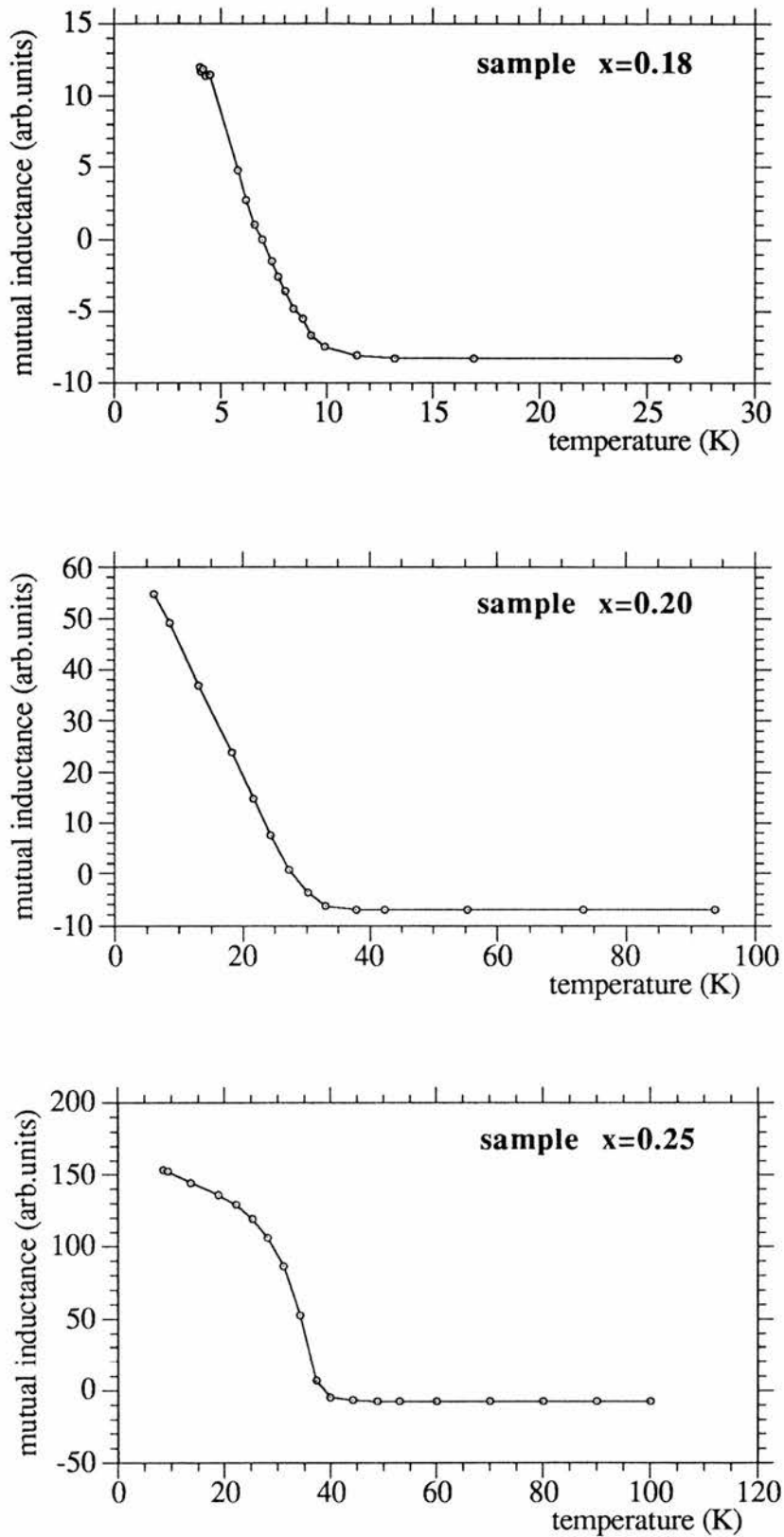


Figure 5.11. Superconducting transition temperatures as measured by AC susceptibility.

## 5.7. Results of the $^{89}\text{Y}$ NMR Experiments

An extensive study using nuclear magnetic resonance has been made at the yttrium site for the  $\text{Y}_{1-x}\text{Ca}_x\text{Ba}_2\text{Cu}_3\text{O}_{6+\delta}$  system. As described previously (Section 4.8.1), the yttrium site is ideal for observing the changes (in a non-interactive manner) that take place on the conduction planes as dopant is added. The MSL 500 Spectrometer, using an external magnetic field  $B_0$  of 11.74T, was used to obtain all spectra. It is important to note that all the spectra obtained here were referenced to an aqueous solution of  $\text{YCl}_3$ , and so 0 Hertz seen on the spectra is in fact the resonance frequency of Y in  $\text{YCl}_3$ .

The  $^{89}\text{Y}$  NMR spectra obtained as the doping concentration of  $\text{Ca}^{2+}$  increases can be seen in Figure 5.12. These spectra were obtained at room temperature and the samples were placed such that the aligned c-axis was parallel to the external magnetic field  $B_0$ . With the exception of the  $x=0.00$  and  $x=0.25$  samples, the spectra appear to be double peaked. Similar spectra were obtained by Webster<sup>5</sup> using the same equipment (and magnetic field strength) for the  $\text{YBa}_2(\text{Cu}_{1-x}\text{Co}_x)_3\text{O}_7$  system. Other reports of double peaked NMR spectra<sup>10,11</sup> have been due to inhomogeneities and misalignment and do not fit the description of the results here. It is possible that the higher magnetic field used for this work has allowed sufficient resolution in the frequency domain to distinguish the two peaks, which would otherwise be seen as a single broad peak. The double-peaked structure has been carefully considered, and a full discussion may be found in Chapter 6.

The magnetic shifts,  $\Delta K$ , and signal linewidths have been plotted in Figures 5.13. and 5.14. respectively. The linewidth remains identical throughout the doping series, with the exception of the  $x=0.00$  sample which is anomalously broad. This indicates that the parent compound is in the antiferromagnetic insulating state and agrees with published data<sup>12</sup>. Interesting results are obtained for the variation in the

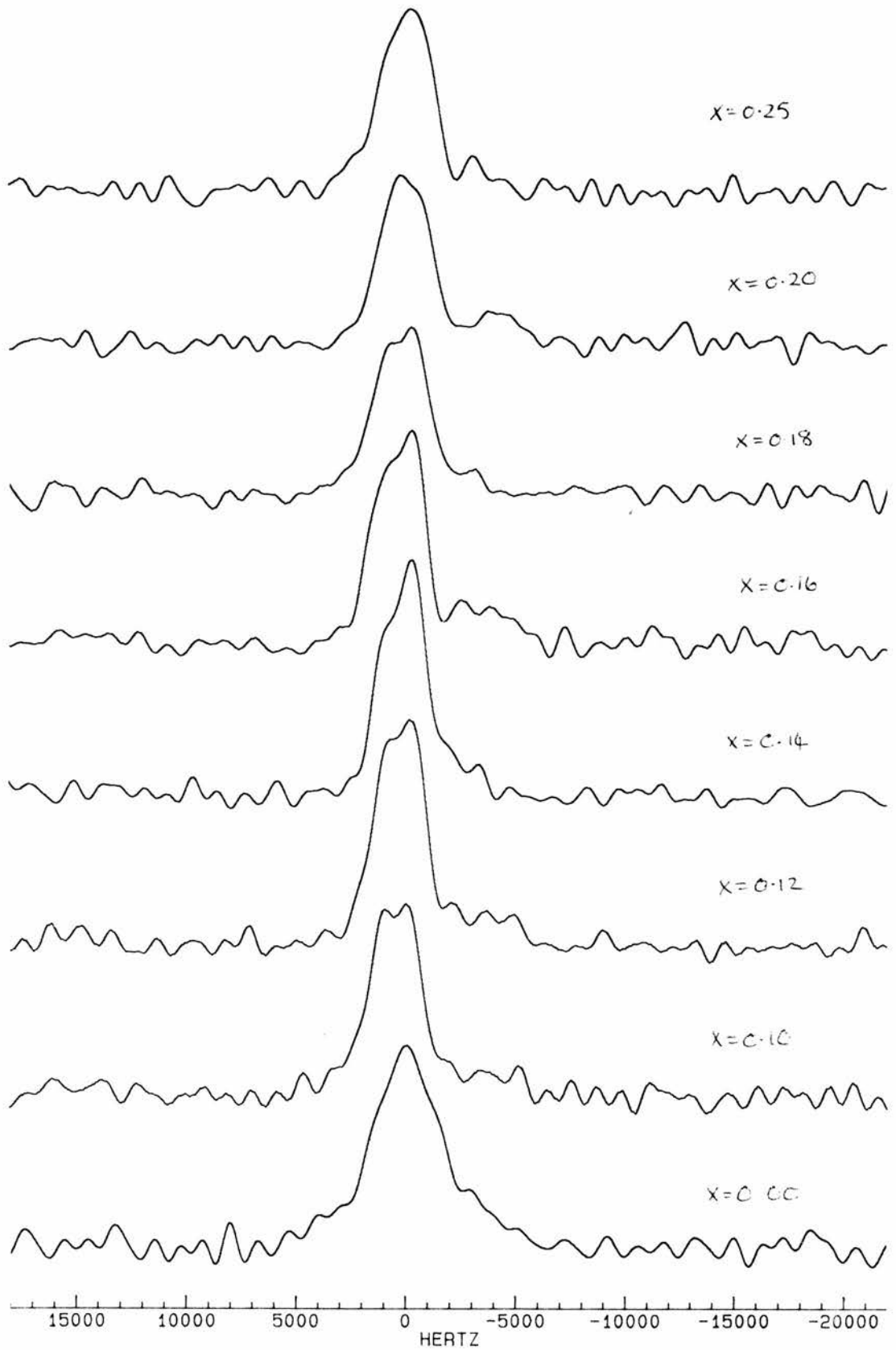


Figure 5.12.  $^{89}\text{Y}$  NMR spectra obtained for all samples at room temperature, orientated such that the crystalline c-axis was placed parallel to the external magnetic field.

magnetic shifts for the doping study (Figure 5.14). The position of both the peaks in the spectra have been plotted, and were found to vary in a consistent manner. Peak 2 (at lower frequency) remained at the same frequency throughout the series, but peak 1 (at higher frequency) shifted from higher frequency at low doping concentration, to lower frequency at higher doping concentration, until at  $x=0.25$  the peaks have almost converged and are indistinguishable. The fact that the parent compound has only a single peak may indicate that the second peak is a feature induced by the dopant.

In order to elucidate the two peaks and as an attempt to study the conduction planes, the  $x=0.14$  sample was studied at various orientations to the magnetic field. The spectra for the  $c$ -axis parallel, at  $30^\circ$ ,  $60^\circ$  and perpendicular to the external field are shown in Figure 5.15. The linewidths and magnetic shifts for each are given in Tables 5.10. and 5.11. respectively. It was interesting to discover that the double-peaked structure disappeared for angles greater than  $45^\circ$  to  $B_0$ , and clearly became a single narrow peak. It is not clear whether Peak 2 has greatly decreased in intensity, or whether it has shifted towards the other such that they are no longer distinguishable.

Orientation (degrees to $\mathbf{B}$ )	$\Delta\nu$ (ppm)
0 (parallel)	104
30	100
60	71
90 (perpendicular)	61

Table 5.10. Signal linewidths,  $\Delta\nu$ , obtained for each orientation of the  $x=0.14$  sample.

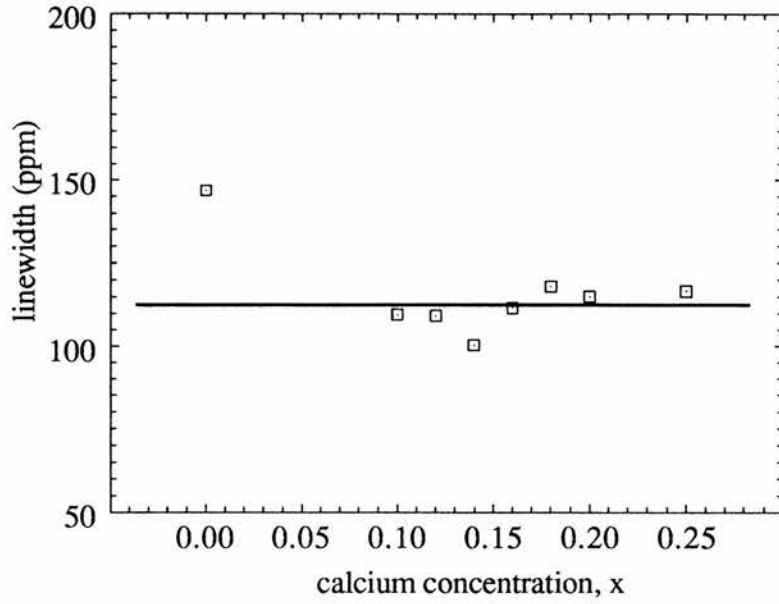


Figure 5.13. Signal linewidths,  $\Delta\nu$ , plotted as a function of doping concentration,  $x$ .

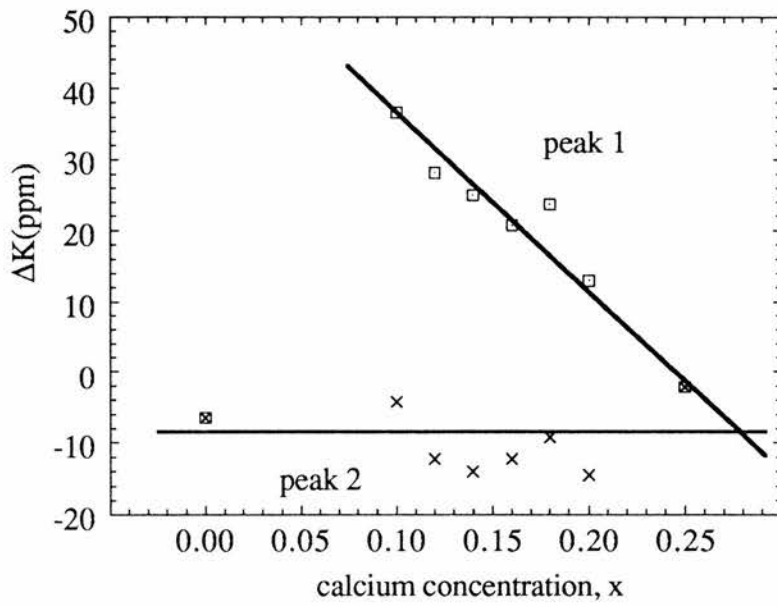


Figure 5.14. The magnetic shifts,  $\Delta K$ , for each peak plotted as a function of doping concentration,  $x$ .

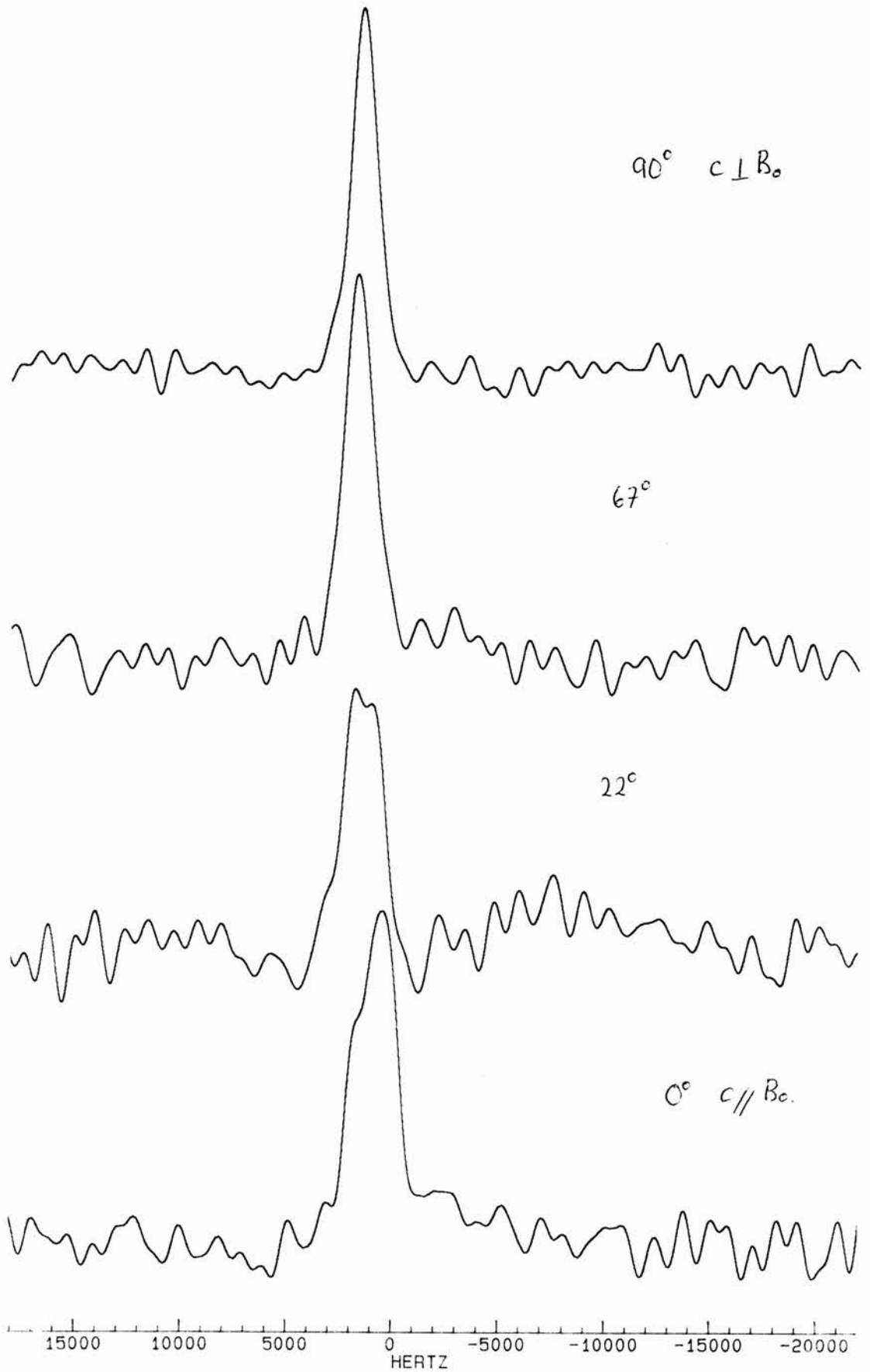


Figure 5.15.  $^{89}\text{Y}$  NMR spectra obtained for the  $x=0.14$  sample at room temperature, with the crystalline  $c$ -axis at various orientations to the external magnetic field.

Orientation (degrees to <b>B</b> )	$\Delta K$ Peak 1 (ppm)	$\Delta K$ Peak 2 (ppm)
0 (parallel)	39.1	-6
30	48.6	15.2
60	44.6	no peak
90 (perpendicular)	58.5	no peak

Table 5.11. Magnetic shifts of each peak,  $\Delta K$ , obtained for each orientation of the  $x=0.14$  sample.

The  $^{89}\text{Y}$  study was then extended to observe behaviour at lower temperatures. Experiments were only carried out on the two metallic samples,  $x=0.25$  and  $x=0.20$ , for temperatures between room temperature and 140K, which was the minimum temperature that could be achieved with the spectrometer. The spectra for the  $x=0.25$  and  $x=0.20$  samples may be found in Figures 5.16 and 5.17. Normally, the signal-to-noise ratio is expected to improve as the temperature of the sample decreases, but as can be seen in the figures, this was not the case. As the temperature of the sample and the solenoid probe cooled below  $\sim 250\text{K}$ , water from the atmosphere condensed and collected in the electronics within the body of the probe and consequently the signal could not be observed. This was a cumulative effect and became worse as time progressed. In order to obtain a signal, the experiments had to be carried out as soon as the probe was cooled from room temperature, rather than simply lowering the temperature of the previous experiment. In addition, the number of acquisitions were reduced to a minimum so that the spectra for the different variable delays for  $T_1$  measurement were comparable. The overall result was diminished but observable spectra. The collection of water in the probe was an inherent design problem of the solenoid probe and could not be eliminated. The linewidths for the temperature dependence data are plotted in Figure 5.18 and the magnetic shifts in Figure 5.19. Where double peaks were observed, the magnetic shift was taken to be at the position of the centre of the linewidth in order to produce more meaningful results. The linewidth of the  $^{89}\text{Y}$  signal was found to be unaffected by the decrease in

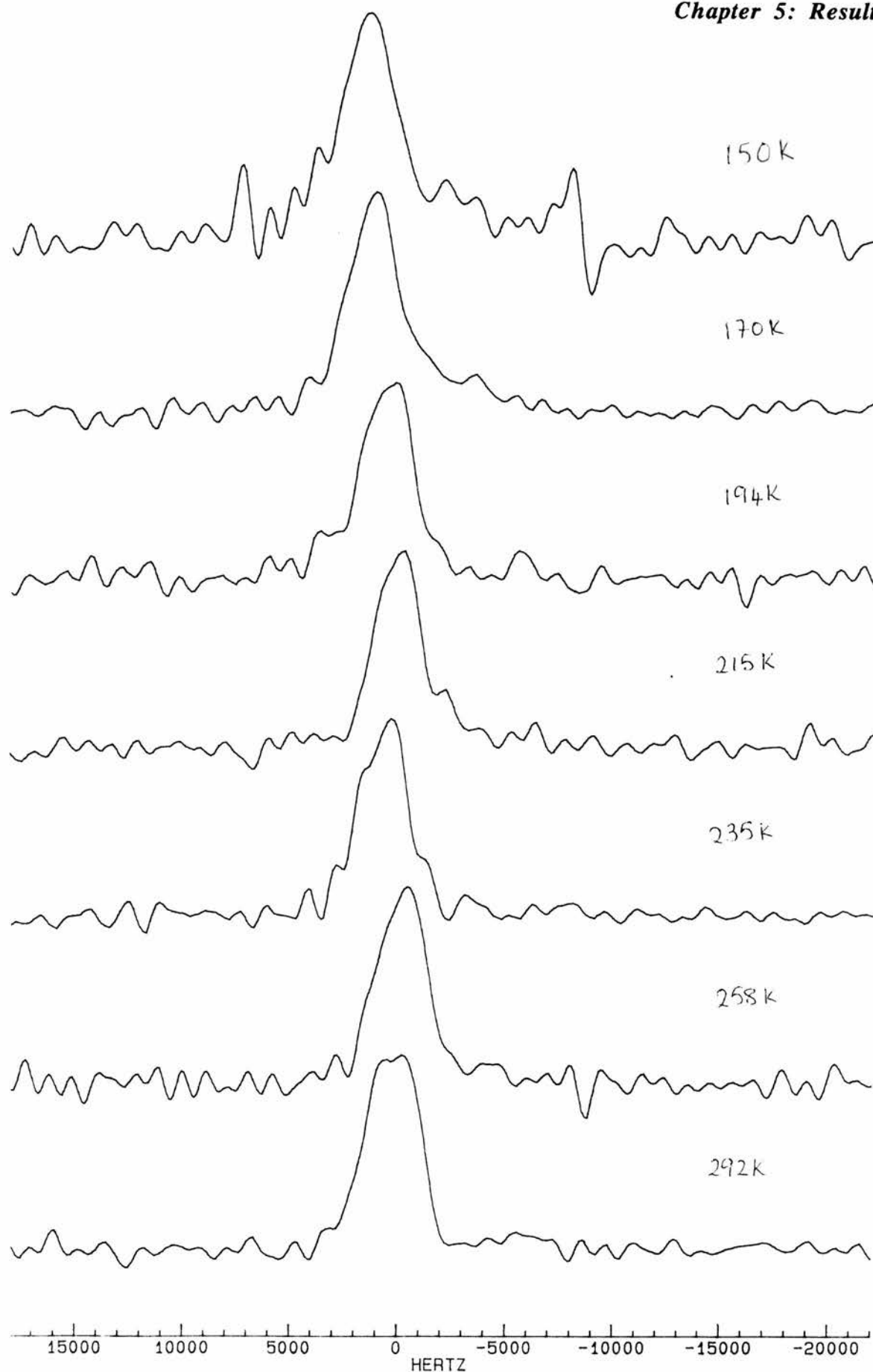


Figure 5.16.  $^{89}\text{Y}$  NMR spectra for the  $x=0.25$  sample, studied as a function of temperature, taken with the crystalline  $c$ -axis placed parallel to the external magnetic field..

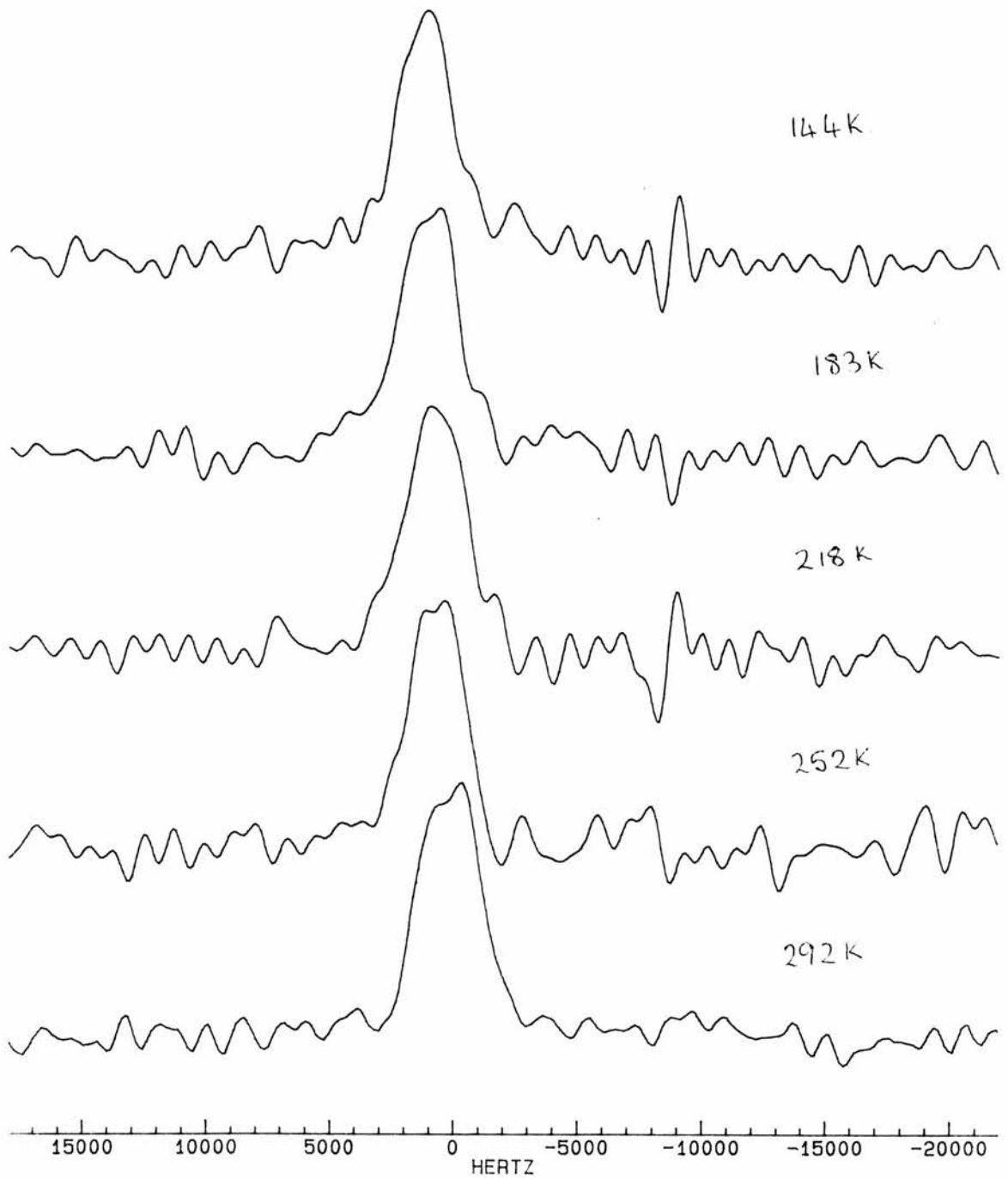


Figure 5.17.  $^{89}\text{Y}$  NMR spectra for the  $x=0.20$  sample, studied as a function of temperature, taken with the crystalline  $c$ -axis placed parallel to the external magnetic field.

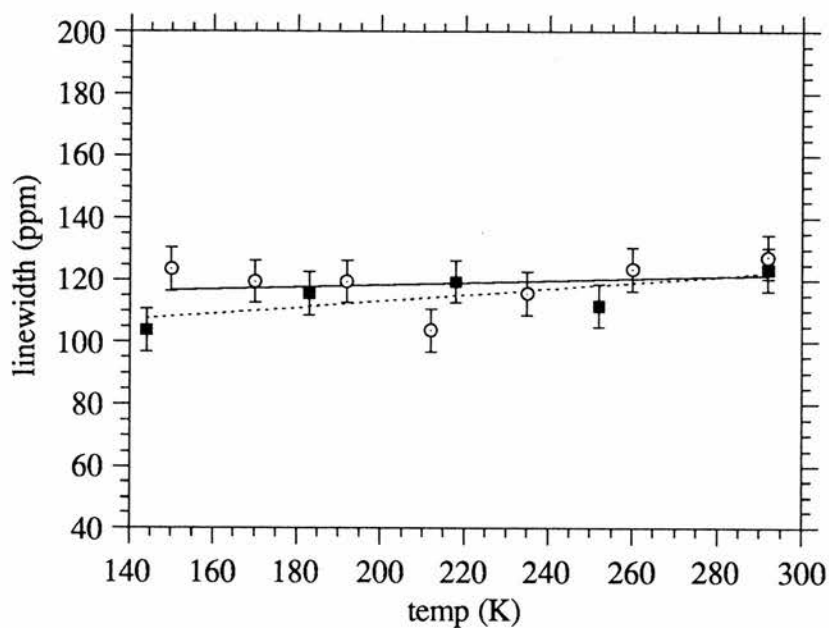


Figure 5.18. Signal linewidths,  $\Delta\nu$ , for the  $x=0.25$  and  $0.20$  samples plotted as a function of temperature.

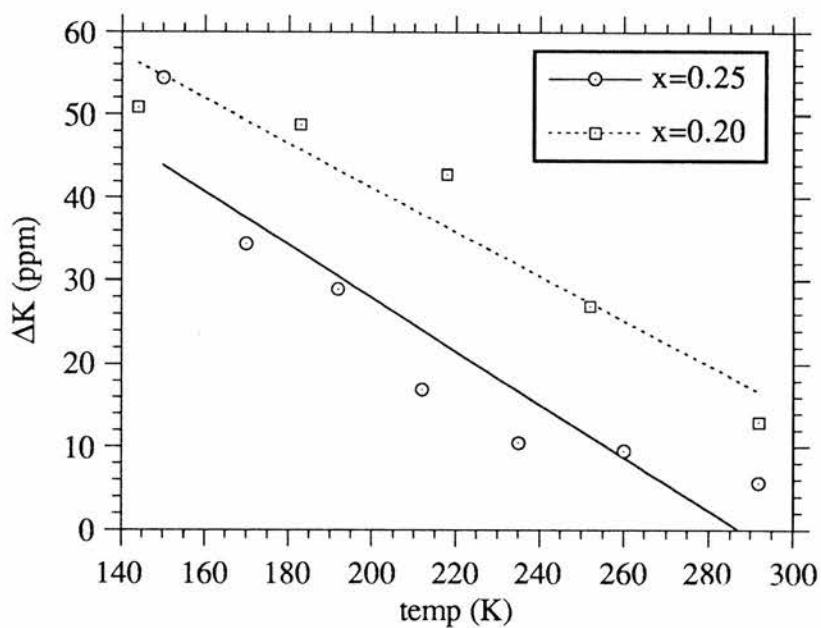


Figure 5.19. The magnetic shifts,  $\Delta K$ , for the  $x=0.25$  and  $0.20$  samples plotted as a function of temperature.

temperature, however in both samples, the peaks were found to shift to higher frequency.

Finally, the spin-lattice relaxation times ( $T_1$ ) were measured, firstly as a function of doping concentration at room temperature and secondly as a function of temperature for the  $x=0.25$  and  $x=0.20$  samples. The method of measuring  $T_1$  has been explained in Section 4.8.4.2. An example of the calculation used to obtain  $T_1$  from the results of a series of experiments using increasing variable delays is shown below.

The results of the experiments are plotted as in Figure 5.20, ie. the intensity of the signal for various delays. A linefit is then made to the data using the equation

$$M(t) = M_0(1 - \exp(-t/T_1))$$

by applying the general curvefit facility available in the KaleidaGraph graphics package for the Apple Macintosh. The parameters for the fitted line are displayed in the table, revealing a value for  $T_1$  ( $m_2$  in the table) with an associated error based on the success of the fit and an R value<sup>13,14</sup> (the correlation coefficient).

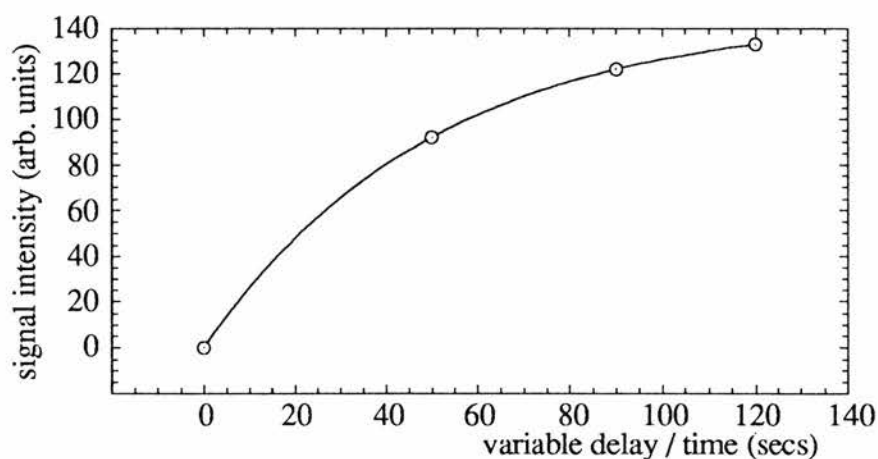


Figure 5.20. The linefit to the data obtained from saturation recovery experiments used to determine the spin-lattice relaxation time of the  $^{89}\text{Y}$  nucleus in  $(\text{Y}_{1-x}\text{Ca}_x)\text{Ba}_2\text{Cu}_3\text{O}_{6+\delta}$ .

Table 5.10. lists the values obtained for  $T_1$ , for all samples at room temperature with associated errors. For the samples in the intermediate state,  $T_1$  appeared to be constant at approximately 50 seconds. As the sample became more metallic (normal state of the superconducting samples)  $T_1$  decreased to  $\sim 25$  seconds. The value obtained for the  $x=0.00$  sample was anomalously small and was due to the ordered antiferromagnetic state of the lattice, that aids the relaxation of the spins.

sample, x	$T_1$ (from linefit)	error	R
0.25	26.25	$\pm 1.52$	0.9992
0.20	30.86	$\pm 0.33$	0.9999
0.18	50.73	$\pm 0.13$	0.9999
0.16	47.64	$\pm 1.53$	0.9999
0.14	35.72	$\pm 1.96$	0.9998
0.12	37.50	$\pm 1.45$	0.9999
0.10	54.88	$\pm 2.7$	0.9995
0.00	10.34	$\pm 0.32$	0.9998

Table 5.12. The variation of  $T_1$  with doping concentration. Values obtained by linefitting to data obtained by the saturation recovery experiment, along with associated errors and an indication of success of the fit.

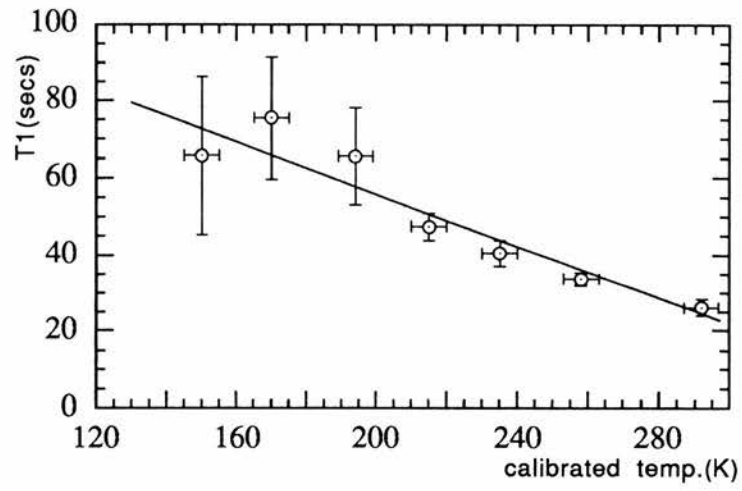
The results of the study of  $T_1$  as a function of temperature for the  $x=0.25$  and  $0.20$  samples are given in Tables 5.11 and 5.12. These are plotted in Figure 5.21. (a) and (b). The errors plotted in the figure take into account the large errors incurred by the poor signal to noise at lower temperatures.  $T_1$  increased with decreasing temperature for both samples.

Temperature(K)	T <sub>1</sub> (from linefit)	error	R
292	26.2	±1.5	0.9999
258	33.7	±0.5	0.9999
235	40.5	±2.9	0.9993
215	47.5	±2.4	0.9997
194	65.7	±12.3	0.9971
170	75.6	±15.5	0.9972
150	~65.8	insufficient data	

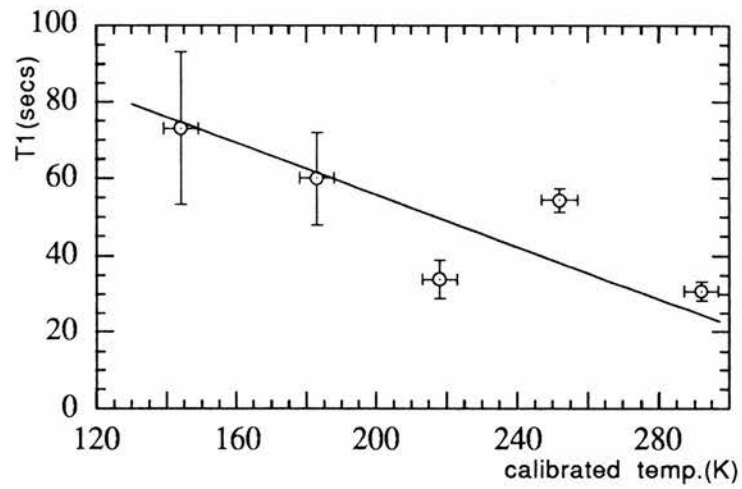
Table 5.13. The variation of T<sub>1</sub> with temperature for the x=0.25 sample. Values obtained by linefitting to data obtained by the saturation recovery experiment, along with associated errors and an indication of success of the fit.

Temperature(K)	T <sub>1</sub> (from linefit)	error	R
292	30.9	0.3	0.9999
252	54.4	6.1	0.9986
218	33.9	2.2	0.9993
183	60.2	2.5	0.9998
144	73.3	1.4	0.9999

Table 5.14. The variation of T<sub>1</sub> with temperature for the x=0.20 sample. Values obtained by linefitting to data obtained by the saturation recovery experiment, along with associated errors and an indication of success of the fit.



(a)



(b)

Figure 5.21. The variation of the spin-lattice relaxation times,  $T_1$ , with temperature for (a) the  $x=0.25$ , and (b) the 0.20 samples.

## 5.8. Results of the $^{63}\text{Cu}$ NMR Experiments

Nuclear magnetic resonance at the copper site in  $\text{Y}_{1-x}\text{Ca}_x\text{Ba}_2\text{Cu}_3\text{O}_{6+\delta}$  has been carried out for the  $x=0.25$  sample. The MSL 500 Spectrometer with an external magnetic field  $B_0$  of 11.74T was used for this study. The method of obtaining the spectra was described in Section 4.8.7. The peak height was used to measure the intensity of the spectra for each frequency interval. The  $^{63}\text{Cu}$  NMR signals for this material were found to be very weak, comparable to the background level.

The orientation of the **c**-axis of the  $x=0.25$  aligned sample was varied between the parallel and the perpendicular position to the applied magnetic field. The spectra for  $\theta=0^\circ, 22^\circ, 45^\circ, 67^\circ$  and  $90^\circ$  are shown in Figure 5.22. There are two main features in the spectra. A small peak can be seen at  $\sim 132.3\text{MHz}$  for all sample orientations. A more prominent peak appears at  $\sim 134.1\text{MHz}$ , which changes in intensity as the orientation is varied. The maximum intensity is observed at  $90^\circ$ , but rapidly decreases away from this position. A plateau exists between the two peaks for all spectra and does not appear to have any orientation dependence.

The sample used in this experiment was finely ground powder mixed with epoxy resin, aligned and set in a magnetic field. By x-ray diffraction the alignment was calculated to be 85% successful, leaving 15% of the sample randomly orientated. In order to discover the effects this may have on the NMR spectra, a further experiment was carried out on a completely randomly orientated sample ( $x=0.25$  powder set in epoxy). The result is shown in Figure 5.23. A broad lineshape is observed for the random powder spectrum, but there are no prominent features. The plateau and the small peak seen at 132.3MHz for the aligned samples may be due to the residual random fraction of powder. These spectra are discussed further in Section 6.7.

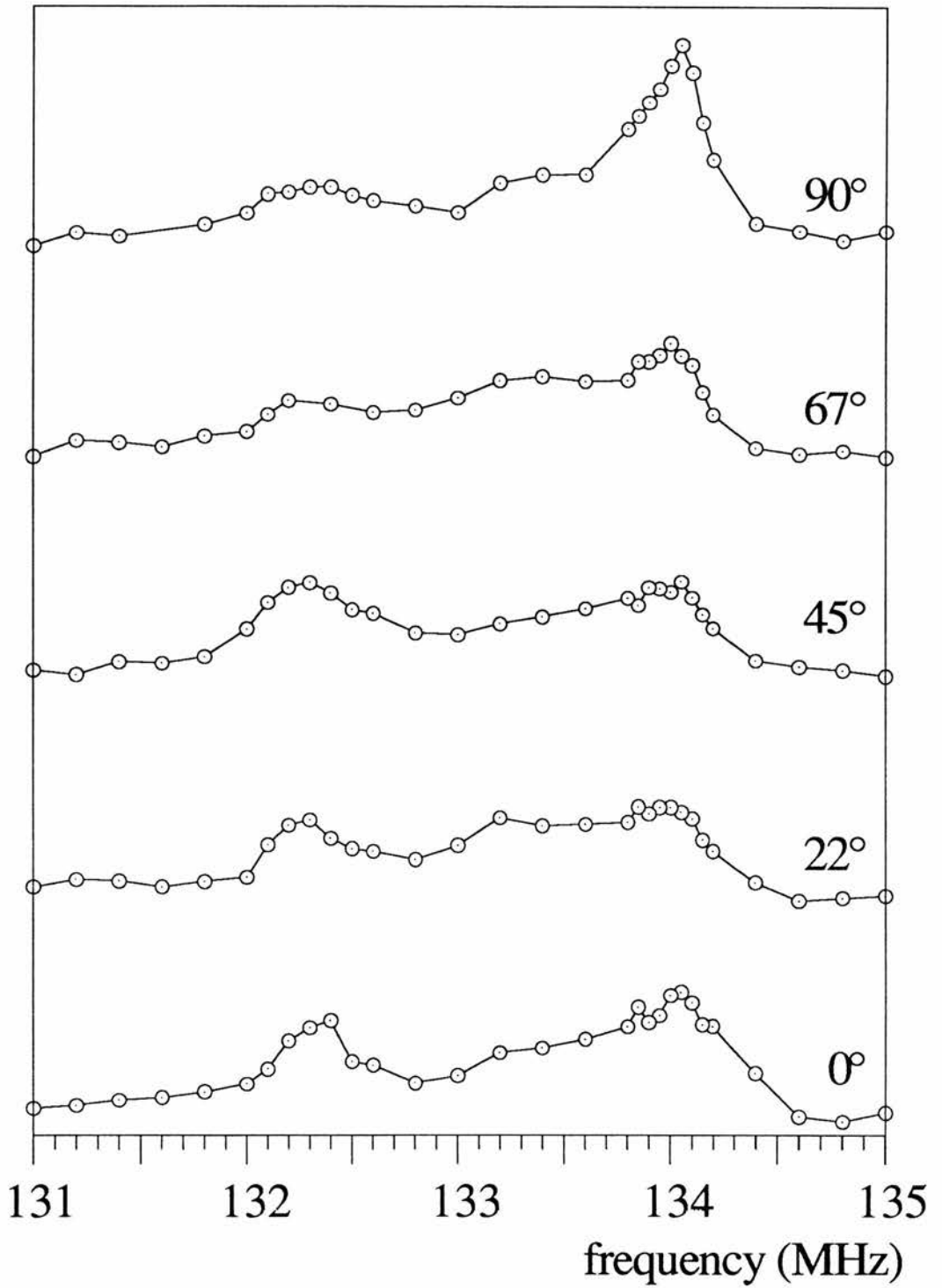


Figure 5.22. Orientation dependence of the aligned sample  $\text{Y}_{1-x}\text{Ca}_x\text{Ba}_2\text{Cu}_3\text{O}_{6+\delta}$  for  $x=0.25$  as seen by  $^{63}\text{Cu}$  NMR. The angle is that of the crystal c-axis to the applied magnetic field  $B_0$ .

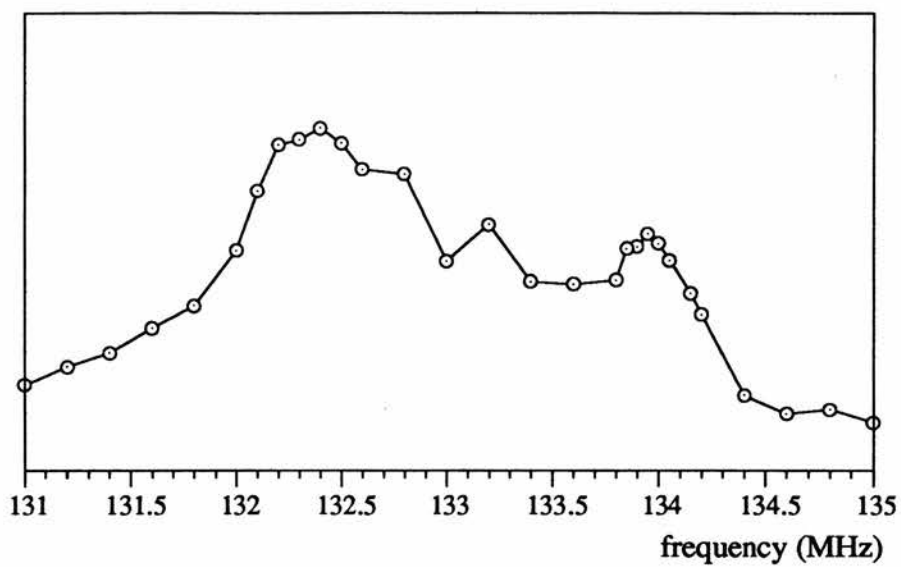


Figure 5.23.  $^{63}\text{Cu}$  NMR spectrum for a randomly orientated powder sample ( $x=0.25$ )

## References

- 1 A.M.T.Bell. *Supercond. Sci. Technol.*, **3** (1990) 55.
- 2 C.Namgung, J.T.S.Irvine, J.H.Binks and A.R.West. *Supercond. Sci. Technol.*, **1** (1988) 169.
- 3 L.H.Greene and B.G.Bagley. "*Physical Properties Of High Temperature Superconductors II*", D.M.Ginsberg (ed.), World Scientific, Singapore (1990).
- 4 A.Lusnikov, L.L.Miller, R.W.Callum, S.Mitra, W.C.Lee and D.C.Johnson. *J.Appl. Phys.*, **65** (1989) 3136.
- 5 W.J.Webster. *PhD Thesis*, University of St.Andrews (1993).
- 6 G.Dai. Private communication.
- 7 L.J.Van der Pauw. *Philips Res. Repts.*, **13** (1958) 1.
- 8 L.J.Van der Pauw. *Philips Res. Repts.*, **16** (1961) 187.
- 9 H.Casalta, H.Alloul and J.-F.Marucco. *Physica C*, **204** (1993) 331.
- 10 G.Dai. *PhD Thesis*, University of St.Andrews (1994)
- 11 H.B.Brom and H.Alloul. *Physica C*, **177** (1991) 297.
- 12 H.Alloul. *Physica B*, **169** (1991) 51.
- 13 A simple definition may be found in: M.G.Kendall and W.R.Buckland. "*A Dictionary of Statistical Terms*", (Oliver and Boyd, 1971).
- 14 John R.Taylor. "*An Introduction to Error Analysis - The Study of Uncertainties in Physical Measurements*", (University Science Books, 1982) p178.

## Chapter 6

# DISCUSSION

### 6.1. Introduction

The experimental results obtained for all the characterisation techniques have been mentioned in Chapter 5. This chapter is a discussion and comparison of the results. Section 6.2 outlines all the information gained about the structure and phase purity of the materials from x-ray diffraction and electron microprobe experiments. It also compares two possible synthesis mechanisms. Section 6.3 follows on with a comparison of the oxygen determinations obtained by thermogravimetric analysis and iodometric titration for the samples. The attempt made to determine the oxygen by quantitative electron probe microanalysis (EPMA) is also discussed. The superconducting transition temperatures obtained by resistivity and susceptibility experiments are compared in Section 6.4. The resistivity experiments also gave information about the conduction properties of the non-superconducting samples. Section 6.5 discusses these results and makes a comparison to various possible conduction mechanisms. Finally, the results obtained by nuclear magnetic resonance (NMR) at the yttrium site and the copper site are discussed in Sections 6.6 and 6.7 respectively.

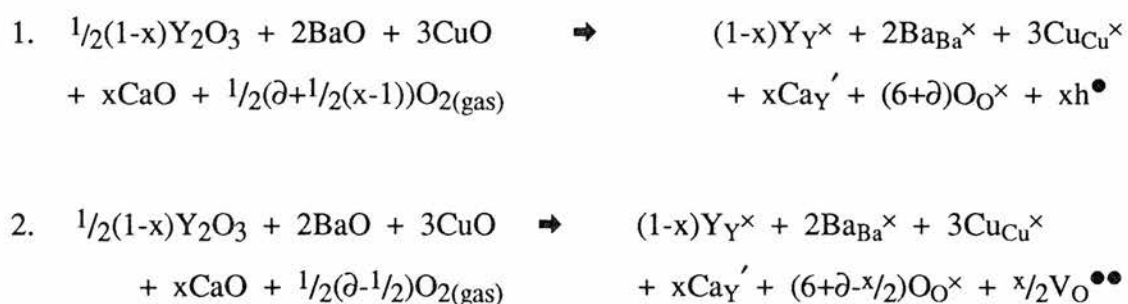
### 6.2. Crystal Structure and Phase Purity

X-ray diffraction indicated that single-phase materials were obtained throughout the  $Y_{1-x}Ca_xBa_2Cu_3O_{6+\delta}$  series, both before and after quenching. Before quenching the crystal structure was orthorhombic, and as the calcium concentration increased, the **a** parameter increased and the **b** parameter decreased (see Table 5.1). This is indicative of the crystal tending towards tetragonality as calcium is increased. In addition, the **c** parameter increased slightly, giving an overall increase in the cell volume, which is

consistent with the calcium substituting onto the yttrium site, as reported by McCarron et al<sup>1</sup>. After quenching, the lattice was refined on a tetragonal structure with space group P4/mmm. In this case, the presence of increasing calcium in the lattice did not significantly change the lattice parameters (refer to Figure 5.3).

Disorder along the *c*-axis has previously been reported for the calcium doped material<sup>2</sup>. The x-ray spectra for the quenched *x*=0.00 and the *x*=0.25 powder samples were compared to see if any line broadening could be observed for (*h*,*k*,*l*≠0) peaks, which would indicate a spread in the *c*-parameter. The linewidths of the doped sample were only 1% broader than for the parent compound, and consequently this evidence for disorder was inconclusive.

There are two possible mechanisms taking place when calcium dopes onto the yttrium site. These have been outlined below using Kröger-Vink notation<sup>3</sup>.



where *h* represents a hole and *V* represents a vacancy. The subscript represents the lattice site and the superscript the associated charge, ie.  $\times$  normal charge for the perfect crystal,  $\bullet$  a released electron and  $'$  a trapped electron. For example,  $Ba_{Ba^\times}$  represents a barium atom sitting on a barium site in the lattice, whatever charge it has because it corresponds to the normal charge in the perfect crystal and  $Ca_{Y'}$  represents a calcium atom sitting on an yttrium site in the lattice, having trapped an electron.

To summarise, substitution of calcium for yttrium can either increase the hole concentration in the lattice, or result in a reduction of oxygen content leaving the hole concentration the same. In practice a combination of both is possible.

It is proposed that prior to quenching, mechanism 2 is the major effect, and after quenching mechanism 1 is in operation. The evidence for this is based on the lattice parameters. The lattice parameters are largely controlled by the quantity of oxygen in the Cu(1) "chain" sites. Loss of oxygen results in a decrease in the **b** lattice parameter (Table 5.1). This is observed as the calcium concentration increases for the unquenched samples. After quenching, the lattice parameters remain unchanged as calcium is introduced, implying that the oxygen concentration remains identical throughout the series and the calcium doping results in an increase of holes in the system. This increase in the number of holes in the lattice causes the lattice to contract, so that despite a slightly larger atom replacing the yttrium, the lattice parameters remain the same.

In order to confirm homogeneity of the samples, the  $x=0.25$  and  $x=0.20$  materials were examined by electron microscopy (see Section 5.4). Only single-phase materials were observed. It is interesting to note that for the commercially produced 99.9% pure  $\text{YBa}_2\text{Cu}_3\text{O}_{6+\delta}$ , two phases were observed (see Figure 6.1). The largest

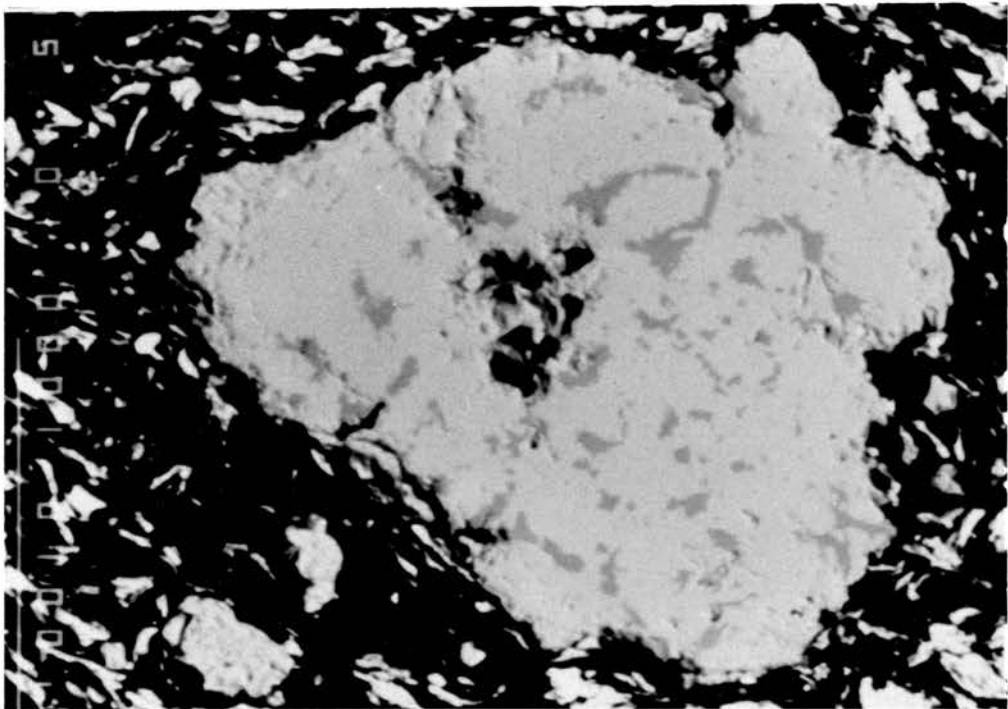


Figure 6.1. Photograph taken by electron microscopy showing two different phases present in the sample. The black patches demonstrate the porosity of the ceramics.

proportion was yttrium barium copper oxide, but the darker phase contained only copper and oxygen.

Electron microscopy showed that the samples were porous, typical of ceramic materials. The quenched samples appeared to have a greater porosity than the higher oxygen compounds. The calcium was evenly distributed throughout the material. It was mentioned in Section 5.2.1 that the pellets were harder to crush, the more calcium they contained. This feature has been observed by other researchers<sup>4</sup>, who discovered that the grain size increased with calcium concentration, and that the closely packed grains were indicative of the improved density of these materials.

### 6.3. Oxygen Concentration

An initial approximation for the oxygen content of the quenched samples was obtained by comparing the lattice parameters to those of published data. Unfortunately, these parameters do not vary greatly in the tetragonal region, and so it could only be said that  $0 \leq \delta \leq 0.4$ .

A more accurate determination was made by thermogravimetric analysis (Section 5.5.2). Slight variations were found between samples, but the average value was  $\delta = 0.155 \pm 0.02$ . The 0.20 sample gave a lower value of  $\delta = 0.00$  and could have been due to the presence of some sort of inert impurity.

The iodometric titration technique was used to determine the oxygen content for the  $x=0.18$  sample, giving an average value of  $\delta = 0.08 \pm 0.02$  (Section 5.5.1). This is a lower value than that obtained by thermogravimetric analysis. The cause of this discrepancy is still unknown, but could either be due to an impurity which was insoluble, or a loss of evolved oxygen for the titration technique.

For both techniques, the calculation of the oxygen content assumed that the stoichiometry of the material was  $Y_{1-x}Ca_xBa_2Cu_3O_{6+\delta}$ . This could not be confirmed by the quantitative electron microprobe method (Section 5.4), and may be incorrect. This would cause the resulting calculated oxygen values to be false.

The final method used to determine the oxygen contents in the sample was electron probe microanalysis (EPMA) (see Section 5.4). This technique was unsuccessful, largely due to an unsuitable standard material for calibration. The two standards used were commercially made products (Aldrich Chemical Company Ltd.), 99.9%  $\text{YBa}_2\text{Cu}_3\text{O}_{6.8(\pm 0.1)}$  2 $\mu\text{m}$  powder, and  $\text{YBa}_2\text{Cu}_3\text{O}_{\sim 6.5}$  unspecified powder size<sup>†</sup>, which was then oxygenated to the 93K superconductor,  $\text{YBa}_2\text{Cu}_3\text{O}_7$ . The 2 $\mu\text{m}$  powder was too finely ground to be used, and so the latter was used as a replacement.

Under quantitative analysis, the components did not form stoichiometric  $\text{YBa}_2\text{Cu}_3\text{O}_x$ . In addition, when the experiment was repeated at exactly the same position on the sample, the results could not be reproduced. There are several reasons why this could occur. The most obvious would be if the sample was not stoichiometric. Even if this was the case, reproducible results would still be expected. The alternative is the build-up of carbon on the surface of the sample in the local area of the electron beam. This is a common problem and results in different thicknesses of carbon for each measurement, giving rise to inconsistent results. This would be especially important for oxygen determination, since the  $\text{O}_{k\alpha}$  x-ray line is heavily absorbed by carbon and can reduce the oxygen count rate substantially. An attempt to avoid this problem was made by setting the samples in conducting epoxy (epoxy loaded with silver grains). The fluctuation in results was reduced but not eliminated.

The oxygen contents determined by thermogravimetric analysis seem reasonable when compared to those obtained by other research groups. Liu<sup>5</sup> reported  $\delta=0.1 \pm 0.01$  for their samples that were annealed at 730°C in argon and then quenched in liquid nitrogen (after falling through air). This method produced a lower oxygen content than that of McCarron<sup>1</sup>, where the samples were simply reduced in flowing argon. These comparisons will be discussed further in the following section on critical temperatures.

<sup>†</sup>This product was of unspecified purity and powder size. Private communication with the manufacturers confirmed that all their  $\text{YBa}_2\text{Cu}_3\text{O}_x$  materials were produced in a large batch, and so it may be assumed that the purity is 99.9%. To produce the  $\text{YBa}_2\text{Cu}_3\text{O}_{6.8}$  material, further oxidation and grinding stages were carried out.

## 6.4. Superconducting Critical Temperature

The transition temperature as measured by resistivity (see Section 5.6.1) is usually taken to be the mid-point of the transition from the normal state ( $T_c(\text{onset})$ ) to the superconducting state ( $T_c(\rho=0)$ ). For the susceptibility experiment (Section 5.6.2)  $T_c$  is considered as the onset of flux exclusion. These two values are compared in Table 6.1. The results are similar, and the discrepancy is simply that caused by the broad transitions.

sample	Resistivity	Susceptibility
x=0.25	49K	38K
x=0.20	32K	31K
x=0.18	13K	9.5K

Table 6.1. Comparison of the superconducting transition temperatures measured by resistivity ( $T_c(\text{mid-point})$ ) and susceptibility ( $T_c(\text{onset})$ ) experiments.  $x$  is the quantity of calcium in the material  $Y_{1-x}Ca_xBa_2Cu_3O_{6+\delta}$ .

McCarron<sup>1</sup> reported  $T_c=50\text{K}$  for his  $x=0.20$  sample with a corresponding oxygen content of  $\delta=0.2$ , and Liu<sup>5</sup> reported  $T_c=20\text{K}$  for  $x=0.25$  and  $T_c=6\text{K}$  for  $x=0.20$  both with oxygen contents  $\delta=0.1$ . Liu explained the decreased transition temperatures of his samples as being due to the reduction of the quantity of oxygen in his samples. Using these as guidelines, the results obtained for our samples for both the oxygen content and the transition temperatures seem reasonable, in that both of these values are between those of Liu's and McCarron's work.

When characterising samples, it is common practice to measure the superconducting volume fraction of the sample. For the ceramic high-temperature superconductors, this has frequently led to misleading results, which indicate that only a small quantity of the whole material is superconducting. Work by Campbell et al.<sup>6</sup> revealed that the values obtained were largely dependent on sample shape, particle size and packing fraction. The greatest cause of reduced magnetisation in the ceramics was

found to be due to the London penetration depth,  $\lambda$ . For the high-temperature superconductors, the density of superconducting holes is relatively small when compared to conventional superconductors. This leads to a large penetration depth for these materials. If a sample is large compared to  $\lambda$ , then the effects of the penetration depth are not significant. Frequently for the ceramic superconductors (especially powdered samples) this is not the case, and this leads to a reduction of the magnetisation of the sample. Often, samples which have been measured to have a reduced superconducting fraction have been misinterpreted and may be completely superconducting with a large penetration depth. Superconducting inhomogeneities in an otherwise non-superconducting sample can usually be found by other techniques such as impurities or inhomogeneities in x-ray diffraction.

The superconducting fractions have therefore not been measured for these samples. The reduction of the magnetisation intensity by  $\sim 90\%$  from the  $x=0.25$  sample to the  $x=0.18$  sample may be an indication of an increase in the penetration depth. More accurate measurements could have been achieved by measuring the magnetisation on sintered samples (then the penetration depth is small compared to the sample size), and by using the same mass of each sample, rather than the volume. This is because the density of the ceramic varied throughout the series. (This does not necessarily mean that the unit cell volume varies greatly between samples, but that the porosity of each sample differs.)

Reduced magnetisation due to large penetration depth or small superconducting fraction can usually be distinguished by the results of resistivity measurements. The resistivity will fall to zero if the bulk of the material is superconducting, but will only be reduced by a small amount if there is a small superconducting fraction (unless the superconducting grains have somehow formed an interconnecting filament through the sample, which can occur with 10% superconducting sample). The samples in this work have therefore been interpreted as having a large superconducting fraction.

For the parent system  $\text{YBa}_2\text{Cu}_3\text{O}_{6+\delta}$ , superconductivity is observed as the average copper valence exceeds  $2+$ . However, for the calcium doped material

$Y_{1-x}Ca_xBa_2Cu_3O_{6.15}$ , superconductivity occurs as the calcium doping concentration exceeds 16%, which corresponds to an average copper valency of  $1.82^+$ . If superconductivity occurs mainly in the planes, then clearly the effects of calcium and oxygen doping are not the same.

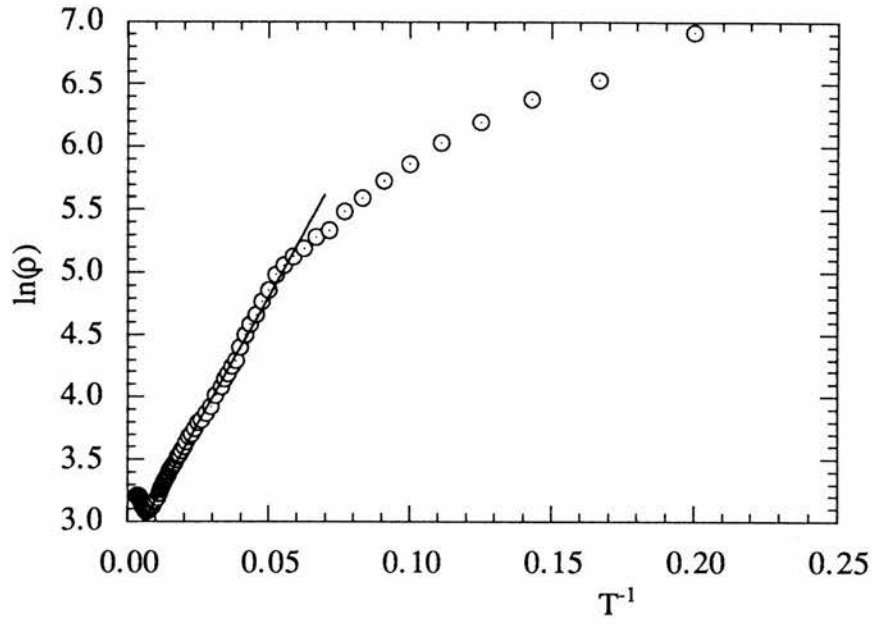
A possible (but somewhat simplified) scenario is as follows. Consider the parent compound with low oxygen content, ie.  $YBa_2Cu_3O_6$ . Any additional oxygen occupies the O(1) and O(5) sites and increases the copper valency at the Cu(1) sites from  $Cu^{1+}$  towards  $Cu^{2+}$ . In addition, if calcium is substituted onto the yttrium site, it is possible that this results in an increase in the copper valency at the Cu(2) sites from  $Cu^{2+}$  towards  $Cu^{3+}$ , allowing  $Cu^{1+}$ ,  $Cu^{2+}$  and  $Cu^{3+}$  ions to be present in the lattice simultaneously. This may suggest that it is the increase in the valency of the copper in the conduction planes that allows superconductivity to occur and that the role of the chain sites is simply to increase the hole concentration, which elevates the transition temperature. This would also account for the transition temperature being as low as  $\sim 40K$ , since there are no Cu-O chains to act as charge reservoirs.

## 6.5. Further Analysis of the Resistivity Results

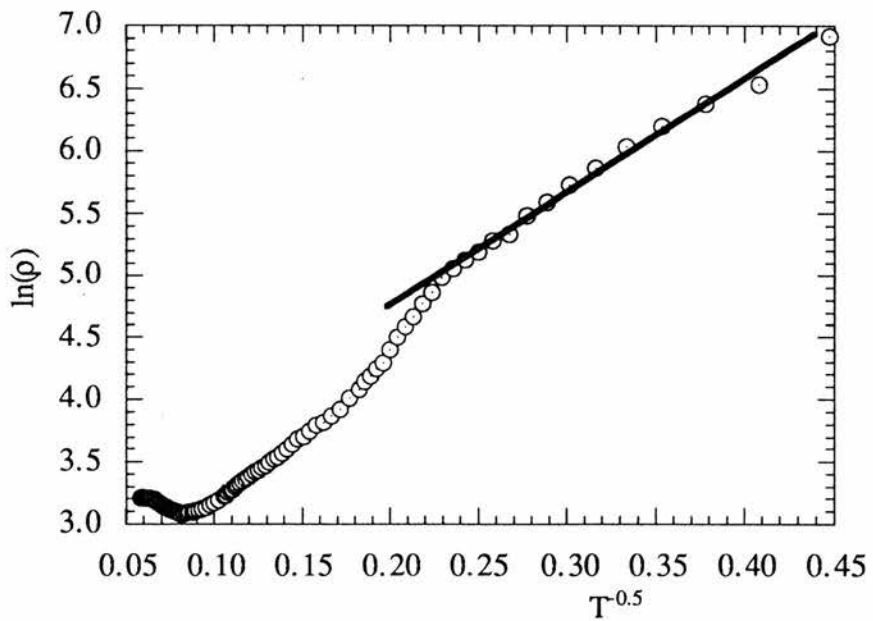
The variation of the resistivity with temperature for all samples was shown in Figure 5.10. For the superconducting samples ( $x=0.25$ ,  $0.20$  and  $0.18$ ) the conductivity in the normal state is of the order  $\sigma \approx 300 \Omega^{-1} \text{cm}^{-1}$  and their mobility is approximately  $0.3 \text{cm}^2 \text{V}^{-1} \text{s}^{-1}$ . (The calculation of the mobility may be found in Appendix A.3.) These values are comparable to those of a poor metal.

The remaining samples are insulating, and the carriers are thermally activated to the conduction band for 100-300K. This is similar to the "saturation" or "exhaustion" region of a semiconductor, which occurs when the concentration of extrinsic carriers attains its maximum value and is temperature independent. Using this analogy, a guess at the activation energy of the localised states would be 40-50meV.

Further analysis has been carried out on the  $x=0.10$  sample. Figure 6.2(a) shows a straight line fitting the data above 15K, indicating semiconducting behaviour



(a)



(b)

Figure 6.2. Resistivity measurement of the  $x=0.10$  sample plotted as (a)  $\ln(\rho)$  as a function of  $T^{-1}$  and (b)  $\ln(\rho)$  as a function of  $T^{-0.5}$ .

with an activation energy of 3.6meV. This is an unusually low number and is hardly consistent with the exhaustion at 100K. Figure 6.2(b) shows a linear region below 16K, indicating the possibility of variable range hopping in the presence of a Coulomb gap<sup>7</sup> with  $T_0=56\text{K}$  and  $\xi=8000\text{\AA}$ . This can probably be expected in a sample this far below the metal-insulator transition.

The  $x=0.14$  sample indicated a possible onset of superconductivity by the resistivity experiment. This could not be confirmed, because temperatures below 3.5K were not available. The susceptibility measurement on this sample, showed no indication of a transition. The resistivity of the  $x=0.16$  sample is replotted on a linear scale in Figure 6.3. The lineshape for this material deviates from that expected for an insulating compound for the region near 25K. A simple explanation for this is that inhomogeneities occur in the  $x=0.16$  sample, and of these, a few in the conduction path go superconducting, with the majority remaining insulating. These unexpected results indicate that the value of the oxygen content fluctuates between samples.

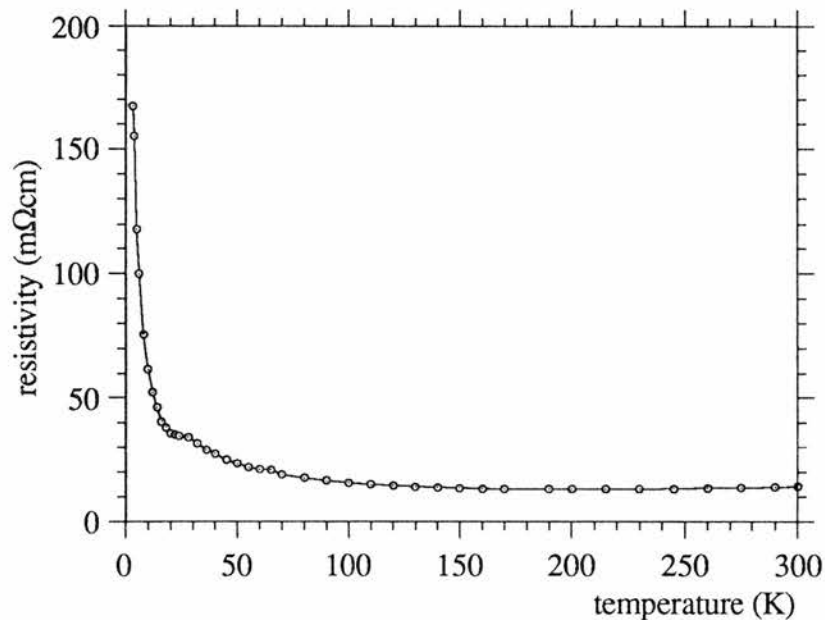


Figure 6.3. The resistivity of the  $x=0.16$  sample plotted as a function of temperature.

## 6.6. Yttrium NMR

The results obtained from the yttrium nuclear magnetic resonance experiments may be found in Section 5.7. This discussion of the  $^{89}\text{Y}$  NMR results has been separated into subsections for clarity.

### 6.6.1. Double-Peaked Spectra

A striking feature of the spectra obtained for the crystalline *c*-axis placed parallel to the applied magnetic field, was a double-peaked structure (for example see Figure 5.12). There are several reasons why this may occur:

- Two peaks could be expected if yttrium occupied two different sites in the lattice, e.g. yttrium on barium sites as well as the yttrium sites.
- Two peaks would be observed if there was also an impurity phase present, that also contained yttrium.
- If the oxygen content was not distributed homogeneously throughout the material, variations in the local environment of the yttriums would be seen.
- If the calcium was not distributed evenly throughout the material and there were regions with high quantities of calcium and low quantities of calcium, then this could give rise to different environments.
- The samples used for this experiment were aligned in epoxy. Two peaks would be expected if some of the sample remained random, i.e. one peak due to the aligned portion, and the other peak due to the random fraction.
- The presence of calcium in the material could be causing local changes within the Y/Ca plane, giving rise to inequivalent yttrium sites in the lattice.

After careful consideration, the first four possibilities in the above list have been eliminated. Yttrium cannot occupy the barium sites under normal conditions, simply due to its size. Also, the lattice parameters indicated substitution onto the yttrium site. For an impurity phase to give rise to such a large signal, it must incorporate approximately 50% of the yttrium nuclei in the sample. No such impurities have been

found by either x-ray diffraction or electron microscopy. Variations in the distribution of oxygen are possible, since this would not easily be observed by x-ray diffraction (due to lack of variation in the lattice parameters at low oxygen). It is improbable that there would be only two different oxygen contents present in the sample (in order to give rise to a double peak), and more likely to be a range of oxygen contents, so these variations would result in a general broadening of the peak. Finally, the possibility of calcium being incorporated inhomogeneously in the sample has been eliminated as the cause of the double peaks. If there were regions of high calcium and low (or no) calcium, then these would have been seen by electron microscopy. In addition, since the solubility limit of calcium in  $(Y_{1-x}Ca_x)Ba_2Cu_3O_{6+\delta}$  is  $x \approx 0.3$ , then the regions of high calcium would also contain the impurities  $BaCuO_2$  and  $CaO$ <sup>8</sup>. No such phases were observed.

This leaves the latter two suggestions as possibilities. These are discussed in more detail below.

#### **6.6.1.1. Aligned and Unaligned Fractions of Sample**

The samples used for the NMR experiments were powders that were aligned and set in an external magnetic field. This procedure is rarely completely successful, which means that there are both random and aligned portions of sample that contribute to the resulting spectra. The quantity of alignment was calculated using x-ray diffraction spectra, but indicated only ~10% random powder. The results may be found in Section 5.3. It is possible that one of the two peaks seen in the yttrium NMR spectra is due to the aligned powder, and the other is due to the remaining random fraction.

The orientation study of the  $x=0.14$  sample (Figure 5.15) demonstrated that one of the peaks is static and the other one is orientation dependent (Table 5.11). For this discussion, the orientation independent peak must be due to the random fraction and the orientation dependent peak due to the aligned portion. Figure 6.4. clarifies this labelling of the peaks, to aid the understanding of the following work.

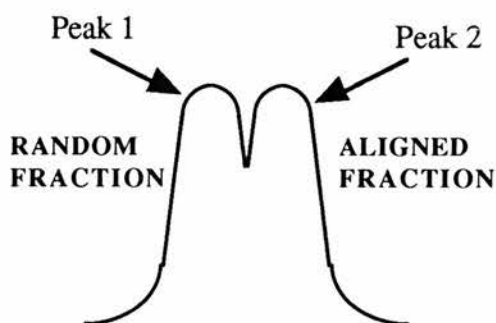


Figure 6.4. Labelling of the double-peaked structure found by  $^{89}\text{Y}$  NMR when considering aligned and random fractions of sample.

The NMR spectrum of an ideal random powder can be found in Chapter 3, Figure 3.8. The maximum occurs for  $\theta=90^\circ$  to the applied magnetic field, with a shoulder in the spectra occurring for  $\theta=0^\circ$ . The position of this maximum peak due to the random portion should therefore correspond to the position of the peak for the aligned fraction when the *c*-axis is perpendicular to the applied field,  $B_0$ . A combination of both would produce a single line (corresponding to  $\theta=90^\circ$ ), with a broader base due to the  $\theta=0^\circ$  shoulder of the random portion.

An attempt has been made to model this merging of the two peaks as the orientation is varied. The peak seen on the left hand side of Figure 6.5 is due to the random portion of sample, which remains at the same frequency for all orientations. This was drawn as a Gaussian for simplicity, though to be more accurate it should have a lineshape similar to that shown in Figure 3.8. The peak shown on the right hand side is due to the aligned portion of sample. The magnetic shift of this peak is orientation dependent and is proportional to  $(3\cos^2\theta-1)$  as mentioned in Section 3.6.4.4. There is a good correlation between this model and the results obtained by experiment.

The room temperature study of the magnetic shifts as a function of calcium doping concentration (Figure 5.12, 5.13 and 5.14) revealed that peak 2 (assigned the aligned peak) did not vary, but that the magnetic shifts of peak 1 (due to the random fraction) showed a linear dependence on doping concentration. This behaviour does not agree with the model, though it can be explained if doping with calcium only affects the magnetic shifts when the crystal *c*-axis is perpendicular to the applied magnetic

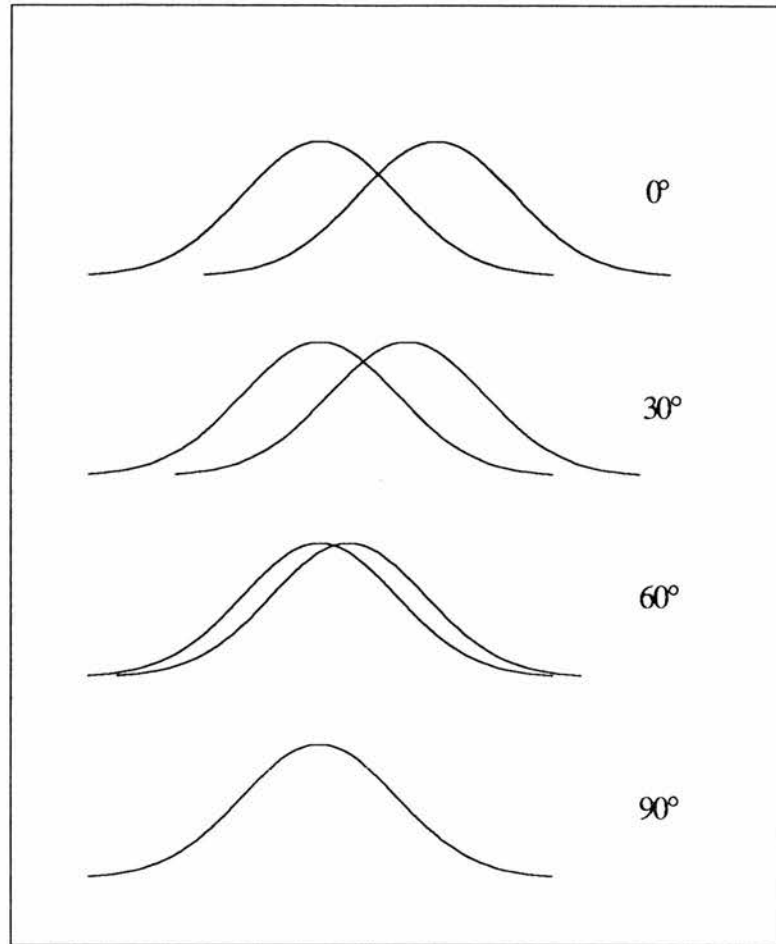


Figure 6.5. Model of the spectra expected at different orientations, if a peak due to a random sample (left-hand side) and an aligned sample (right-hand side) are superimposed. The angle is that of the aligned crystal c-axis to the applied magnetic field  $B_0$ .

field, and so the increase in calcium doping causes the shift to vary for the random sample spectrum (due to the perpendicular component), but leaves the aligned spectrum unchanged.

#### 6.6.1.2. Inequivalent Yttrium Sites Due to the Presence of Calcium

The presence of homogeneously distributed calcium in the material may produce different local environments, for example the spin susceptibility experienced by an yttrium atom surrounded only by other yttriums may not be the same as that of an yttrium with one or more calcium neighbours. These differences could give rise to peaks at two different shifts in the spectra, as will be demonstrated. This possibility is supported by two additional observations. Firstly, only a single peak is observed for

the parent compound which contains no calcium. Secondly, the positions of the two peaks are very similar, indicating only small changes in the two different local environments is observed, as would be expected.

Several models were attempted in order to explain the experimental data. Each of the models were based on the effects (produced at an yttrium site) of having yttrium atoms or calcium atoms in the neighbouring sites.

The basis of the first model is shown in Figure 6.6. The central site was considered as being an yttrium, since it is the yttrium nucleus that is being observed in this work. Initially the nearest-neighbour sites were assumed to be all yttriums (as would be the case for the parent compound). The changes in the local environment of the central yttrium was then calculated (on an arbitrary scale) if one of the nearest neighbours was a calcium, along with the probability of this occurring. This was repeated for two nearest neighbour calciums, then three calciums and so on.

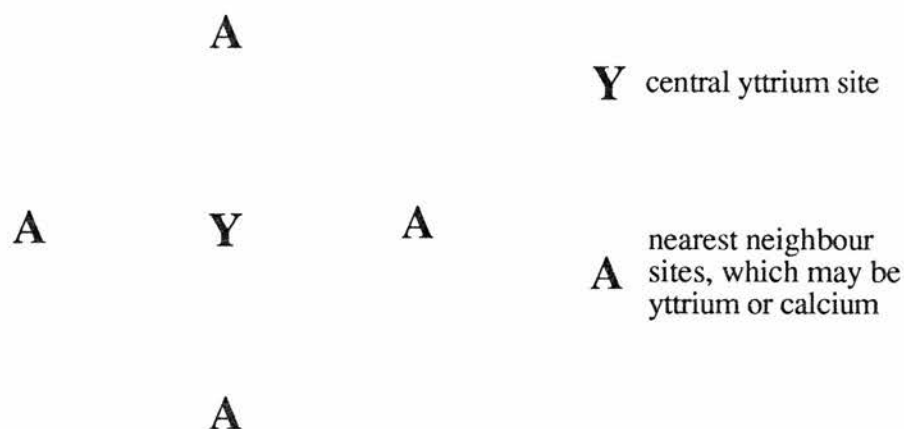


Figure 6.6. First model used for calculation, showing a central yttrium nucleus and the relative positions of the four nearest neighbour sites.

The second model was an improvement of the first in that the next-nearest neighbours were also taken into account, as shown in Figure 6.7. A calcium atom is equally likely to be at a nearest-neighbour site or a next-nearest-neighbour site, however the effect of the calcium on the central yttrium is not the same in each case.

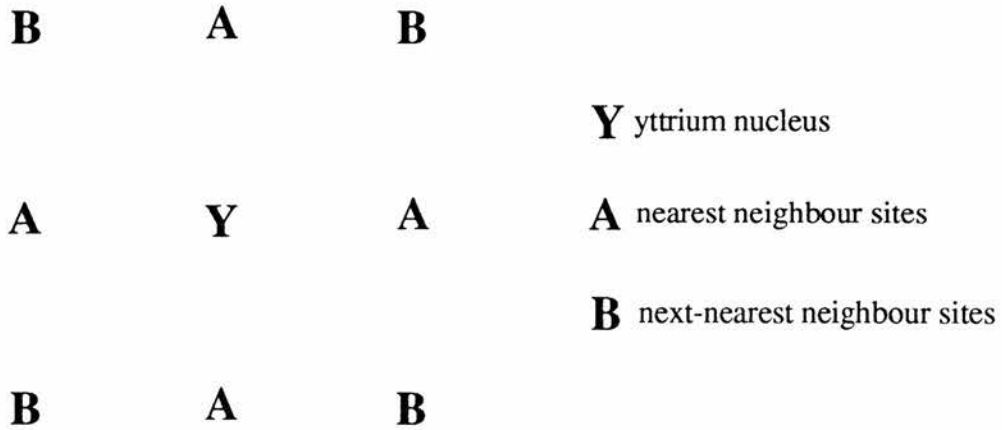


Figure 6.7. Second model used for calculation, showing an yttrium nucleus surrounded by four nearest neighbour and four next-nearest neighbour yttrium/calcium sites.

For this model the effect has been assumed to be inversely proportional to the distance from the central yttrium. If the distance between Y and A (on the diagram) is 1, then the distance between Y and B is  $\sqrt{2}$ . Therefore the changes in the local environment caused by a next-nearest-neighbour (B) is less (by a factor  $1/\sqrt{2}$ ) than that caused by a nearest-neighbour (A).

The third and most successful model<sup>9</sup> involved further modifications to this idea. Again, both nearest and next-nearest neighbours were taken into account. This time however, the nuclei were considered to interact via the Cu(2) plane copper atoms in the lattice. This may be explained more technically as the modification of the spin susceptibility of Cu(2) sites next to a Y/Ca site. The neighbouring yttriums or calciums then experience this modification via the same coppers. The basis of this model is shown in Figure 6.8.

The central yttrium will experience a modification of the spin susceptibility via two of the copper sites for a nearest neighbour calcium (A), but only via one copper site for a next-nearest neighbour calcium (B). The probability of having all combinations of yttrium and calcium neighbours were calculated (using the percentage of calcium doping concentration, and the binomial coefficients to take into account the 8 possible sites and so on). The magnitude of the spin susceptibility modification was calculated on an arbitrary scale for each of these combinations. It is important to note that in some

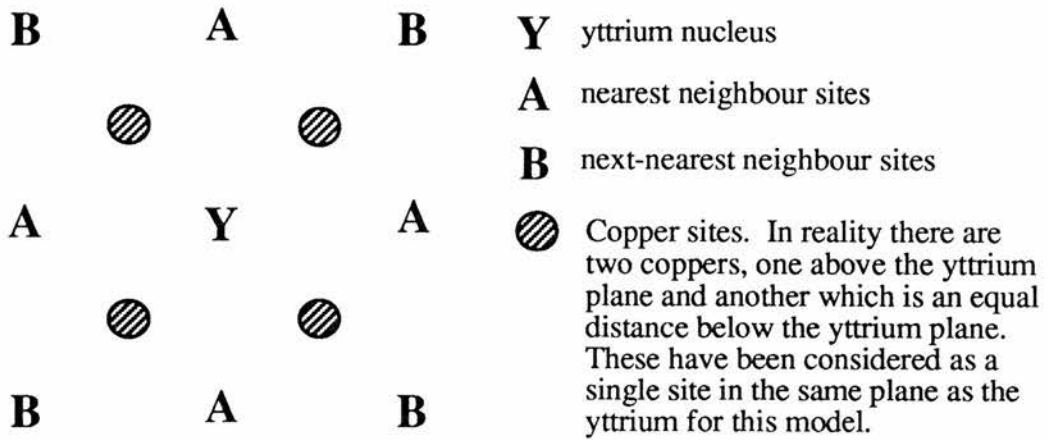


Figure 6.8. Third model used for calculation, showing an yttrium nucleus in the centre of four copper sites and the relative positions of the nearest neighbour and next-nearest neighbour yttrium/calcium sites.

cases two or more different combinations lead to the same magnitude of spin susceptibility modification, eg. two next-nearest neighbours have the equivalent effect as one nearest-neighbour. When this occurs the probabilities of each of the contributing combinations are added. The results of this model are shown in Figure 6.9 for the 10%, 12%, 14%, 16%, 18%, 20% and 25% calcium doping.

Although the model is a very simple one, the results are remarkably similar to those observed experimentally. Using this model the  $x=0.00$  sample would give rise to a single peak since there is only yttrium present. As calcium is introduced, two major peaks would be observed in the spectra, one due to a central yttrium surrounded solely by yttrium neighbours (seen on the right at 23 arb.units) and the other due to nearest and next-nearest neighbour calciums (seen on the left at 22 arb.units). The probabilities of having more than two calciums as nearest and next-nearest neighbours become negligible and can be seen at the lower end of the scale. At  $x=0.25$  a single peak would again be observed. It is also interesting to note that the overall linewidths for all doped samples are expected to be approximately equivalent, which is supported by experiment.

This basic model does not account for the observed shift of the higher frequency peak towards the static one as the calcium concentration increases (see Figure

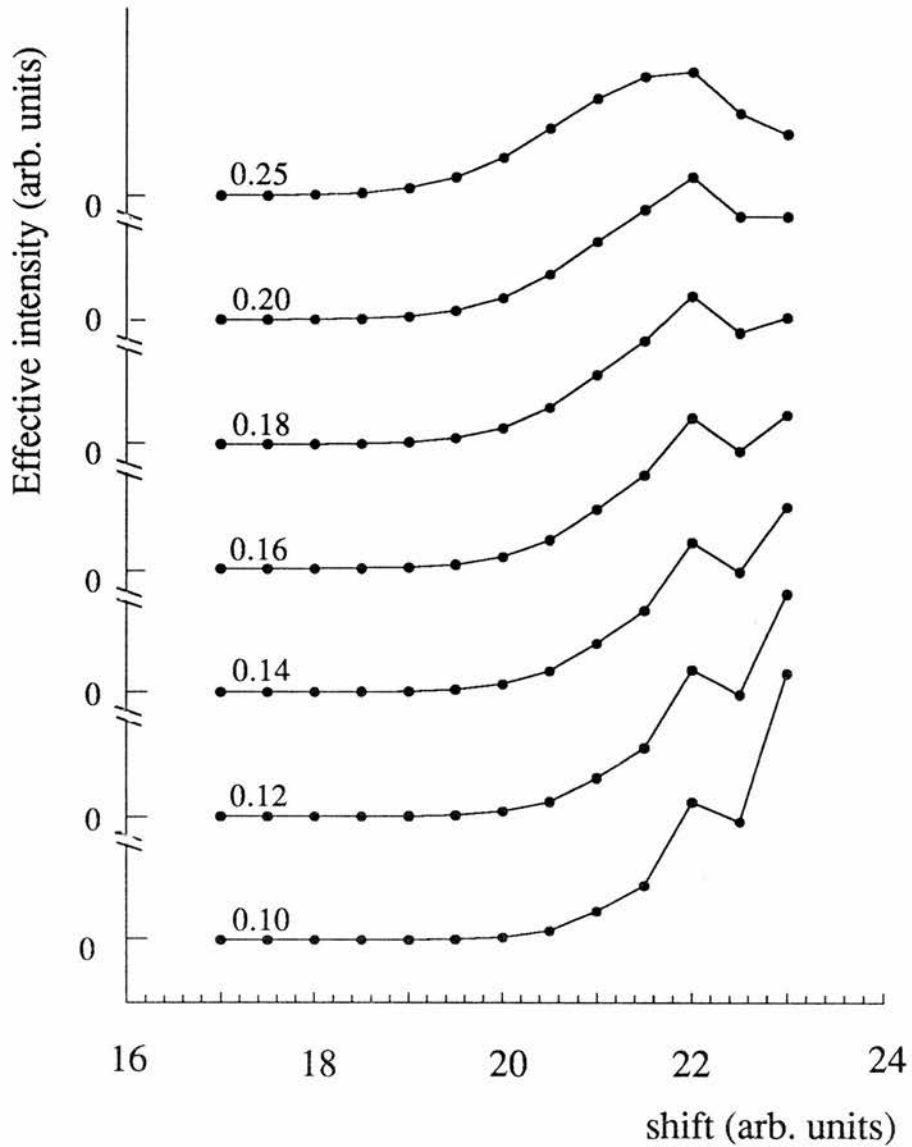


Figure 6.9. Nearest and next-nearest neighbour model via interactions with the plane coppers.

5.14). It may be possible that the spin susceptibility experienced by a central yttrium surrounded only by neighbouring yttriums may experience the same internal magnetic fields throughout the doping study, which would account for the static peak (peak 2 in the experimental data). The other peak should therefore be due to an yttrium with both calcium and yttrium neighbours. This labelling of the experimental peaks is shown in Figure 6.10 for clarity. Although the above model also shows this peak to be static, it is very likely that slight deviations from the model could cause the line to shift

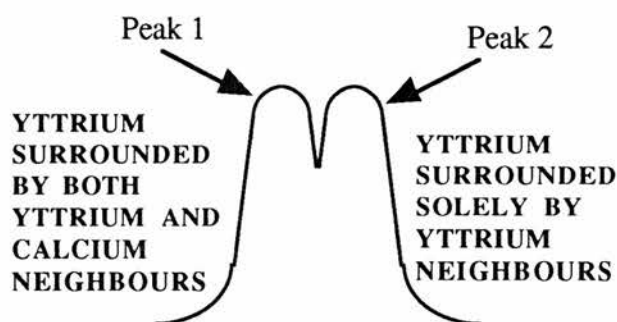


Figure 6.10. Labelling of the double-peaked structure found by  $^{89}\text{Y}$  NMR for the model of inequivalent yttrium sites due to the presence of calcium.

(especially a linear shift with hole doping), since the local environment of the yttrium is changing.

The orientation dependence of the peaks must now be considered for this model. In the experimental data, peak 2 either disappeared or merged with peak 1 when the angle of the sample was turned beyond  $45^\circ$ . Peak 1 exists for all orientations. The NMR spectrum of an aligned sample has an orientation dependence proportional to  $(3\cos^2\theta - 1)$  as mentioned in the previous section. For this model, both of the peaks are due to aligned portions of sample and so both are expected to be orientation dependent. For the samples with the *c*-axis perpendicular to the magnetic field, these two peaks could be in the same position, or merged so that they are not distinguishable. It is proposed that the magnitude of the orientation dependent shifts are different for the two peaks, as demonstrated in Figure 6.11, causing a separation of the peaks as the sample moves towards the parallel position to the magnetic field. The scale on the x-axis is arbitrary, since only the relative positions of the peaks are important. This model fits the experimental data well and shows significant separation of the peaks beyond  $45^\circ$ .

### 6.6.1.3. Comparison of the Two Models

The model explaining the data in terms of aligned and random fractions of sample gave very similar results to those obtained by experiment for the orientation study. In order to produce  $^{89}\text{Y}$  NMR peaks of equivalent intensity for aligned and random fractions of sample, then  $\sim 50\%$  alignment would be required. The x-ray

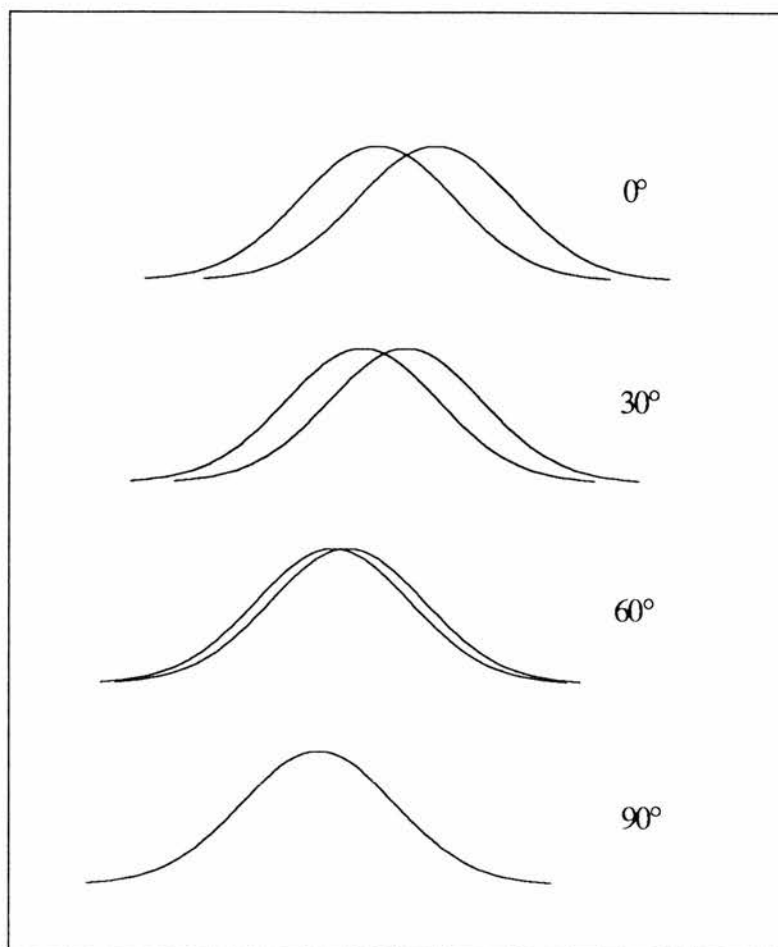


Figure 6.11. Model of the spectra expected at different orientations, if the two peaks in the spectra demonstrate different magnitudes of orientation dependence. The angle is that of the aligned crystal  $c$ -axis to the applied magnetic field  $B_0$ .

spectra of the aligned samples indicated an average alignment of 89%, the minimum being 85% for the  $x=0.25$  and  $x=0.12$  samples. All calculations of alignment are only approximations, and x-ray diffraction is a surface technique which as a consequence, can underestimate the quantity of misalignment. However, after carefully studying the x-ray spectra of the first samples aligned (unsuccessfully) for this work, and the x-ray spectra for the samples obtained by Dai<sup>10</sup>, I have come to the conclusion that the samples are well aligned, and that the figures obtained by calculation are reasonable. Since the aligned proportion is nearer 90%, the peak due to the random fraction should be much less intense.

The model of the data in terms of inequivalent yttrium sites in the lattice due to the presence of yttrium and calcium neighbours, appears to explain many of the experimental results. The spectra obtained for all doping concentrations at room temperature are explained by the model, showing the merging of the peaks as the doping concentration increases, the obvious absence of a second peak for the  $x=0.00$  and explains why the  $x=0.25$  sample would be a single line. In addition, it shows that the linewidths for all doping concentrations should be approximately equivalent. The orientation dependent spectra may be explained in terms of different magnitudes of the magnetic shifts for the two peaks, demonstrating convergence as the angle to the magnetic field increases. Against this model, an orientation study of the parent compound  $\text{YBa}_2\text{Cu}_3\text{O}_7$  was carried out by Webster<sup>11</sup>, and a double-peaked structure was again observed for the sample position with the *c*-axis parallel to the magnetic field. The second peak in this case could not be due to a dopant, unless it was caused by the oxygen present in the O(1) sites, forming chains in the *b* direction.

### 6.6.2. Temperature Dependence of the Samples

The metallic/superconducting samples  $x=0.25$  and  $0.20$  were studied as a function of temperature, from room temperature down to  $\sim 140\text{K}$ . The spectra may be found in Figures 5.16 and 5.17, and the linewidths and magnetic shifts are plotted in Figures 5.18 and 5.19 respectively. Unfortunately for these two samples, the two peaks in the spectra are hardly distinguishable. It was therefore not possible to study the temperature dependence of the individual peaks.

The quantity of hole doping to the conduction planes in the parent compound  $\text{YBa}_2\text{Cu}_3\text{O}_x$  has been studied by Alloul et al.<sup>12</sup>. They found a temperature dependence of the magnetic shifts due to hole doping, such that smaller shift occurred at lower temperature.

Before continuing, it is important to note that the magnetic shifts in Alloul's work were taken with respect to the true origin of the  $^{89}\text{Y}$  nucleus, which was found by Alloul et al.<sup>12</sup> and Balakrishnan et al.<sup>13</sup> to be at approximately  $+200\text{ppm}$  relative to a

solution of  $\text{YCl}_3$ . Bearing this in mind, the magnetic shifts shown in Figure 5.19 are less at lower temperature, in agreement with Alloul's work. In addition, the magnetic shifts observed in this work are dependent upon calcium doping concentration, such that increasing doping concentration gives rise to a greater magnetic shift. This is compared to a similar study carried out by Dai<sup>10</sup> and Webster<sup>11</sup>. Dai's spectra were double peaked, and this had been explained by random and aligned fractions of sample. When taken to lower temperature, his peak due the aligned portion of sample had a magnetic shift which was strongly temperature and concentration dependent, whereas the peak due to the random fraction remained unchanged. Webster's results were similar to those observed here and demonstrated a shift of  $\sim 30$ ppm over the temperature range for both peaks. This supports the idea that neither of the peaks observed in these spectra (or Webster's spectra) are due to misalignment.

### 6.6.3. Spin-Lattice Relaxation of the Samples

The spin-lattice relaxation times,  $T_1$ , for all samples at room temperature are given in Table 5.12.  $T_1$  increases from 26 seconds to  $\sim 50$  seconds as the sample goes from the metallic/superconducting state to the insulating intermediate state. This is expected, since in metals the conduction electrons provide an extremely strong relaxation mechanism. The  $x=0.25$  and  $x=0.20$  samples can be classified only as poor metals, which would explain why the spin-lattice relaxation times are not greatly different to the intermediate samples.

$T_1$  decreases quite substantially to 10 seconds for the undoped  $x=0.00$  sample. This material is an antiferromagnetic insulator, as discussed previously, and it is likely that this magnetic order in the lattice aids the relaxation process.

For the more metallic samples, a temperature dependence study was carried out. Both  $T_1$  and the magnetic shifts were measured, and may be found in Figures 5.21 and 5.19 respectively. Figure 6.12 shows the magnetic shift plotted against  $(T_1 T)^{-0.5}$  to look for a Korringa-type temperature dependence. The magnetic shift for our work has been measured with respect to that of an aqueous solution of  $\text{YCl}_3$ . It can be separated

into two contributions, the chemical shift ( $^{89}\sigma$ ) and the spin contribution ( $^{89}K_S$ ). Alloul<sup>12</sup> demonstrated that the chemical shift in YBCO is temperature independent, so that the temperature dependency of  $\Delta K$  is solely due to the spin contribution.  $^{89}\sigma$  was measured to be  $\sim +200$ ppm and so in order to achieve a meaningful gradient,  $-\Delta K$  is plotted.

Figure 6.12 could show a linear relationship but the errors are large, casting doubt on a definite Korringa temperature dependence ( $K^2T_1T=\text{constant}$ ). Other high-temperature superconductors have been found to exhibit a  $KT_1T=\text{constant}$  temperature dependence. A linear relationship for  $-\Delta K$  plotted against  $(T_1T)^{-1}$  would confirm this. Figure 6.13 shows this relationship, but again the errors are large and so no conclusions can be reached.

## 6.7. Copper NMR

Copper is an interesting nucleus to observe since it plays a vital role in the superconductivity of all the high-temperature cuprate superconductors discovered so far. The copper nucleus has spin  $I=3/2$  and consequently a quadrupole moment. There are two naturally occurring stable isotopes of copper,  $^{63}\text{Cu}$  which is 69.2% abundant and  $^{65}\text{Cu}$  which is 30.8% abundant. Only the resonance of the  $^{63}\text{Cu}$  nucleus has been observed here, which may be found near 133MHz for  $B_0=11.74\text{T}$ . The resonance of the  $^{65}\text{Cu}$  nucleus occurs around 142MHz and so does not complicate the spectra observed in this work.

As mentioned previously in Section 2.2.1, two inequivalent copper sites exist in the YBCO structure. These are the Cu(1) sites sandwiched between two barium planes and the Cu(2) sites between an yttrium plane and a barium plane. The Cu(2) sites form a parallel set of conduction planes that can support superconductivity. In YBCO one-third of the coppers are on the Cu(1) sites and two-thirds on the Cu(2) sites.

An orientation study of the aligned  $x=0.25$  sample was carried out at room temperature. The results can be found in Figure 5.22. The NMR signal observed was

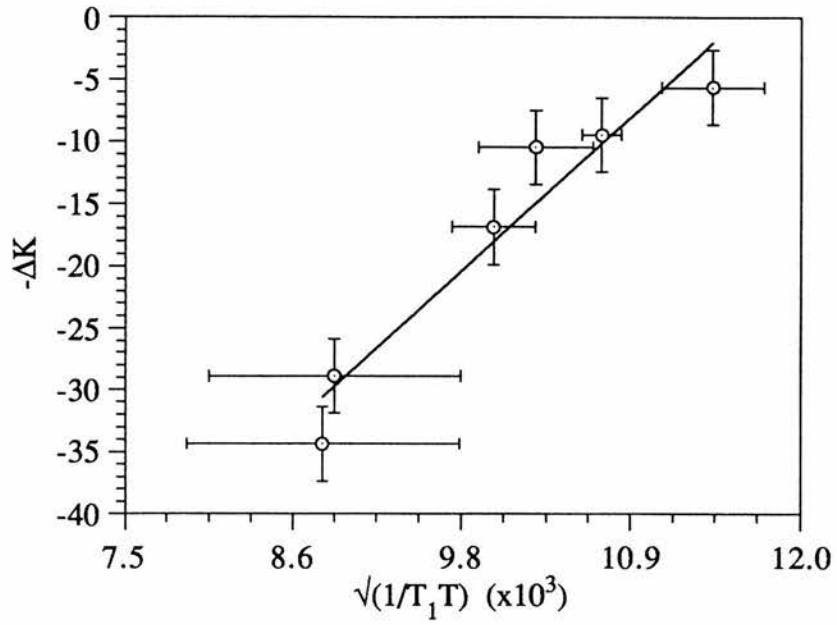


Figure 6.12.  $-\Delta K$  is plotted against  $(T_1 T)^{-0.5}$  to identify a possible Korringa temperature dependence ( $K^2 T_1 T = \text{constant}$ ) for the  $x=0.25$  sample.

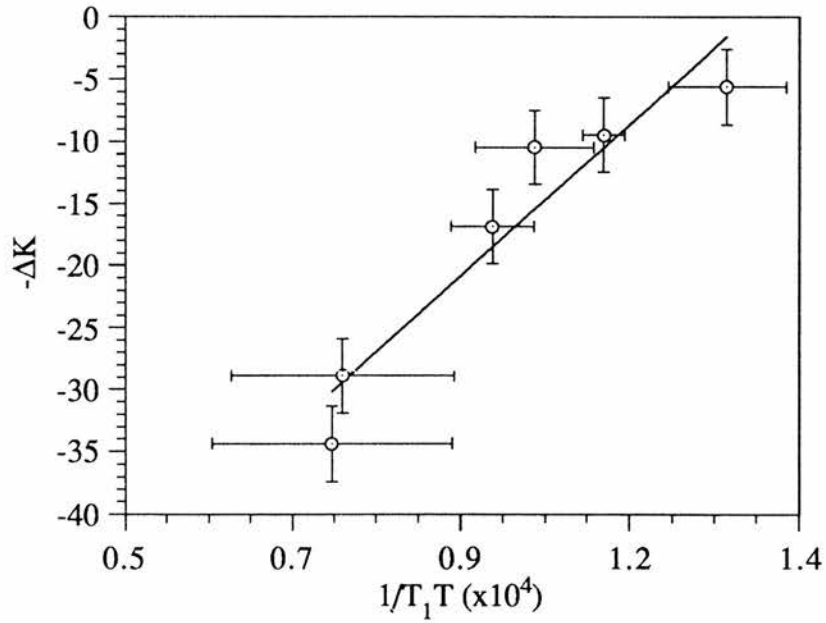


Figure 6.13.  $-\Delta K$  is plotted against  $(T_1 T)^{-1}$  in search of a  $KT_1 T = \text{constant}$  temperature dependence for the  $x=0.25$  sample.

considerably weak and broad, extending from 132.0MHz to 134.5MHz. The spectra consist of two peaks (at 132.3 MHz and 134.1MHz) connected by a plateau. The peak seen at 132.3MHz decreases in intensity as the sample orientation moves away from the parallel position (relative to  $B_0$ ). A large, narrow peak is seen at 134.1MHz for the perpendicular orientation, which diminishes rapidly as the sample is rotated leaving a residual broad signal.

$^{63}\text{Cu}$  NQR (nuclear quadrupole resonance) has been studied by Vega et al. for the  $(\text{Y}_{1-x}\text{Ca}_x)\text{Ba}_2\text{Cu}_3\text{O}_6$  material<sup>14,15</sup>. This work distinguished the two copper sites for samples with  $x \geq 0.10$  (below this value the samples were antiferromagnetic, causing extremely large shifts that are difficult to find). The Cu(2) signal was found to be very broad with no distinguishing features, and the spin-lattice relaxation time  $T_1$  was short (less than 1ms). In contrast, the Cu(1) signal exhibited a large narrow peak with a longer  $T_1$ . This longer spin-lattice relaxation time was an indication that the Cu(1) sites did not contribute to the conduction process, but instead the holes introduced by calcium doping were added to the  $\text{CuO}_2$  planes inducing a breakdown in the antiferromagnetic ordering.

By comparison of our results to those reported by Vega et al. the major peak seen at 134.1MHz was assigned to the Cu(1) sites, and the broad background signal to the Cu(2) sites. The expected orientation dependence of these features is discussed below, along with the various ideas that have been considered to explain the deviations from this behaviour.

The behaviour of the Cu(1) peak may possibly be explained if the principal axis of the quadrupole coupling for Cu(1) sites is parallel to the crystal  $c$ -axis in  $\text{YBa}_2\text{Cu}_3\text{O}_6$  and is axially symmetric. This is in contrast to the principal axis for Cu(1) in the  $\text{YBa}_2\text{Cu}_3\text{O}_7$  material, but is reasonable since the crystal has tetragonal structure with equally (though sparsely) occupied O(1) and O(5) sites. The magnitude of the quadrupole shift is proportional to  $(1-\cos^2\theta)(9\cos^2\theta-1)$  which can be calculated from the second order quadrupole expression shown Section 3.6.4.5, for  $I=3/2$  and  $m=1/2$ . Consequently, when the sample is placed parallel to  $B_0$  a single line would be expected

with no quadrupole shift ( $\theta=0^\circ$ ). For the case when the sample is perpendicular to  $B_0$  a single line would again be expected, but with a strong quadrupole shift ( $\theta=90^\circ$ ). For the experimental data, no line is observed for the parallel position. Deviations from this ideal behaviour have been considered below.

The first idea considered the effects of having aligned and random fractions of sample. The sample used for this study was calculated by x-ray diffraction to have an 85% portion of aligned sample, the remaining 15% being random. The resulting lineshape would be an addition of the aligned spectrum and the random powder spectrum. The spectra expected for the aligned sample for  $\theta=0^\circ$  and  $90^\circ$  were described above and gave rise to narrow peaks for both orientations, but with different shifts. In order to determine the contribution due to the random powder pattern,  $^{63}\text{Cu}$  NMR was carried out on a completely random portion of  $x=0.25$  sample set in epoxy. The random powder spectrum can be found in Figure 5.23. The resulting line was broad, extending between 132MHz and 134.5MHz. The addition of the two contributions should therefore give rise to a narrow peak added to a broad line for each orientation. The narrow line expected for the parallel orientation is not observed experimentally.

The second consideration, was if the particles were not all aligned parallel to the assigned  $c$ -axis, but deviated within an angle  $\phi$ . The principal axis of the quadrupole coupling would therefore also vary by an angle  $\phi$ . If the sample was then placed in the magnetic field  $B_0$ , this variation in  $\phi$  would cause a variation in the quadrupole shifts resulting in a broadening of the Cu(1) line. Figure 6.14 shows a plot of  $(1-\cos^2\theta)(9\cos^2\theta-1)$  and demonstrates the variation in the quadrupole shift caused by deviation in the angle  $\phi$ . An angle of  $\phi=15^\circ$  was used as a demonstration. Broadening would be expected for both the parallel and perpendicular orientations of the sample. The curvature at these points causes a slightly larger broadening effect for  $\theta=90^\circ$  than for  $\theta=0^\circ$  (for  $\phi=15^\circ$   $Q=0\pm 0.496$  and for  $\phi=90^\circ$   $Q=-1\pm 0.63$ , where  $Q$  is the quadrupole shift). This idea therefore explains a greater broadening effect for the parallel orientation than for the perpendicular orientation, but seems to underestimate the

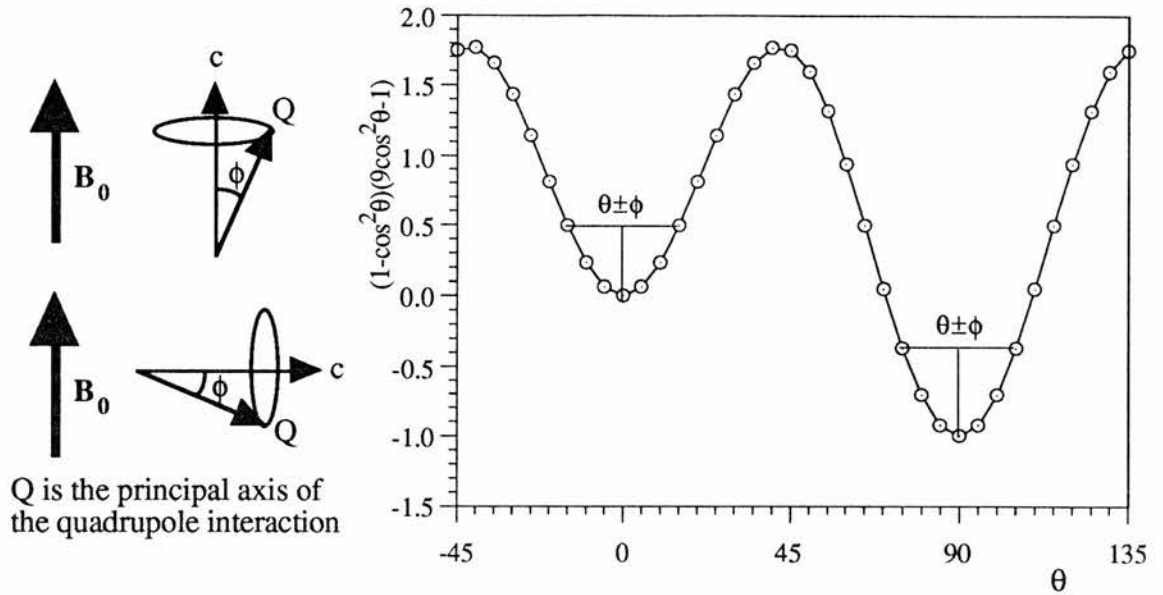


Figure 6.14. Diagram to show possible line broadening effects caused by slight variations in the direction of the  $c$ -axis, that cause variations of angle  $\phi$  for the quadrupole interaction.

magnitude of the broadening for the parallel position when compared to the experimental data.

The next consideration is a simple variation in the magnitude of the  $c$ -parameter in the unit cell, as has been suggested by HREM experiments<sup>2</sup> and SAED experiments<sup>5</sup>. The magnitude of the  $c$ -parameter determines the magnitude of the quadrupole interaction. For the case where the sample  $c$ -axis is parallel to  $B_0$ , no quadrupole shift results ( $\theta=0^\circ$ ) and so a single sharp line should be observed. When the sample is perpendicular to the  $c$ -axis, there would be a large quadrupole shift ( $\theta=90^\circ$ ) but with various magnitudes, resulting in a broader line for this position. This is demonstrated in Figure 6.15. So in summary, a narrow line would be expected for the parallel orientation and a broadened line for the perpendicular orientation. This does not explain the experimental data.

The final consideration takes the above situation one step further. If the length of the  $c$ -axis varies locally within the lattice, for example near the calcium sites (caused by the slightly larger calcium replacing the yttrium) then the adjoining unit cells must



Figure 6.15. Variations in the magnitude of the quadrupole interaction caused by differences in the length of the  $c$ -axis. In the parallel orientation this has no effect on the line, but in the perpendicular position, the magnitude of the quadrupole shift varies, causing line broadening.  $B_0$  is the direction of the magnetic field, and  $Q$  is the principal axis of the quadrupole interaction.

compensate by a canting of the  $a$ - $b$  plane (see Figure 6.16). Even though the direction of the  $c$ -axis remains unchanged, this canting effect may vary the direction of the principal axis of the quadrupole interaction. In addition, the magnitude of the  $c$ -parameter is varying as described above. When the sample  $c$ -axis is placed parallel to  $B_0$ , a sharp line would occur due to the variation in the magnitude of  $c$  (as above), in addition to a broadening effect caused by the variation in direction of the principal axis of the quadrupole interaction (similar to second consideration described above). For the sample in the perpendicular position, broadening occurs due to a variation in magnitude of the quadrupole shift, in addition to the further broadening effect caused by a variation in the angle of the principal axis of the quadrupole interaction. This would result in the destruction of the line for the sample in the perpendicular position, as well as broadening for the parallel orientation. Again, this does not correspond to the experimental data obtained.

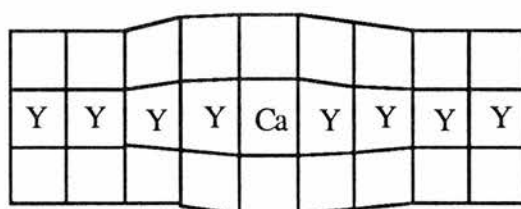


Figure 6.16. Schematic diagram to show how the copper planes may have to cant to compensate for a longer  $c$ -parameter caused by the substitution of yttrium with a slightly larger calcium atom. This would become more disordered as the concentration of dopant increases.

It is interesting to note that the lineshape of the random powder spectrum seen in Figure 5.23 fits the theoretical description for a nucleus with quadrupole effects and asymmetry parameter  $\eta=0$  (see Section 3.6.4.5, Figure 3.11). By comparison of the ideal lineshape and that obtained experimentally, the larger peak at 132.3MHz corresponds to the case where  $\cos\theta=\sqrt{(5/9)}$  ( $\theta=41.8^\circ$ ) and the smaller peak at 133.9MHz corresponds to that of  $\cos\theta=0$  ( $\theta=90^\circ$ ). This position of the smaller peak for the quadrupole shift for  $\theta=90^\circ$  is the precise position of the narrow line observed for the aligned spectra, indicating that the peak assignments have been made correctly. A line with no quadrupole shift would occur at  $\cos\theta=1$  ( $\theta=0^\circ$ ) and the position at which this would be expected can be calculated using the scale of the random powder spectrum obtained. The position of the narrow line expected for the sample in the parallel position should be near 133.3MHz. There was no evidence for a line at this position, unless it had been broadened to the extent that it could not be distinguished from the Cu(2) broad line (and random fraction contribution). These results lead to many possibilities for further work in this area.

So of the above suggestions, only one gave rise to a broadening of the Cu(1) peak in the parallel orientation and that was for a variation in angle of the principal axis of the quadrupole interaction about the assigned *c*-axis. This idea also caused a broadening of the line for the perpendicular orientation, but to a lesser extent. None of the explanations give rise to both the narrow line for the perpendicular orientation and the broad line for the parallel orientation.

To confirm these results, a more thorough study of the material needs to be carried out using  $^{63}\text{Cu}$  NMR. An accurate measurement of the spin-lattice relaxation time for both Cu(1) and Cu(2) sites would optimise the pulse parameters used for the experiment and could result in enhanced lineshapes. The location of the Cu(1) line for the parallel orientation could then be determined, by comparing the areas of the spectra for the different orientations. An orientation study over the whole range of doping concentrations could confirm whether the magnitude of the broadening of the line for

the perpendicular position is doping concentration dependent, supporting the work by Vega et al.<sup>14,15</sup>

As a final note, the  $^{63}\text{Cu}$  NMR study by Webster<sup>11</sup> on the  $\text{YBa}_2(\text{Cu}_{1-x}\text{Co}_x)_3\text{O}_7$  system at 1.5K demonstrated a destruction of the copper lines (both Cu(1) and Cu(2)) for the parallel orientation as the cobalt concentration increased from 0.0% to 4.0%. In the perpendicular position, the lineshape remained unchanged. The broadened copper line for the parallel orientation may be an inherent property of doped cuprate superconductors, but as yet there is no explanation why.

## References

- 1 E.M.McCarron, M.K.Crawford and J.B.Parise. *J. Solid State Chem.*, **78** (1989) 192.
- 2 J.B.Parise. P.L.Gai, M.K.Crawford and E.M.McCarron. *Mat. Res. Soc. Proc. High  $T_c$  Supercond.*, San Diego, **Proc. 156** (1989) 105. (Edited by J.Jorgensen et al.).
- 3 F.A.Kröger. "*The Chemistry of Imperfect Crystals*", North Holland, Amsterdam (1964).
- 4 M.R.Chandrachood, I.S.Mulla and A.P.B.Sinha. *Solid State Comm.*, **68** (1988) 5967.
- 5 R.S.Liu, J.R.Cooper, J.W.Loram, W.Zhou, W.Lo, P.P.Edwards, W.Y.Liang and L.S.Chen. *Solid State Commun.*, **76** (1990) 679.
- 6 A.M.Campbell, F.J.Blunt, J.D.Johnson and P.A.Freeman. *Cryogenics*, **31** (1991) 732.
- 7 B.I.Shklovskii and A.L.Efros. "*Electronic Properties of Doped Semiconductors*", Springer-Verlag (1984).
- 8 A.Manthiram, S.-J.Lee and J.B.Goodenough. *J. Solid State Chem.*, **73** (1988) 278.
- 9 H.F.Booth, D.P.Tunstall and J.T.S.Irvine. *Physica C*, **235-240** (1994) 1585.
- 10 G.Dai. *PhD Thesis*, University of St.Andrews (1994).
- 11 W.J.Webster. *PhD Thesis*, University of St.Andrews (1993).
- 12 H.Alloul, T.Ohno and P.Mendels. *Phys. Rev. Lett.*, **63** (1989) 1700.
- 13 G.Balakrishnan, R.Dupree, I.Farnan, D.McPaul and W.E.Smith. *J. Phys. C: Solid State Phys.*, **21** (1988) L848.
- 14 A.J.Vega, M.K.Crawford, E.M.McCarron and W.E.Farneth. *Physica C*, **162-164** (1989) 165.

- <sup>15</sup> A.J.Vega, M.K.Crawford, E.M.McCarron and W.E.Farneth. *Phys. Rev. B*, **40** (1989) 8878.

## Chapter 7

### CONCLUSIONS AND FURTHER WORK

In this work, samples of  $(Y_{1-x}Ca_x)Ba_2Cu_3O_{6.15}$  with  $0.00 \leq x \leq 0.25$  were synthesised. X-ray diffraction and electron microscopy were carried out to determine crystal structure, phase purity and homogeneity of the samples. The value of the reduced oxygen content was confirmed by thermogravimetric analysis and iodometric titration. Resistivity and susceptibility measurements mapped the phase diagram for the system, determining the antiferromagnetic phase, the superconducting phase and an intermediate insulating phase. Nuclear magnetic resonance measurements (NMR) were then taken for the samples, which had been uniaxially aligned in the *c*-direction. The magnetic shifts and spin-lattice relaxation times were studied by  $^{89}Y$  NMR as functions of both doping concentration and temperature. Magnetic shift data for the  $x=0.25$  sample was also obtained by NMR for the quadrupole nucleus  $^{63}Cu$ .

This system is interesting because it is an antiferromagnetic insulator for  $x=0.00$ , becomes a superconductor beyond  $x=0.25$  and has an intermediate insulating region. Superconductivity occurs in the absence of Cu-O chains confirming that the chain sites are not essential for superconductivity. This provides an interesting comparison of the doping mechanisms for calcium and oxygen.  $(Y_{1-x}Ca_x)Ba_2Cu_3O_{6.15}$  has many advantages over other high-temperature superconducting systems. It remains tetragonal throughout the solid solubility range, avoiding complications in the interpretation of results when the orthorhombic-tetragonal structural transition coincides with the superconducting transition. Calcium only substitutes onto the yttrium site in the lattice, unlike other dopants which may substitute for more than one site, which again simplifies the interpretation of results. Since calcium has a similar ionic radius to yttrium, minimal structural changes should occur

on substitution and so any changes in the properties of the material should only be due to the introduction of holes.

The careful synthesis and quenching procedure used here produced pure, single-phase materials as determined by x-ray diffraction and electron microscopy. The problems frequently encountered in high-temperature superconductivity due to impurity phases caused by incomplete reaction of the starting materials or by reaction with container walls were therefore avoided. The lattice parameters (as determined by x-ray diffraction) did not vary throughout the series and confirmed that the calcium had substituted onto the yttrium site. The synthesis mechanism for the samples was determined. For the reduced oxygen material, the oxygen content was found to remain the same as the calcium concentration increased, resulting in an increase in the quantity of holes in the conduction planes. This is in contrast to the behaviour for the  $(Y_{1-x}Ca_x)Ba_2Cu_3O_7$ , where the oxygen concentration was found to decrease through the series leaving the hole concentration unchanged.

All samples were required to have the same oxygen content, so that any change in the characteristics could only be due to the holes introduced by the calcium. Thermogravimetric analysis determined the value of  $\delta$  to be  $0.155 \pm 0.02$ . The  $x=0.20$  sample was found to be less, having  $\delta \approx 0.00$ . This could have been due to some sort of impurity. For this study it would have been ideal if all the O(1) oxygen had been removed, but in practice this is very difficult. Improvements on the quenching technique could reduce  $\delta$  further, for example by quenching the sample into liquid nitrogen in a closed oxygen-free system. Such a system could not be designed for our equipment, because the glassware would not have withstood the sudden increase in pressure caused by the sample falling into liquid nitrogen.

The oxygen content of the  $x=0.18$  sample was also determined by iodometric titration. The value obtained was  $\delta = 0.08 \pm 0.02$ , lower than that obtained by thermogravimetric analysis. This discrepancy can be explained by either an inert impurity or by loss of oxygen gas in the titration technique. The latter was thought to be the most likely, since the samples appeared pure when observed by x-ray diffraction

and electron microscopy. An attempt to measure the oxygen concentration by quantitative electron-probe microanalysis (EPMA) was made. This technique was abandoned since a suitable standard sample for calibration could not be found (copper oxide impurities were present) and the results obtained were not repeatable, even on the same part of the sample. Overall, the values obtained for  $\delta$  by thermogravimetric analysis seemed the most reliable and seemed reasonable when compared to values obtained by Liu et al.<sup>1</sup> and McCarron et al.<sup>2</sup> It would have been preferable to confirm the results by another technique, or simply to repeat the experiments more times to give greater insight into the spread of the values. The accurate measurement of the oxygen concentration in cuprate superconductors is a continuing problem.

AC susceptibility measurements revealed three of the samples to be superconductors, the  $x=0.18$ ,  $0.20$  and  $0.25$  samples with  $T_c=9.5\text{K}$ ,  $31\text{K}$  and  $38\text{K}$  respectively. The intensity of the signal increased with doping concentration, indicating either an increased volume fraction or a decrease in the penetration depth for the superconductor. Resistivity demonstrated 100% superconductivity and so a decrease in the penetration depth is the most likely explanation. Resistivity measurements confirmed superconductivity in these samples with  $T_c=13\text{K}$  for the  $x=0.18$  sample,  $T_c=32\text{K}$  for the  $x=0.20$  sample and  $T_c=49\text{K}$  for the  $x=0.25$  sample. The difference between these values and those obtained by susceptibility measurement is due to the broad transitions (taking place over  $\sim 15\text{K}$ ), making it difficult to define  $T_c$ . The maximum transition temperature occurred at the solid state limit for the  $x=0.25$  sample, in agreement with work by McCarron et al.<sup>2</sup> and Liu et al.<sup>1</sup>

Resistivity measurements determined the  $x=0.25$ ,  $0.20$  and  $0.18$  samples to be poor metals in the normal state, with a conductivity of  $\sigma \approx 300\Omega^{-1}\text{cm}^{-1}$ . Unexpected results were obtained for the  $x=0.18$  and  $0.16$  samples. The  $0.18$  sample showed a deviation in the resistivity measurement around  $25\text{K}$ , which can be attributed to a small fraction of superconducting material. The  $x=0.16$  sample appeared to show the onset of a superconducting transition at the limits of the available temperature range. This onset of a superconducting transition was not observed by AC susceptibility. Both of

these anomalies can be explained by variations in the oxygen content, implying that the oxygen determinations were not accurate enough for the purposes required here. The remaining samples appeared to be insulating and so the results obtained for the  $x=0.10$  sample was analysed in more detail. It demonstrated semiconducting behaviour at higher temperatures, transferring to possible variable range hopping with a Coulomb gap below 15K. Finally, the  $x=0.00$  sample was found to be an antiferromagnetic insulator, confirming results obtained by Alloul et al.<sup>3</sup> using  $^{89}\text{Y}$  NMR.

The samples used for NMR were powders mixed with epoxy, which were then aligned and set in a magnetic field, resulting in uniaxially aligned samples in the  $c$ -direction. The second alignment attempt was very successful, producing samples that were  $\sim 90\%$  aligned. This was due to the improved method of grinding the sample to a fine powder using a ball-mill in an atmosphere of argon rather than air, to prevent clustering. The problems encountered by other researchers<sup>4,5</sup> due to poorly aligned samples were therefore avoided.

The  $^{89}\text{Y}$  NMR spectra exhibited an interesting double-peaked structure, which was found to be doping concentration and orientation dependent. An attempt was made to elucidate the cause of the peaks, by comparing several models to the experimental data. No conclusion was reached, though two of the suggestions seemed equally likely. The first of these suggestions was that the two peaks were due to aligned and random portions of the sample, but this was contradicted by the  $\sim 90\%$  alignment calculated by comparison of the x-ray spectra. The model (which assumed 50% alignment) compared well with the experimental orientation dependence spectra, but did not account for the linear shift of one of the peaks with doping concentration. This can be explained if calcium doping only affects the magnetic shifts when the crystal  $c$ -axis is perpendicular to the applied magnetic field, but does not affect the parallel orientation. The second suggestion was that the presence of calcium in the material causes local changes within the Y/Ca plane, giving rise to inequivalent yttrium sites in the lattice. Several models were calculated, the most successful of which considered an yttrium atom, the neighbouring Cu(2) copper sites and the nearest and next-nearest

neighbour Y/Ca atoms. An yttrium atom was said to sense any modifications of the spin susceptibility of the eight (four above the yttrium plane and four below) neighbouring Cu(2) plane coppers caused by the presence of neighbouring calcium atoms. A two dimensional model was sufficient (in the yttrium plane), due to the anisotropy of the unit cell. This model compared well to the doping concentration dependent spectra, showing double peaks with similar overall linewidths for all the doped samples, merging to indistinguishable peaks at 25% doping concentration. This model would also give rise to a single peak for the 0% doped material, since no calcium is present. This second model implies that there may be a calcium/yttrium superstructure in the lattice. Further work could be carried out to ascertain this, for example by muon spectroscopy.

The  $^{89}\text{Y}$  NMR study confirmed the  $x=0.00$  sample to be an antiferromagnetic insulator, by an increase in the linewidth (as reported by Alloul et al.<sup>3</sup>) and a decrease in the spin-lattice relaxation time, which was an indication of increased magnetic order in the lattice. It would be interesting to measure the Néel temperature ( $T_N$ ) for this material, to confirm the value of 412K reported by Alloul. An improved method of finding  $T_N$  would be to measure the linewidth and spin-lattice relaxation time of the  $^{89}\text{Y}$  nucleus (both of these are measured by the same experiment) as a function of temperature, for the temperature range 300-450K. In this way  $T_N$  could be pin-pointed more accurately by the simultaneous increase in signal linewidth and the decrease of  $T_1$ .

The temperature dependence of the  $^{89}\text{Y}$  spectra demonstrated the shift of both peaks by  $\sim 30\text{ppm}$  over the temperature range 140-300K similar to results obtained by Webster for the cobalt doped  $\text{YBa}_2\text{Cu}_3\text{O}_7$  system<sup>6</sup>. Our results were not the same as those obtained by Dai<sup>4</sup> for a partially aligned sample, where one of the peaks was found to be temperature dependent and the other remained unchanged. This supports the argument that the double-peaks are due to some other mechanism than misalignment. Alloul found a temperature dependence of the magnetic shifts due to hole doping by oxygen, similar to those observed for calcium doping<sup>7</sup>. This suggests that the holes introduced by substitution of calcium mimic the hole doping effect of

oxygenation. Due to the size of the errors for the temperature and the spin-lattice relaxation time, it remains unclear whether a Korringa-type temperature dependence ( $K^2T_1T=\text{constant}$ ) exists for the superconductors in this material, or whether the relationship is nearer that of  $KT_1T=\text{constant}$ , as is more commonly observed for the ceramic superconductors.

Finally, an orientation dependence study was carried out for the  $x=0.25$  sample by  $^{63}\text{Cu}$  NMR. This experiment distinguished between the Cu(1) and Cu(2) sites. The Cu(2) sites contributed to a broad, weak line observed between 132.0MHz and 134.5MHz. The Cu(1) sites gave rise to more interesting features. A large, narrow line was observed for the sample orientated with the  $c$ -axis perpendicular to the magnetic field, but this rapidly disappeared away from this position. The other feature observed was a small line at 132.3MHz, which could either have been due to a diminished Cu(1) line for the parallel orientation, or the random fraction of the sample.

Several situations were considered to explain the observed data. The first was a sample with both random and aligned portions of sample. The second was if the particles were not all aligned parallel to the assigned  $c$ -axis, but deviated within an angle  $\phi$ . The third consideration was a variation in the length of the  $c$ -parameter in the unit cell, since disorder along the  $c$ -axis has previously been reported using HREM techniques<sup>8</sup>. The final possibility was if this variation in the  $c$ -parameter caused the copper planes to cant (both Cu(1) and Cu(2)), which would occur for example, if a unit-cell with a small  $c$ -parameter took the adjoining position to a unit-cell with large  $c$ -parameter. Of the above suggestions, only the ones that involved a variation in angle of the principal axis of the quadrupole interaction about the  $c$ -axis would account for the substantial broadening of the Cu(1) line in the parallel orientation. This would also be accompanied by a broadening of the line in the perpendicular position, but to a lesser extent. None of the suggestions accounted for both the broad line in the parallel orientation and the narrow line in the perpendicular orientation.

By comparing the NMR spectrum obtained for a random sample ( $x=0.25$ ) to the theoretical lineshape for a second order quadrupole interaction of a random powder, the

positions of the quadrupole shift for  $q=90^\circ$  and  $q=41.8^\circ$  were determined. Using these values as a calibration, the expected position of the line for  $q=0^\circ$  was calculated to be 133.3MHz. There was no evidence for the line at this position, unless it had been broadened to the extent where it could not be distinguished from the broad, low intensity Cu(2) line.

$^{63}\text{Cu}$  results obtained by Webster<sup>6</sup> for the  $\text{YBa}_2(\text{Cu}_{1-x}\text{Co}_x)_3\text{O}_7$  system at 1.5K also demonstrated a well defined line for the perpendicular orientation, but the destruction of the line for the parallel orientation. This may be a common feature of doped superconductors and should be studied further.

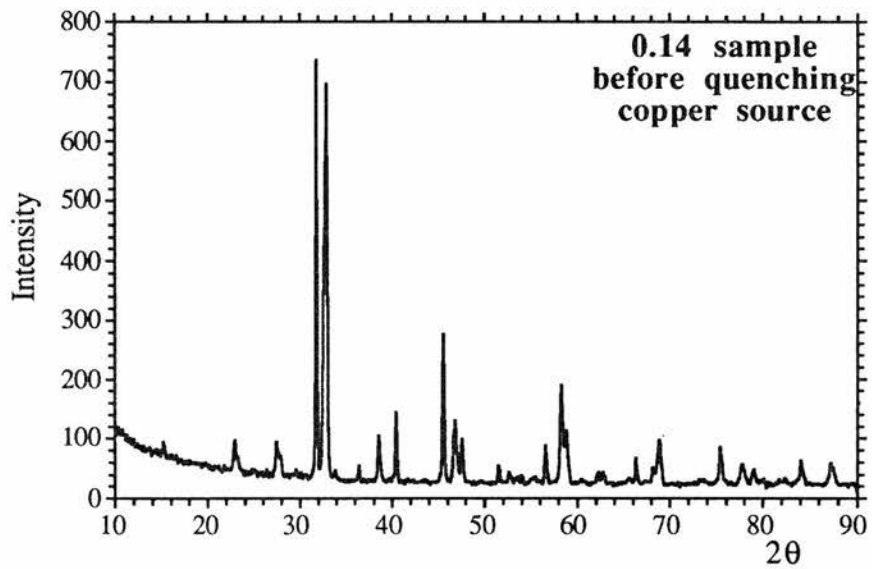
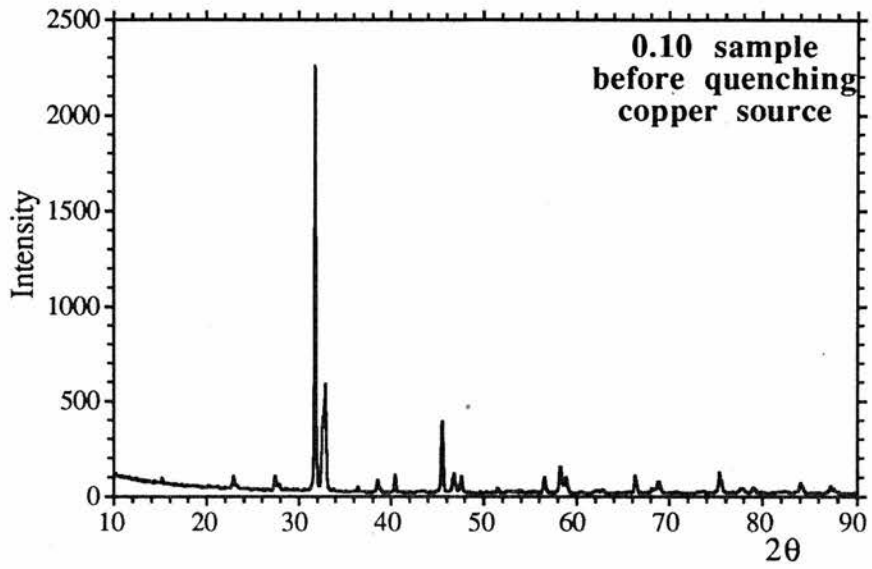
There are many possibilities for further study of this material by  $^{63}\text{Cu}$  NMR. An accurate measurement of the spin-lattice relaxation times for Cu(1) and Cu(2) would allow more suitable pulse parameters to be chosen, resulting in signal enhancement. If the spectra were improved, then it would be possible to determine the position of the line for the sample in the parallel orientation, by comparing the area of the spectra for different orientations. Finally, an orientation study over the whole range of samples could confirm whether the broadening of the line in the perpendicular position is doping concentration dependent, suggesting increasing disorder in the structure as more calcium is introduced. This would support work by Vega et al.<sup>9</sup> who obtained evidence for small variations in the local structure by  $^{63}\text{NQR}$  measurements. This was indicated by a gradual broadening of the Cu(1) peaks as calcium was introduced.

## References

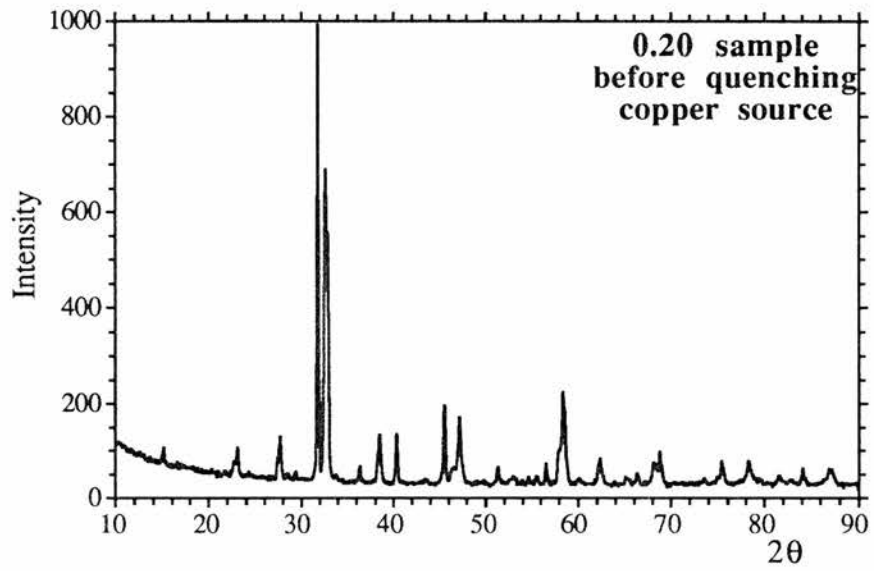
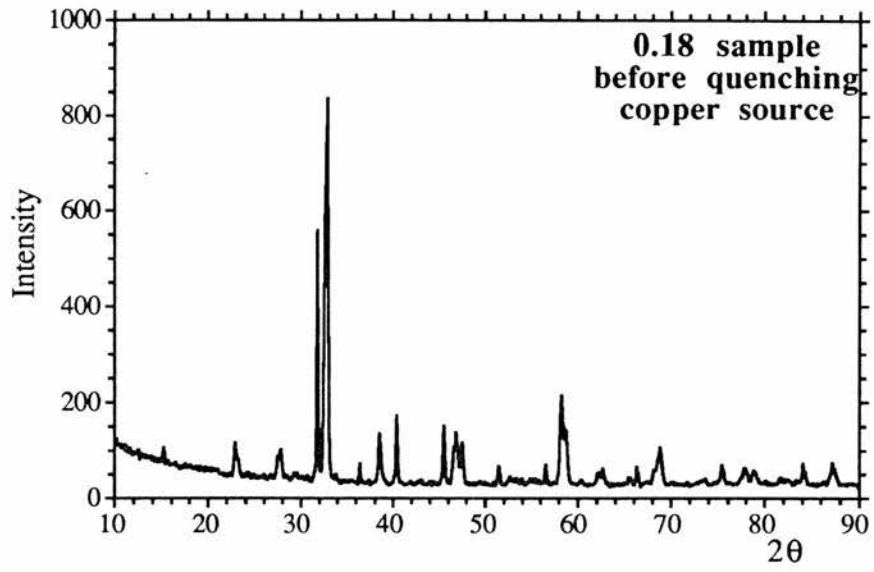
- 1 R.S.Liu, J.R.Cooper, J.W.Loram, W.Zhou, W.Lo, P.P.Edwards, W.Y.Liang and L.S.Chen. *Solid State Commun.*, **76** (1990) 679.
- 2 E.M.McCarron, M.K.Crawford and J.B.Parise. *J. Solid State Chem.*, **78** (1989) 192.
- 3 H.Alloul. *Physica B*, **169** (1991) 51.
- 4 G.Dai. *PhD Thesis*, University of St.Andrews (1994).
- 5 H.Alloul. Private communication.
- 6 W.J.Webster. *PhD Thesis*, University of St.Andrews (1993).
- 7 H.Alloul, T.Ohno and P.Mendels. *Phys. Rev. Lett.*, **63** (1989) 1700.
- 8 J.B.Parise, P.L.Gai, M.K.Crawford and E.M.McCarron. *Mat. Res. Soc. Proc. High Tc Supercond.*, San Diego, **Proc. 156** (1989) 105. (Edited by J.Jorgensen et al.).
- 9 A.J.Vega, M.K.Crawford, E.M.McCarron and W.E.Farneth. *Phys. Rev. B*, **40** (1989) 8878.

# APPENDIX 1

## X-Ray Spectra For Samples Before Quenching

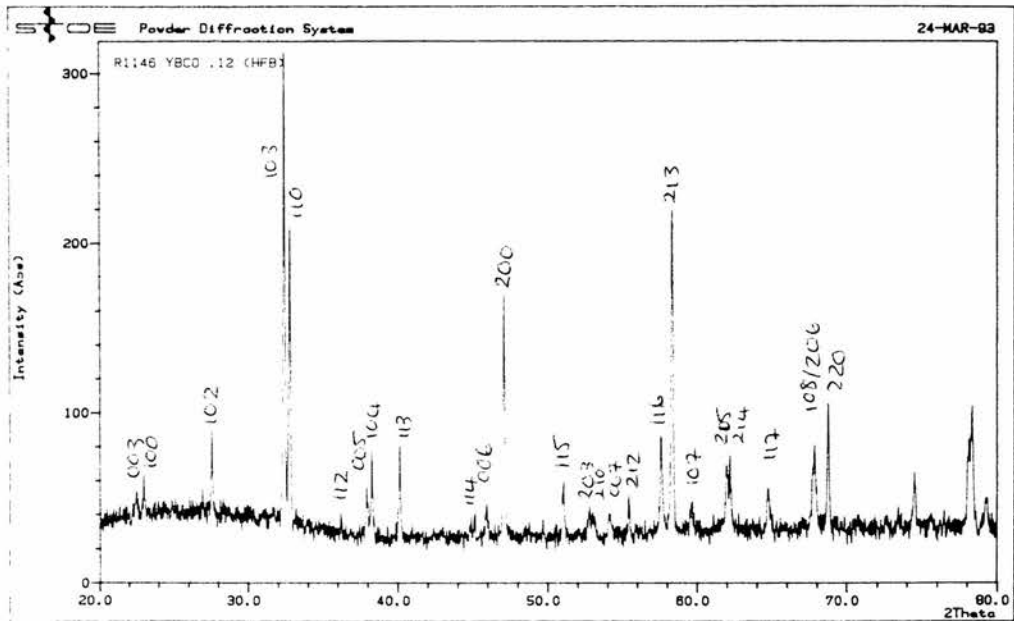
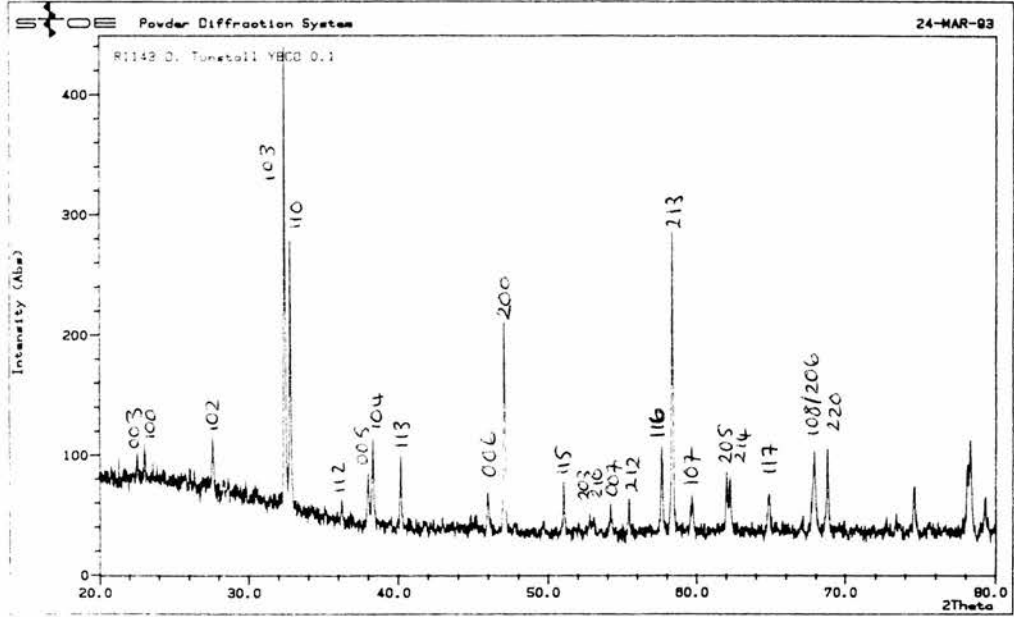


*Appendix 1: X-Ray Spectra For Samples Before Quenching*

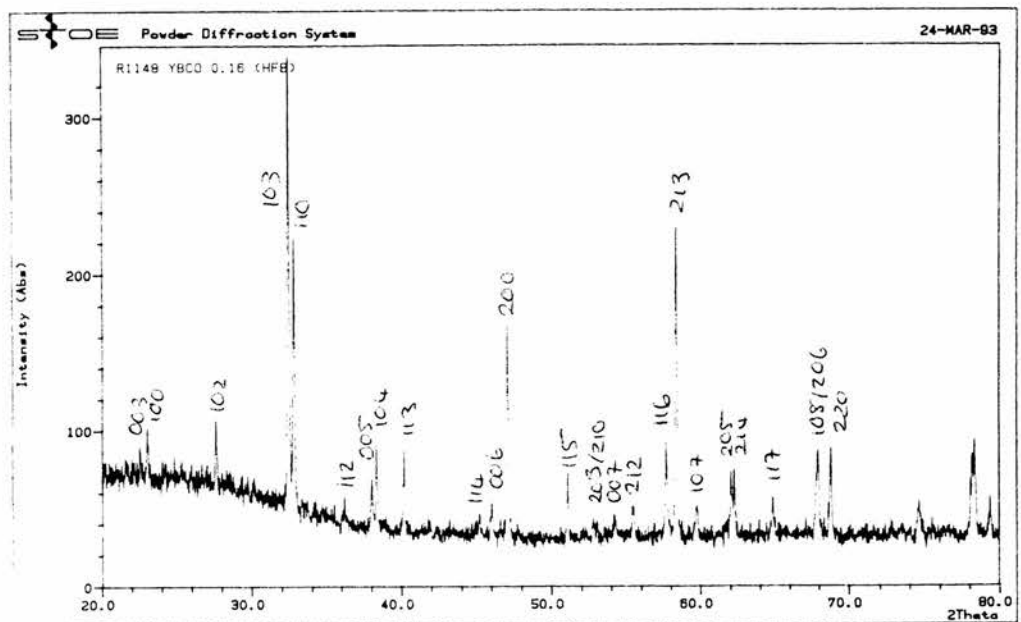
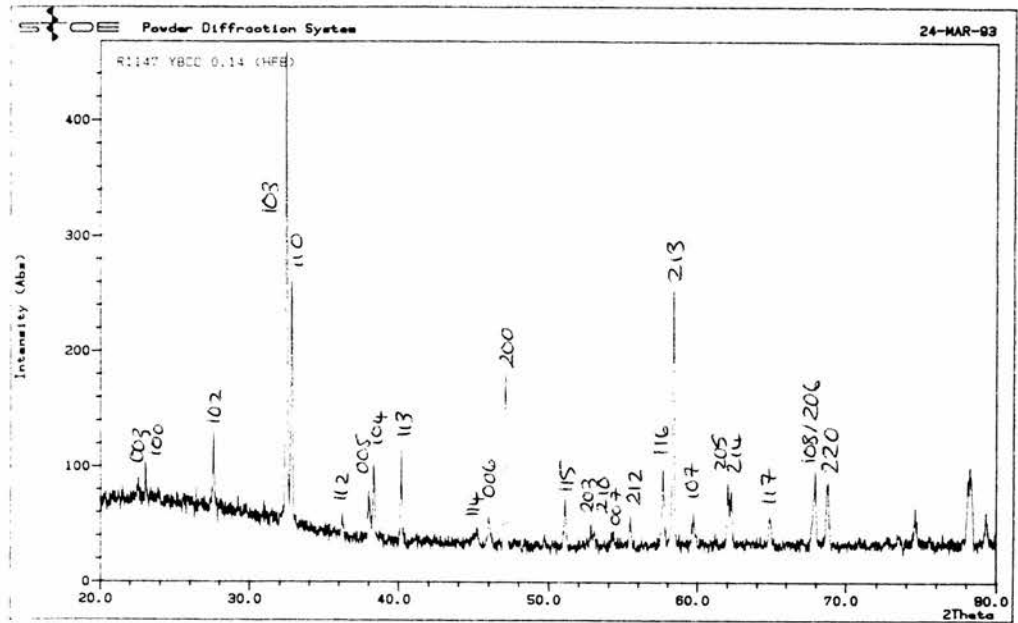


# APPENDIX 2

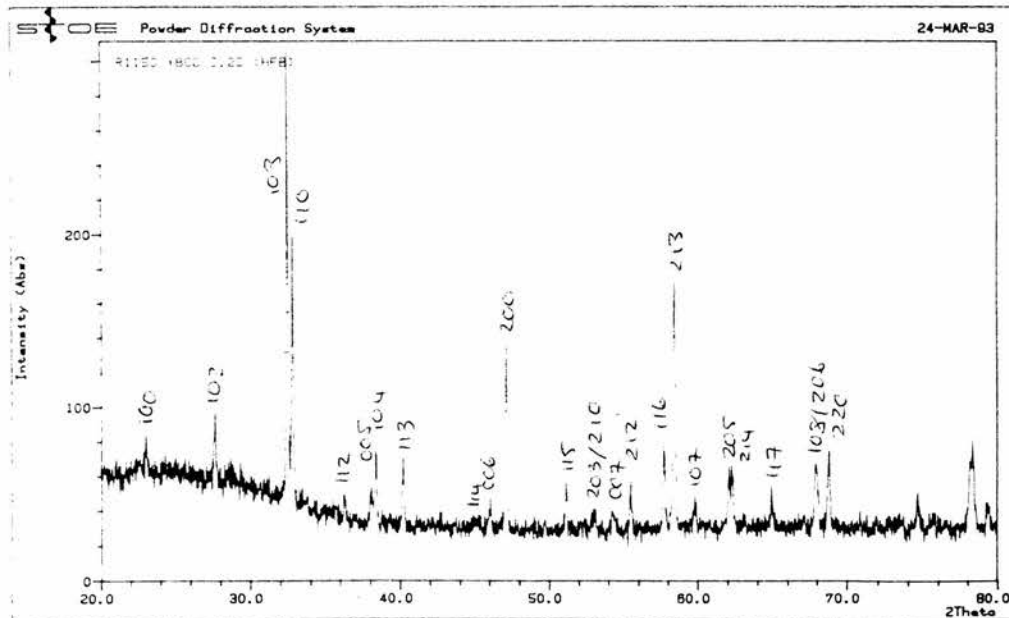
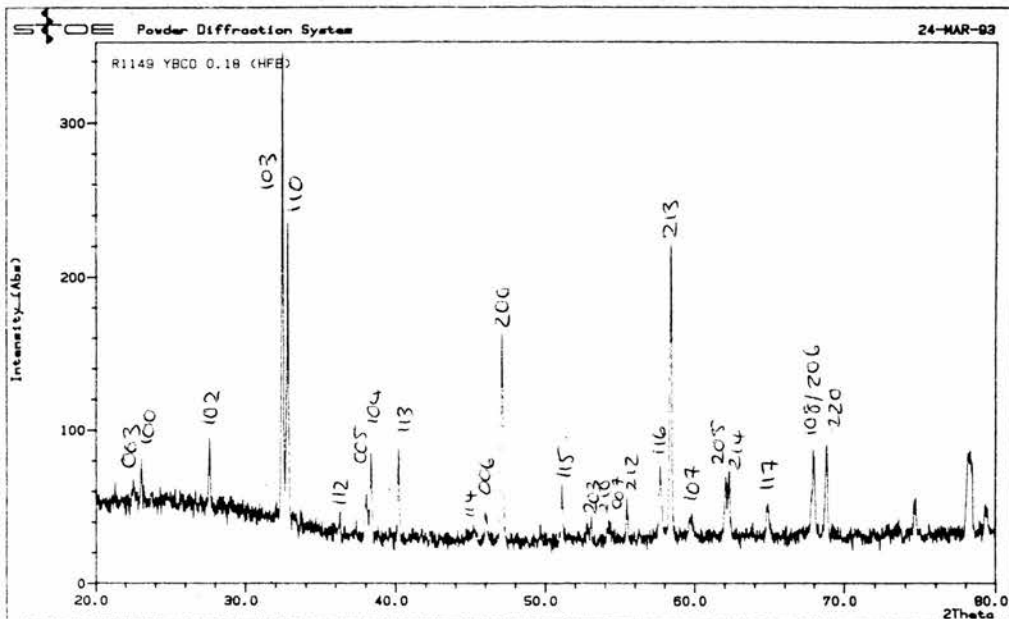
## X-Ray Spectra For Quenched Powder Samples



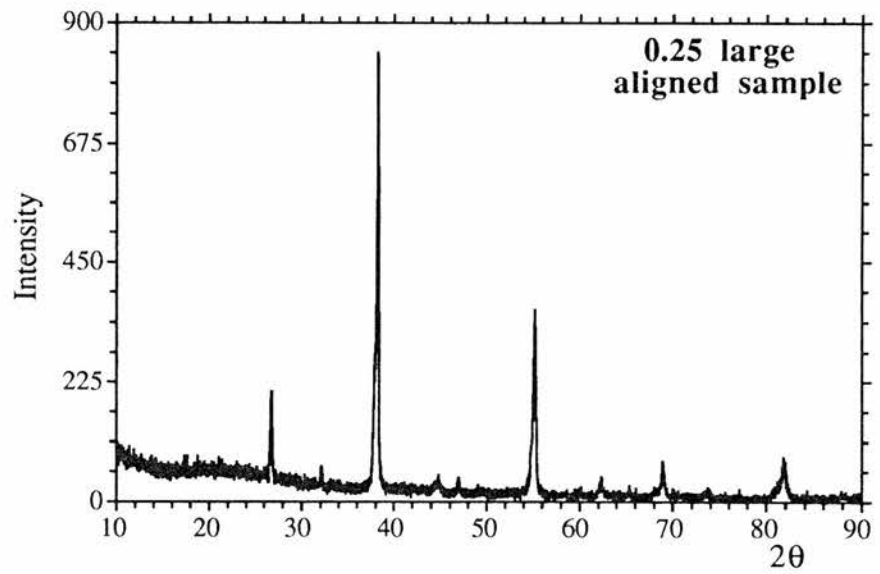
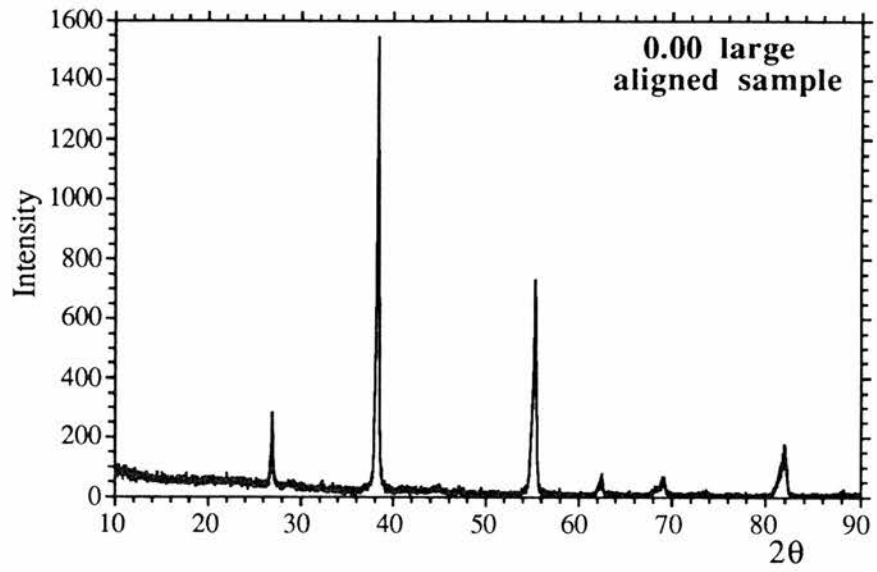
## Appendix 2: X-Ray Spectra For Quenched Powder Samples



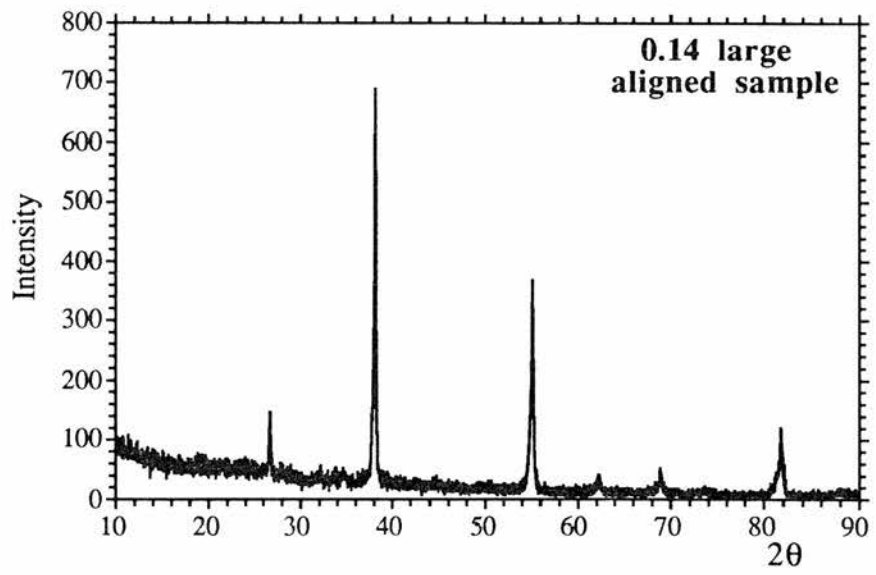
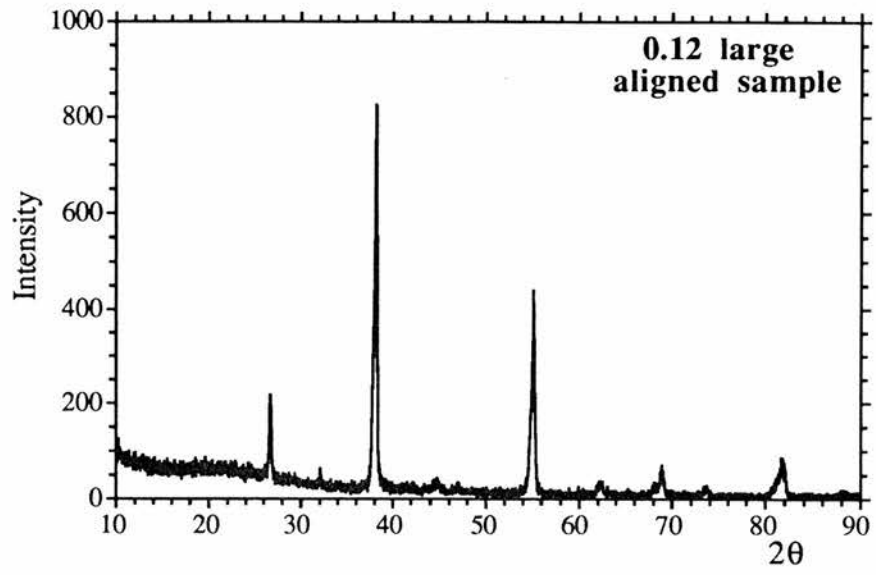
Appendix 2: X-Ray Spectra For Quenched Powder Samples



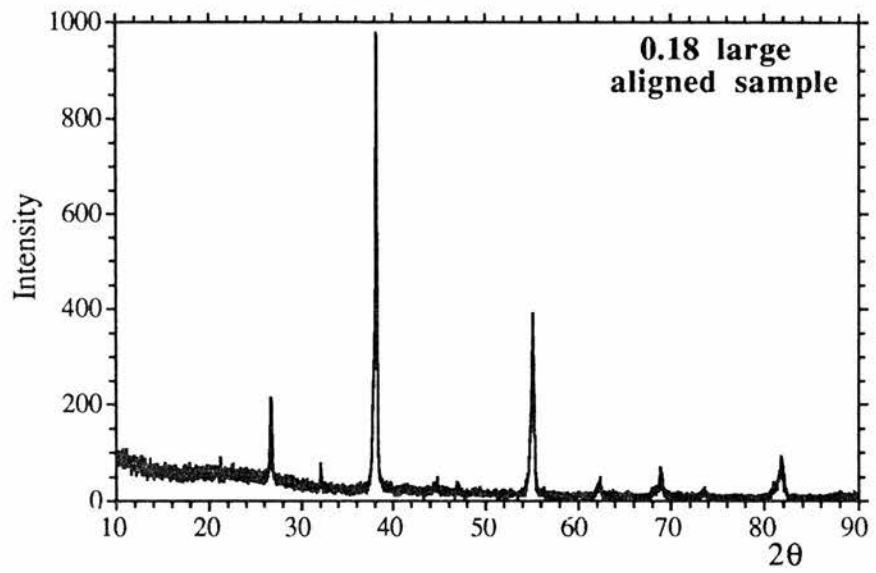
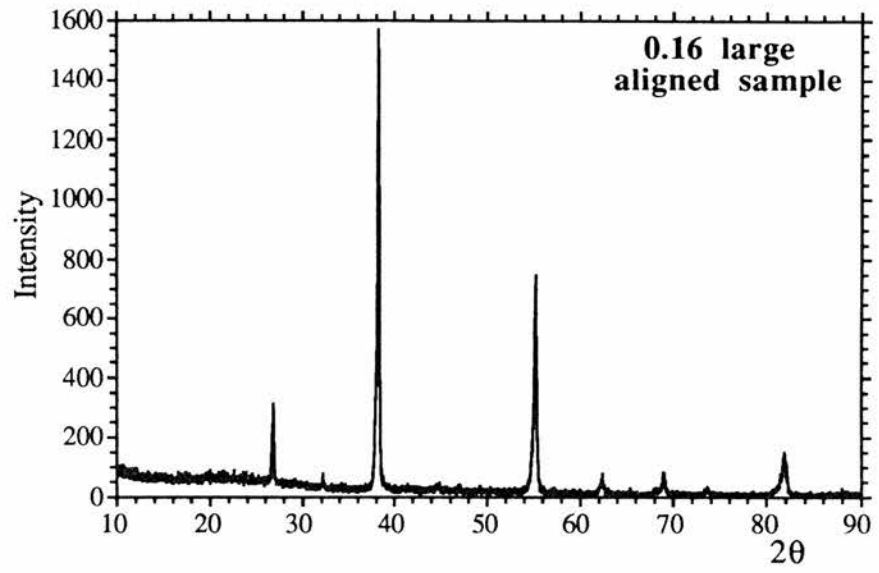
# APPENDIX 3



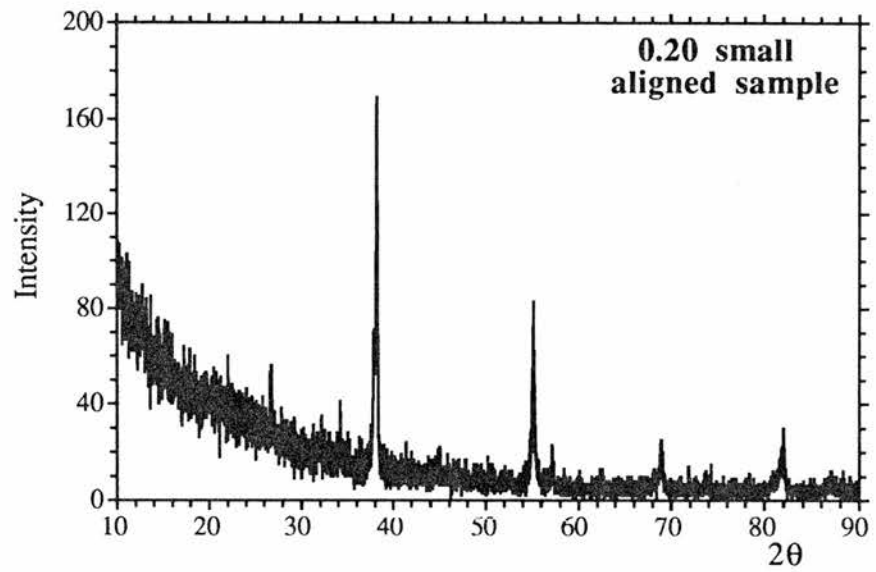
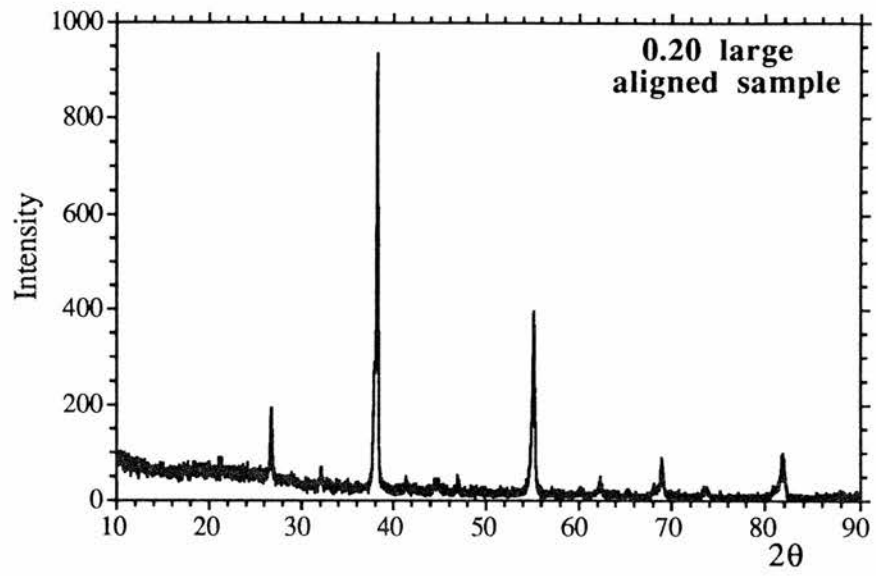
*Appendix 3: X-Ray Spectra - Aligned Samples*



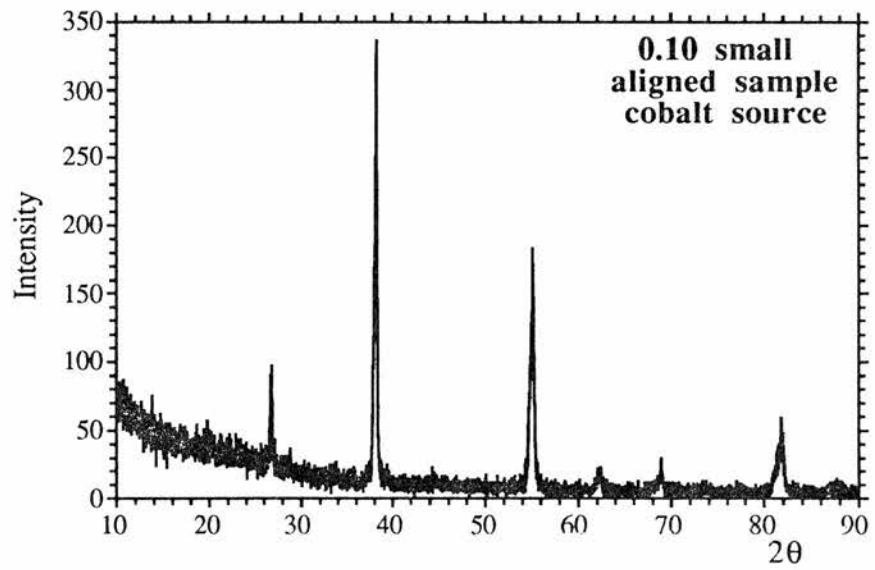
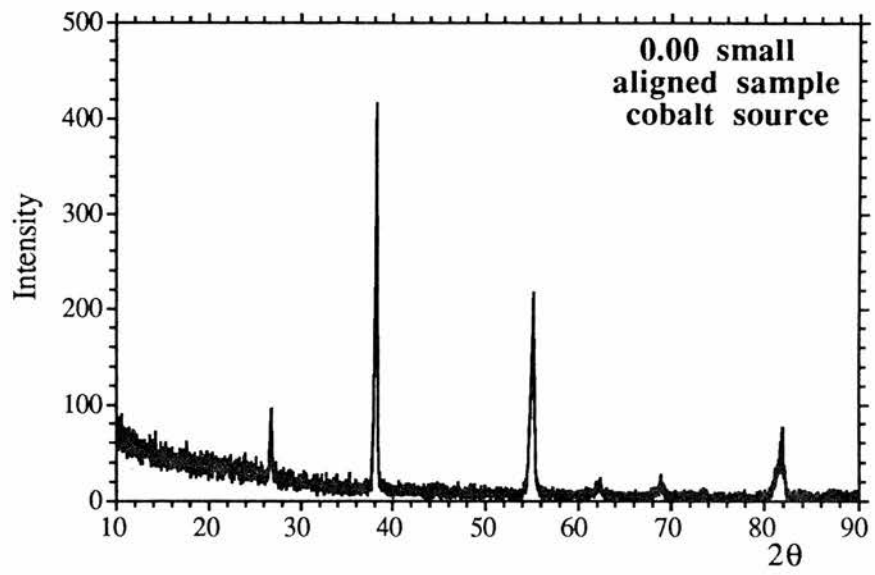
*Appendix 3: X-Ray Spectra - Aligned Samples*



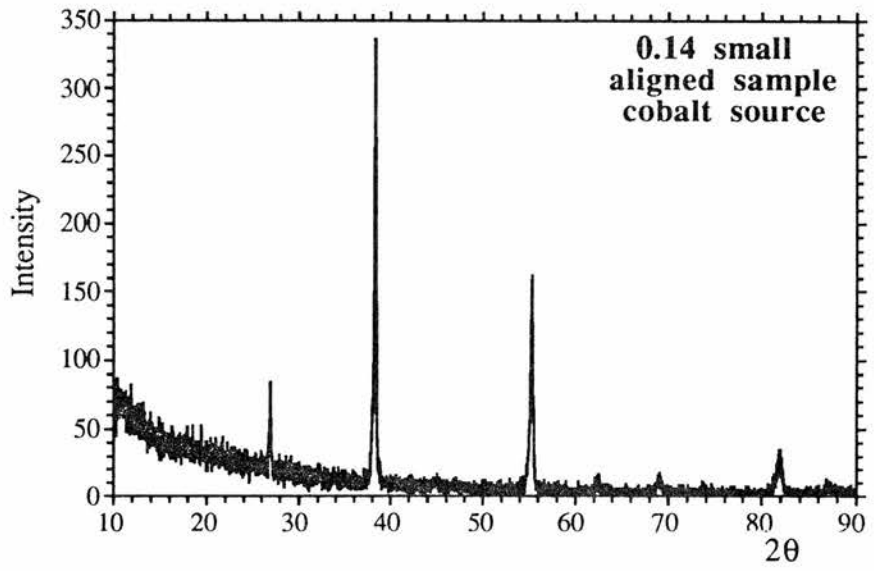
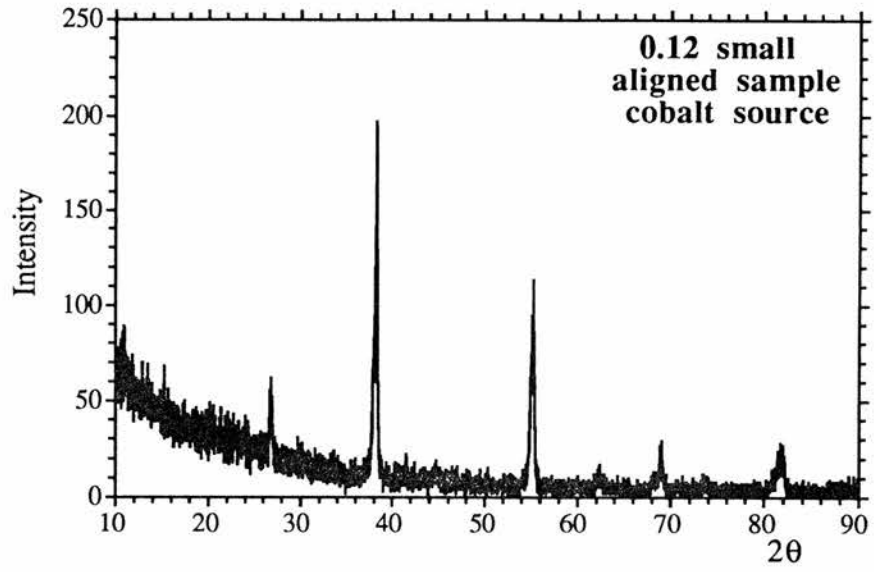
*Appendix 3: X-Ray Spectra - Aligned Samples*



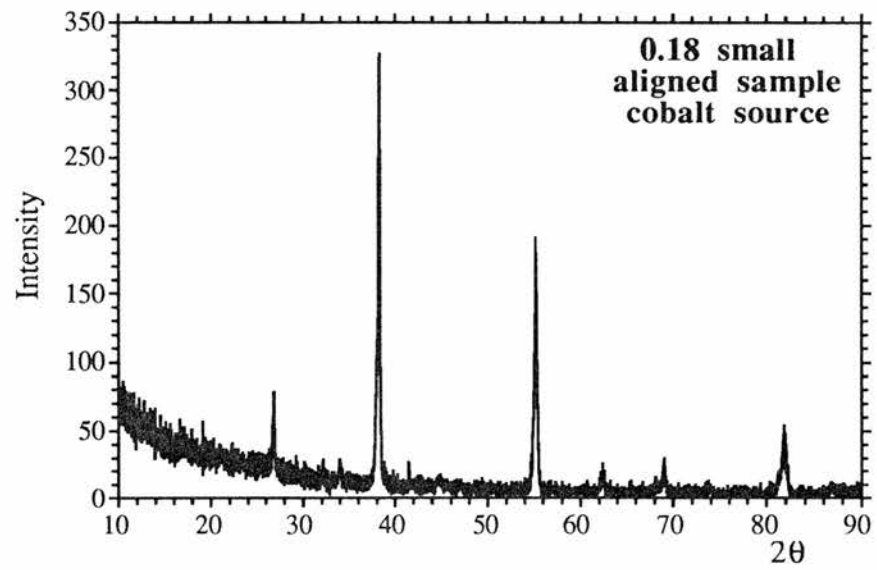
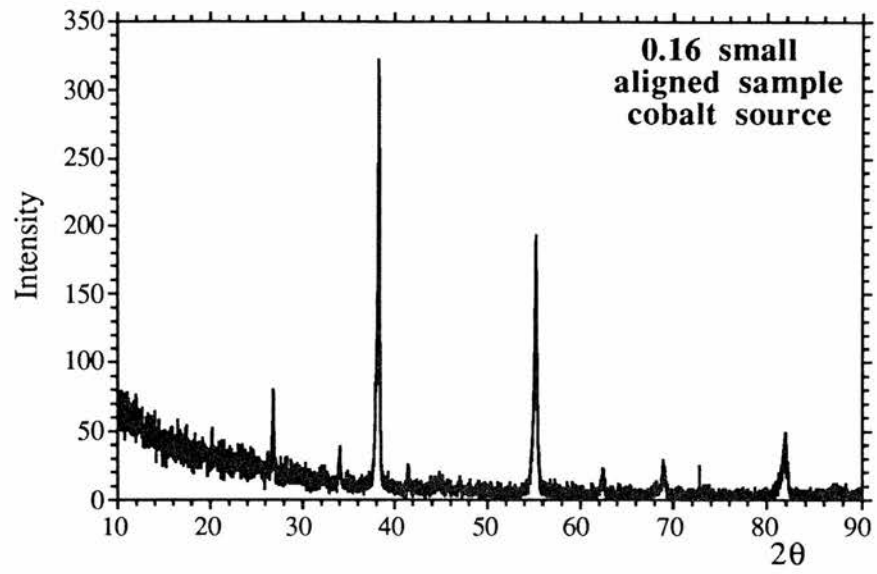
*Appendix 3: X-Ray Spectra - Aligned Samples*



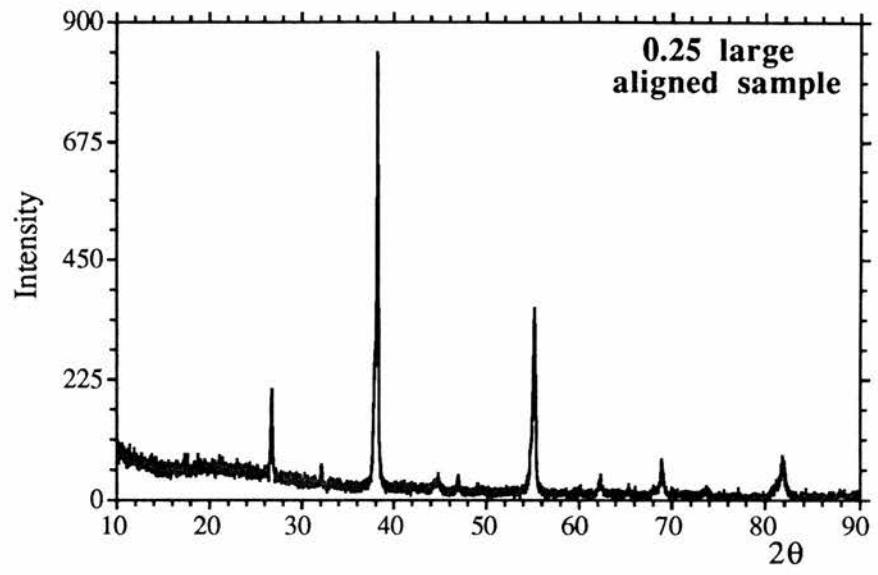
*Appendix 3: X-Ray Spectra - Aligned Samples*



*Appendix 3: X-Ray Spectra - Aligned Samples*



*Appendix 3: X-Ray Spectra - Aligned Samples*



0.25 small



## APPENDIX 4

### Calculation of the Mobility

The electrical conductivity,  $\sigma$ , is the sum of contributions due to electrons and holes in the system. For most cuprate superconductors, only conduction holes exist, so that

$$\sigma = ne\mu$$

where  $e$  is the charge of an electron,  $\mu$  is the mobility which is defined as the magnitude of the drift velocity per unit electric field,  $n$  is the carrier concentration and may be calculated from the Hall number. In this case, the system may be classed as a simple metal (since only holes conduct) and so the Hall number gives the carrier concentration per formula unit volume. For  $\text{YBa}_2\text{Cu}_3\text{O}_x$ , the Hall number is  $\sim 1$  at room temperature; the carrier concentration  $n$  is  $\sim 7 \times 10^{21} \text{ cm}^{-3}$ .

The above equation may be rearranged (and the values substituted) to find the mobility.

$$\mu = \sigma / ne$$

$$\mu \approx 300 \Omega^{-1} \text{cm}^{-1} \text{ from experimental data}$$

$$e = 1.6022 \times 10^{-19} \text{ C}$$

$$n \approx 7 \times 10^{21} \text{ cm}^{-3}$$

This gives the value  $\mu \approx 0.3 \text{ cm}^2 \text{V}^{-1} \text{s}^{-1}$

## APPENDIX 5

### Contributions to Scientific Journals and Meetings

#### Publications:

H.F.Booth, D.P.Tunstall and J.T.S.Irvine. "A Study of  $(Y_{1-x}Ca_x)Ba_2Cu_3O_{6+\delta}$  by  $^{89}Y$  NMR", *Physica C*, **235-240** (1994) p1585.

D.P.Tunstall, G.P.Dai, W.J.Webster, H.Booth, S.Arumugam, R.-S.Liu and P.P.Edwards. "A Thallium, Yttrium and Copper NMR Study of the  $(Tl_{0.5}Pb_{0.5})Sr_2(Ca_{1-y}Y_y)Cu_2O_{7-\delta}$  System", *Superconductor Science and Technology*, **6** (1993) p33-41.

G.Dai, D.P.Tunstall, W.J.Webster, H.Booth, S.Arumugam, R.-S.Liu and P.P.Edwards. "Yttrium NMR Study in the  $(Tl_{0.5}Pb_{0.5})Sr_2(Ca_{1-y}Y_y)Cu_2O_7$  System", *Proceedings of the Beijing International Conference: High Temperature Superconductivity (BHTSC '92)*, p461-5, (World Scientific, Singapore).

#### Poster Contributions To Scientific Meetings:

H.F.Booth, D.P.Tunstall and J.T.S.Irvine. "Calcium Doped YBCO; An NMR Study", *The 4th International Conference on the Materials and Mechanisms of Superconductivity - High Temperature Superconductors, Grenoble (France)*, July 1994.

H.F.Booth, G.J.Stockham and D.P.Tunstall. "Temperature Dependence of Resistivity in Quenched  $(Y_{1-x}Ca_x)Ba_2Cu_3O_{6+\delta}$ ", *Condensed Matter and Materials Physics Conference (CMMP '93)*, Leeds, December 1993.

H.F.Booth, D.P.Tunstall and J.T.S.Irvine. "The Interaction Between Calcium Content and Oxygen Stoichiometry in Quenched  $(Y_{1-x}Ca_x)Ba_2Cu_3O_{6+\delta}$ ", *Condensed Matter and Materials Physics Conference (CMMP '92)*, Sheffield, December 1992.

D.P.Tunstall, G.P.Dai, H.Booth, S.Arumugam, R.-S.Liu and P.P.Edwards.  
"(Tl<sub>0.5</sub>Pb<sub>0.5</sub>)Sr<sub>2</sub>(Ca<sub>1-x</sub>Y<sub>x</sub>)Cu<sub>2</sub>O<sub>7</sub>; Thallium, Yttrium and Copper NMR in a  
Superconductor", *British Radio-Frequency Spectroscopy Group Meeting (BRFSG*  
*'92), Nottingham, April 1992.*

**Other Conferences, Meetings and Courses Attended:**

*British Radio-Frequency Spectroscopy Group Meeting - NMR in Solids (BRFSG '93),  
University of St.Andrews, 14<sup>th</sup>-15<sup>th</sup> September 1993.*

*Condensed Matter and Materials Physics Conference (CMMP '94), Warwick,  
December 1994.*

*Solid State Chemistry and Superconductivity II - International Conference,  
U.M.I.S.T., 20<sup>th</sup>-22<sup>nd</sup> September 1993.*

*Low Temperature Techniques Course, University of Birmingham, 6<sup>th</sup> November  
1991.*

*Microcomputers in Experimental Physics, The Institute of Physics, 28<sup>th</sup> April 1992.*

*2<sup>nd</sup> Workshop on Magnetic Measurement Techniques, Rutherford-Appleton  
Laboratory, 17<sup>th</sup> November 1993.*